

**Russian Academy of Sciences
Siberian Branch
Institute of Computational Technologies**

**«Tsunami Hazard Assessment Project»
02H – 12**

Final Stage

Project Coordinators:

Leonid B.Chubarov
Viacheslav K.Gusiakov

Principal Investigators:

Leonid B.Chubarov
Viacheslav K.Gusiakov
Alexander D. Rychkov

Prepared by:

Sonya A.Beisel, PhD, Researcher
Leonid B.Chubarov, PhD, Professor
Viacheslav K.Gusiakov, PhD, Professor
Tamara V.Kalashnikova, Computer graphics
Gayaz S.Khakimzyanov, PhD, Professor
Andrey G.Marchuk, PhD, Professor
Alexander D. Rychkov, PhD, Professor

Novosibirsk,
2013

Introduction	4
1. Overview of data availability and numerical algorithms used for tsunami modeling	5
1.1. <i>Historical tsunamis in Japan – general overview.....</i>	5
1.2. <i>Problems of parameterization of sources of historical tsunamis</i>	11
1.3. <i>Digital bathymetry and its optimization</i>	13
1.4. <i>Description of the numerical techniques</i>	16
1.5. <i>Calculation of initial bottom displacements</i>	18
1.6. <i>Calculation of “wet line”</i>	22
1.7. <i>1D calculation of run-up.....</i>	22
1.7.1. <i>Analytical formulas</i>	23
1.7.2. <i>Run-up calculation using the analytic solution at the shoreline</i>	24
1.7.3. <i>1D Run-up calculation using the large particles method.....</i>	28
1.8. <i>2D calculation of run-up.....</i>	28
1.9. <i>Problems associated with verification of numerical models</i>	32
2. Results of numerical experiments	43
2.1. <i>1854 Ansei-Tokai tsunami</i>	45
2.1.1. <i>Basic information on earthquake and tsunami.....</i>	45
2.1.2. <i>Adopted source model and calculation of initial bottom displacement.....</i>	48
2.1.3. <i>Calculation domain and virtual coastal points</i>	49
2.1.4. <i>Analysis of computed wave height distribution</i>	49
2.1.5. <i>1D calculation of tsunami run-up and estimation of inundation limits.....</i>	51
2.1.6. <i>2D calculation of tsunami run-up and estimation of inundation limits.....</i>	56
2.2. <i>1923 Kanto tsunami</i>	59
2.2.1. <i>Basic information on earthquake and tsunami.....</i>	59
2.2.2. <i>Adopted source model and calculation of initial bottom displacement.....</i>	62
2.2.3. <i>Calculation domain and virtual coastal points</i>	63
2.2.4. <i>Analysis of computed wave height distribution</i>	64
2.2.5. <i>1D calculation of tsunami run-up and estimation of inundation limits.....</i>	65
2.2.6. <i>2D calculation of tsunami run-up and estimation of inundation limits.....</i>	71
2.3. <i>1944 Tōnankai tsunami.....</i>	73
2.3.1. <i>Seismotectonic features of the area. Basic information on earthquake and tsunami.....</i>	73
2.3.2. <i>Adopted source model and calculation of initial bottom displacement.....</i>	75
2.3.3. <i>Calculation domain and virtual coastal points</i>	75
2.3.4. <i>Analysis of computed wave height distribution</i>	76
2.3.5. <i>1D calculation of tsunami run-up and estimation of inundation limits.....</i>	78
2.3.6. <i>2D calculation of tsunami run-up and estimation of inundation limits.....</i>	84
2.4. <i>1946 Nankai tsunami</i>	88
2.4.1. <i>Seismotectonic features of the area. Basic information on earthquake and tsunami.....</i>	88
2.4.2. <i>Adopted source model and calculation of initial bottom displacement.....</i>	91
2.4.3. <i>Calculation domain and virtual coastal points</i>	92
2.4.4. <i>Analysis of computed wave height distribution</i>	92
2.4.5. <i>1D calculation of tsunami run-up and estimation of inundation limits.....</i>	94
2.4.6. <i>2D calculation of tsunami run-up and estimation of inundation limits.....</i>	100
2.5. <i>2011 Tohoku tsunami.....</i>	104
2.5.1. <i>Basic information on earthquake and tsunami.....</i>	104
2.5.2. <i>Adopted source model and calculation of initial bottom displacement.....</i>	106
2.5.3. <i>Calculation domain and virtual coastal points</i>	106
2.5.4. <i>Analysis of computed wave height distribution</i>	107

2.5.5.	<i>1D calculation of tsunami run-up and estimation of inundation limits.....</i>	<i>109</i>
2.5.6.	<i>2D calculation of tsunami run-up and estimation of inundation limits.....</i>	<i>115</i>
3.	Analysis of sensitivity of computed wave heights on the source and friction parameters (for the 2011 Tohoku tsunami)	128
3.1.	<i>Analysis of sensitivity of computed wave heights on the source parameters (for the 2011 Tohoku tsunami).....</i>	<i>128</i>
3.2.	<i>Analysis of sensitivity of computed wave heights on the friction parameter (for the 2011 Tohoku tsunami).....</i>	<i>149</i>
4.	Conclusions (applicability of numerical algorithms for reproducing of main features of selected historical tsunamis).....	151
4.1.	<i>General conclusions</i>	<i>151</i>
4.2.	<i>Conclusions for Section 3.1</i>	<i>151</i>
5.	References.....	152

Introduction.

Tsunamis are a series of the long-period oceanic waves generated by underwater earthquakes, submarine or subaerial landslides or volcanic eruptions. They are among the most dangerous and complex natural phenomena, being responsible for great losses of life and extensive destruction of property in many coastal areas of the World Ocean. The tsunami phenomenon includes three overlapping but quite distinct physical stages: (1) generation by any external force that disturbs a water column, (2) propagation with a high speed in the open ocean and (3) run-up in the shallow coastal water and inundation of the dry land. Most tsunamis occur in the Pacific, but they are known in all other areas of the World Ocean like the Atlantic and the Indian oceans, the Mediterranean and many marginal seas. Tsunami-like phenomena happen even in lakes, large man-made water reservoirs and big rivers.

In terms of documented total damage and loss of human lives, tsunamis do not come first among other natural hazards. With an estimated 750,000 fatalities, resulted from tsunamis for all historical times (Gusiakov et al., 2007), they rank fifth after earthquakes, floods, typhoons and volcanic eruptions. However, because they can affect densely populated and usually well-developed coastal areas, tsunamis can have an extremely adverse impact on the socioeconomic infrastructure of society, which is strengthened by their full suddenness, terrifying rapidity, and their potential for heavy destruction of property and high percentage of fatalities among the population exposed to their action.

In tsunami waves, water particles move in ellipses with the horizontal axis exceeding the vertical one in ratio from 1:10 to 1:100, involving in movement the whole water column from surface to bottom. Dominating the horizontal component of movement is one of the basic features of tsunamis that differs them from ordinary storm waves. In deep water, tsunami height hardly exceeds one meter, and they do not present any danger for ships in the open sea. When approaching the shore, where the water depth decreases, the height of waves and the current velocity increase, reaching a maximum near the coastline. Due to their great wavelength, tsunamis rarely approach the coast as breaking waves, normally, they appear as a quick succession of floods and ebbs producing strong (up to 10 m/s) currents (Bryant, 2001)

Destruction from tsunamis results from the three main factors: inundation of salt water, dynamic impact of water current, and erosion. Considerable damage is also caused by floating debris that emphasize a destructive force of the water flood. Flotation and drag force can destroy frame buildings, overturn railroad cars and move big ships deeply in-land. Ships in harbors and port facilities can be damaged by strong currents and surge action caused by even weak tsunamis.

Most of destructive tsunamis can be roughly divided into two categories: local or regional and trans-oceanic. For local tsunamis, destructive effect is confined to the nearest coast located within one hour of propagation time (from one hundred to one thousand km). In all tsunamigenic regions of the World Ocean,

most of damage and casualties come from local tsunamis. Far less frequent but potentially much more hazardous are trans-oceanic tsunamis capable of widespread distribution. Formally, this category includes the events that had run-up higher than 5 meters at a distance of more than 5000 km. Historically, all trans-oceanic tsunamis are known in the Pacific with only two exceptions – the 1755 Lisbon tsunami, that reached the Caribbean with 5-7m waves and the 2004 Sumatra tsunami, that resulted in fatalities as far as at the east coast of Africa (Somalia).

The present report summarizes the results obtained during the pilot study for numerical modeling of tsunami generation, propagation and coastal flooding for the eastern coast of Japan undertaken by the contract between the AIG and the joint research team consisted from the tsunami experts of the Tsunami Laboratory of the Institute of Computational Mathematics and Mathematical Geophysics SB RAS and experts in numerical modeling of the Institute of Computational Technologies SB RAS. The main purpose of the pilot project was the capacity demonstration for building of throughout technological chain for realistic numerical modeling of tsunami generation, propagation and coastal flooding for further application in assessment of potential damage to insured property in tsunami-prone coastal areas.

1. Overview of data availability and numerical algorithms used for tsunami modeling

1.1. Historical tsunamis in Japan – general overview

Japan is located in tectonically very complicated area that is a junction of three major tectonic plates – Eurasian Plate, Pacific Plate and Philippine Plate. The latter two contact with the Eurasian Plate along the subduction type of boundaries that are morphologically displayed themselves as deep water trenches where major subduction earthquakes periodically occur. General map of regional seismicity in and around Japan is shown in Fig. 1.1.1. The main area of the shallow-depth earthquakes is connected with the leading edge of the continental lithosphere overriding the subducting oceanic thrust in the wide stripe located east of the Japanese archipelago. Namely, within this stripe all the major tsunamigenic earthquakes, including the 2011 Tohoku mega-quake, occur. Source mechanism of this largest tsunamigenic earthquakes is predominantly low-angle thrust, however, for some of them reverse dip-slip mechanisms are also possible (Lobkovsky, Baranov, 1982).

Another area where the large tsunamigenic earthquakes repeatedly occur is associated with the major tectonic boundary stretching along the western coast of Honshu and Hokkaido islands in the eastern part of the Japan Sea from the Noto peninsula to the north. This boundary marks the contact between the Euroasia Plate and Japan Microplate. The focal mechanisms of these major earthquakes are predominantly dip-slip reverse faulting on a plane dipping relatively steeply (Fukao, Furumoto, 1975).

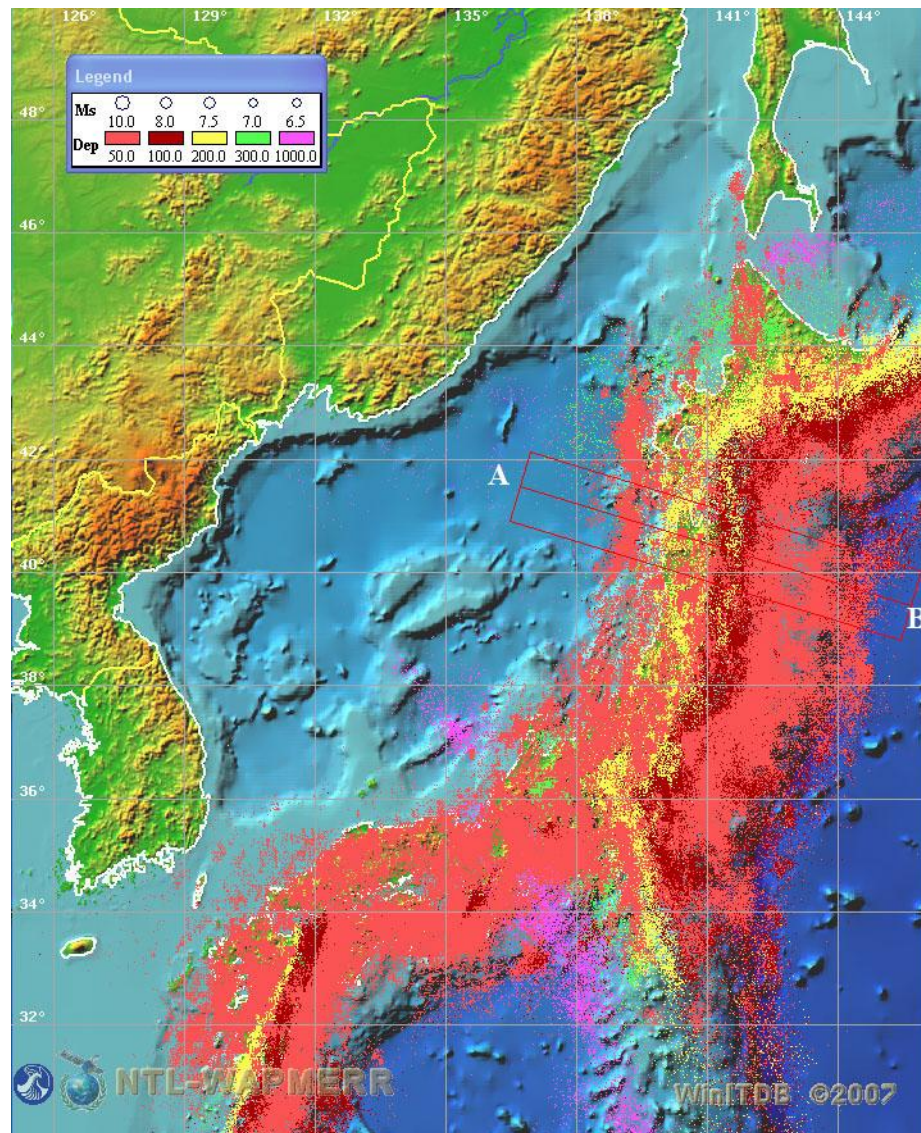


Fig. 1.1.1. Visualization of the full JMA seismic catalog. Epicenters of nearly 2,100, 000 earthquakes occurred from 1923 to 2011 are shown.

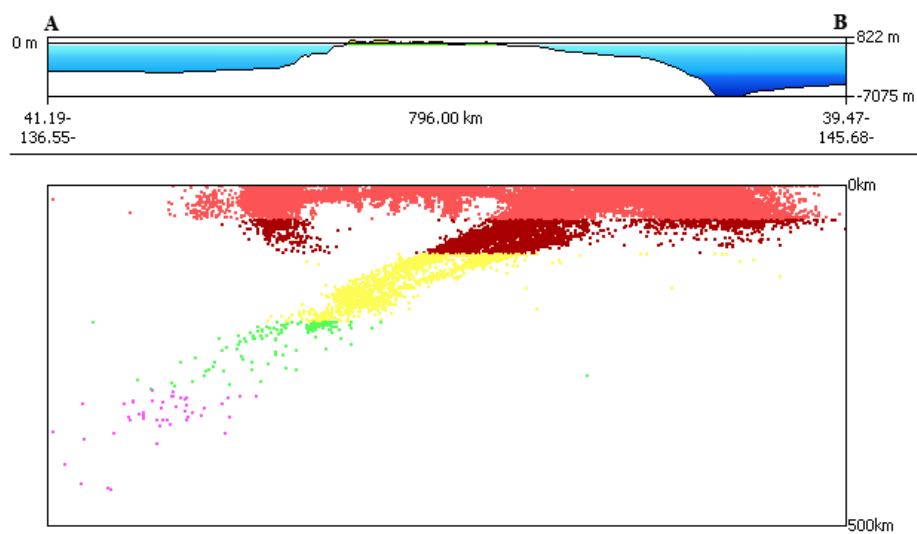


Fig. 1.1.2. Vertical cross section of the seismicity pattern along the profile A-B in Fig. 1.1.1.

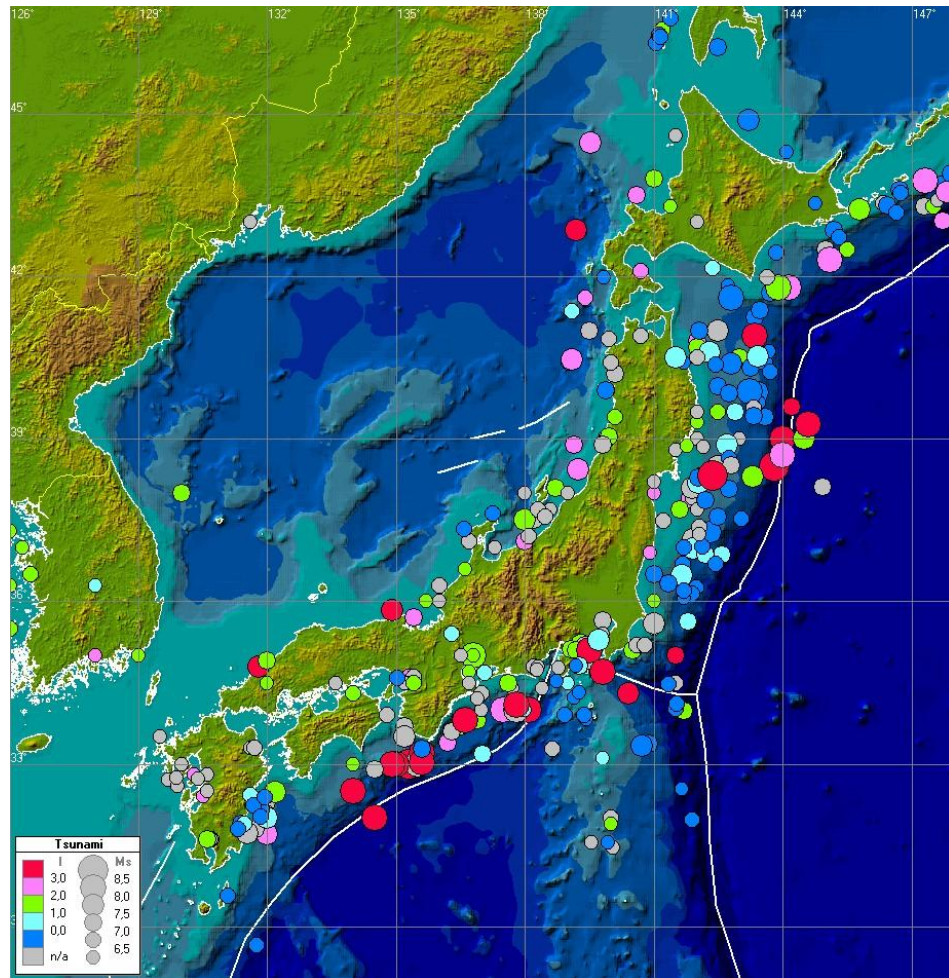


Fig. 1.1.3. Location map of historical tsunamigenic earthquakes occurred in Japan (within the area 29° – 47° N, 126° – 148° E). Positions of 317 historical events occurred from 684AD to 2012 are shown. Size of circles is proportional to the event magnitude M_s , color represents the tsunami intensity I (on the Soloviev-Imamura scale), gray color represents the tsunamigenic events with unknown intensity. Solid white lines show the position of the main tectonic boundaries in the region.

Location map of tsunamigenic earthquakes in the Japan Sea is shown in Fig. 1.1.3. Altogether, there are historical evidences for about **317** tsunamigenic events occurred in this area since 684AD (Soloviev, Go, 1974; Iida, 1984; Watanabe, 1985). However, reliable quantitative data, allowing to locate the position of sources and to evaluate the size (magnitude) of the earthquakes, exist only for instrumental period (since 1900). Among these 317 historical events, there were about **30** destructive tsunamis with maximum run-ups more than 10 m that resulted in numerous fatalities (more than 1000 victims) and large material destruction and damage. Location map of sources of these tsunamis is shown in Fig. 1.1.4. It is interesting to note that only **14** events from the list of top 30 deadliest Japanese tsunamis are included in the list of top 30 largest (by their magnitude) submarine earthquakes in Japan. This fact clearly demonstrates that magnitude value is an important but not the only parameter controlling the destructive effect of a tsunami generated by a submarine earthquake. Detailed consideration of the actual dependence of tsunami intensity on the source magnitudes (both M_s and M_w) is given in (Gusiakov, 2011). Here, in Fig. 1.1.5 we reproduce just one of basic pictures given in this study – dependence of tsunami intensity I on M_w magnitude

for submarine earthquake occurred from 1900 to 2012 in the Japan – Kuril-Kamchatka – Alaska-Aleutian regions.

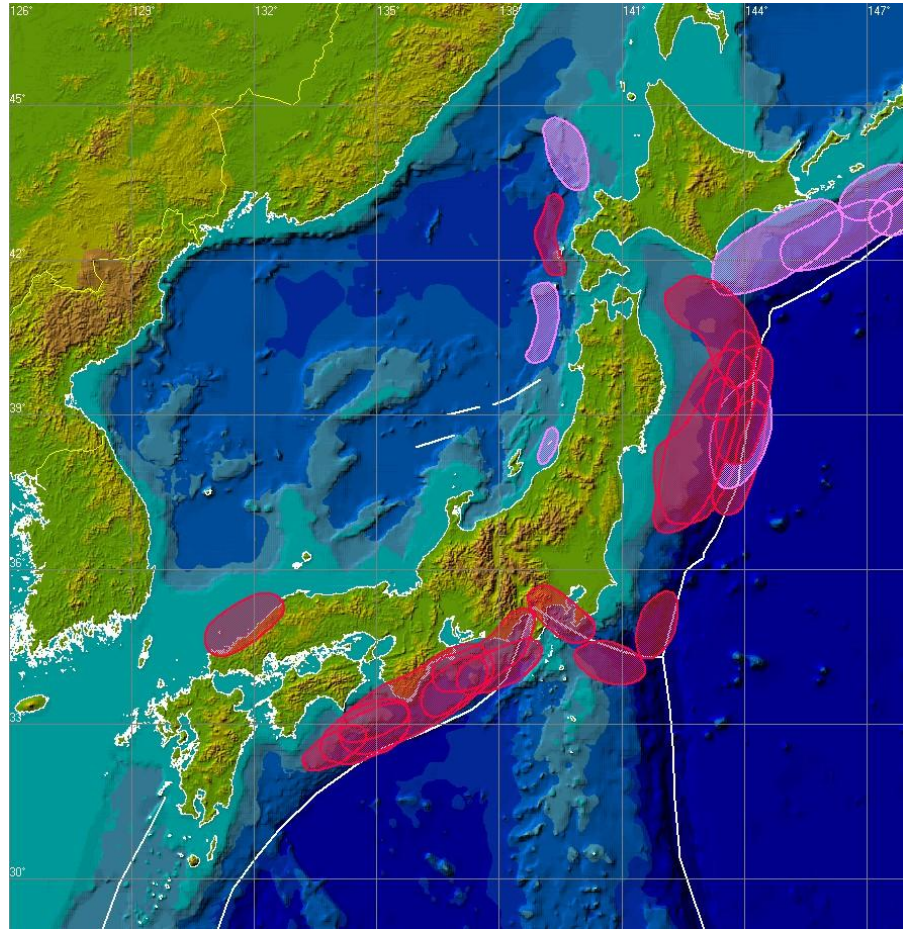


Fig. 1.1.4. Location map of largest historical tsunamigenic earthquakes occurred in Japan from 684 AD to 2011. Color represents the estimated tsunami intensity I (on the Soloviev-Imamura scale): red - $I \geq 3$, magenta - $2 \leq I < 3$. Solid white lines show the position of the main tectonic boundaries in the region.

The diagram $I(M_w)$ clearly demonstrates that there is little to no correlation of tsunami intensity on the source earthquake magnitude. We can note only a general trend for the growth of intensity with an increase of magnitude. Scattering of the data is considerable and in the magnitude range 7.0 – 8.0, where the majority of tsunamigenic earthquakes occur, exceeds six grades on the intensity scale. This means that tsunami heights at the coast may differ more than 64 times for the earthquakes with similar magnitudes. Such a strong scattering makes prediction of wave heights in the near-field, based solely on the source magnitude, be a very difficult task.

The solid line in Fig. 1.1.5 shows the theoretical dependence I on M_w

$$I = 3.55 \cdot M_w - 27.1 \quad (1.1)$$

obtained in (Chubarov, Gusiakov, 1985) by means of numerical modeling of tsunami generation and propagation. In that work, a series of calculations were made for a set of typical tsunamigenic sources with different M_w value placed in a basin with a model relief representing basic features of the coastal morphology (shelf, continental slope, deep-water terrace, deep-water trench). As one can see

from Fig. 1.1.5, relation (1.1) correctly enough reflects a general trend of the growth of tsunami intensity with M_w magnitude. Systematic deviation can be noted only at its upper end for the largest possible tsunamis (1952 Kamchatka, 1960 Chile, 1964 Alaska, 1957 Aleutians) where the actual tsunami intensity is 1 or 2 units less than can be expected from formula (1.1).

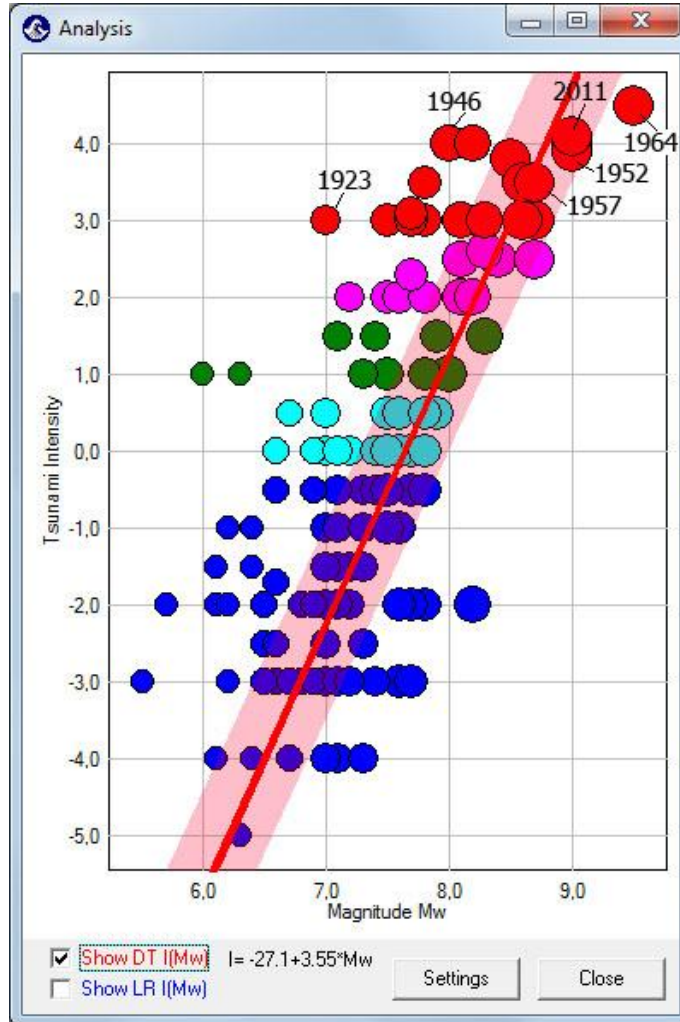


Fig. 1.1.5. Dependence of tsunami intensity I on M_w magnitude for submarine earthquake occurred from 1900 to 2012 in the Japan – Kuril-Kamchatka – Alaska-Aleutian regions. Solid red line shows the expected dependence I on M_w obtained in (Chubarov, Gusiakov, 1985). Wide pink strip shows the confidence area around this line (taking into account the actual accuracy of intensity determination).

The reasons for so significant scattering of tsunami intensity for the earthquakes with similar magnitudes are multi-fold. Several factors contributing to this effect can be indicated:

- (1) a difference in the water depth in a source area. The earthquake in the deep ocean disturbs a greater volume of water that increases the initial tsunami energy. This effect was first noted by I.Iida (Iida, 1970) who analyzed the intensity of the Japanese tsunamis depending on positions of their sources on the continental slope. One should also take into account that part of events presented in Fig. 1.1.3 and Fig. 1.1.4 had source areas partly located within

the coast. Such events are obviously less effective generators of tsunami than an earthquake entirely located under the sea bottom.

- (2) a difference in the earthquake source mechanisms. Results of numerical modeling of tsunami generation by an earthquake model (Gusiakov, 1974; Alekseev, Gusiakov, 1984; Comer, 1984) shows that earthquakes with a dip-slip or a low-angle thrust mechanism generate larger tsunami waves as compared to earthquakes having predominantly strike-slip components in their sources. For a model source with a given seismic moment, a pure strike-slip fault generates tsunamis with only 1/10 of deep-water amplitudes as compared to a vertical dip-slip fault (Gusiakov, 1976).
- (3) a difference in the earthquake focus depth. For a point model source increasing focus depth from 30 to 60 km decreases the deep-water amplitudes twice (Gusiakov, 1976). Historical data show that the earthquakes with a focus depth exceeding 80 km do not practically generate significant tsunamis.
- (4) a difference in tectonic settings of the source area (marginal seas, subduction zones, deep-water oceanic plate, etc.). Soloviev (1989) noted that for a given magnitude the earthquakes in the Mediterranean Sea and in the Japan Sea produce a tsunami with intensity at least 1 unit higher than the earthquakes in the subduction zones of the Pacific. A larger thickness of deformable bottom sediments, accumulated in marginal seas, can be the main reason of that.

However, the influence of all these factors on tsunami intensity should be within one order of magnitude (in terms of deep-water wave heights) and therefore cannot explain the whole range of actual scattering in the intensity-magnitude relation. Possibly, the most important factor controlling the resulted intensity is the degree of involvement of secondary mechanisms (foremost being submarine slides and slumps) in the tsunami generation process. This problem was investigated in greater detail in (Gusiakov, 2001).

When discussing the intensity–magnitude relation, a special attention is needed for consideration of the so-called “tsunami-earthquakes” problem. This term was originally introduced by H.Kanamori in the beginning of the 70s for designation of a specific type of submarine earthquakes that generate an anomalously large tsunami as compared to their surface-wave magnitude (Kanamori, 1972). For example, one of the largest in the last century Aleutian tsunami of April 1, 1946 with a maximum run-up 42 m in the source area (Unimak Island) and 20 m in the far-field (Marquesas Islands) was generated by an earthquake of quite a moderate magnitude ($M_s = 7.4$). The magnitude of the earthquake that generated the Sanriku tsunami of June 15, 1896 with 27000 fatalities, is estimated to be as 7.4–7.6. Analyzing these and some other “strange” earthquakes, H.Kanamori proposed the term “tsunami-earthquake” for the events, generating anomalously large tsunami waves as compared to 20-sec surface waves

that used in M_s determination. According to his interpretation, they were the events with an anomalously large time (more than 100 sec) of a rupture process in the source that decreases the excitation of seismic surface waves and increases their tsunami potential. The full list of ten tsunami-earthquakes identified so far is given in (Gusiakov, 2011). On the $I(M_w)$ diagrams these events clearly stand out ordinary tsunamigenic earthquakes by their increased intensity values. However, they can be mixed with tsunamigenic earthquakes with confirmed slumping mechanism in their sources like the Papua New Guinea earthquakes of July 17, 1998.

1.2.Problems of parameterization of sources of historical tsunamis

The main purpose of the Pilot Project is the verification of mathematical models, numerical algorithms and computer codes developed in the ICT and ICMG SB RAS for tsunami modeling. According technical specification to the Pilot Project, five historical tsunamigenic events occurred near eastern coast of Japan were selected for such verification. They are the 2011 Tohoku, 1946 Nankai, 1944 Tonankai, 1923 Kanto and 1854 Ansei-Tokai tsunamigenic earthquakes.

The total time range of the selected events covers more than 150 years. During this period the level of data completeness and the degree of the data accuracy considerably changed, that is why the amount and quality of the observational data available for example, for the 1854 Ansei-Tokai tsunami and 2011 Tohoku tsunami is incomparable. The instrumental measurements of the 2011 Tohoku tsunami heights (both as maximum run-up heights and inundation depths), obtained by the Joint Tohoku Earthquake Tsunami Research Survey Group (Mori et al., 2011), have highest possible accuracy reaching few meters in geographical coordinates and few centimeters in water level as well as density of measurements (more than 5700 measured heights). However, systematic field survey of destructive tsunamis started only in 1992 after the September 2, 1992 tsunami in Nicaragua. For earlier historical events, observational data collected in catalogs and databases are mainly based on witness reports and other anecdotal sources that are not fully reliable especially for old historical events. For these events, it is sometimes difficult to distinguish between two types of measurement (run-up height and inundation depth) as well as assign the exact location for the reported measurement that is quite often given as the name of a coastal settlement or village. On average, accuracy of observational data for old historical events can be of order of several kilometers in distance and few meters in height. As a result, the direct correspondence of computed and measured heights for historical tsunamis occurred in pre-GPS period (earlier 1992) is always questionable.

However, reliability and accuracy of available observations is only a part of problem. Another part is the degree of confidence in knowing the actual source parameters (position and size of the fault, its depth, type of mechanism, amount of slip). While documenting the coastal tsunami manifestation can be achieved by using methods of direct or indirect measurements, all source parameters can be restored only by solving the *inverse problem* that has intrinsic limitations on data

accuracy and restoration methodology used. Both were a subject of dramatic changes over the last one hundred years. It is well known that most of inverse problems in geophysics are ill-posed and their solvability strongly depends on the amount and quality (accuracy) of the input data, restoration algorithm used and its numerical implementation (Kabanikhin, 2009). On the top of all, the solution found can be non-unique that means that a solution found cannot be necessarily coinciding with the actual source. So far, theorems of uniqueness were obtained only for a small part of specific inverse problems in geophysics.

In relation to the task of restoration of a tsunami source in the deep ocean by means of wave forms recorded at the coast, Russian mathematician V.Kaistrenko (Kaistrenko, 1973) showed that in its general statement, the problem doesn't have an unique solution and gave an example of so-called "non-observable" tsunami source. The uniqueness can be achieved if source function $f(t, x, y)$ is presented as convolution of two functions $\Phi(t) \cdot \Psi(x, y)$. That can be a realistic approximation of the source process only in case of infinite velocity of rupture propagation.

Regarding the quality of seismological data available in catalogs, one should take into account the following. The whole period of historical observations can be roughly divided into three main parts: pre-instrumental: (prior ca. 1900), early instrumental (1900-1963), instrumental (1963- ca.1990), and modern instrumental period (after 1990). During the pre-instrumental period only macro-seismic estimates of magnitude and source location are available. Both are based on the reported level of seismic shaking in different locations. The accuracy of magnitude for this period is ± 1 , accuracy of source location is $\pm 1 \div 2^\circ$. During the early instrumental period the level of accuracy in magnitude and location measurements was actually the same because mechanical short-period seismometers used in all countries could not provide precise measurement of earthquake energy and the level of processing technique (and the knowledge of internal Earth structure) could not provide adequate location of the earthquake source. The deployment of the WWSSN network (World-Wide Standardized Seismographic Network) in the beginning of 60th, initiated by the need to monitor the compliance of the 1963 treaty banning above-ground testing of nuclear weapons, was the major step in improvement of quality and accuracy of seismological data. The new, long-period magnitude scale M_s was proposed and replaced the Richter short-period magnitude. As a result, magnitude estimates became more homogeneous and their accuracy increased to ± 0.5 and location increased (globally) to $\pm 0.5 \div 1^\circ$. The next major step in improvement of seismological data occurred only 30 years later when new type of instruments (very-broad band digital seismometers) were introduced and moment-magnitude M_w estimates could be obtained directly from seismograms. For the modern major earthquakes their accuracy is considered to be $\pm 0.1 \div 0.2$, but for many smaller events the differences between M_w estimates provided by different agencies still can be up to 0.5. New algorithms of data

processing based on better knowledge of the Earth interior structure allowed to reach accuracy in (final) source location $\pm 0.1 \div 0.2^\circ$.

Finally, even in the best-studied cases like the 2004 Sumatra and 2011 Tohoku earthquakes, the limitation factor for matching of computed and measured tsunami run-up heights is availability of reliable bathymetric data. It was established long ago that for direct comparison of computed and measured run-up heights we need to have a computational grid with resolution in 5–10 m for the shallow water area. Except some specific cases (like the 1993 Okushiri tsunami selected as benchmark for calibration of run-up models) such an accuracy is still inaccessible for tsunami modelers for most of coastal areas of the World Ocean.

Types of data used for restoration of source parameters of historical tsunamigenic earthquakes include:

- 1) Reported source coordinates and set of instrumental magnitudes (M_s , M_w , M_l , M_e , etc.)
- 2) Aftershocks distribution
- 3) Measured and reported data on co-seismic displacement of source area
- 4) Reported data of spatial distribution of seismic shaking and damage to constructions
- 5) Distribution of reported and measured tsunami wave heights
- 6) Reported data on tsunami fatalities
- 7) Reported data on time of arrival tsunami wave to coastal locations
- 8) Data on identified land and submarine faults
- 9) Geomorphological features of source area and nearby coast/

Relative importance, level of completeness and detalization of these data strongly depend on historical period. For events occurred in instrumental (1963–1990) and highly-instrumental period (after 1990), most informative data are the parametric source data and distribution of aftershocks. For early instrumental period (1900–1963), magnitude and epicenter coordinates can be not very reliable, but distribution of aftershocks is still can be used for their rough estimation. For pre-instrumental period (before 1900), data on co-seismic displacement and distribution of tsunami heights are the most important data for restoration of size and position of a tsunami source. At last, for old historical events, reported fatalities can be the only data that allow roughly estimate the source location and its spatial extend.

1.3.Digital bathymetry and its optimization

Modeling of tsunami generation and propagation from the source area to the coast, as well as the definition of a "wet line" was performed on a uniform square grid with a step of 15 arc seconds (approximately 400 – 450 m), obtained by bilinear interpolation of a piece of "GEBCO-2008 30 sec" freeware digital bathymetric array.

The following calculation domains we used for numerical modeling (see also Fig. 1.3.1):

- 1 (2011): 135.7E – 149.0E, 33.0N – 44.5N, 3193*2761 nodes of 15-second grid
- 2 (1923): 135.7E – 144.0E, 33.0N – 38.0N, 1993*1201 nodes of 15-second grid
- 3 (1946): 131.3E – 139.0E, 29.0N – 36.0N, 1849*1681 nodes of 15-second grid
- 4 (1944): 131.3E – 142.0E, 30.0N – 37.0N, 2569*1681 nodes of 15-second grid
- 5 (1854): 131.3E – 142.0E, 30.0N – 37.0N, 2569*1681 nodes of 15-second grid

Event numbers are in accordance with the Table 1.3.1.

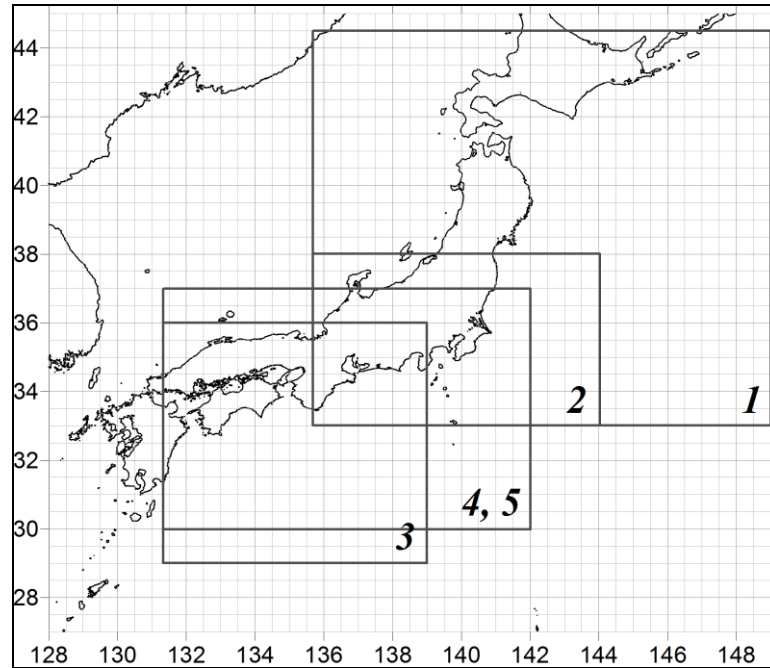


Fig. 1.3.1. Calculation domains used for numerical modeling of historical events. 1 – 2011 Tohoku, 2 – 1923 Kanto, 3 – 1946 Nankai, 4,5 – 1944 Tonankai and 1854 Ansei-Tokai

At the stage of pre-processing, the bathymetric data was optimized, that included some simplifying correction of coastline as well as modification of the depth in the coastal area:

In order to prevent the effect of "drying" in modeling the waves interaction with the reflecting wall on the shoreline (without runup calculation), depths below a certain threshold ($0 < h < h_{\min}$) were replaced by the value h_{\min} . For the event No. 1 $h_{\min} = 30m$, for the events No. 2-5 $h_{\min} = 10m$.

In order to reduce the numerical instability caused by the mismatch of the digital coastline to the requirements of a computational algorithm, its certain correction was performed. This adjustment included the removal or expansion of small islands, narrow straits and capes to a size sufficient for the pattern used in numerical scheme. Areas of digital bathymetry, requiring such a correction, were also determined by the results of the test calculations in the selected computational domains for model sources.

Finally, the additional correction of the "GEBCO-2008 30 sec" digital array coastline was made to adapt it to the coastline in the "Google Earth" application. The most significant modification of the coastline was carried out within the

prefectures Mie, Aichi (Fig. 1.3.2, left) and Miyagi (Fig. 1.3.2, right). On these figures, the original coastline is represented in red, and the result of correction—in yellow.

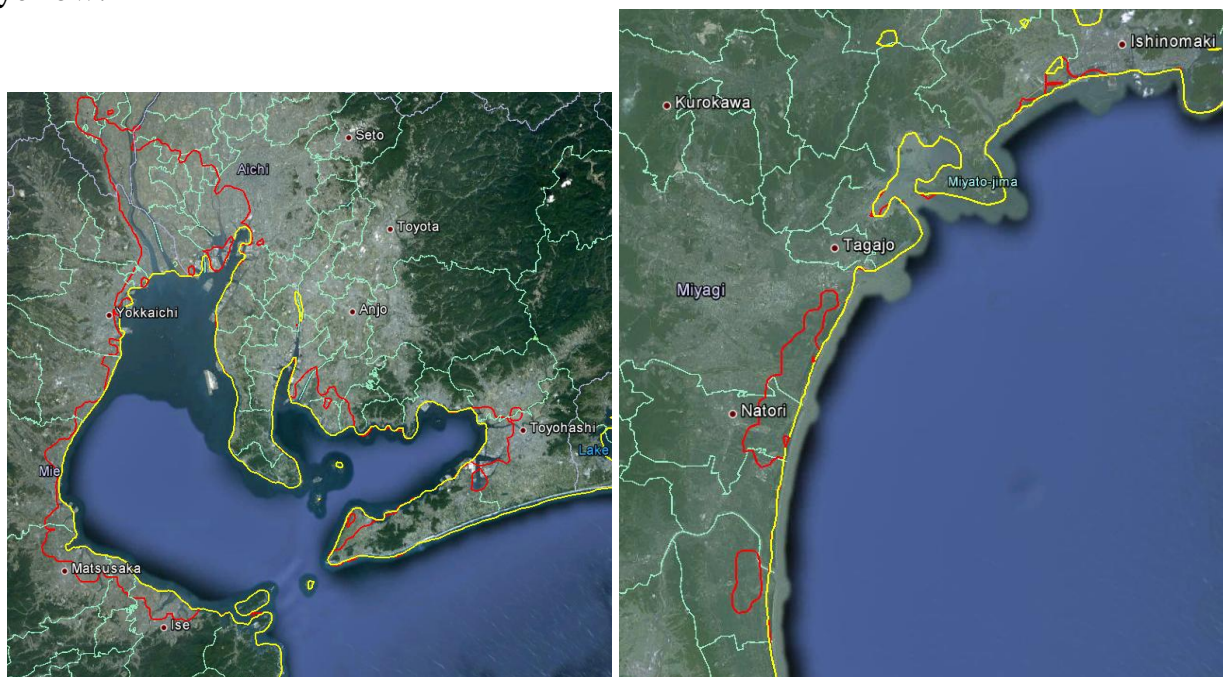


Fig. 1.3.2. Examples of the shoreline before (red line) and after (yellow line) the correction.

For each of the five events (Tohoku, 2011; Kanto, 1923; Nankai, 1946; Tonankai, 1944; Ansei-Tokai, 1854) the areas for the 2D modeling of coastal inundation have been selected. One of these areas for each event was the same used for the one-dimensional (1D) simulation runup on the first stage. For the most studied event "Tohoku, 2011", four areas were considered (near the city of Iwaki, Sendai, Miyako and Koborinai). For the other events – two ones. The limits of the respective areas are given in the Table 1.3.1.

The corresponding arrays with bathymetry and topography information have been built. For the computation the inundation zones from the "Tohoku, 2011" tsunami in two areas ("Iwaki" and "Sendai") 3sec DEM (SRTM version 2.1, http://dds.cr.usgs.gov/srtm/version2_1/SRTM3/Eurasia/) was used as a source of topography; bathymetry was taken from the GEBCO-30 sec. For the coastal area "Koborinai" we used existing detailed DEM/DBM data on the grid with step 0.4 arc sec (approximately 10 m on O_x and 12 m on O_y). For the coastal area "Miyako" we used data of the topography and bathymetry obtained after our digitizing of the map (Japanese Bathymetric Chart № 6370-1, scale 1:50,000), purchased from the Japan Hydrographic Association (JHA). The resulting digitized grid increment was approximately 15 meters.

For the events of 1854, 1923, 1944 and 1946 both the topography and bathymetry were taken from the GEBCO-30 sec.

It should be noted that the adjustment of the various sets of bathymetry and topography data is an extremely complex process, especially in cases where contours of the coastline have big difference in these arrays. Therefore, for the

further studies obtaining the homogeneous digital elevation data of coastal areas and the depths of the adjacent waters becomes critically important point.

Table 1.3.1. Regions for 2d calculation of inundation zones: limits, grid steps and way to input the perturbation

event year	region limits (degrees)	grid step $\Delta x \times \Delta y$ (meters)	perturbation entering
2011	141.9755–142.03122 E 39.784–39.7928 N ("Koborinai")	3×2	1 mareogram in the east
	141.9175–142.02 E 39.545–39.653 N ("Miyako")	15×15	1 mareogram in the north
	140.7–141.1 E 37.9–38.3 N ("Sendai")	40×40	mareograms in the south and east
	140.85–141.175 E 36.9625–37.175 N ("Iwaki")	30×30	mareograms in the south and east
1923	139.125–139.6375 E 35.175–35.425 N	60×60	mareograms in the south
	139.6–140.2 E 35.25–35.75 N	60×60	mareograms in the south
1946	133.625–133.775 E 33.375–33.575 N	30×30	mareograms in the south and east
	135.028 E, 33.758 N; 135.113 E, 33.939 N; 135.203 E, 33.897 N; 135.119 E, 33.716 N (rotated region)	20×20	1 mareogram on the side opposite to the shore
1944	135.957 E, 33.709 N; 135.987 E, 33.761 N; 136.062 E, 33.718 N; 136.033 E, 33.666 N (rotated region)	10×10	1 mareogram on the side opposite to the shore
	136.189 E, 34.066 N; 136.249 E, 34.139 N; 136.376 E, 34.033 N; 136.315 E, 33.959 N (rotated region)	25×25	1 mareogram on the side opposite to the shore
1854	137.65–137.75 E 34.59583–34.72083 N	20×25	mareograms in the south and east
	136.85–137.05 E 34.3–34.4 N	20×20	mareograms in the south and east

1.4. Description of the numerical techniques

This section presents the results of simulation of flooding of selected coastal areas by the tsunami waves for each of the five historical events, mainly, in the form of maps showing the inundation limits for the selected coastal areas. In determining the structure and a set of presented figures, it was decided to demonstrate

- the relative position of the initial elevation, coastal areas for 2D run-up calculation and straight cross-sections, along which 1D modeling has been carried out on the first stage of the Project;
- features of different topography and bathymetry reliefs being in use;
- a comparison of inundation zones, obtained by 1D and 2D run-up modeling;
- dependence of the calculated inundation zones on some parameters of physical models, numerical algorithm parameters and input data.

Each of the following drawings is accompanied by the detailed signature.

As already mentioned above, 4 coastal areas for the event "Tohoku, 2011" have been considered, and in two of them ("Koborinai" and "Miyako") calculations were performed using the detailed DEM and DBM; for coastal areas "Sendai" and "Iwaki" calculations were performed using detailed DEM (SRTM-3 sec, version 2.1) and DBM GEBCO-30 sec.

For each of the four other historical events 2 coastal areas have been selected for run-up simulation, and calculations were performed using DEM/DBM GEBCO-30 sec.

The most interesting, in our view, are the results of "Tohoku, 2011" tsunami modeling. This event is the most studied, and is accompanied by a huge amount of field data and publications. Finally, our simulations have been performed for this event using the most detailed data on the topography and bathymetry.

The first analysis of the simulation results shows that runup heights, obtained by the 2D modeling of Koborinai Bay inundation, are about 30 meters, which is consistent with field data. In Miyako heights of 15 – 20 meters have been observed, while our calculated values are 15 – 25 meters. In the area of Sendai observed runup was to a height of about 10 – 15m, and the calculations were obtained for about 25 – 30 meters. Finally, in the vicinity of the city of Iwaki runup heights of 7 – 10 meters have been observed, and the calculated values are about the same when using DEM SRTM-3 sec (version 2.1) and reach 12 meters when using DEM GEBCO-30 sec.

The resulting difference between the observed and calculated values can be explained by the fact that the calculations used zero Chezy coefficient (i.e., zero friction), except for the parametric analysis for Koborinai Bay. The absence of differences for the coastal area "Iwaki", when using DEM SRTM-3 sec (version 2.1), can be due to very rough topography relief, reproducing the effect of "artificial" friction, which was enough for run-up calculation in coastal areas that are not located directly in front of the source. At the same time, the great variation in the observed and measured heights in the vicinity of Sendai may be due to the need to improve the model of the tsunami source. As it is known, none of the proposed models of the source of relevant tsunamigenic earthquakes are able to reproduce the actually position of maximum heights peak (observed at latitudes near 39°N) but move it to the south at 38-38.5° N, where our coastal area "Sendai" is located.

When comparing the results of 1D and 2D modeling, note that the one-dimensional modeling approach clearly assumes the frontal approach of a wave to the coast, along the corresponding 1D cross-sections, , that, in fact, is not always true. But it should be noted a very good agreement between the results of 1D and 2D simulation for the area "Iwaki", which is explained by the fact that in the 2D calculations waves approaching the coast just to the south-east, along the one-dimensional cross-sections. This confirms the applicability of the proposed 1D technology in such situations.

1.5. Calculation of initial bottom displacements

Calculation of initial bottom displacement in this study is based on the STATIC computer code developed in the Novosibirsk Tsunami Laboratory in 1978. The code is based on formulas obtained in (Gusiakov, 1978) for deformation of the free surface of a homogeneous elastic half-space produced by an internal spatial dislocation that is a model of an earthquake source (Fig. 1.5.1). The numerous tests show that the formulas obtained in (Gusiakov, 1978) are fully coincide with the formulas later obtained in the widely cited work (Okada, 1985) with an accuracy order of 0.001%. Examples of calculation of static displacement of elastic halfspace for two basic type of dislocation source (vertical dip-slip and vertical strike-slip) are shown in Fig. 1.5.1.

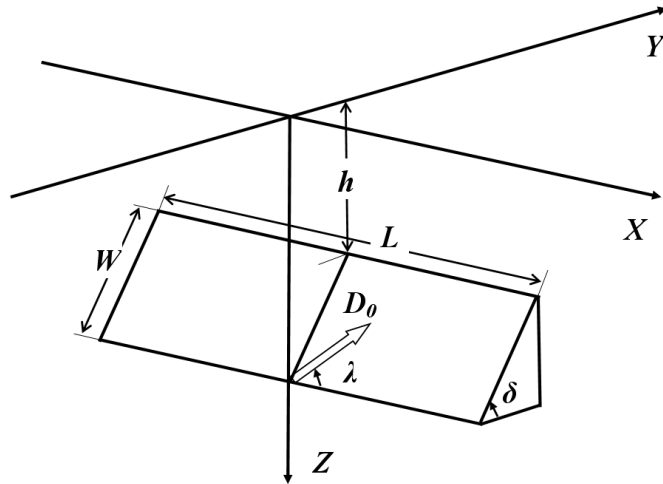


Fig. 1.5.1. Spatial dislocation model of an earthquake source.

The elastic half-space is characterized by three parameters – ρ (density), λ_0 (module of elasticity) and μ (module of rigidity). The internal dislocation source is characterized by six parameters – L (length of the fault, in km), W (width of the fault, in km), δ (dip angle), λ (slip angle), D_0 (amount of displacement on the fault, in m), h_0 (depth to the upper edge of the fault). The seismic moment M_0 of this source is expressed by the formula

$$M_0 = \mu \cdot L \cdot W \cdot D_0 \quad (1.2)$$

Seismic moment M_0 can be connected to the moment-magnitude of an earthquake M_w by the correlation formula (Kanamori, 1977)

$$M_w = (\log M_0 - 9.1)/1.5 \quad (1.3)$$

where M_0 is measured in N·m. The magnitude M_w can be connected to the tsunami intensity I on the Soloviev-Imamura scale by the correlation formula

$$I = 3.55 \cdot M_w - 27.1 \quad (1.4)$$

obtained in (Chubarov, Gusiakov, 1985). In turn, the tsunami intensity I is calculated on the basis of average run-up height H_{av} observed at the nearest coast, using the formula proposed in (Soloviev, 1972)

$$I = 1/2 + \log_2 H_{av}. \quad (1.5)$$

Among the numerous scales proposed for measuring tsunami strength (see survey of this scales in Gusiakov (2009)), Soloviev-Imamura scale I is most closely related to the total tsunami energy.

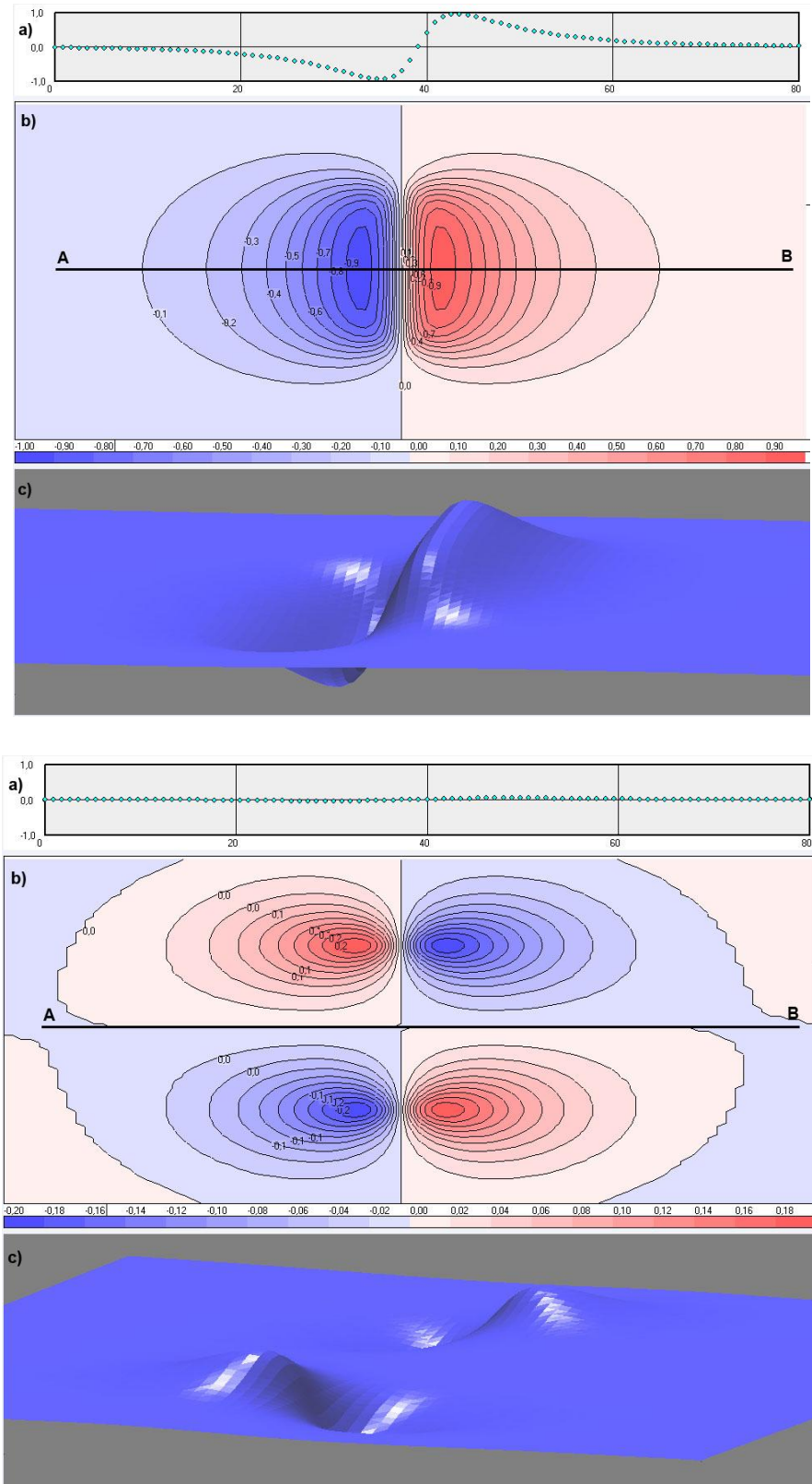


Fig. 1.5.2. Static displacement produced by a dislocation source shown in Fig. 1.5.1 for vertical dip-slip fault with $\delta=90^\circ$, $\lambda=90^\circ$ (above) and vertical strike-slip fault with $\delta=90^\circ$, $\lambda=0^\circ$ (below), shown as vertical cross section, isolines and 3D view of deformation of the free surface of elastic half-space.

Knowing the vertical displacement at the surface of elastic half-space U_z , we can calculate the total absolute volume of surface displacement V_{abs} by

integrating $|U_z|$ displacement over the source area where we know U_z . Under an assumption that co-seismic deformation occurred instantaneously (more specifically, during the one time step used in tsunami propagation model) we can also calculate the initial (static) tsunami energy E_0 by formula (Kajiura, 1970)

$$E_0 = \frac{1}{2} \rho_0 g \iint_S U_z^2 dS \quad (1.6)$$

where ρ_0 – density of water and g - acceleration of gravity.

The U_z values calculated on the surface rectangular grid having dimension NI by MI and spatial steps Dx and Dy , is used as initial deformation of the sea surface that is assumed to be identical to the vertical deformation of the sea bottom, since (1.2) rupture propagation velocity is considered to be much higher than tsunami propagation velocity and (1.3) rise time of bottom deformation is considered to be much shorter than typical tsunami period.

This initial free surface deformation is used to calculate wave propagation from the source area to the coast using the nonlinear equations of shallow water in spherical coordinates, taking into account the Coriolis force. Calculation of wave generation and propagation is performed using a previously developed MGC software package which has been thoroughly tested on the calculations in the model and real water areas (Shokin et al., 2008).

Parameters for the set of basic source models used in this study (see Fig. 1.5.3) are listed in Table 1.5.1.

Table 1.5.1 Source parameters of five historical events selected for further analysis

	Events/Param	M_w	Epicenter, deg	h_0 , km	L , km	W , km	D_0 , m	δ , deg	λ , deg	θ , deg
1.	2011Tohoku	9.0	38.9N, 141.7E	20	300	150	25	10	88	20
2.	1946 Nankai	8.1	33.N, 134.5E	10	150	50	5	20	90	50
3.	1944 Tonankai	8.1	33.9N, 136.6E	10	150	50	5	20	90	45
4.	1923 Kanto	7.9	35.5N, 139.9E	10	150	70	5	20	90	120
5.	1854 Ansei-Tokai	8.4	34.4N, 137.0E	5	150	100	4	24	113	65
			34.8N, 137.8E	5	115	70	4	24	71	17

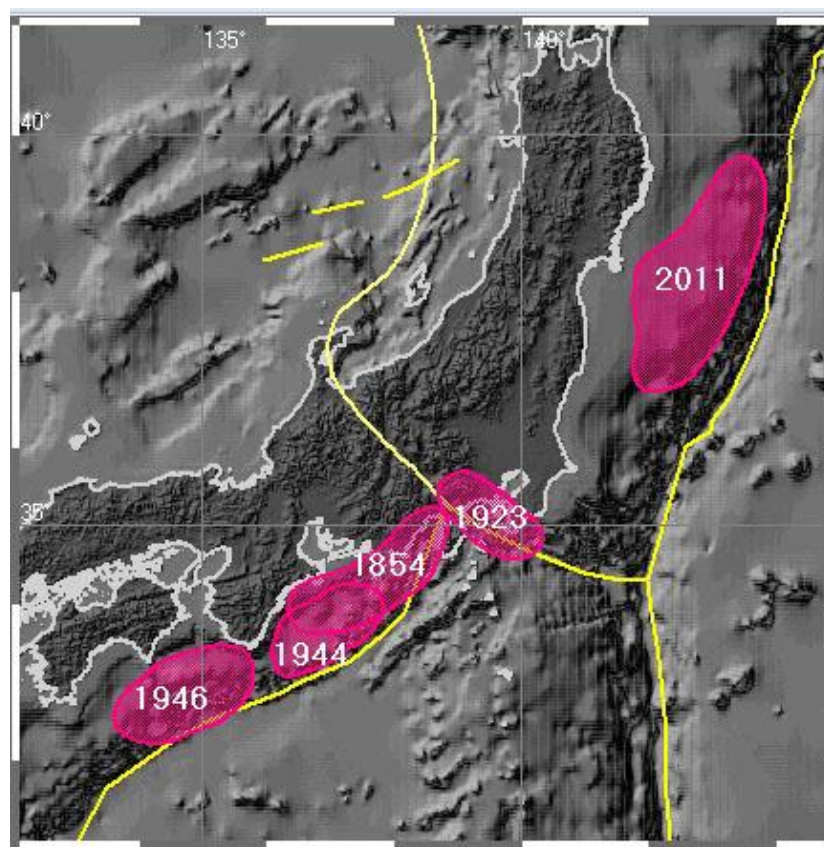


Fig. 1.5.3. Map of the area and position of historical tsunamigenic events selected for numerical modeling. Solid yellow lines show the main plate boundaries in the region.

1.6. Calculation of “wet line”

The first step in determining the possible impact of tsunami on the coast is calculation of the so-called "wet-line"—the distribution of the maximum and minimum wave heights and the sum of their absolute values—on the wall installed along the shoreline at depth h_{\min} . To this end, the calculations of generation and propagation of tsunami for 4 hours of physical time were carried out with MGC software system for each historical event (see Table 1.3.1). During these calculations, maximum and minimum wave heights in the entire computational domain were determined. In order to plot the wet line, the values at each nodes belonging to the fragments of the coastline were selected. The number of such nodes for the events considered and the corresponding computational domains ranged from 3826 to 5592, the average distance between them – about 500 m.

1.7.1D calculation of run-up

The modeling of tsunami runup on the beach was carried out according to the following technology.

At first, the coastal areas with following properties are chosen:

- calculated values of wave heights in the wet line exceed the mark of 2 m;
- coastline is not indented by small scale bays and is not shielded from the direct impact of tsunami;
- the selected coastal area contains human settlements;
- the relief of the land includes a sufficiently broad band with a slight elevation

above sea level.

Next, cross-sections are made within these areas connecting the 10-20 meter isoline of topography with 100 m isobath.

2D calculations are carried out, similar to those given for the construction of a wet line, to define the dynamic characteristics of the flow in the tide-gauge points set at "sea" ends of cross-sections (at a depth of 100 m) as well as at the nodes lying on the intersection of the shoreline with the selected cross-sections.

Thereafter, the one-dimensional calculations of waves runup on the shore along the selected cross-sections are carried out using the initial free surface displacement above the relevant cross-section and the marigram at the seaward ends of cross-sections as boundary condition. At that, only the main part of the total tidal curve is used—the first wave approaching the shore, and after running it into a computational domain, boundary condition is replaced by the free (open) condition.

During these one-dimensional calculations, the values of the vertical (height) and horizontal (extent) runup along selected cross-sections are computed, which then are used to determine the geographical position of the boundary of area flooding taking into account the digital terrain land. This "approximate" boundary line is constructed as an intersection of relief and planes passing through the points of maximum runup on adjacent cross-sections.

When interpreting the calculation results and analyzing the corresponding images, it should be taken into account that the 1D runup modeling was performed using "non-optimized" topography and bathymetry relief data, and that there is a natural difference between the GEBCO data sets and satellite images used in Google Earth.

1.7.1. Analytical formulas

The well known analytic formulas were used also to calculate the wave runup over the linear slope. In these formulas, the maximum vertical runup height R depends on the characteristics of the wave above the selected marine point (seaward end of the corresponding slope) (a_w – amplitude, λ_w – length, T_w – period), as well as on the parameters of a model area (h_w – depth at the marine point, L_w – distance from this point to the initial shoreline, θ_w – flat slope angle).

Despite the large number of works connected with the analytical relations to determine the height and distance of wave runup, formulas proposed in (Synolakis, 1987; Pelinovsky, Mazova, 1992) have been chosen. This choice was determined by the effective comparison of the results obtained by these relations with the results of laboratory and numerical experiments.

It should be taken into account that the application of analytical relations requires approximation of the real topography and land in the coastal area by the simplest linear profile, and this determines the need for proper interpretation of the results, i.e. understanding of their preliminary, proximate character. However, such a coarsening of the problem statement can be comparable to the distortions introduced by the use of "real" repeatedly interpolated digital topography and

bathymetry relief. Note also that each of the relations used is accompanied by a clear indication of the range of its applicability.

The formula in (Synolakis, 1987) calculates the maximum vertical solitary wave runup on a relatively steep flat slope coupled with the horizontal bottom, the depth of which is given by the value h_w :

$$\frac{R}{h_w} = 2.831 \sqrt{\cot \theta_w} \left(\frac{a_w}{h_w} \right)^{5/4} \quad (1.7)$$

Condition for its applicability is the inequality:

$$\frac{a_w}{h_w} \gg (0.288 \tan \theta_w)^2. \quad (1.8)$$

In addition, formula (1.7) is valid only for non-breaking waves, i.e. when the following condition is satisfied:

$$\frac{a_w}{h_w} < 0.479 (\tan \theta_w)^{10/9}.$$

The values resulting from (1.7) are in good agreement with the numerical results obtained by its authors, but they are slightly higher than the experimental data, that can be caused by neglecting of the fluid viscosity effects in the mathematical models being in use. Another analytical formula for the approximate determination of the wave runup on the flat inclined bottom is proposed in (Pelinovsky, Mazova, 1992):

$$\frac{R}{a_w} = 2\pi \sqrt{\frac{2h_w \cot \theta_w}{\lambda_w}}, \quad (1.9)$$

where $\lambda_w = T_w \sqrt{gh_w}$.

This formula is applicable only for relatively steep slopes satisfying

$$\tan \theta_w > 14.03 \left(\frac{a_w}{h_w} \right)^{2/5} \left(\frac{\lambda_w}{h_w} \right)^{-1}, \quad (1.10)$$

as a wave breaking occurs near the shoreline on a very gentle slope.

Given that $L_w = h_w \cot \theta_w$, the formula (1.9) can be rewritten as:

$$\frac{R}{a_w} = 2\pi \sqrt{\frac{2L_w}{\lambda_w}}. \quad (1.11)$$

1.7.2. Run-up calculation using the analytic solution at the shoreline

Consider a flat layer of a liquid bounded by a free surface and an impermeable bottom. We suppose the liquid is in the gravitational field and is incompressible and nonviscous. The Cartesian coordinate system Oxy is chosen, so that the equation of the free surface of the resting liquid has the form $y=0$; in this case $y=-h(x)$ is a known function describing the relief of the bottom and the adjacent land. We assume that the surface waves are long and spread along the normal to the straight shoreline. Under the indicated assumptions, the problem of

the wave run-up on a beach can be solved (Ovsyannikov, 1981) within the nonlinear shallow water model described by the equations

$$\frac{\partial \mathbf{u}}{\partial t} + \frac{\partial \mathbf{f}}{\partial x} = \mathbf{G}, \quad x > x_0(t), \quad t > 0. \quad (1.12)$$

Here

$$\mathbf{u} = \begin{pmatrix} H \\ Hu \end{pmatrix}, \quad \mathbf{f}(\mathbf{u}) = \begin{pmatrix} Hu \\ Hu^2 + gH^2/2 \end{pmatrix}, \quad \mathbf{G}(\mathbf{u}) = \begin{pmatrix} 0 \\ gHh_x \end{pmatrix}$$

while t is the time, $u(x,t)$ is the horizontal component of the velocity vector averaged over the depth, $H = \eta + h$ is the total depth, $\eta(x,t)$ is the free surface deviations from the rest level $y=0$, g is the acceleration of gravity, $x_0(t)$ is the movable left boundary of the solution domain (the movable shoreline).

Equations (1.12) are supplied with the boundary condition

$$H(x_0(t), t) = 0, \quad t \geq 0 \quad (1.13)$$

and the initial conditions

$$H(x, 0) = H_0(x), \quad u(x, 0) = u_0(x), \quad x \geq x_{00}, \quad (1.14)$$

where $x_0(t)$ is the required coordinate of the shoreline (Fig. 1.7.1), $x_{00} = x_0(0)$ is the position of this point at the initial time moment. In the numerical experiments we bounded the domain from the right by a sufficiently distant boundary $x = L$ where we posed the boundary conditions $\eta(L, t) = \eta_L(t)$.

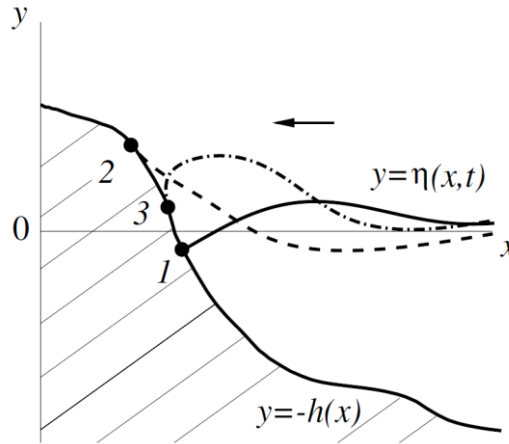


Fig. 1.7.1. Free boundary $y = \eta(x, t)$ and the shoreline $x_0(t)$ corresponding to it (•) for
(1) – $H_x(x_0(t)) \neq 0$, (2) – $H_x(x_0(t)) = 0$, (3) – $H_x(x_0(t)) = \infty$.

Equations (1.12) can be rewritten in the nondivergent form:

$$\mathbf{u}_t + \mathbf{A}\mathbf{u}_x = \mathbf{G} \quad (1.15)$$

where $\mathbf{A} = \partial \mathbf{f} / \partial \mathbf{u}$ is the Jacobi matrix. Its eigenvalues $\lambda_{1,2}$ are calculated by the formulas

$$\lambda_1 = u - \sqrt{gH}, \quad \lambda_2 = u + \sqrt{gH}. \quad (1.16)$$

We suppose that for $x > x_0(t)$ the total depth is positive $H(x, t) > 0$. Then we have $\lambda_1 \neq \lambda_2$ and system of equations (1.15) is hyperbolic. At the shoreline $x_0(t)$ eigenvalues (1.16) are the same (due to the condition $H(x_0(t), t) = 0$) and hence the line $x = x_0(t)$ is the characteristic of multiplicity two (Hibberd, Peregrine, 1979) similar to the problem of the ideal gas outflowing into the vacuum, where their separating boundary is a multiple characteristic. This analogy allows us to apply the method of calculating analytic solutions to the ideal gas equations in the neighborhood of the gas-vacuum boundary developed in (Bautin, Deryabin, 2005) to our case of shallow water equations.

Depending on the initial conditions, three cases are possible, and we study them separately. These cases are: $H'_0(x_{00}) \neq 0$, $H'_0(x_{00}) = 0$, and $H'_0(x_{00}) = \infty$, and in this case we always have

$$H_0(x_{00}) = 0. \quad (1.17)$$

In order to calculate the surface wave run-up on a beach, we used a predictor-corrector scheme on an adaptive grid (Shokin, Khakimzyanov, 2006) approximating equations (1.12) with the second order and preserving the monotonicity of the numerical solution profiles in the linear case. The adaptive grid $\{x_j^n\}$, $j = 0, \dots, N$, was constructed by the equidistribution method (Khakimzyanov et al., 2001) and had movable concentrations in the neighborhood of the wave crests and troughs, or near the shoreline $x_0(t^n)$, which was matched with the leftmost calculation node x_0^n in each time layer $t = t^n$. This matching allowed to trace clearly the motion of the shoreline even on a coarse grid (with a little number N of nodes).

In order to calculate the values x_0^{n+1} , H_0^{n+1} , and u_0^{n+1} in the $(n+1)^{\text{th}}$ time layer, we need difference boundary conditions at the shoreline. For the calculation of the total depth we use formula $H(x_0(t), t) = 0$ and assume $H_0^{n+1} = 0$.

If the difference derivative $H_{x,0}^n$ determined in the n th time layer by the formula

$$H_{x,0}^n = \frac{H_1^n - H_0^n}{x_1^n - x_0^n} \quad (1.18)$$

satisfies the condition

$$m \leq H_{x,0}^n \leq M \quad (1.19)$$

where $0 < m \ll M$, m and M are given numbers, then we can use the partial sum of series

$$q(x, t) = \sum_{k=0}^{\infty} q_k(x) \frac{(t - t_0)^k}{k!}$$

Which for $x_0(t)$ has the form

$$x_0(t) = x_{00} + x_{01}(t - t_0) + x_{02} \frac{(t - t_0)^2}{2} + \dots + x_{0k} \frac{(t - t_0)^k}{k!} + \dots$$

for the approximate calculation of the new position of the shoreline; for this sum we take the following:

$$x_0(t) = x_{00} + x_{01}(t - t_0) + x_{02} \frac{(t - t_0)^2}{2} \quad (1.20)$$

Taking into account that

$$x_{01} = u_0(x_{00}), \quad x_{02} = -g\eta'_0(x_{00}),$$

where $\eta_0(x) = H_0(x) - h(x)$, and $t - t_0 = \tau$, we come to the following

$$x_0^{n+1} = x_0^n + u_0^n \tau - g\eta_{x,0}^n \frac{\tau^2}{2}. \quad (1.21)$$

In order to determine the velocity u_0^{n+1} , we use the simplest approximation

$$\frac{u_0^{n+1} - u_0^n}{\tau} = -g\eta_{x,0}^n \equiv -g \frac{\eta_1^n - \eta_0^n}{x_1^n - x_0^n}. \quad (1.22)$$

In the numerical solution of the problem we assume that the second case $H'_0(x_{00}) = 0$ is realized under the condition

$$|H_{x,0}^n| < m, \quad (1.23)$$

where m is the small positive number. Now for the calculation of the values x_0^{n+1} and u_0^{n+1} for the sake of simplicity, we use the modified Euler scheme which gives exact solution for the case of flat slope

$$y = -h(x) = -k(x - x_{00}).$$

For the criterion of the third case, i.e., the wave breaking, we use the inequality

$$|H_{x,0}^n| > M,$$

where M is the sufficiently large positive number. The calculation of x_0^{n+1} and u_0^{n+1} is performed now with the help of the following difference scheme:

$$x_0^{n+1} = x_0^n + \tau u_* + \frac{\tau^2}{2} g f(x_0^n), \quad u_0^{n+1} = u_* + \tau g f(x_0^n) + \frac{\tau^2}{2} g u_* f'(x_0^n). \quad (1.24)$$

In this case for the calculation of u_* we use the values $u_{00} = u_1^n$ and $H_{00} = H_1^n$ after the «jump» (at the first grid node adjacent to the shoreline), i.e.,

$$u_* = u_1^n - 2\sqrt{gH_1^n}.$$

Note that for flat slope $y = -h(x) = -k(x - x_{00})$ formulas (1.24) describe exactly analytic solution

$$x_0(t) = \frac{k}{2} g (t - t_0)^2 + u_* (t - t_0) + x_{00}, \quad U^0(t) = k g (t - t_0) + u_*.$$

This method is described in detail in the paper (Bautin et al., 2011)

1.7.3. 1D Run-up calculation using the large particles method

One-dimensional test calculations for the verification of the large particles method were carried out using the code that implements the 2D model. This algorithm is described in Section 1.8.

1.8. 2D calculation of run-up

The inundation zones have been calculated using a method of large particles (see next section). Grid spacing ranged from 2 to 40 m in different areas (see Table 1.3.1). Chezy coefficient value in all the calculations was equal to 0 by default.

To enter the disturbance (incoming wave) for the runup calculation, mareograms recorded on water boundaries of these coastal areas were used. These mareograms have been previously calculated during the simulation of wave propagation in the global computational domains from the seismic source to the coast. The statements of the problems for such preliminary calculations repeated those that were used in the first stage of the Project for the calculation of wave heights on the "wet wall".

In the case when the tsunami wave comes in the computational domain at the direct angle to the shoreline (type A), only one mareogram was recorded in the center of the border opposite to the coast. In cases where the wave comes at the oblique angle (type B), mareograms along both boundaries facing to the incoming wave were recorded (see Table 1.3.1). For suppression of the reflected wave in these records, additional calculations were performed, in which the modified relief (relief without coastal land) was used, similarly to the first stage of the Project: in this modified relief all values of bathymetry and topography above the value $z = -h_{\min}$ (see the first report) were replaced by this value.

Using the obtained mareograms, the calculation of tsunami run-up on the shore in the selected coastal areas have been performed. The perturbation was introduced into the area in two ways. In cases A, the incoming wave was performed as a flat front with profile that repeats the mareogram, while the condition of reflection on the both adjacent water boundaries has been set. In cases B, the perturbation was introduced to the computation domain by linear interpolation of recorded values in space and time, and there was an open free condition on the third water boundary.

Results of the numerical experiments allowed to compare inundation limits within the "Iwaki" coastal area obtained with the use of the DEM GEBCO-30sec and SRTM-3sec (version 2.1), as well as obtained with the 1D calculations. For the Koborinai bay, calculated results have been compared with field data, and a parametric study of the inundation zones dependence on the resolution of the computational grid and on the magnitude of the friction force (Chezy coefficient value) has been conducted.

For the events of 1854, 1923, 1944 and 1946 the inundation zones in the selected areas have been calculated in a similar way. The grid steps ranged from 10 to 60 meters, the value of the Chezy coefficient was $n = 0$. In all coastal areas

where 1D simulations had been held previously, the comparison of inundation zones obtained by both methods has been made.

The problem of 2D modeling of wave runup on the beach with a complex shoreline was considered in shallow water model. Given the force of friction, averaged over the depth, the system of equations describing the motion of such waves in a Cartesian coordinate system (the coordinate plane $z=0$ coincides with the surface of the undisturbed water) has the following form

$$\begin{aligned}\frac{\partial H}{\partial t} + \frac{\partial Hu}{\partial x} + \frac{\partial Hv}{\partial y} &= 0, \\ \frac{\partial Hu}{\partial t} + \frac{\partial Hu^2}{\partial x} + \frac{\partial Huv}{\partial y} + \frac{g}{2} \frac{\partial H^2}{\partial x} &= gH \frac{\partial h}{\partial x} - uHC_R, \\ \frac{\partial Hv}{\partial t} + \frac{\partial Huv}{\partial x} + \frac{\partial Hv^2}{\partial y} + \frac{g}{2} \frac{\partial H^2}{\partial y} &= gH \frac{\partial h}{\partial y} - vHC_R,\end{aligned}\tag{1.25}$$

where $H(x, y, t)$, $h(x, y)$ – water depth and bottom profile respectively, $u(x, y, t)$, $v(x, y, t)$ – Cartesian coordinates of the velocity vector $\vec{u}(x, y, t)$, C_R – friction coefficient, g – acceleration of gravity.

To determine the coefficient C_R the Manning's formula was used:

$$C_R = \frac{\rho g n^2}{H^{4/3}} |\vec{u}|, \text{ where } n - \text{Chezy coefficient.}$$

The lateral boundary conditions are reflective, non-reflective or ingoing with time-varying values $H(\cdot, \cdot, t)$ obtained in the solution of auxiliary problems – calculations of wave propagation with reflective wall along the shoreline. All water parameters in (1.25) are being assumed to be 0 on the land.

For the numerical solution of (1.25) the method of large particles (large-particle-method – LPM) was used, which is based on the ideas of the classical method of particle-in-cell (particle-in-cell – PIC), first introduced in (Harlow, 1955). In recent years, a similar method – SPH (smoothed particle hydrodynamics – SPH) – has been proposed, which algorithms and results in problems of wave hydrodynamics are described in (Oger et al., 2006; Dalrymple, Rogers, 2006; Gomez-Gesteira et al., 2010; Monaghan, 1994; Vacondio et al., 2012; Hong-Ming Kao, Tsang-Jung Chang, 2012). Unlike the PIC, SPH has no Euler step (see below). This allowed, on the one hand, making this method more robust and applicable to the calculation of flows in complex areas, but on the other hand, it was necessary to develop a number of complex smoothing procedures for describing the interactions between the particles, which does not provide fully conservative method.

In the LPM, used in our work with respect to the problems of tsunami waves dynamics in the shallow-water theory, as well as in the SPH method, particles are used as "elementary water column», called below "large particles", which motion is being described in two stages – the Lagrangian and Eulerian. This substantially

simplifies accounting the interaction between the particles, while ensuring the accurate reproduction of the run-up (run-down) of water on dry land and strict implementation of conservation laws.

Note that the number of particles needed for solving 2D problems in the SPH method with required accuracy is approximately 100,000 (De Leffe et al., 2010). This number is comparable to the number of difference grid nodes in the LPM, but the software's implementation of LPM is much simpler and the number of operations required to calculate the motion of a single particle is about two orders of magnitude smaller than in the SPH.

For 2D modeling of tsunami run-up we use the method that has been designed in the early 80th for computing compressible flows of a continuous medium (Belotserkovskii, Davydov, 1982) as a further development of Harlow's method of "particle-in-cell". The method is based on splitting the original differential equations in accordance with the physical processes they represent. It can be used to solve systems of evolution equations. The procedure may establish the existence of steady-state solutions.

The method is widely used to investigate aerodynamic flows, diffraction problems, transonic flows, interaction phenomena of radiation and matter, etc.

The solution process for an evolution system is divided into two chronological stages, each of which consists of three steps: an Eulerian and a Lagrangian. One first considers the variation of the internal state of a subsystem – a "large particle" (Eulerian step), and then — the motion of this subsystem with the interior state of the subsystem left unchanged (Lagrangian).

The large-particle method may be interpreted from various points of view: the splitting method, the mixed Euler–Lagrange method, computation in local Lagrangian coordinates (Eulerian step) with scaling on the previous grid (Lagrangian step), the difference notation for conservation laws for a fluid element (large particle), and the Eulerian difference scheme.

For the numerical solution of (1.25) the large particle method has been used. Use of the "classical" particle method was not possible due to the statistical nature of its solution. This solution does not satisfy the hydrostatic equilibrium of the water in rest, and significantly distorts the process of propagation. Method of large particles does not have this drawback and provides a balanced differential scheme. The choice of this method is also due to the performers' wide experience in its application to the solution of various complex problems.

In its implementation an uniform rectangular difference grid has been used.

Implementation of the large particles method is conducted in two stages. On the first (Euler) step all the convective terms are dropped in (1.25), and the system is written as:

$$\begin{aligned}
\frac{\partial H}{\partial t} &= 0, \\
\frac{\partial u}{\partial t} + g \frac{\partial(H-h)}{\partial x} &= -u C_R, \\
\frac{\partial v}{\partial t} + g \frac{\partial(H-h)}{\partial y} &= -v C_R.
\end{aligned} \tag{1.26}$$

On the second (Lagrangian) step the transport equation are solved:

$$\begin{aligned}
\frac{\partial H}{\partial t} + \frac{\partial Hu}{\partial x} + \frac{\partial Hv}{\partial y} &= 0, \\
\frac{\partial Hu}{\partial t} + \frac{\partial Hu^2}{\partial x} + \frac{\partial Huv}{\partial y} &= 0, \\
\frac{\partial Hv}{\partial t} + \frac{\partial Huv}{\partial x} + \frac{\partial Hv^2}{\partial y} &= 0.
\end{aligned} \tag{1.27}$$

To solve the system (1.26) – (1.27) an explicit difference scheme of the first order of accuracy is constructed.. Note that due to irregularity of the coastline for the numerical solution with a detailed resolution, as noted above, it is necessary to use a sufficiently fine difference grid. Therefore, the application of scheme with first-order accuracy, which has also monotone properties, is justified. For its construction the staggered grid was used (see Fig. 1.8.1). Values of the total depth $H_{i,j}$ and the depth of the undisturbed free surface $h_{i,j}$ are being approximated at the integer nodes, speeds $u_{i+1/2,j}$ and $v_{i,j+1/2}$ – at the half-integer ones.

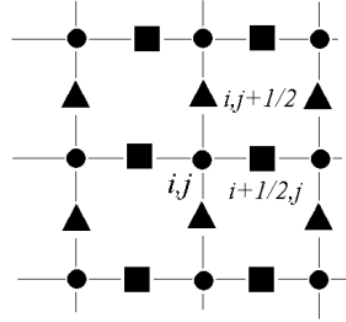


Fig. 1.8.1. The pattern of the difference scheme: $H_{i,j}$, $h_{i,j}$ (circles), $u_{i+1/2,j}$ (square boxes) and $v_{i,j+1/2}$ (triangles).

Difference scheme of the first step is:

$$\begin{aligned}
\tilde{H}_{i,j} &= H_{i,j}^n, \\
\tilde{u}_{i+1/2,j} &= (u_{i+1/2,j}^n - \Delta t ((H-h)_{i+1,j}^n - (H-h)_{i,j}^n) / \Delta x) / (1 + \Delta t C_R), \\
\tilde{v}_{i,j+1/2} &= (v_{i,j+1/2}^n - \Delta t ((H-h)_{i,j+1}^n - (H-h)_{i,j}^n) / \Delta y) / (1 + \Delta t C_R).
\end{aligned}$$

On the second step an upwind difference scheme for the transport equations (1.27) is used:

$$H_{i,j}^{n+1} = \tilde{H}_{i,j} - \Delta t ((\tilde{q}_{i+1/2,j} - \tilde{q}_{i-1/2,j}) / \Delta x + (\tilde{q}_{i,j+1/2} - \tilde{q}_{i,j-1/2}) / \Delta y),$$

$$\tilde{q}_{i+1/2,j} = \begin{cases} \tilde{H}_{i,j} \tilde{u}_{i+1/2,j} & \text{if } \tilde{u}_{i+1/2,j} > 0, \\ \tilde{H}_{i+1,j} \tilde{u}_{i+1/2,j} & \text{if } \tilde{u}_{i+1/2,j} < 0 \end{cases}, \quad \tilde{q}_{i,j+1/2} = \begin{cases} \tilde{H}_{i,j} \tilde{v}_{i,j+1/2} & \text{if } \tilde{v}_{i,j+1/2} > 0, \\ \tilde{H}_{i,j+1} \tilde{v}_{i,j+1/2} & \text{if } \tilde{v}_{i,j+1/2} < 0 \end{cases}.$$

Similar expressions to calculate values $(Hu)_{i+1/2,j}^{n+1}$ and $(Hv)_{i,j+1/2}^{n+1}$ can be written.

The stability condition for the difference scheme is the inequality

$$\Delta t \leq \alpha \cdot \min \left\{ \frac{\Delta x}{|u| + \sqrt{gH}}, \frac{\Delta y}{|v| + \sqrt{gH}} \right\}$$

in all grid nodes, where $0 < \alpha < 1$ is the empirical stability factor (its value $\alpha = 0.5$ was used in our calculations).

1.9.Problems associated with verification of numerical models

The main purpose of the Pilot Project is the verification of mathematical models, numerical algorithms and computer codes developed in the ICT and ICMMG SB RAS for tsunami modeling. According technical specification to the Pilot Project, five historical tsunamigenic events occurred near the eastern coast of Japan were selected for such verification. They are the 2011 Tohoku, 1946 Nankai, 1944 Tonankai, 1923 Kanto and 1854 Ansei-Tokai tsunamigenic earthquakes.

The total time range of the selected events covers more than 150 years. During this period the level of data completeness and the degree of the data accuracy considerably changed, that is why the amount and quality of the observational data for these tsunamis is incomparable. The instrumental measurements of the 2011 Tohoku tsunami heights, obtained by the Joint Tohoku Earthquake Tsunami Research Survey Group, have highest possible accuracy reaching few meters in geographical coordinates and few centimeters in water level as well as density of measurements (more than 5700 measured heights). However, systematic field survey of destructive tsunamis started only in 1992. For earlier historical events, observational data are mainly based on witness reports and other anecdotal sources. Accuracy of observational data for old historical events can be of order of several kilometers in distance and few meters in height. What is more important, it is not always clear from historical observations what type of measurement (inundation depth or run-up height) they report. That is why the direct correspondence of computed and measured heights for historical tsunamis occurred earlier 1992 is always questionable.

However, reliability of available observations is only a part of problem. Another part is the degree of confidence in knowing the actual source parameters (position, size, type of mechanism, energy scale). While documenting the coastal tsunami impact can be achieved by using methods of direct or indirect measurements, all source parameters can be restored only by solving the inverse problem that has intrinsic limitation on data accuracy and restoration methodology used. Both were a subject of dramatic changes over the last one hundred years. It is

well known that most of inverse problems in geophysics are ill-posed and their solvability strongly depends on quality of the input data and restoration algorithm used and its numerical implementation (Kabanikhin, 2009). Besides, the solution found can be non-unique (so far, theorems of uniqueness were obtained only for a small part of specific inverse problems possible in geophysics).

Regarding the quality of seismological data available in catalogs, one should take into account the following. The whole period of historical observations can be roughly divided into three main parts: pre-instrumental: (prior ca. 1900), early instrumental (1900-1963), instrumental (1963- ca.1990), and modern instrumental period (after 1990). During the pre-instrumental period only macro-seismic estimates of magnitude and source location are available. Both are based on the reported level of seismic shaking in different locations. The accuracy of magnitude for this period is ± 1 , accuracy of source location is $\pm 1 \div 2^\circ$. During the early instrumental period the level of accuracy in magnitude and location measurements was actually the same because mechanical short-period seismometers used in all countries could not provide precise measurement of earthquake energy and the level of processing technique (and the knowledge of internal Earth structure) could not provide adequate location of the earthquake source. The deployment of the WWSSN network (World-Wide Standardized Seismographic Network) in the beginning of 60th, initiated by the need to monitor the compliance of the 1963 treaty banning above-ground testing of nuclear weapons, was the major step in improvement of quality and accuracy of seismological data. The new, long-period magnitude scale M_s was proposed and replaced the Richter short-period magnitude. As a result, magnitude estimates became more homogeneous and their accuracy increased to ± 0.5 and location increased (globally) to $\pm 0.5 \div 1^\circ$. The next major step in improvement of seismological data occurred only 30 years later when new type of instruments (very-broad band digital seismometers) were introduced and moment-magnitude M_w estimates could be obtained directly from seismograms. For the modern major earthquakes their accuracy is considered to be $\pm 0.1 \div 0.2$, but for many smaller events the differences between M_w estimates provided by different agencies still can be up to 0.5. New algorithms of data processing based on better knowledge of the Earth interior structure allowed to reach accuracy in (final) source location $\pm 0.1 \div 0.2^\circ$.

Finally, even in the best-studied cases like the 2004 Sumatra and 2011 Tohoku earthquakes, the limitation factor for matching of computed and measured tsunami run-up heights is availability of reliable bathymetric data. It was established long ago that for direct comparison of computed and measured run-up heights we need to have a computational grid with resolution in 5-10 m for the shallow water area. Except some specific cases (like the 1993 Okushiri tsunami selected as benchmark for calibration of run-up models) such an accuracy is still inaccessible for tsunami modelers for most of coastal areas of the World Ocean.

Numerical methods for calculating the wave run-up on the shore were verified on well-known test problems (*benchmarks*) (Long-wave runup models, 1996).

In 1D-case the problem of solitary wave run-up on a flat slope with slope β , matching with flat bottom of depth H_0 , was considered. The initial wave profile and velocity were defined by the formulas

$$\eta(x,0) = \frac{A}{ch^2(Z)}, \quad Z = \sqrt{\frac{3A}{4(H_0 + A)^3}} \cdot \frac{(x - x_0)}{H_0}, \quad u(x,0) = -\frac{\eta \sqrt{g(H_0 + A)}}{H_0 + \eta},$$

where A – amplitude, x_0 – initial position of the wave crest (Fig. 1.9.1).

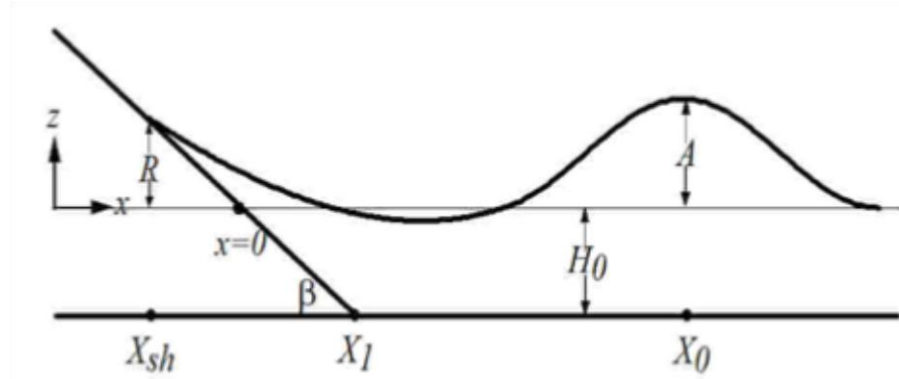


Fig. 1.9.1. Sketch of the 1D test-problem.

As mentioned in paragraph 1.7.1, C.E.Synolakis received an analytical solution for the determination of the vertical run-up in such a setting (Synolakis, 1987):

$$\frac{R}{H_0} = 2.831 \sqrt{\text{ctg} \beta} \left(\frac{A}{H_0} \right)^{5/4} \quad (1.28)$$

This formula is applicable within $(0.288 \tan \beta)^2 \ll \frac{A}{H_0} < 0.479 (\tan \beta)^{10/9}$.

To verify the numerical algorithms we considered a set of problems with the following values of parameters:

Table 1.9.1. 1D run-up calculations: different solitary wave amplitudes vs slope angle

$\text{ctg} \beta$	19.85	19.85	19.85	19.85	19.85	19.85	19.85	19.85	19.85	19.85
A/H_0	0.005	0.01	0.015	0.02	0.025	0.03	0.035	0.04	0.045	0.05

Table 1.9.2. 1D run-up calculations: different slope angles vs solitary wave amplitude

A/H_0	0.01	0.01	0.01	0.01	0.01	0.01	0.01	0.01
β	1°	2°	$\sim 2.88^\circ$ ($\text{ctg} \beta = 19.85$)	4°	5°	8°	10°	

Table 1.9.3. 1D run-up calculations: different slope angles and solitary wave amplitudes

β	10°	10°	10°	15°	15°	15°
A/H_0	0.1	0.15	0.02	0.1	0.15	0.2

The following figure compares the runup values obtained from the analytical formula (1.28), with those calculated using the large particles and method using analytical relations at the shore. Additionally the results of numerical calculations of other authors and data from laboratory experiments (Synolakis, 1987; Synolakis, 1991) are presented:

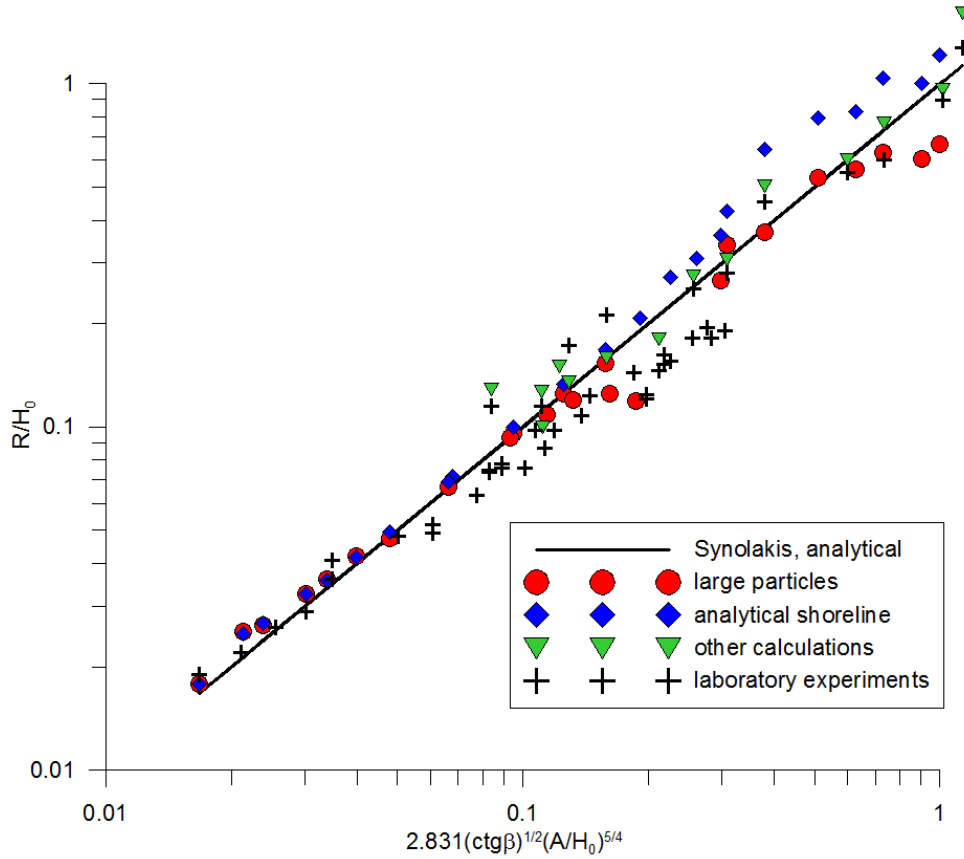


Fig. 1.9.2. Comparison of the calculated run-up values with analytical values, the results of other authors and the experimental ones.

The series of computational experiments were aimed at comparing mathematical models with experimental data and estimating the sensitivity of the employed model and algorithms to the parameters of bottom and land friction for 2D problems.

The model water area was a rectangular 30-m-wide by 25-m-long flat-bottom basin at the U.S. Army Engineer Waterways Experiment Station. The island in the center of basin had the shape of a truncated, right circular cone with radii $R_0 = 3.6\text{m}$ at the toe and $R_1 = 1.1\text{ m}$ at the crest. The vertical height of the island was $H_1 = 0.625\text{ m}$, with 1V on 4H beach face (i.e. $\beta \approx 14^\circ$). The water depth was set at $H_0 = 0.32\text{m}$ in the basin (see Fig. 1.9.3).

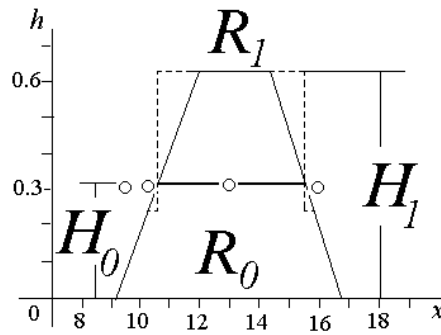


Fig. 1.9.3. Sketch of the 2D test-problem – conic island (side view).

The X-axis was perpendicular to the wavemaker and the Y-axis was parallel to the wavemaker. The origin was located at the end of the wavemaker, and the center of the island was located at $X = 12.96\text{m}$ and $Y = 13.8\text{m}$ (see Fig. 1.9.4).

In the laboratory experiment, the incoming solitary wave was generated by the horizontal shift of the directional spectral wave generator. Wave heights $A_0 = 0.015, 0.03, 0.06\text{m}$ were simulated for cases A, B, C, respectively.

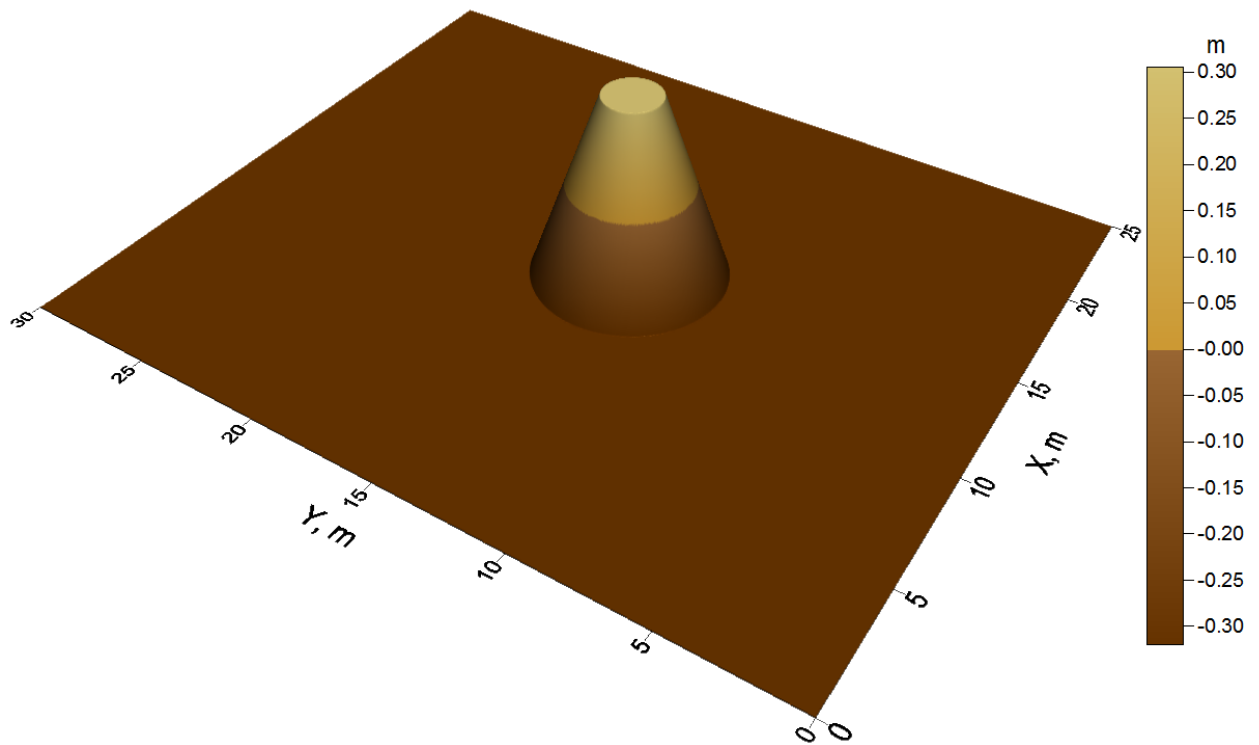


Fig. 1.9.4. Relief of the model basin (2D test-problem).

Laboratory data which are available to compare the results of numerical simulations include mareograms at 4 of 27 wave gages: #6, 9, 16, 22 (Fig. 1.9.5, Table 1.9.4. Location and depth under wave gages (2D test-problem)Table 1.9.4). Sensor #6 is set directly in front of the island, the sensor #9 – in the front-side shallow waters of the island, sensor #16 – in the right-side, the sensor #22 – in the back-side. In addition, the maximum runup on the perimeter of the island in 24 points was fixed.

Table 1.9.4. Location and depth under wave gages (2D test-problem)

gage #	x	y	H
6	9.36	13.80	0.317
9	10.36	13.80	0.082
16	12.96	11.22	0.079
22	15.56	13.80	0.083

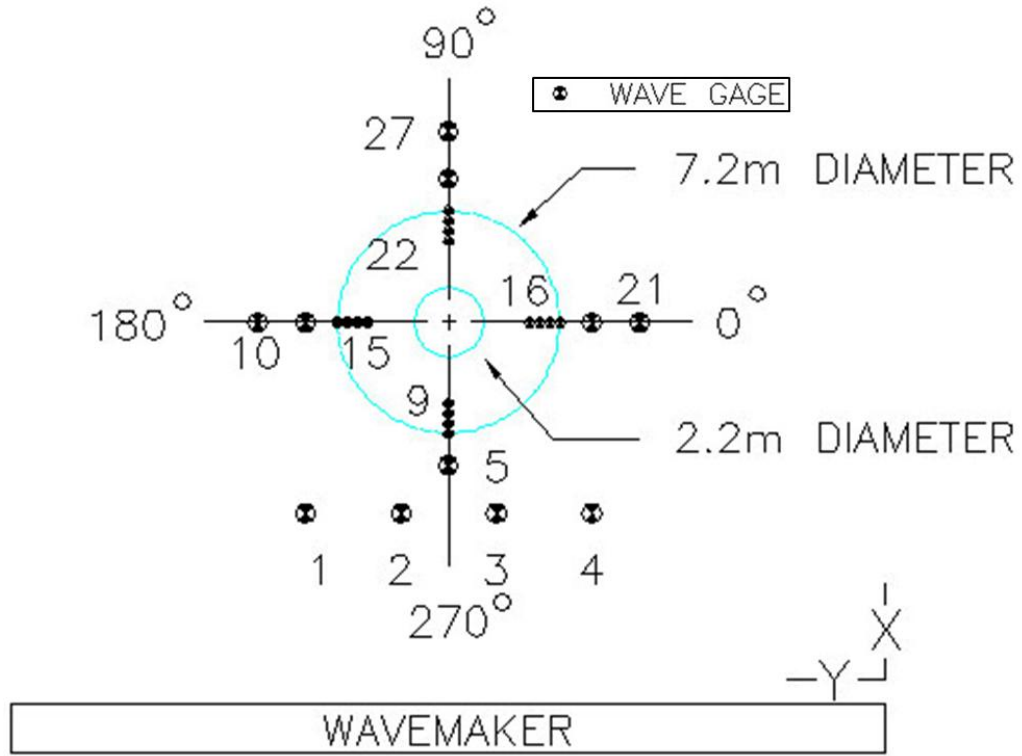


Fig. 1.9.5. Sketch of the wave gage position (top view).

The computational model simplification included the simplified method for description of the solitary wave generation (in the present study we did not simulate the motion of the wave generator and limited themselves only to specifying an incoming solitary wave with the amplitude A_0):

$$\eta(0, y, t) = A_0 \operatorname{sech}^2 \left\{ \left(\frac{3A_0}{4H_0^2(H_0 + A_0)} \right)^{1/2} (x_0 - ct) \right\}, \quad c = \sqrt{g(H_0 + A_0)}.$$

At the closest to the boundary internal node of the respective grid the values of the normal velocity component u_n were obtained from the relation

$$u = \frac{c\eta}{H + \eta}.$$

The second component of the velocity vector (tangential) v at the boundary was calculated from the relation $u_y = v_x$, being a corollary of the assumption of the quasi-potential velocity vector \mathbf{u} . It holds exactly at the bottom section with a constant depth. On the other boundaries absorbing boundary conditions described

by the well-known Sommerfeld condition $f_t + cf_n = 0$ along the external normal \mathbf{n} to the boundary are posed.

The present results correspond to the experiments (A) – $A_0^A = 0.015$ m and (B) – $A_0^B = 0.03$ m. The grid spacing is 2 cm.

The character of the wave process development (Fig. 1.9.6) differs qualitatively insignificantly in the cases (A, B): the solitary wave flows passed the model island with its amplitude increasing considerably in the immediate vicinity of the island and generates the zone of the wave energy concentration which propagates towards the outlet boundary of the calculation domain leaving behind a system of concentric waves disappearing through the absorbing boundaries. Shown in the figure free surface elevations at successive time moments were calculated for the Case A without a bottom friction.

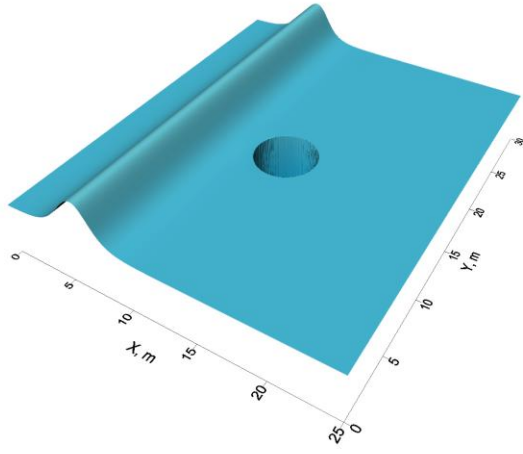
Due to the fact that the specification of the boundary data in the laboratory and numerical experiments were different, the goal of calculations was to obtain not quantitative agreement, but a good qualitative description of the wave process.

As the results below show, the calculated values are in good agreement with the laboratory data and, in particular, well reproduce the change in the vertical wave runup around the island: the maximum run-up occurs on the front side, and then, when going round the island, it is gradually reduced, and on the back side there is another extremum value (Fig. 1.9.6 (e), Fig. 1.9.7).

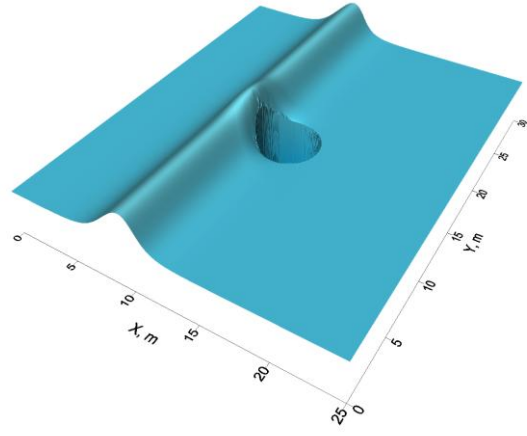
Table 1.9.5 shows the calculated values of maximum vertical run-up on the front and back sides of the island in comparison with experiment data and with calculated in (Takagi, 1996) using finite element method without bottom friction.

Table 1.9.5. Comparison of calculated values of maximum vertical run-up on the front and back sides of the island, experiment data and calculated in (Takagi, 1996)

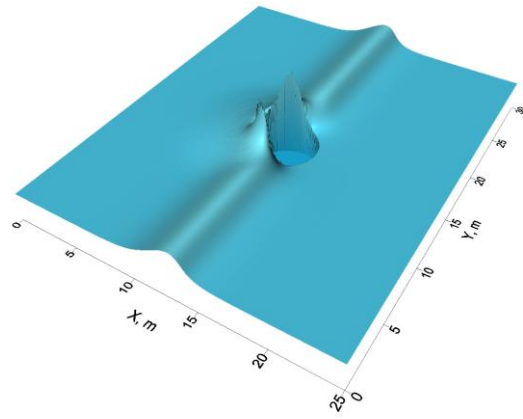
	Case A						Case B				
	computed				computed (Takagi, 1996)	exper.	computed			computed (Takagi, 1996)	exper.
Chezy coef.	0	0.002	0.004	0.005			0	0.002	0.004		
R (cm) front side	4.5	4.1	3.6	3.6	4.9	3.2	11.5	9.1	7.1	8.7	7.4
R (cm) back side	3.5	3.1	2.5	2.1	4.1	2.2	9.1	6.1	4.1	7.2	8.6



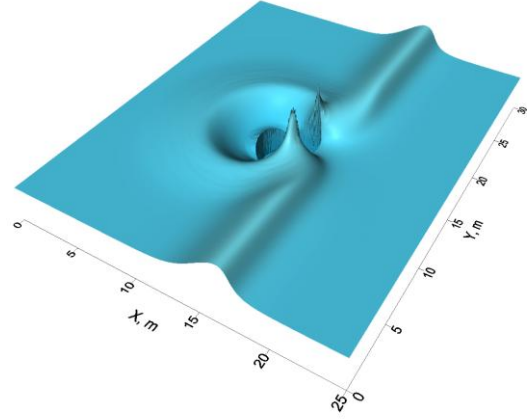
(a)



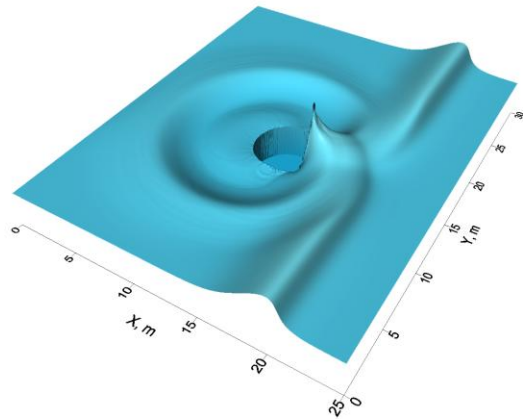
(b)



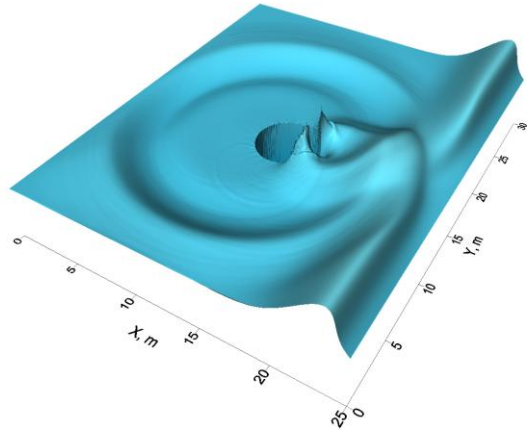
(c)



(d)



(e)



(f)

Fig. 1.9.6. Free surface elevations at successive time moments.

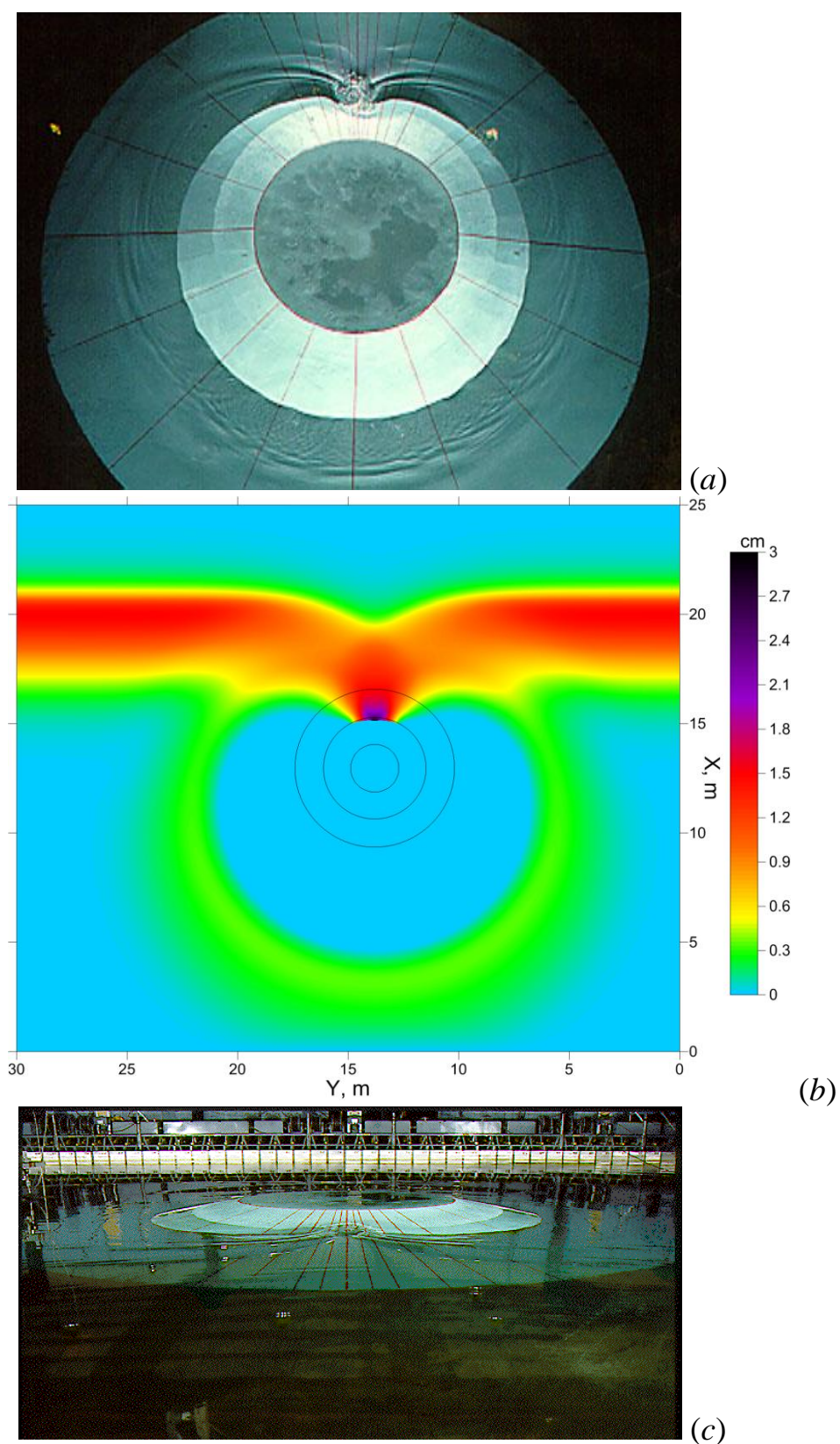


Fig. 1.9.7. Interaction of the solitary wave with the conical island: (a) – top view (laboratory experiment, <http://chl.erdc.usace.army.mil/chl.aspx?p=s&a=Projects;35>), the solitary wave comes from below; (b) – the same, for computed result, (c) – back (shadow) view (laboratory experiment); the time moment corresponds to the phase (e) in the Fig. 1.9.6.

Analysis of the wave run-up over the island perimeter (Fig. 1.9.8) calculated for different friction coefficients and the comparison of computed run-up data with the experimental ones is of greatest informational value. It demonstrates the trends of the emergence of the shadow zone in the "north-east" part of the island and the considerable increase in the run-up in its "northern" part which had already been mentioned.

Shown in the figure results clearly demonstrate the non-linearity of the studied process. This is manifested in the fact that if the low amplitude of the incident wave (Case *A*) one can select the parameter of friction (Chezy coefficient), for which the results of numerical simulations come close to the experimental data along the entire perimeter of the conical island, with increasing amplitude (Case *B*) of the incident waves this single parameter cannot be selected. In this case, the experimental data on the back splash in the shadow area of the island is well reproduced at zero Chezy coefficient, and the rest sides – at its value equal to 0.004. It should also be noted that with the increase of the amplitude of the incident wave the difference between the results obtained with different coefficients of friction increases.

The comparison of computed results with the experimental data shows that in spite of the considerable simplification of the initial perturbation, the computational model fairly adequately represents the process of the solitary wave interaction with an obstacle and when the friction coefficient is defined properly the results of the numerical modeling tend to provide the convergence of the solution corresponding to the experimental data.

Modeling the solitary wave interaction with an island and the comparison of the results with the laboratory data showed satisfactory agreement of the model and algorithm and the wave processes under study, in spite of the certain simplifications. This fact makes it possible to consider the suggested computational model a reliable tool for tsunami inundation modeling. At the same time, the results of test calculations indicate that for adequate quantitative estimates of runup we need adequate data on the properties of the land regions (growth, ground, building structures and so forth).

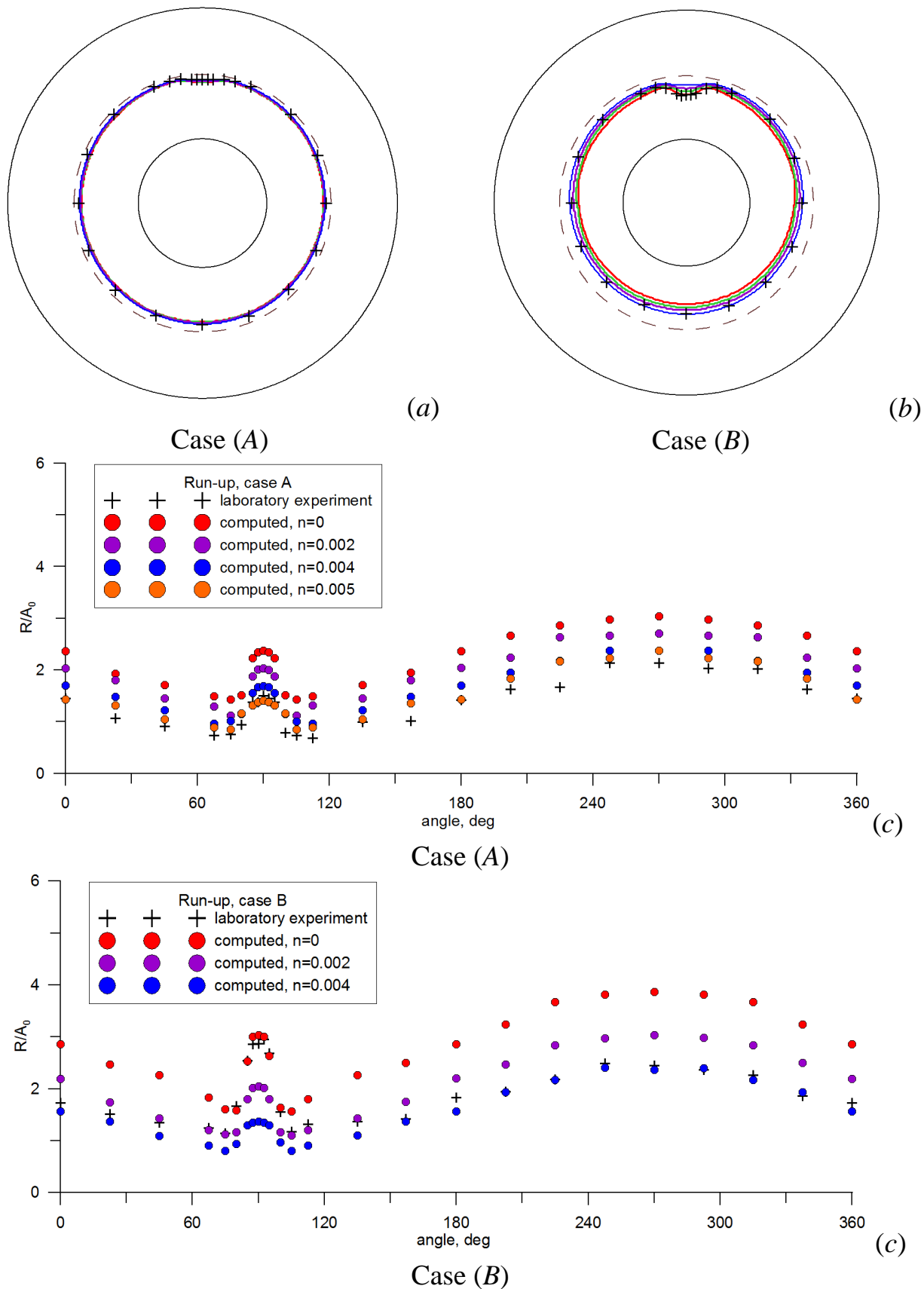


Fig. 1.9.8. Top – calculated inundation zones (colored lines) and experimental data (crosses), bottom – maximum wave run-up heights around the islands for cases A and B. Line color corresponds to the dots color in the legends.

The mareograms (Fig. 1.9.9) shown were obtained in the course of the experiment (A) by means of the large particles method. Red lines correspond to the computed mareograms and black – to the experimental data. Comparing these curves we conclude that the first waves are described well, and following computed oscillations are some simplified.

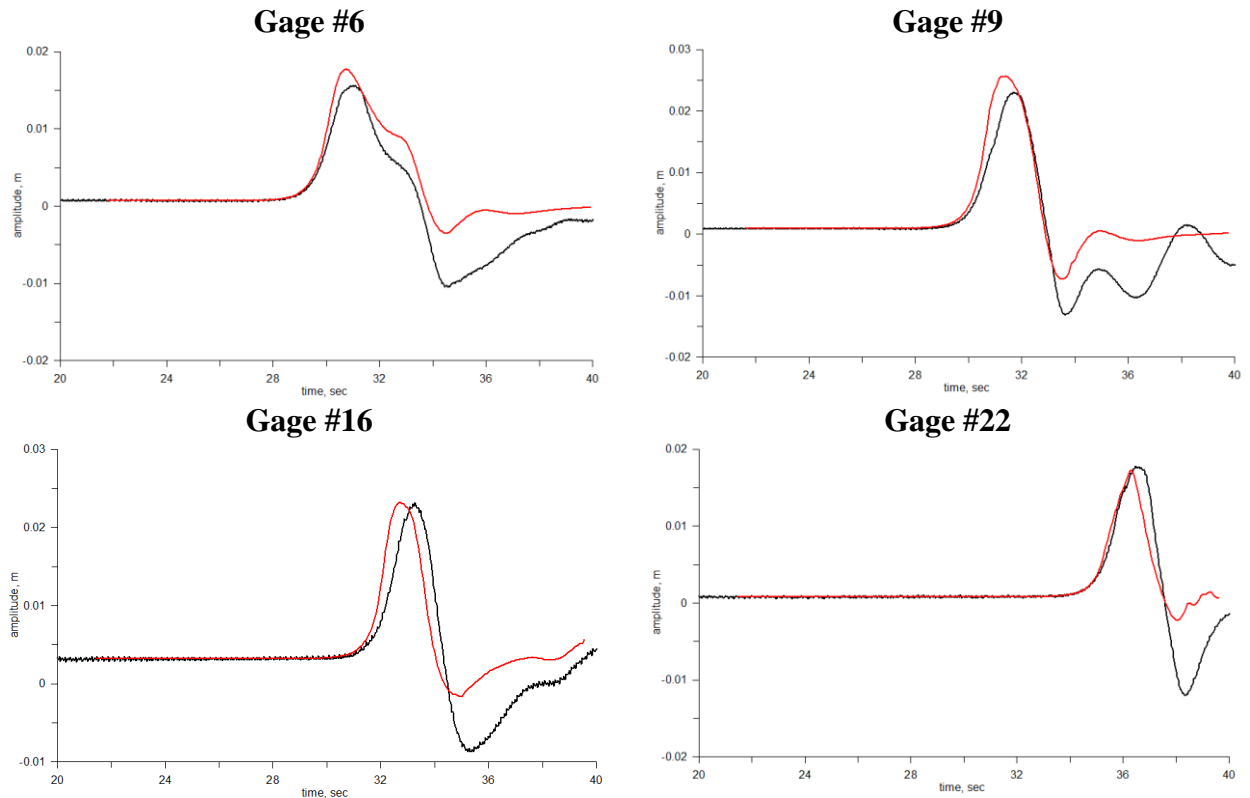


Fig. 1.9.9. Mareograms at the selected gages: red lines – numerical results, black – experimental ones.

2. Results of numerical experiments

This section presents the results of simulation of flooding of selected coastal areas by the tsunami waves for each of the five historical events, mainly, in the form of maps showing the inundation limits for the selected coastal areas. In determining the structure and a set of presented figures, it was decided to demonstrate

- the relative position of the initial elevation, coastal areas for 2D run-up calculation and straight cross-sections, along which 1D modeling has been carried out on the first stage of the Project;
- features of different topography and bathymetry reliefs being in use;
- a comparison of inundation zones, obtained by 1D and 2D run-up modeling;
- dependence of the calculated inundation zones on some parameters of physical models, numerical algorithm parameters and input data.

Each of the following drawings is accompanied by the detailed signature.

As already mentioned above, 4 coastal areas for the event «Tohoku, 2011» have been considered, and in two of them («Koborinai» and «Miyako»)

calculations were performed using the detailed DEM and DBM; for coastal areas "Sendai" and "Iwaki" calculations were performed using detailed DEM (SRTM-3 sec, version 2.1) and DBM GEBCO-30 sec.

For each of the four other historical events 2 coastal areas have been selected for run-up simulation, and calculations were performed using DEM/DBM GEBCO-30 sec.

The most interesting, in our view, are the results of "Tohoku, 2011" tsunami modeling. This event is the most studied, and is accompanied by a huge amount of field data and publications. Finally, our simulations have been performed for this event using the most detailed data on the topography and bathymetry.

The first analysis of the simulation results shows that runup heights, obtained by the 2D modeling of Koborinai Bay inundation, are about 30 meters, which is consistent with field data. In Miyako heights of 15 – 20 meters have been observed, while our calculated values are 15 – 25 meters. In the area of Sendai observed runup was to a height of about 10 – 15m, and the calculations were obtained for about 25 – 30 meters. Finally, in the vicinity of the city of Iwaki runup heights of 7 - 10 meters have been observed, and the calculated values are about the same when using DEM SRTM-3 sec (version 2.1) and reach 12 meters when using DEM GEBCO-30 sec.

The resulting difference between the observed and calculated values can be explained by the fact that the calculations used zero Chezy coefficient (ie, zero friction), except for the parametric analysis for Koborinai Bay. The absence of differences for the coastal area "Iwaki", when using DEM SRTM-3 sec (version 2.1), can be due to very rough topography relief, reproducing the effect of "artificial" friction, which was enough for run-up calculation in coastal areas that are not located directly in front of the source. At the same time, the great variation in the observed and measured heights in the vicinity of Sendai may be due to the need to improve the model of the tsunami source. As it is known, none of the proposed models of the source of relevant tsunamigenic earthquakes are able to reproduce the actually position of maximum heights peak (observed at latitudes near 39°N) but move it to the south at 38-38.5° N, where our coastal area "Sendai" is located.

When comparing the results of 1D and 2D modeling, note that the one-dimensional modeling approach clearly assumes the frontal approach of a wave to the coast, along the corresponding 1D cross-sections, that, in fact, is not always true. But it should be noted a very good agreement between the results of 1D and 2D simulation for the area "Iwaki", which is explained by the fact that in the 2D calculations waves approaching the coast just to the south-east, along the one-dimensional cross-sections. This confirms the applicability of the proposed 1D technology in such situations.

2.1.1854 Ansei-Tokai tsunami

2.1.1. Basic information on earthquake and tsunami

The M8.4 December 7, 1854 Ansei-Tokai earthquake was the first in series of three major earthquakes that struck the Tokai region of Japan during the Ansei era (1854-1960). It was followed up by another strong M8.4 earthquake (Ansei-Nankai) that ruptured southern part of the Nankai Trough on the next day, December 24, 1854. The Ansei-Tokai quake occurred about 9 o'clock in the morning and was felt over a large area, including the prefectures of Tochigi, Kanagawa, Yamanashi, Shizuoka, Nagano, Aichi, Gifu, Mie, Shiga, Fukui and Nara. The zone of greatest destruction had a length of 260 km and a width of 120 km. Damage from the earthquake was particularly severe in the coastal areas of Shizuoka Prefecture from Numazu to Tenryu River, with many houses being damaged or destroyed.

The earthquake occurred in pre-instrumental period of seismological observations so its magnitude and source location can be estimated only from macroseismic effects (intensity of shaking, vertical co-seismic displacement of coastal area, distribution of tsunami heights). The magnitude value, listed in the modern seismic catalogs for the 1854 Ansei-Tokai quake is 8.3-8.4.

Data on damage and fatalities resulted from the earthquake and tsunami greatly vary over different sources. Quite often, they are listed for both earthquakes (occurred on December 23 and December 24) together.

Data on the observed heights for this tsunami are also somewhat contradictory. The 21 m height indicated in (Iida, 1984) for Osatsu (34.385N, 136.910E), located in the eastern edge of the Shima Peninsula, Mie Prefecture maximum is not confirmed by the data from (Watanabe, 1985) who indicates for this area height 8-10m. Also, NGDC database lists 21m height for Toba (34.485N, 136.817E), Mie Prefecture that also is not confirmed by the data from (Watanabe, 1985) and (Soloviev, Go, 1974). Possibly, these uncertainties are the result of mixture of the data of both large tsunamis that occurred in adjacent areas on December 23 and 24, 1854.

In most severe affected coastal area, centered on the Suruga Bay, run-up heights were within the range of 4–6 m. At Iruma(34.628N, 138.810E), located at the southern part of the Izu Peninsula, run-up heights of 13.2 and 16.5 m have been measured, much higher than most of the surrounding area (Sugawara et al., 2005). This and the deposition of the unusual sand dome, with an estimated volume of 700,000 m³, is interpreted to have been caused by the effects of resonance in the V-shaped Iruma bay.

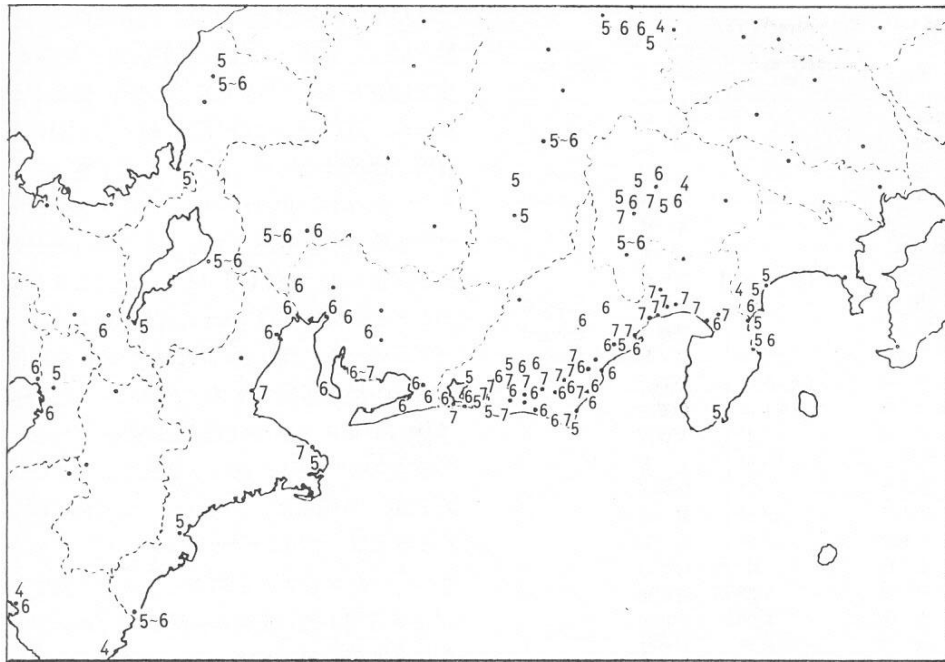


Fig. 2.1.1 Distribution of the reported seismic intensities (on the 7-grade JMA scale) for the 1854 Ansei-Tokai earthquake (Watanabe, 1985).

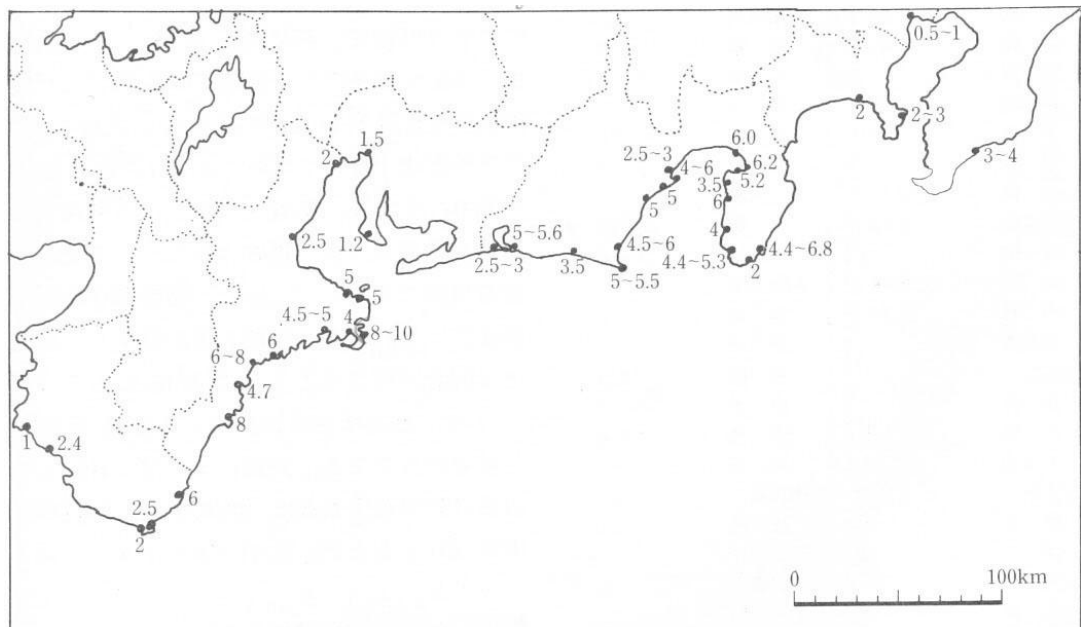


Fig. 2.1.2 Distribution of the reported wave heights for the 1854 Ansei-Tokai tsunami (Watanabe, 1985).

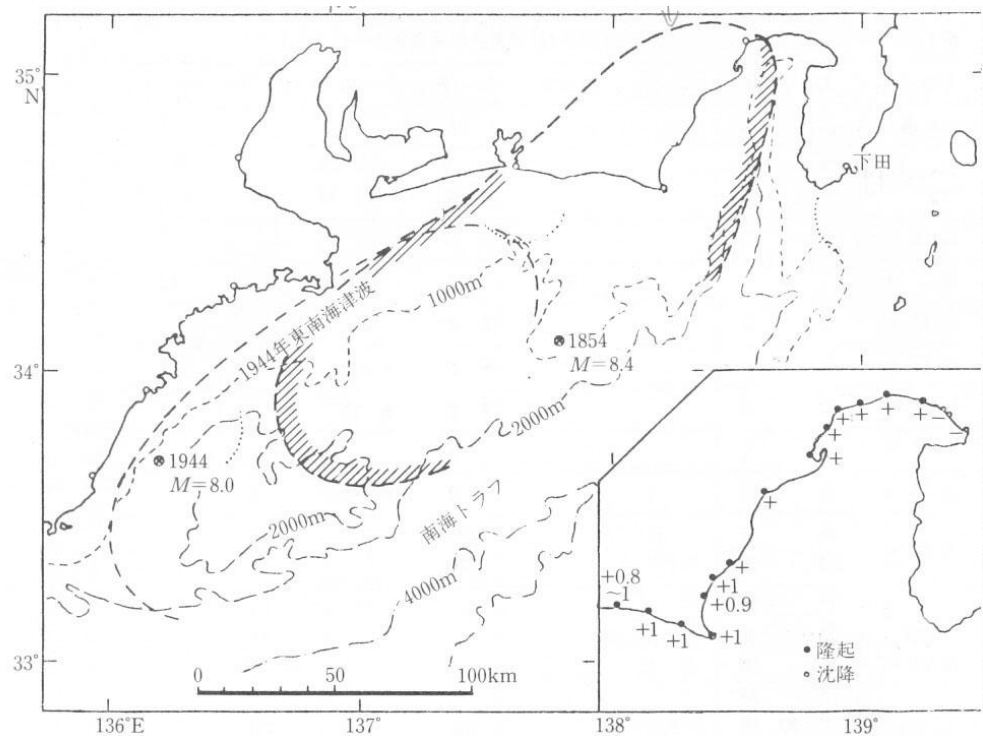


Fig. 2.1.3. Estimated position of a source of the 1854 Ansei-Tokai tsunami shown as shaded ellipse. Insert figure shows distribution of measured vertical co-seismic displacement along the west coast of Suruga Bay (Watanabe, 1985).

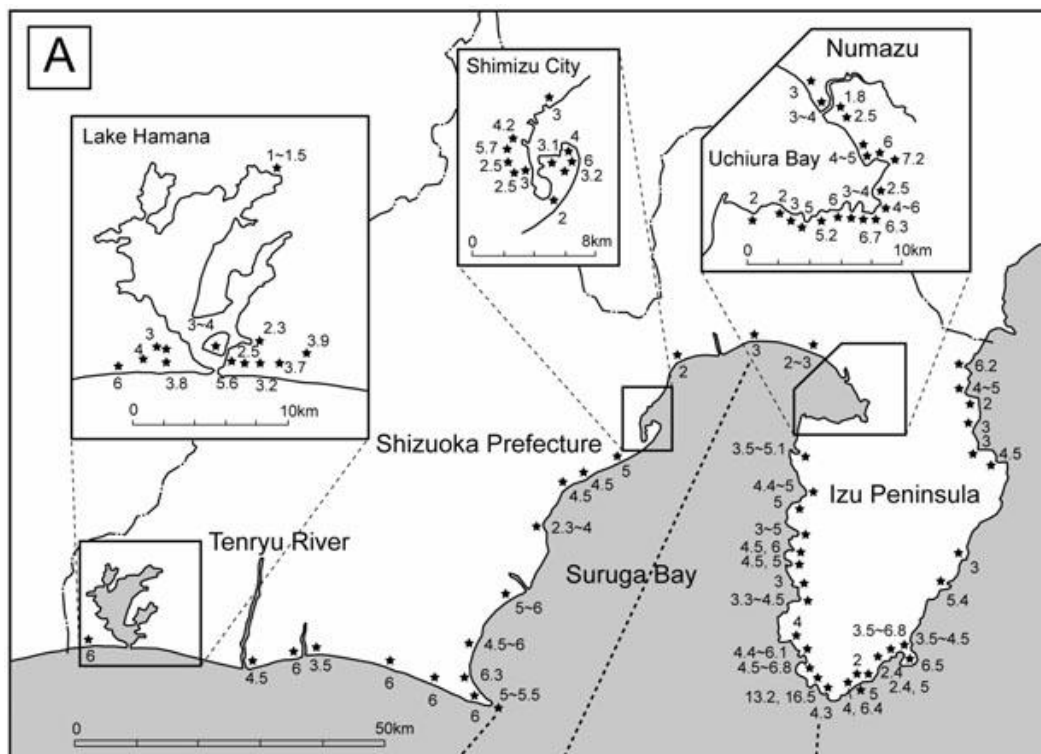


Fig. 2.1.4. Measured heights of the 1854 Ansei-Tokai tsunami along the coast of Shizuoka Prefecture (Sugawara et al., 2005).

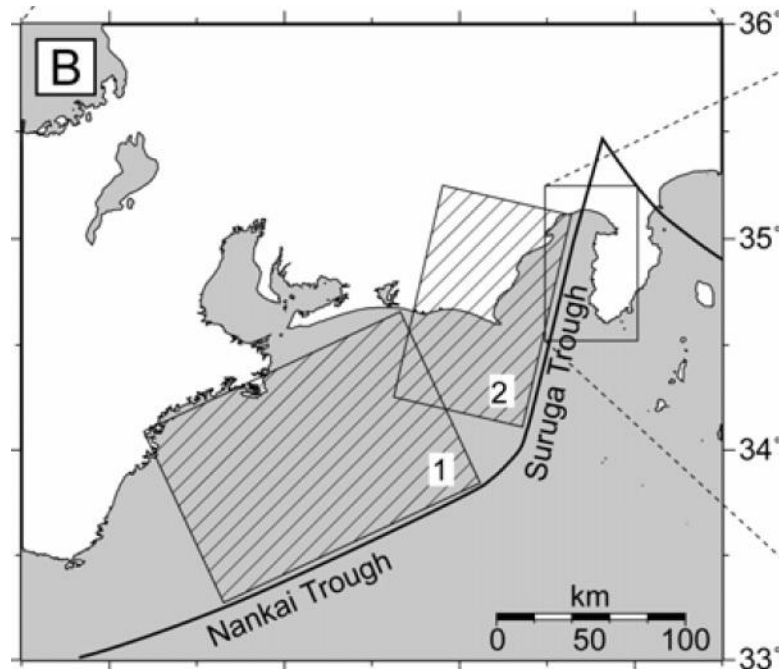


Fig. 2.1.5. Rupture planes in the source of the 1854 Ansei-Tokai earthquake proposed in (Sato, 1989).

2.1.2. Adopted source model and calculation of initial bottom displacement

The adopted model of the 1854 Ansei Tokai earthquake consists of two fault planes:

Plane1: $Lat = 34.4^{\circ}N$, $Lon = 137.0^{\circ}E$, $h_0 = 5$ km, $L = 150$ km, $W = 100$ km, $D_0 = 4.0$ m, $\delta = 24^{\circ}$, $\lambda = 113^{\circ}$, $\theta = 65^{\circ}$;

Plane2: $Lat = 34.8^{\circ}N$, $Lon = 137.8^{\circ}E$, $h_0 = 5$ km, $L = 115$ km, $W = 70$ km, $h_0 = 4$ km, $\delta = 34^{\circ}$, $\lambda = 71^{\circ}$, $\theta = 18^{\circ}$.

Calculated bottom displacement for this model source is shown in Fig. 2.1.6.

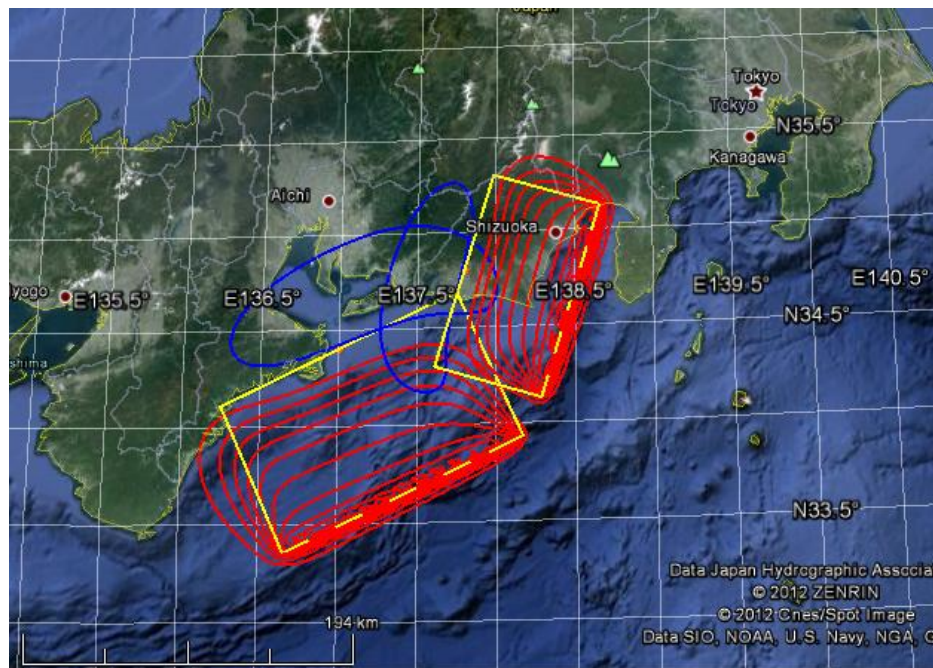


Fig. 2.1.6. Calculated bottom displacements for the adopted model of the 1854 Ansei-Tokai earthquake overlaid on the Google Earth map. Red color shows uplifted areas, blue color – subsided areas.

2.1.3. Calculation domain and virtual coastal points

Modeling of tsunami generation and propagation was carried out in the rectangular computational grid with dimension 2569×1681 and spatial step 15 angular seconds in both directions covering the area within $30^{\circ}00'N - 37^{\circ}00'N$, $131^{\circ}18'E - 142^{\circ}00'E$. The minimum water depth h_{\min} in the area was adopted to be equal 10 m. Tsunami heights were calculated at 5592 virtual mareograph points distributed along the coastline (Fig. 2.1.7).

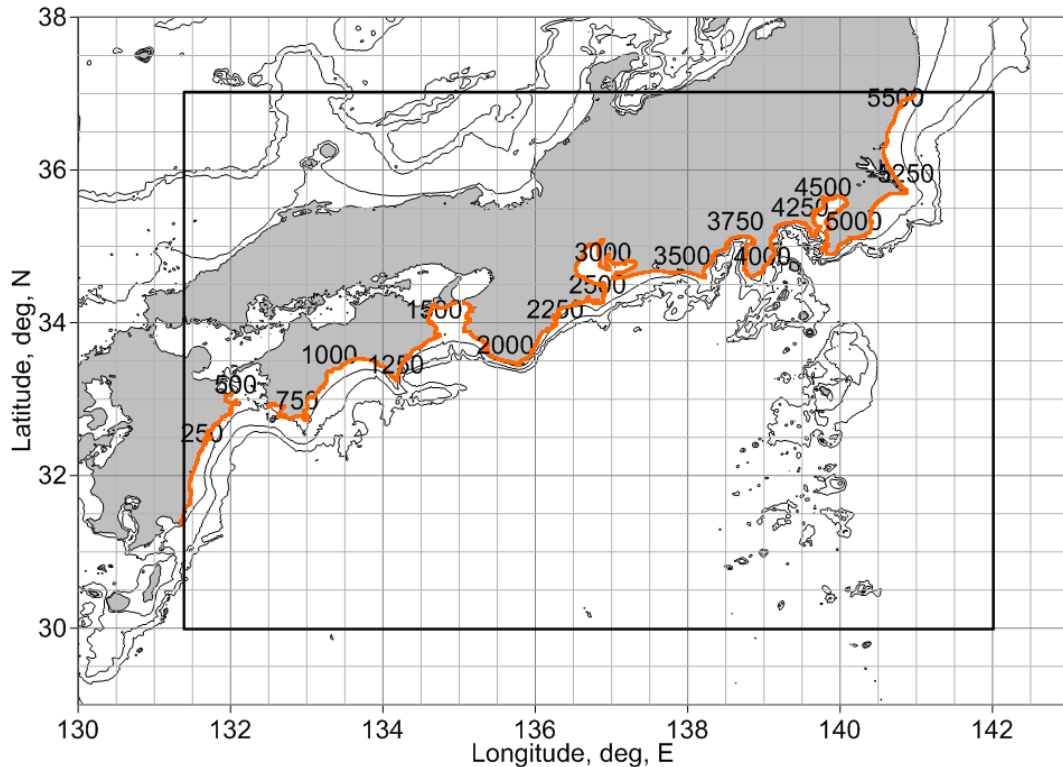


Fig. 2.1.7. The computational domain (plotted as solid black rectangle) with 100m, 500m and 1000m depth isobaths adopted for the 1854 Ansei-Tokai tsunami modeling. Spatial distribution of 5592 coastal virtual gauges is shown as orange numbered dots.

2.1.4. Analysis of computed wave height distribution

Numerical modeling of tsunami propagation was made for 4 hours of physical time using MGC package (Shokin et al., 2008) for tsunami modeling that is based on the non-linear shallow water system written in spherical coordinates. Results of computation are shown in Fig. 2.1.8 – Fig. 2.1.10.

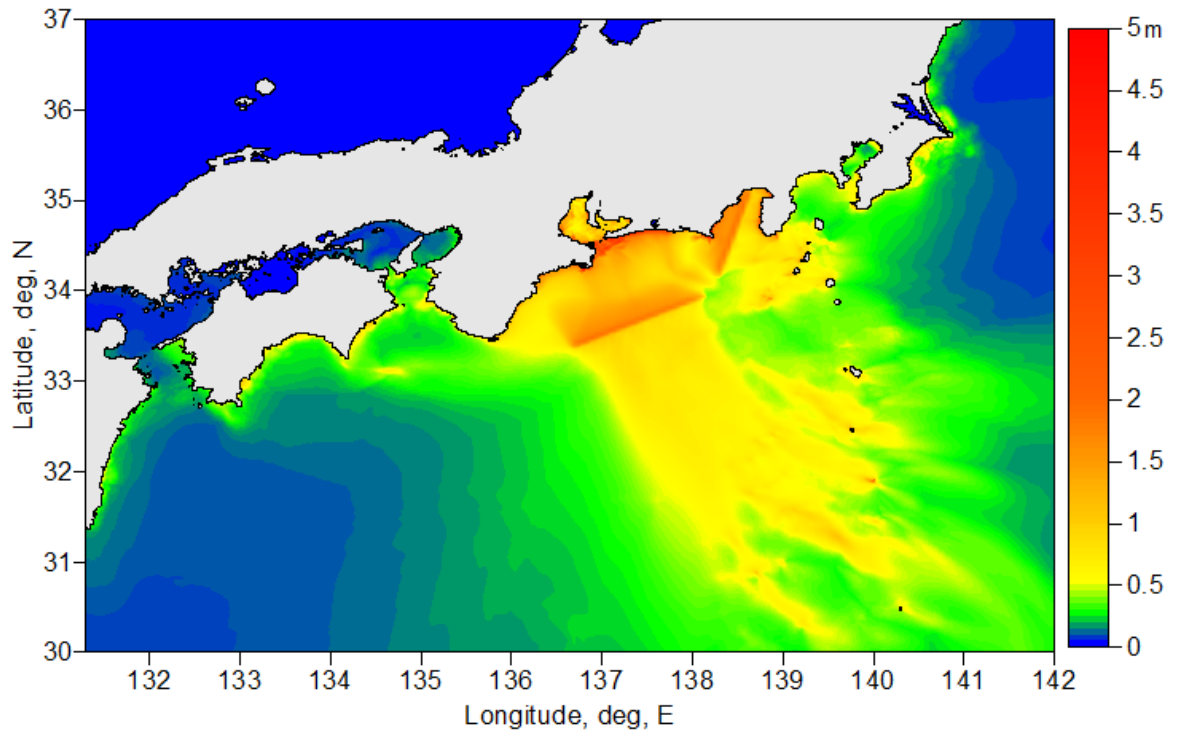


Fig. 2.1.8. Energy flux for the modeled 1854 Ansei-Tokai tsunami.

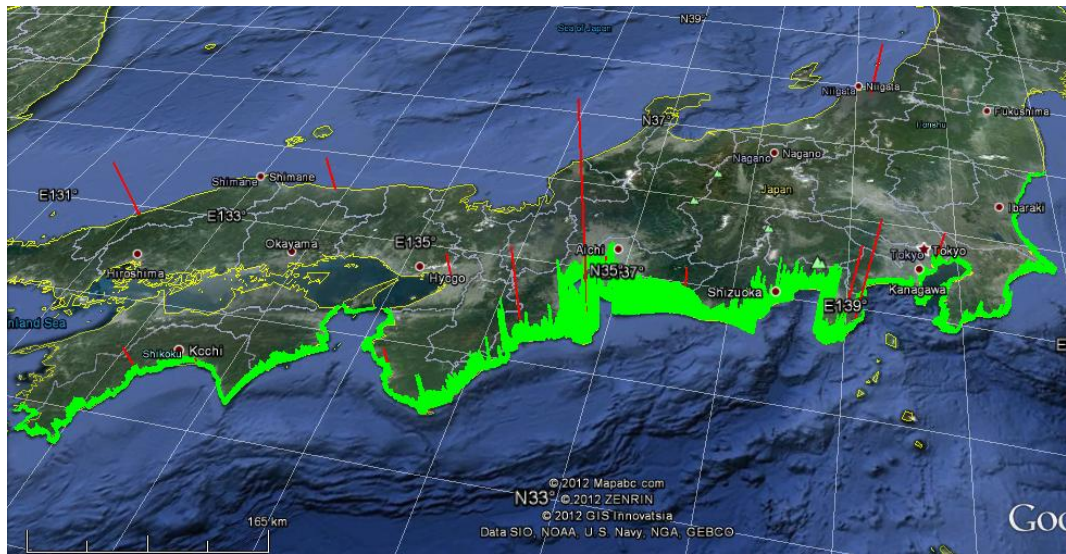


Fig. 2.1.9. Distribution of observed run-ups heights (red) of the 1854 Ansei-Tokai tsunami and computed maximum tsunami wave heights (green) calculated at the vertical wall put at the depth of 10 m for 5592 virtual coastal points. Some reported run-up heights (as retrieved from the NGDC/NOAA Tsunami Database) obviously have wrong coordinates.

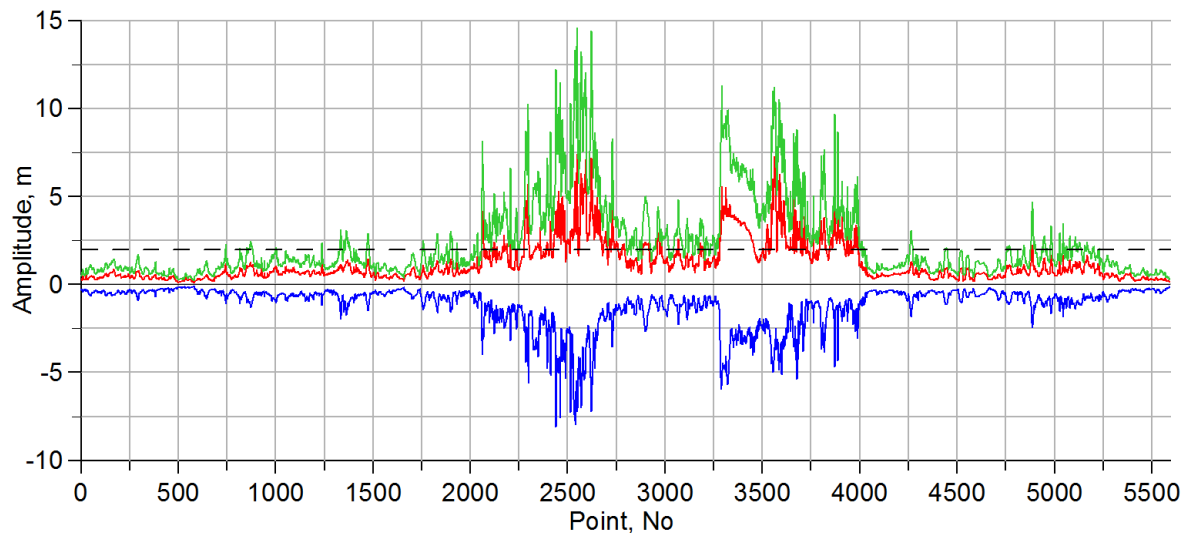


Fig. 2.1.10. Distribution of computed maximum positive (red line) wave amplitudes, maximum negative (blue line) wave amplitudes and maximum wave heights (green line) over 5592 coastal virtual gauges. Spatial location of these gauges is shown in Fig. 2.1.7.

2.1.5. 1D calculation of tsunami run-up and estimation of inundation limits

For test calculation of run-up heights for the 1854 Ansei-Tokai tsunami, a part of coastal plain near town Hamamatsu, Shizuoka Prefecture was selected where 10 profiles for 1D calculation of tsunami run-up were built (Fig. 2.1.11). Position of these profiles relatively to the adopted tsunami source is shown in Fig. 2.1.12. Since the maximum wave amplitudes obtained in 2D calculation for this area was only 3m, the land part of profiles was cut at the elevation of 10m. Starting point of all profiles was at the depth 100m.



Fig. 2.1.11. Position of 10 profiles, selected for one-dimensional calculations of run-up heights for the 1854 Ansei-Tokai tsunami. Solid black line represents the coastline. Isolines of land relief overlaid on the Google Earth map are for levels of 5 m (red), 10 m (orange), 20 m (yellow), 30 m (green). The white line shows the 100m depth contour.

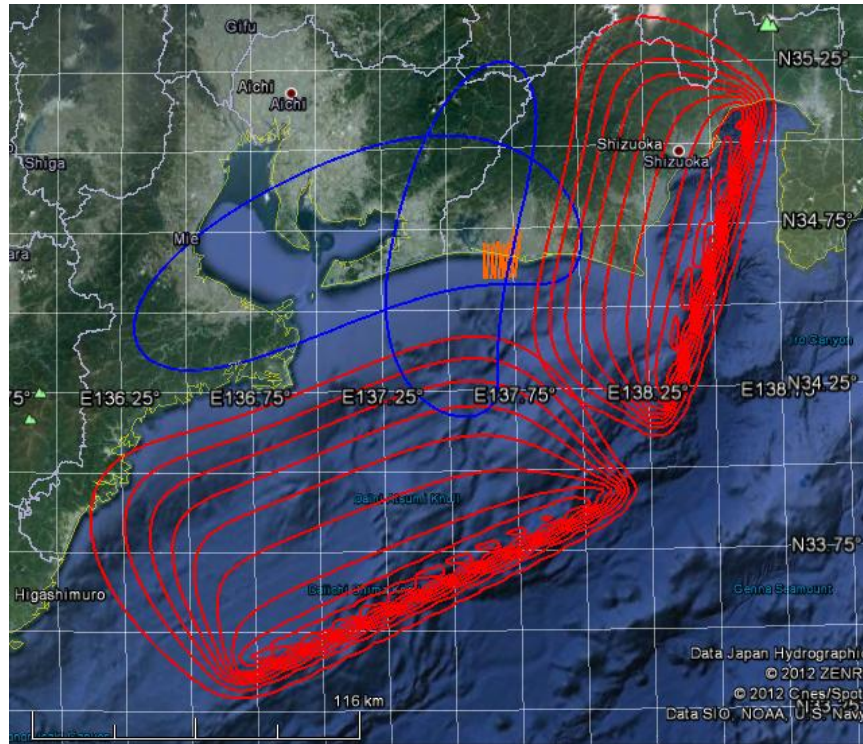


Fig. 2.1.12. Location of coastal profiles (orange lines) selected for 1D run-up modeling relatively source area of the 1854 Ansei-Tokai tsunami. Calculated co-seismic displacements for the adopted earthquake source model are shown as isolines of vertical displacement (red color shows uplifted areas, blue color - subsided areas).

All profiles selected for 1D modeling contain a fairly steep underwater part and rather flat land part, the length of which increases significantly when moving to the East along the coastline. This fact is certainly reflected in the characteristics of the splash on the beach. Calculated inundation distance along the profiles varies from 1.9 to 3.2 km (see Table 2.1.2).

Table 2.1.1. Land and bottom relief along the profiles selected for 1D modeling of run-up of the 1854 Ansei-Tokai tsunami.

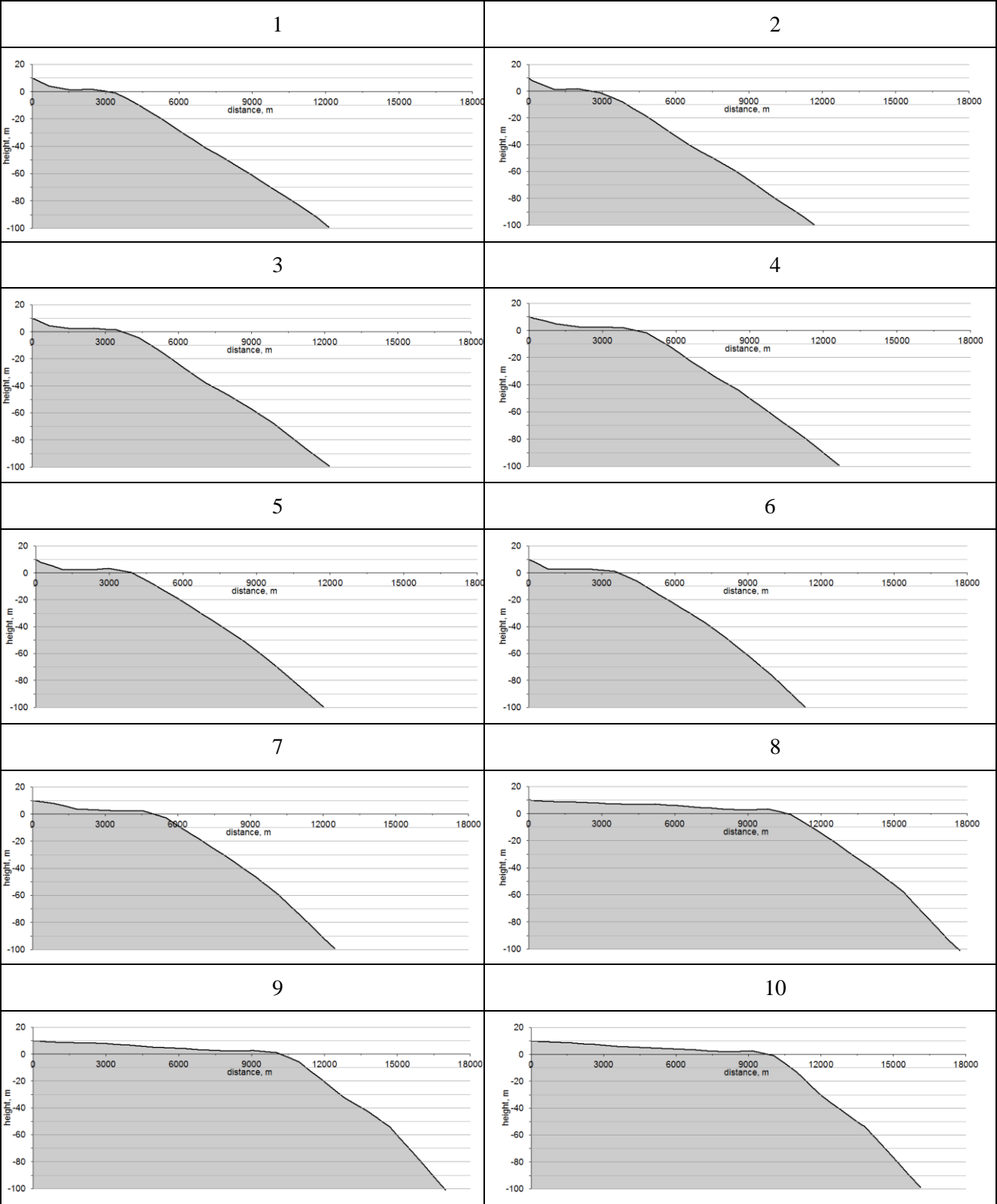


Table 2.1.2. Characteristics of 1854 Ansei-Tokai run-up heights, calculated in the 1D simulation along the selected cross-sections

Index number of cross-section	Calculated run-up height (m)	Calculated run-up distance (m)	Initial longitude of shoreline point (grad)	Initial latitude of shoreline point (grad)	Calculated longitude of run-up point (grad)	Calculated latitude of run-up point (grad)
1	4.83	2499.8	137.6429	34.6781	137.6432	34.7009
2	3.91	1939.8	137.6565	34.6776	137.6579	34.6952
3	4.86	3039.6	137.6727	34.6728	137.6747	34.7003
4	4.83	3213.7	137.6876	34.6705	137.6908	34.6996
5	4.12	3081.4	137.7023	34.6664	137.7049	34.6943
6	4.22	3030.3	137.7152	34.6653	137.7179	34.6928
7	3.83	3121.3	137.7270	34.6630	137.7314	34.6911
8	3.38	2579.3	137.7393	34.6595	137.7430	34.6827
9	3.17	3077.9	137.7522	34.6568	137.7570	34.6844
10	2.96	2711.2	137.7649	34.6521	137.7695	34.6764

Table 2.1.3. A comparison of characteristics of the 1854 Ansei-Tokai tsunami, calculated in the 2D simulation as “wet line” on the vertical wall (maximum positive wave amplitude), as run-up height obtained in 1D simulation along the selected profiles and as run-up height calculated by analytical formulas proposed in (Synolakis, 1987) and (Pelinovsky, Mazova, 1992). Red color marks values obtained outside of applicability of analytical formulas.

Index number of cross-section	Maximum positive amplitude on the wall, calculated in the 2D simulation (“wet line”) (m)	Runup heights, calculated in the 1D simulation (m)	Runup height, calculated by analytical formula of Synolakis, 1987 (m)	Runup height, calculated by analytical formula of Pelinovsky, Mazova, 1992 (m)	Observed data (m)
1	2.93664	4.825218	16.66475	4.457306	3
2	3.03009	3.913582	16.45369	4.70917	
3	2.792	4.862185	16.42955	3.983639	
4	2.70497	4.829395	16.28821	5.022887	
5	2.54114	4.118302	16.32009	4.653591	
6	2.45174	4.224107	15.17842	3.210338	
7	2.50575	3.828586	13.76618	3.257846	
8	2.19867	3.382664	14.85394	2.936788	
9	2.17669	3.173193	14.18236	3.869507	
10	2.09367	2.963047	13.04434	3.608318	
Average	2.54314	4.012028	15.31815	3.970939	3

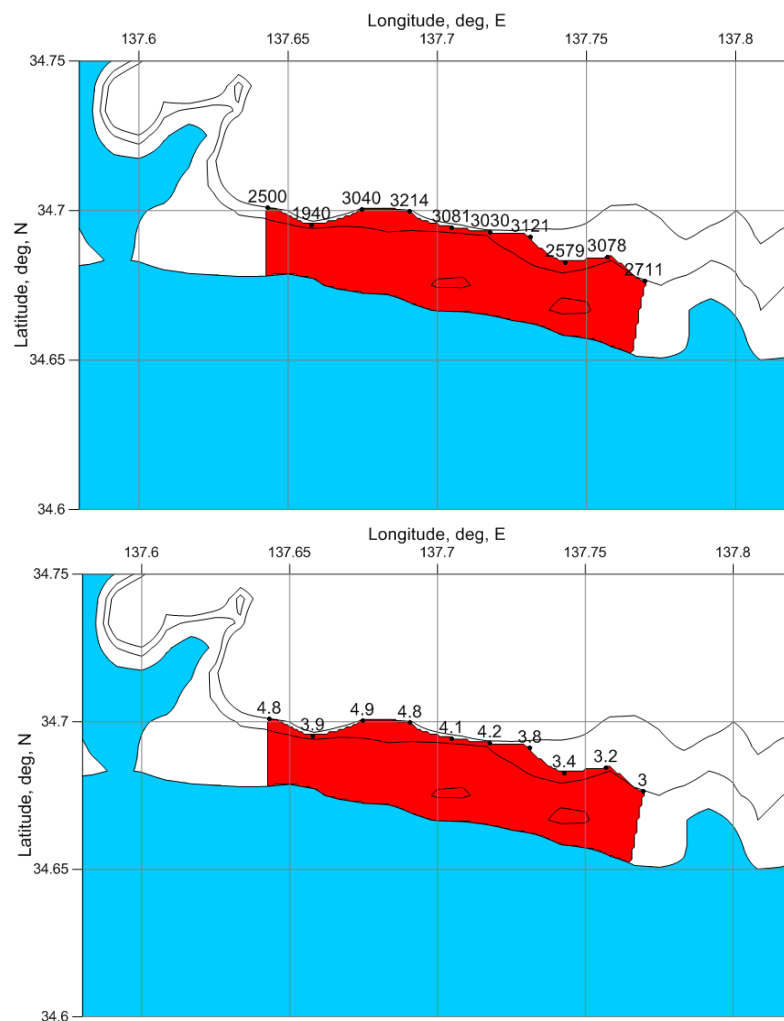


Fig. 2.1.13. The area of coastal flooding and run-up heights for the 1854 Ansei-Tokai tsunami, calculated in the 1D simulation; digits near black dots show (in m) inundation distance (upper figure) and run-up height (lower figure). 3 m and 5 m isolines of land relief are also shown.

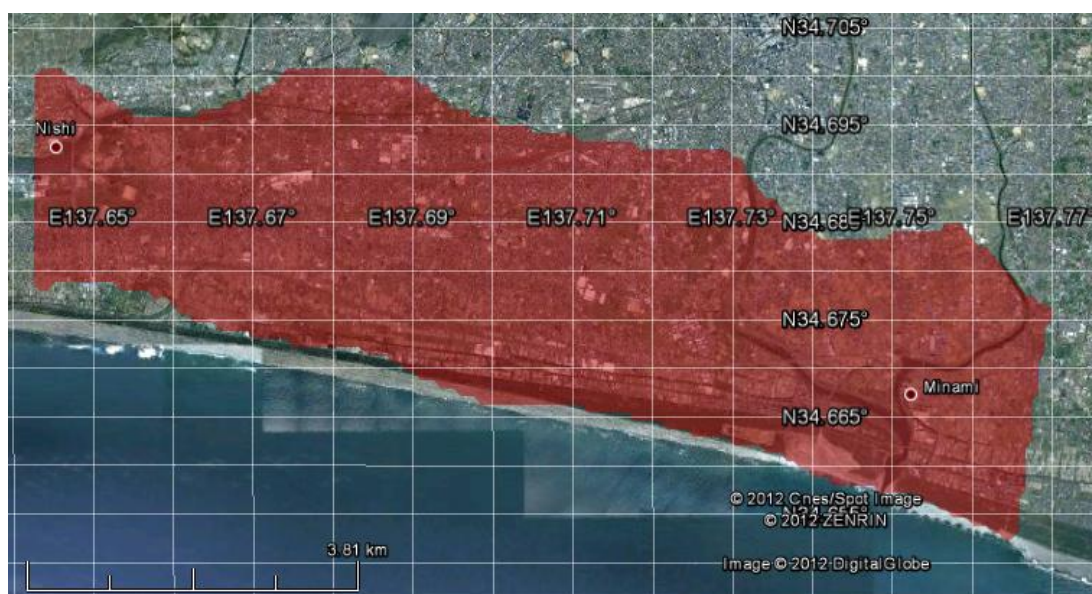


Fig. 2.1.14. Area of inundation near Hamamatsu calculated in 1D run-up modeling overlaid on Google Earth map.

2.1.6. 2D calculation of tsunami run-up and estimation of inundation limits

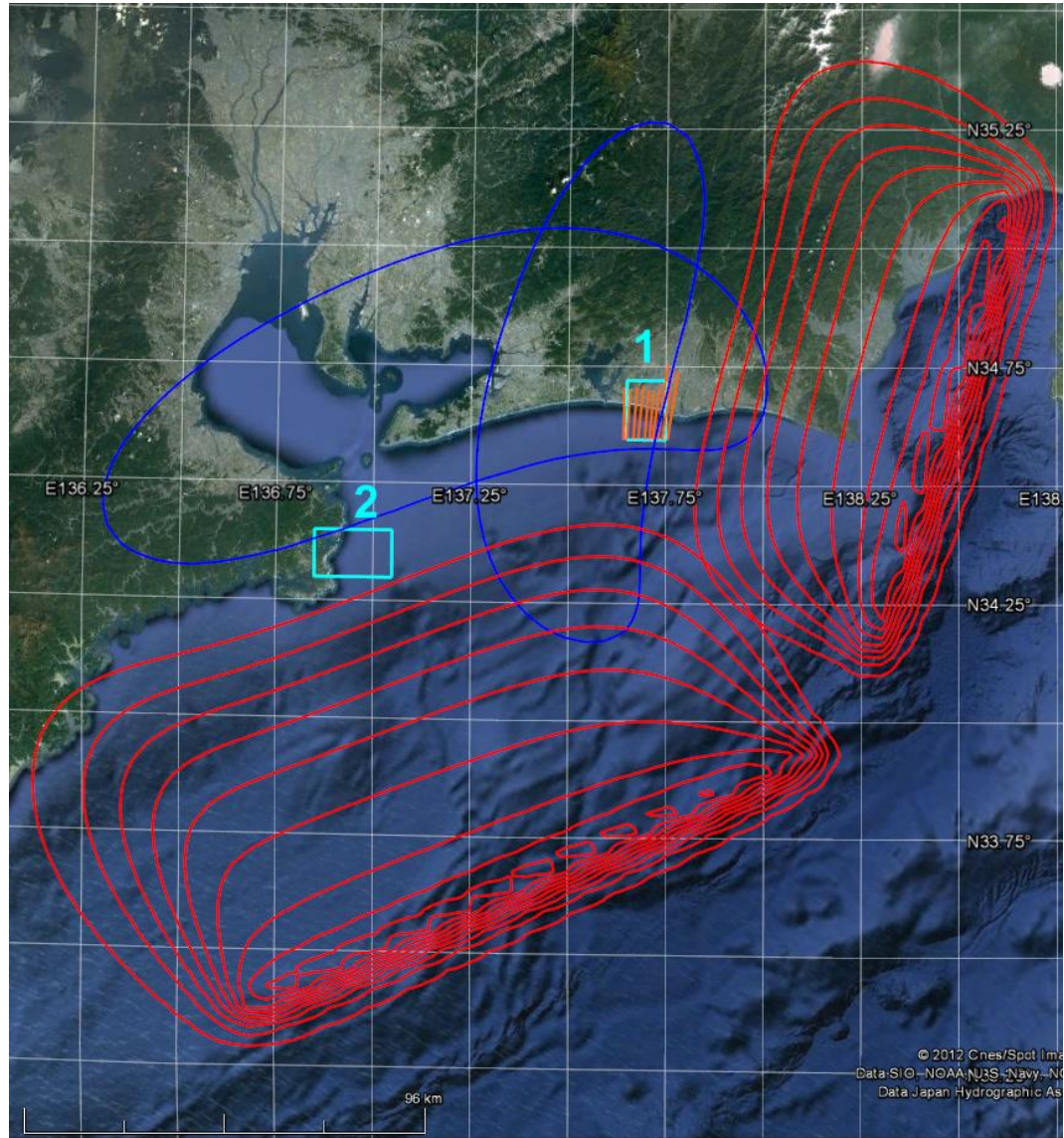


Fig. 2.1.15. Location of two coastal areas (shown as light blue rectangles) selected for 2D modeling of run-up of the “Ansei-Tokai, 1854” tsunami. Position of the model source is shown as isolines of initial vertical bottom displacement (red – uplift, blue – subsidence). Straight orange lines show vertical cross-sections used for 1D run-up modeling.

Coastal area 1



Fig. 2.1.16. Location of coastal area 1 (shown as light blue rectangle) selected for 2D modeling of run-up of “Ansei-Tokai, 1854” tsunami. Color lines show relief isolines of the DEM/DBM GEBCO-30sec: white line – isobath 100m, black – position of the shoreline for undisturbed sea water (0 m), red – isoline 5 m, orange – 10 m, yellow – 20 m, green – 30 m. Straight orange lines show vertical cross-sections used for 1D run-up modeling.

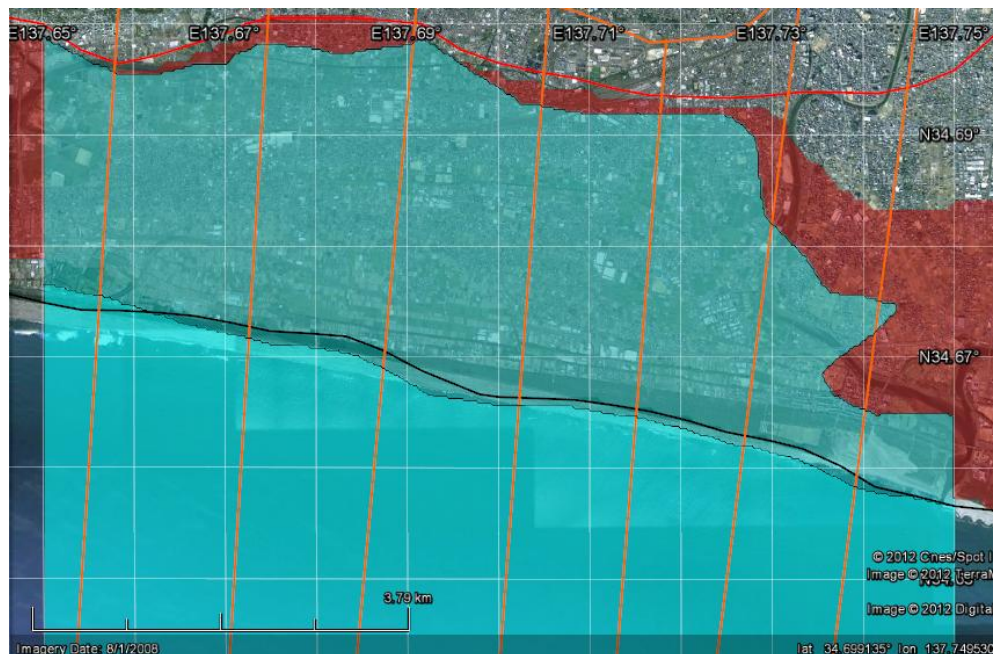


Fig. 2.1.17. Inundation zones from “Ansei-Tokai, 1854” tsunami calculated for the coastal area 1 by 2D modeling (blue shading) and 1D modeling (red shading) using DEM/DBM GEBCO-30sec. Color lines show relief isolines: black – position of the shoreline for undisturbed sea water (0 m), red – isoline 5 m, orange – 10 m, yellow – 20 m, green – 30 m. Straight orange lines show vertical cross-sections used for 1D run-up modeling. Incoming wave is introduced to the coastal area during the 2D run-up modeling through the southern and eastern boundaries.

Coastal area 2

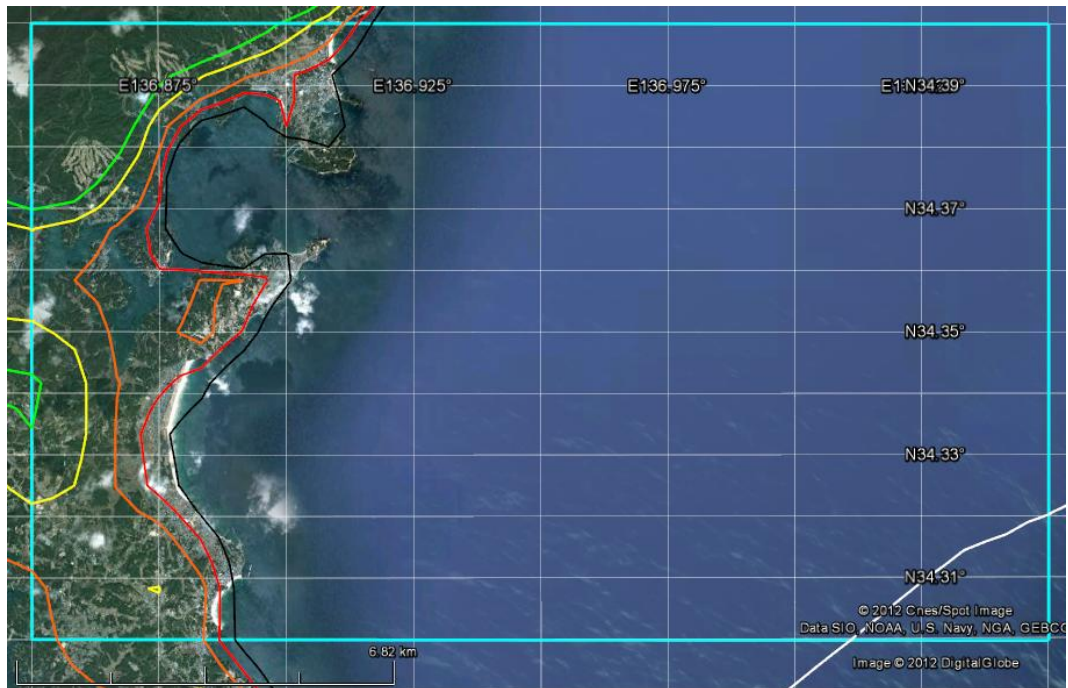


Fig. 2.1.18. Coastal area 2 (shown as light blue rectangle) selected for 2D modeling of run-up of “Ansei-Tokai, 1854” tsunami. Color lines show relief isolines of the DEM/DBM GEBCO-30sec: white line – isobath 100 m, black – position of the shoreline for undisturbed sea water (0 m), red – isoline 5 m, orange – 10 m, yellow – 20 m, green – 30 m.

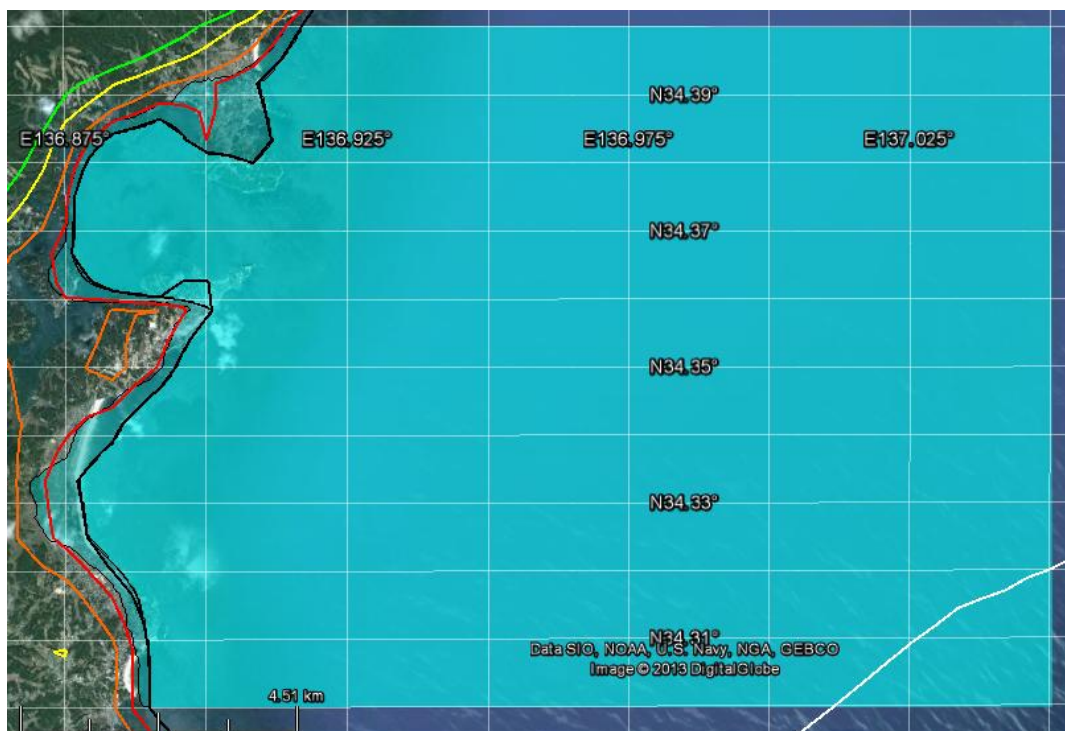


Fig. 2.1.19. Inundation zone (blue shading) from “Ansei-Tokai, 1854” tsunami calculated for the coastal area 2 by 2D modeling using DEM/DBM GEBCO-30sec. Color lines show relief isolines: white line – isobath 100 m, black – position of the shoreline for undisturbed sea water (0 m), red – isoline 5 m, orange – 10 m, yellow – 20 m, green – 30 m. Incoming wave is introduced to the coastal area through the southern and eastern boundaries.

2.2.1923 Kanto tsunami

2.2.1. Basic information on earthquake and tsunami

The **Great Kantō earthquake** struck the vast area of Kanto plain in the central part of Honshu Island at 11:58:44 JST (2:58:44 UTC) on Saturday, September 1, 1923. This was the most powerful earthquake ever recorded in the region and the deadliest earthquake in all Japanese history. It devastated the capital city of Tokyo, the major Japanese port city of Yokohama, nearby prefectures Chiba, Tokyo, Kanagawa and Shizuoka, and caused widespread damage in surrounding prefectures Ibaraki, Saitama and Yamanashi. Duration of strong shocks was reported to be between 4 and 10 minutes. According witness reports, people could not stand on feet, trees were uprooted. Destruction of private houses, many of them had cooking fire inside, initiated numerous fires that soon merged into a giant fire storm strengthened by wind that killed thousands of people. K.Iida (Iida, 1984) lists the following data for damage produced by the earthquake and follow-up tsunami: **99,331** deaths, **43,476** missed, **128,266** houses completely destroyed, **447,128** burned houses, **868** houses swept away.

Earthquakes occurred in the early days of instrumental seismology (official JMA catalog starts on January 14, 1923), however, it was well recorded by all seismic stations available in Japan at that time. The nearest stations recorded 1700 aftershocks during the first three days after the main shock (Soloviev, Go, 1974). Due to the absence of long-period instruments at that time, magnitude of the main shock could be measured only in P and S waves and assigned to be 7.9. Other magnitudes, obtained recently by using different methodologies are $M_s = 7.9-8.2$, $M_w = 7.5-8.1$, $M_t = 8.0$ and vary depending on the method and data used.

Also, there is no instrumental data allowing to specify source mechanism of this event. It should be assigned based on consideration of seismotectonic features of the area, and some secondary data like distribution of observed seismic intensities (Fig. 2.2.1) and measured co-seismic displacement of coastal areas around the source (Fig. 2.2.2).

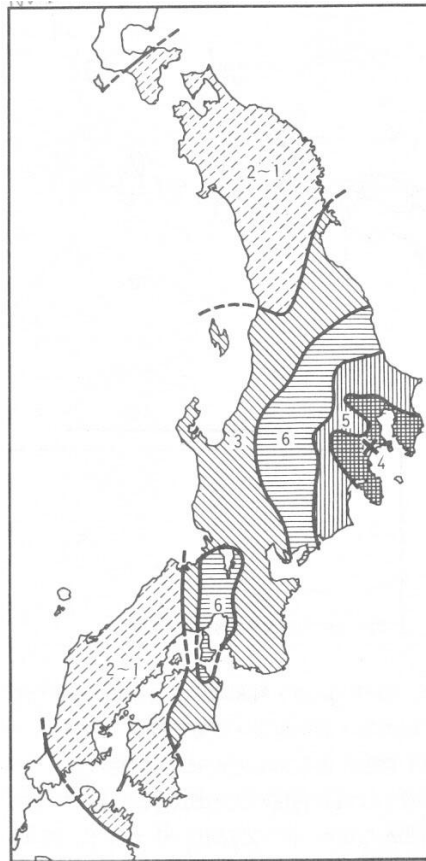


Fig. 2.2.1. Map of observed seismic intensity measured on 7-grade JMA scale (Watanabe, 1985).

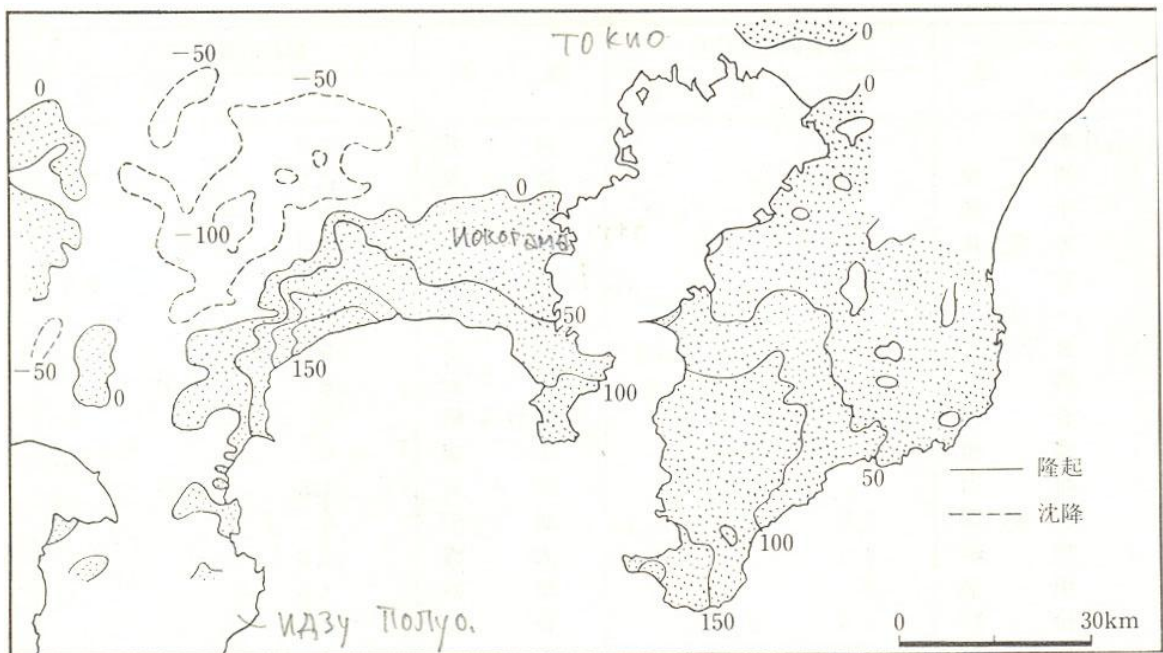


Fig. 2.2.2. Map of measured vertical co-seismic displacement (Watanabe, 1985).

The main seismotectonic feature of the area is the presence of the Sagami Trough, a deep-water trench stretching in south-east direction from the Sagami Bay into the Pacific Ocean. The Sagami Trough marks the subduction boundary separating the Japan Micro-Plate plate (that is the southern end of the Okhotsk Plate) from the subducting Philippine plate.

In the Sagami Bay area, orientation of this trough is ca. 120°N. (Soloviev, Go, 1974) give source area of this tsunami as ellipse with dimension 140x80 km covering entirely the Sagami Bay and the large part of the Boso Peninsula. Watanabe (1985) doesn't show the position of the tsunami source at all.

NGDC/NOAA Tsunami Database (2012) contains 84 wave heights for this event, distribution of 66 of them is shown in Fig. 2.2.3. The largest run-up heights (10-12 m) were observed at the Oshima Island, at several points on the western coast of Sagami Bay and near Ainohama, located at the southernmost tip of the Boso Peninsula.

On the northern part of Sagami Bay and to the south from the tsunami source, as far as Shimoda, the mean rise of water was 3 m, and the maximal rise was 6-9 m; inside the Tokyo Bay, the rise was 1-1.5 m. At most places, the first wave was maximal, and the second and subsequent waves were weaker (Soloviev, Go, 1974).

At the southern part of the Boso Peninsula, according to a municipal worker, a wave appeared on the horizon from the south, about 4 km away, almost immediately after the shock. Especially large damage was observed at Ainohama city. Wave arrived at Ainohama in about 5-6 minutes. In this time, the eyewitness had time to run home (the home was 300 m from the city hall), help evacuate the child and mother and return to work. The wave arrived about 10 minutes after the shock. Having flooded Ainohama and being reflected from the shore, the waves spread in different directions: some towards Sakataru, and some towards Mera, where they caused destruction. The homes washed away at Ainohama and vicinity were carried back to the coast of Heisa'ura Gulf, floated to the east. This debris was found on the Chik'ura (Soloviev, Go, 1974).

The maximal rise of water was 12 m at Atami, on the western coast of Sagami Bay, in a zone of depression. At Atami, according to the chief physician at one of the hospitals, the water began to retreat about 5-6 minutes after the earthquake. The magnitude of the ebb was about twice the magnitude of the maximal usual ebb. However, soon afterward, a tidal wave approached and washed away the homes on shore. A second, stronger wave appeared in about 5-6 minutes. At the top of the bay, which has a V-shape, the height of rise of water was 12 m, halfway from the entrance to the top it was 4.5 m, and at the entrance it was only 1.5 m. The tsunami approached Atami from the northeast, and homes were carried off in the same direction; they were later washed ashore at Yoshihama and Fuku'ura (Soloviev, Go, 1974).

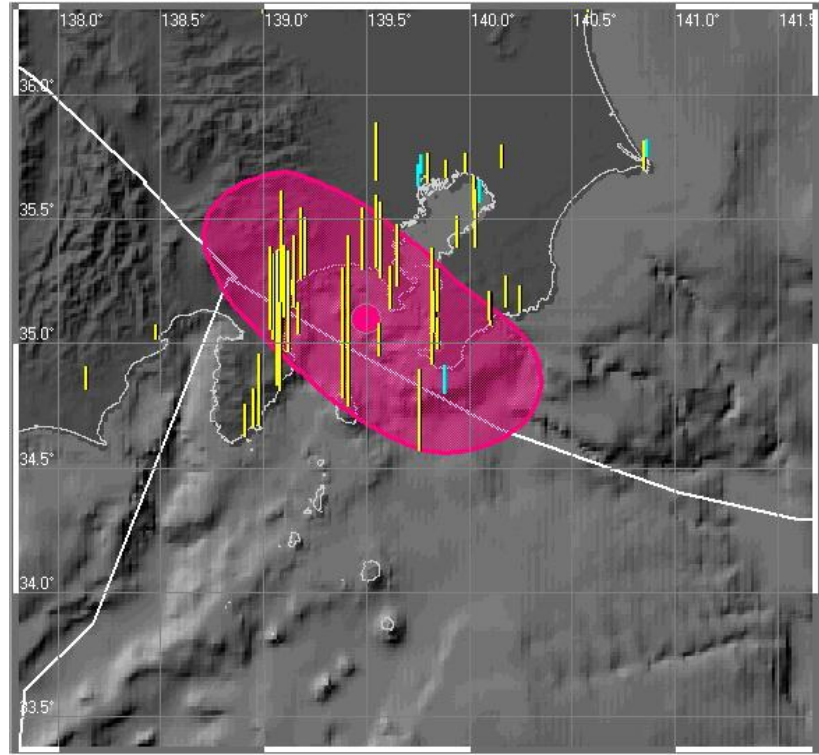


Fig. 2.2.3. Distribution of observed tsunami wave heights as reported by NGDC/NOAA database (vertical yellow lines). Visualization is made in the PDM/TSU graphic shell. Shaded ellipse shows the position of the adopted tsunami source. White lines mark the position of the main plate boundaries.

2.2.2. Adopted source model and calculation of initial bottom displacement

Based on consideration of all the above data, the following source was adopted as a model for the 1923 Kanto earthquake:

Coordinates of the center of the lower edge of the fault: $Lat = 35.5^\circ N$, $Lon = 139.9^\circ E$, magnitude: $M_w = 7.9$, depth of the upper edge of the fault: $h_0 = 10 \text{ km}$, fault size: $L = 150 \text{ km}$, $W = 70 \text{ km}$, displacement: $D_0 = 5.0 \text{ m}$, dip-angle: $\delta = 20^\circ$, slip-angle: $\lambda = 90^\circ$, strike-angle: $\theta = 120^\circ$.

Calculated static displacement for this model source is shown in Fig. 2.2.4.

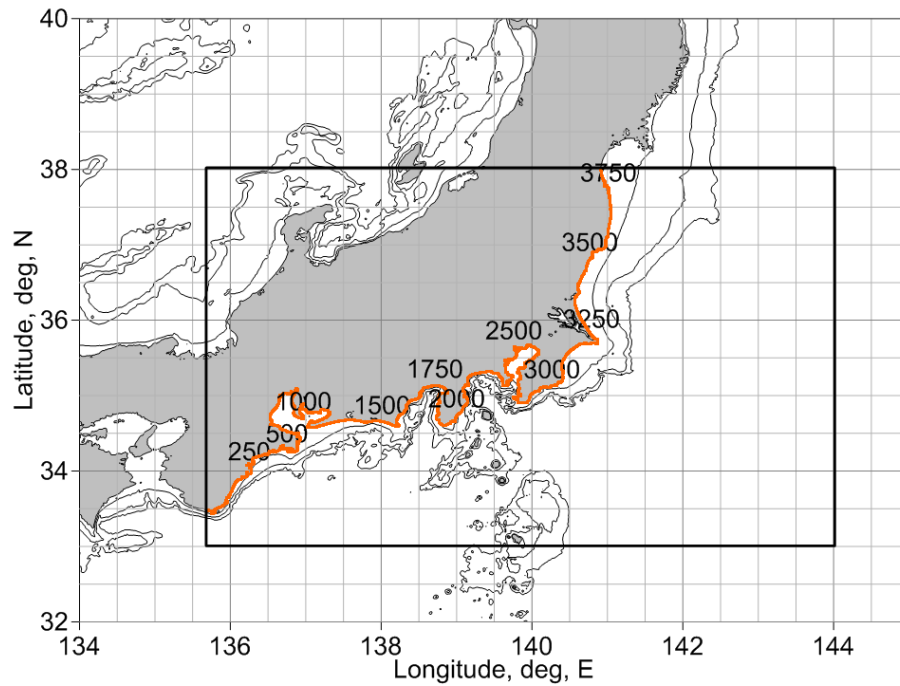


Fig. 2.2.5. The computational domain (plotted as solid black rectangle) with 100m, 500m and 1000m depth isobaths adopted for the 1923 Kanto tsunami modeling. Spatial distribution of 3826 coastal virtual gauges is shown as orange numbered dots.

2.2.4. Analysis of computed wave height distribution

Numerical modeling of tsunami propagation was made for 4 hours of physical time using MGC package (Shokin et al., 2008) for tsunami modeling that is based on the non-linear shallow water system written in spherical coordinates.

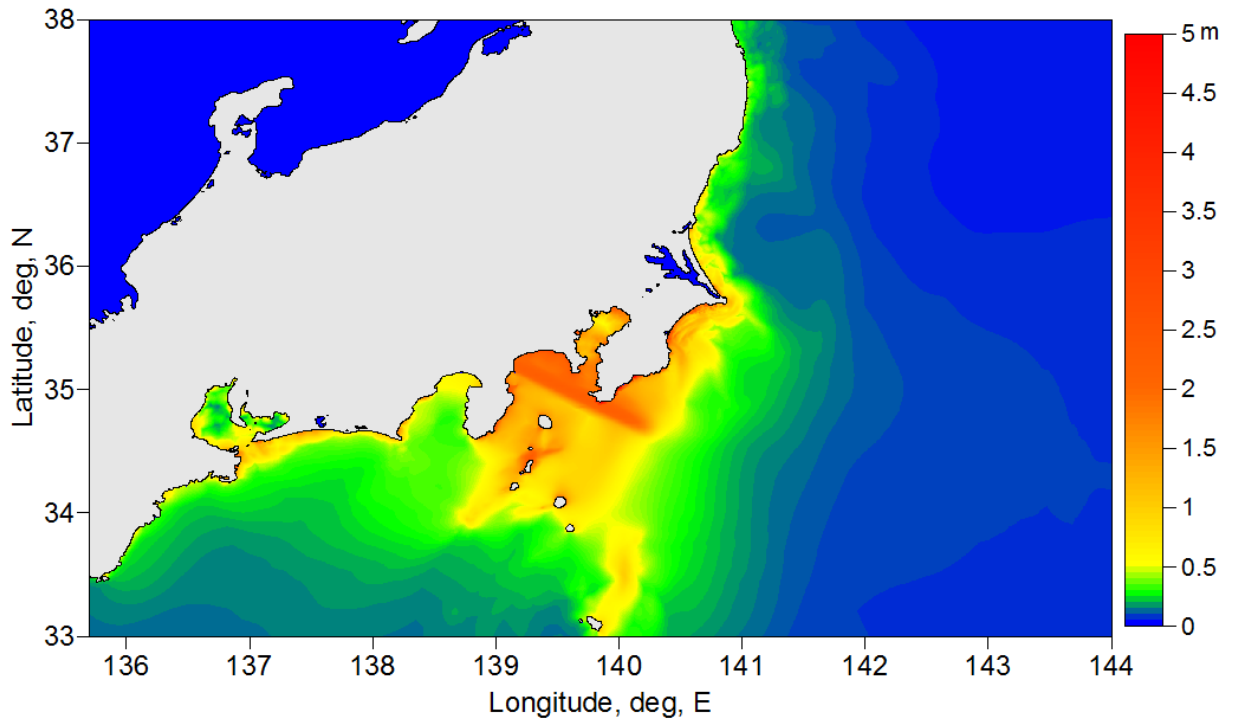


Fig. 2.2.6. Energy flux for the modeled 1923 Kanto tsunami.

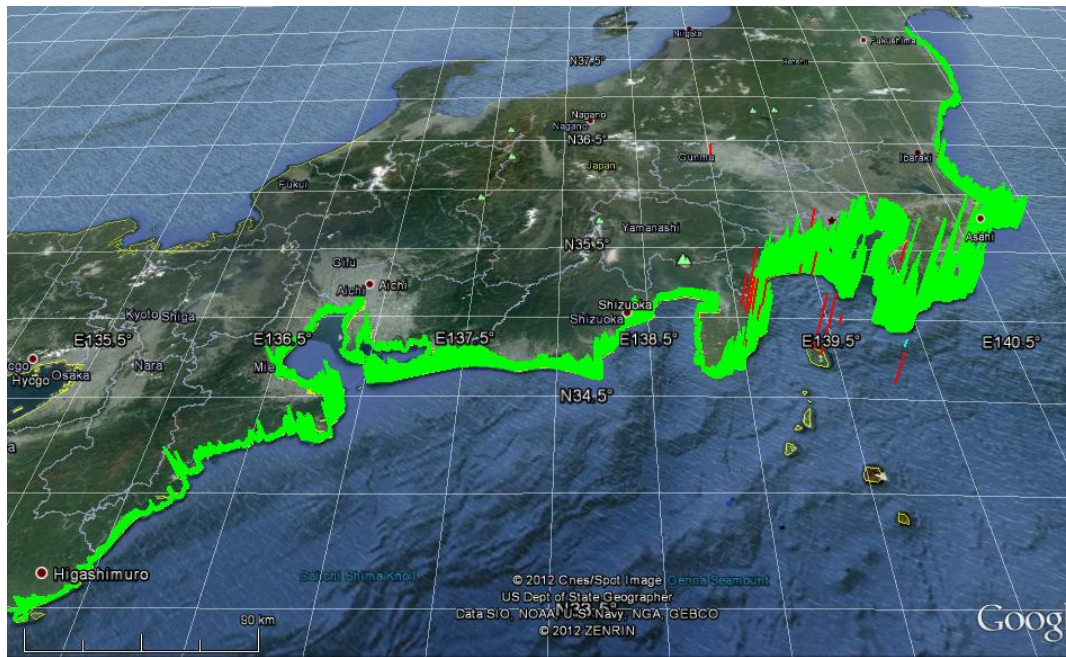


Fig. 2.2.7. Distribution of observed (red) and computed maximum (green) tsunami wave heights calculated at the vertical wall put at the depth of 10 m for 3826 virtual coastal points.

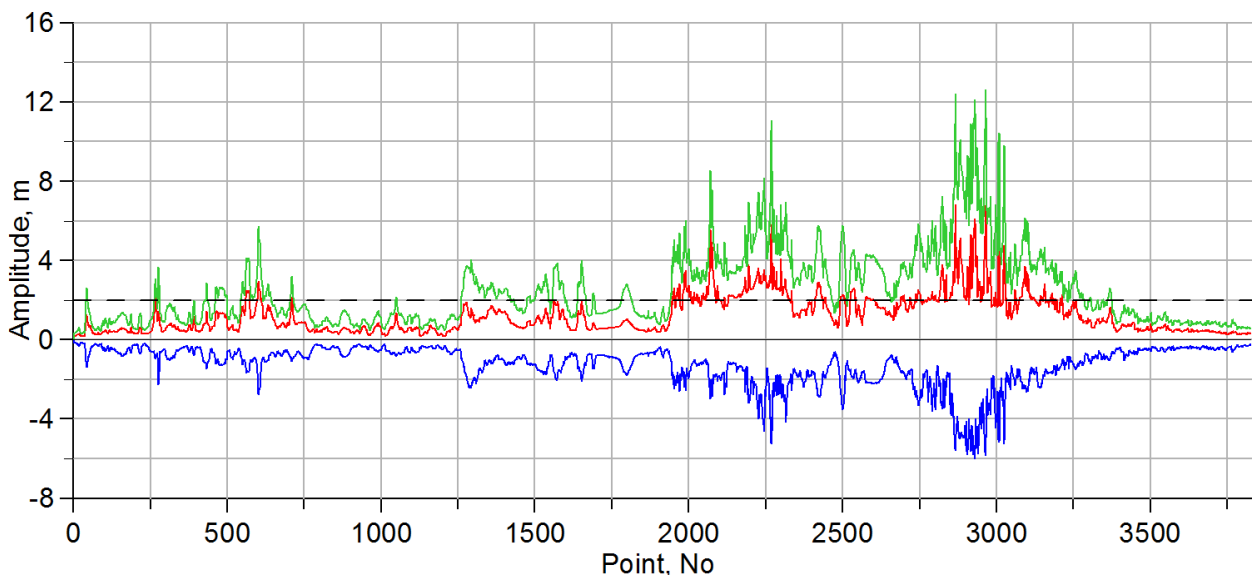


Fig. 2.2.8. Distribution of computed maximum positive (red line) and maximum negative (blue line) amplitudes along with maximum wave heights (green line) over 3826 coastal virtual gauges. Spatial location of these gauges is shown in Fig. 2.2.5.

2.2.5. 1D calculation of tsunami run-up and estimation of inundation limits

For test calculation of tsunami run-up for the "1923 Kanto" case, a part of Kanagawa Prefecture coast was selected. This is the densely populated part of Kanagawa coast with nearby towns Hiratsuka, Chigasaki, Fujisawa, having relatively low and smooth land relief that allows to use one-dimension approximation of tsunami run-up.

Since the degree of roughness of land topography essentially increases for elevations above 10 m, and calculated maximum of wave heights at the vertical wall do not exceeds 4 m, we stopped the selected vertical cross-sections at the elevation 10 m. Starting points for all profiles are at the depth 100m (Fig. 2.2.9).

Location of the selected profiles relatively the area of the initial source displacements is shown in Fig. 2.2.10.



Fig. 2.2.9. Position of 11 numbered (white color text) profiles, selected for one-dimensional calculations of run-up heights for the 1923 Kanto tsunami. Solid black line represents the coastline. Isolines of land relief overlaid on the Google Earth map are for levels of 5 m (red), 10 m (orange), 20 m (yellow), 30 m (green). The white line shows the 100m depth contour.

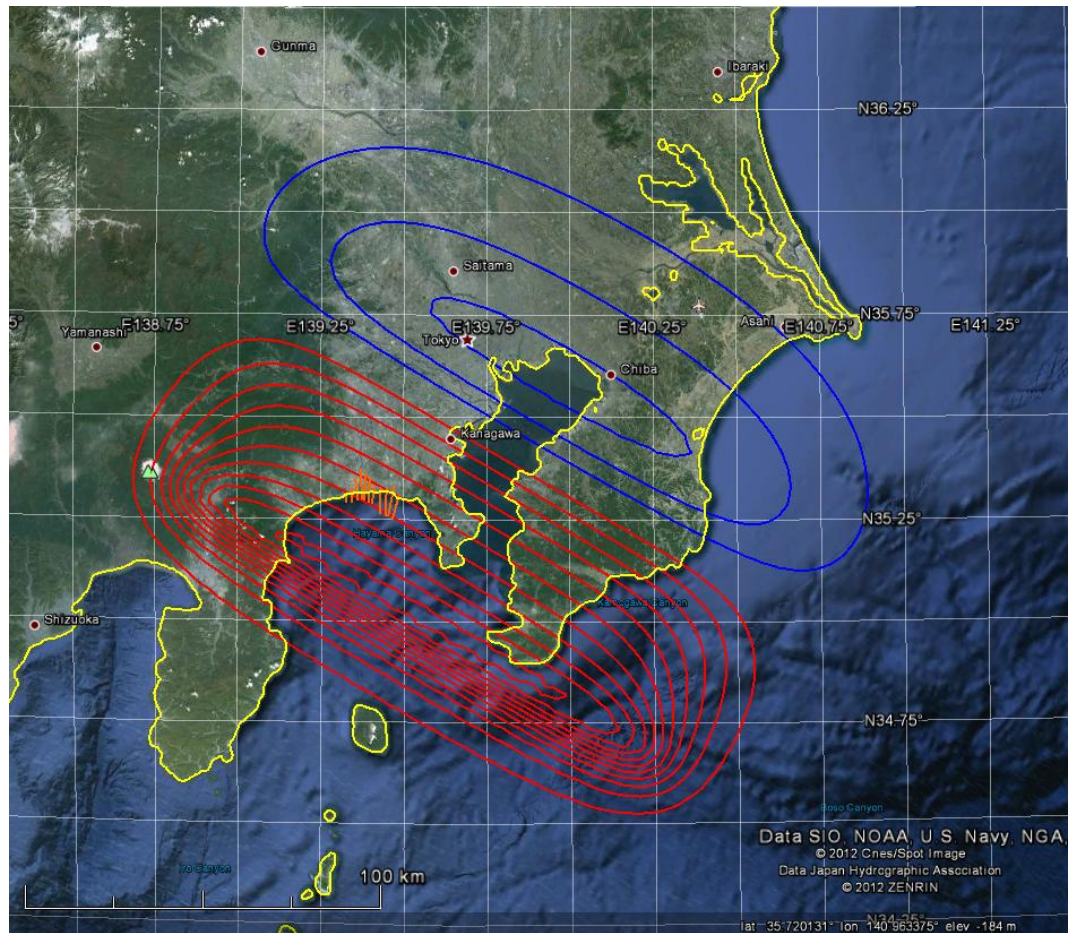


Fig. 2.2.10. Location of coastal profiles (orange lines) selected for 1D run-up modeling relatively source area of the 1923 Kanto tsunami. Calculated co-seismic displacements for the adopted earthquake source model are shown as isolines of vertical displacement (red color shows uplifted areas, blue color - subsided areas).

According to the adopted technology, for each profile the specific boundary conditions are calculated at the sea edge of the profile. These boundary conditions are represented by time histories (calculated waveforms) obtained during the computation of tsunami propagation in two-dimensional statement. At the entering (sea edge) point of each profile, the main part of the computed waveform was used as the input profile for run-up modeling. After starting the 1-D run-up calculation, this boundary condition was replaced with the condition of free wave passage. Table 2.2.1 shows the vertical cross-sections of land and bottom for 10 selected coastal profiles.

Table 2.2.1. Land and bottom relief along the profiles selected for 1D modeling of run-up of the 1923 Kanto tsunami.

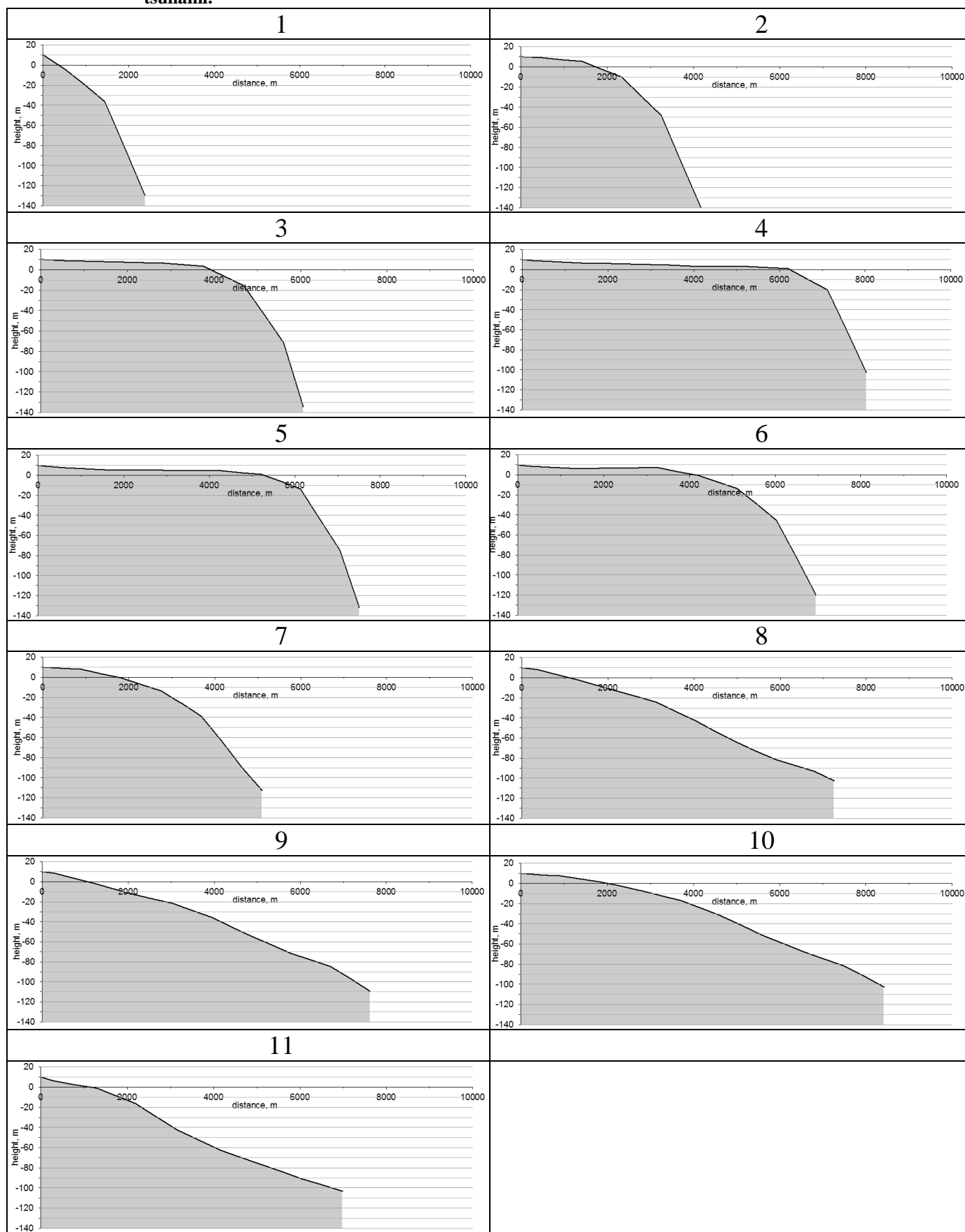


Table 2.2.2. Characteristics of 1923 Kanto tsunami runup, calculated in the 1D simulation along the selected cross-sections.

Index number of cross-section	Calculated runup height (m)	Calculated runup distance (m)	Initial longitude of shoreline point (grad)	Initial latitude of shoreline point (grad)	Calculated longitude of runup point (grad)	Calculated latitude of runup point (grad)
1	3.23	118.4	139.3254	35.3097	139.3252	35.3107
2	4.32	255.1	139.3448	35.3138	139.3446	35.3161
3	3.41	167.0	139.3602	35.3151	139.3600	35.3166
4	4.81	3175.1	139.3744	35.3163	139.3733	35.3451
5	5.92	3914.9	139.3839	35.3160	139.3850	35.3516
6	7.76	3507.3	139.3976	35.3173	139.3998	35.3491
7	7.36	781.9	139.4112	35.3173	139.4128	35.3243
8	4.66	419.2	139.4314	35.3182	139.4316	35.3220
9	4.58	418.8	139.4492	35.3180	139.4494	35.3218
10	5.05	724.7	139.4682	35.3151	139.4698	35.3215
11	4.63	677.3	139.4838	35.3005	139.4858	35.3064

Table 2.2.3. A comparison of the characteristics of the 1923 Kanto tsunami, calculated in the 2D simulation as “wet line” on the vertical wall (maximum positive wave amplitude), as run-up height obtained in 1D simulation along the selected profiles and as run-up height calculated by analytical formulas proposed in (Synolakis, 1987) and (Pelinovsky, Mazova, 1992). Red color marks values obtained outside of applicability of analytical formulas.

Index number of cross-section	Maximum runup on the wall, calculated in the 2D numerical simulation (“wet line”) (m)	Runup heights, calculated in the 1D simulation (m)	Runup height, calculated by analytical formula of Synolakis, 1987 (m)	Runup height, calculated by analytical formula of Pelinovsky, Mazova, 1992 (m)	Observed data (m)
1	2.52847	3.234253	9.082251	2.32824	
2	3.23356	4.318679	11.428073	4.160724	
3	2.63232	3.413236	13.520493	3.178573	
4	2.5296	4.81058	14.460104	2.926529	
5	2.5405	5.922715	8.777229	3.358345	
6	2.66206	7.760562	11.455948	3.794464	
7	2.79784	7.363278	14.481542	3.852911	1.8
8	3.03543	4.655133	18.567011	4.23128	
9	3.25051	4.582917	17.238809	4.460486	
10	3.25421	5.05377	18.865928	5.239087	
11	2.87206	4.633629	17.158059	3.682088	5.0
Average	2.84878	5.068068	14.094132	3.746612	5

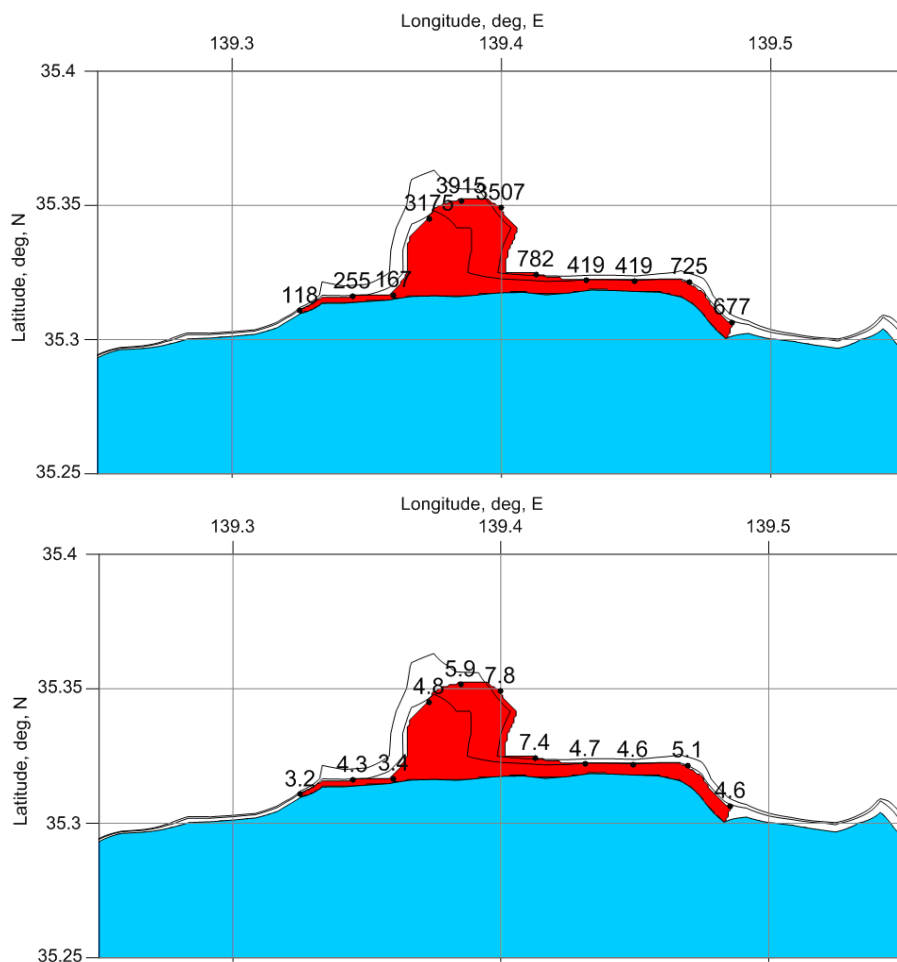


Fig. 2.2.11. The area of coastal flooding and run-up heights for the 1923 Kanto tsunami, calculated in the 1D simulation; digits near black dots show (in m) inundation distance (upper figure) and run-up height (lower figure). 5 and 7 meter isolines of the relief are also shown.



Fig. 2.2.12. Area of inundation between Hiratsuka and Chigasaki calculated in 1D run-up modeling overlaid on the Google Earth map. The calculated (under 1D approach) area of flooding overlaid on Google Earth map.

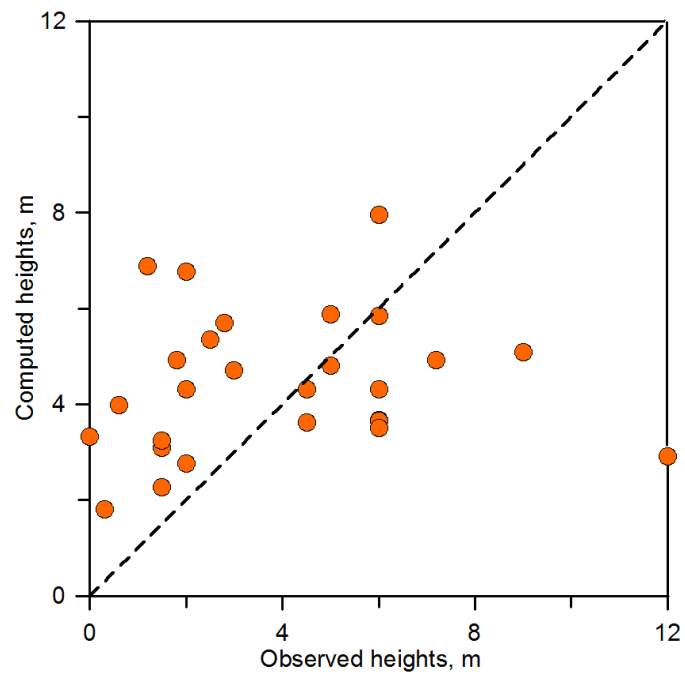


Fig. 2.2.13. Comparison of computed maximum heights versus measured run-up heights for the 1923 Kanto tsunami.

2.2.6. 2D calculation of tsunami run-up and estimation of inundation limits

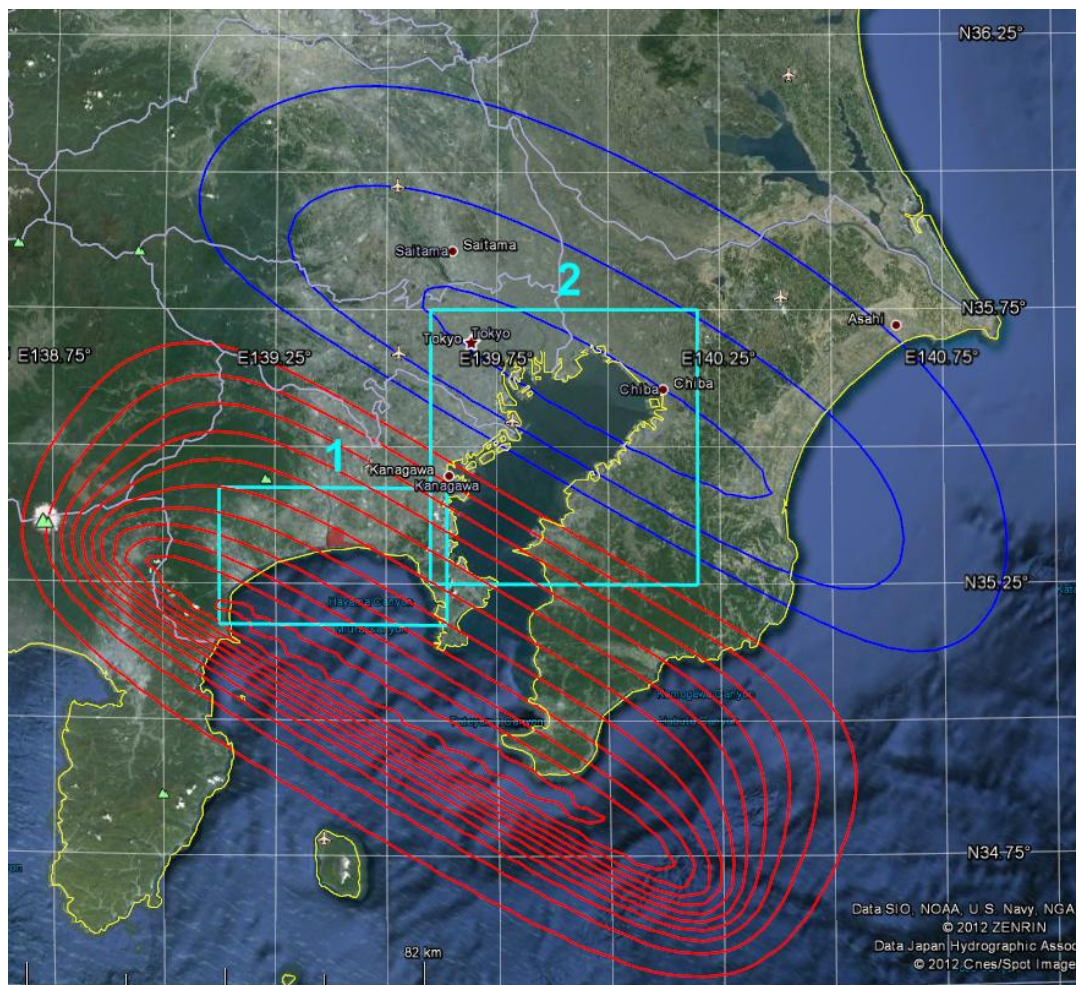


Fig. 2.2.14. Location of two coastal areas (shown as light blue rectangles) selected for 2D modeling of run-up of the “Kanto, 1923” tsunami. Position of the model source is shown as isolines of initial vertical bottom displacement (red – uplift, blue – subsidence).

Coastal area 1

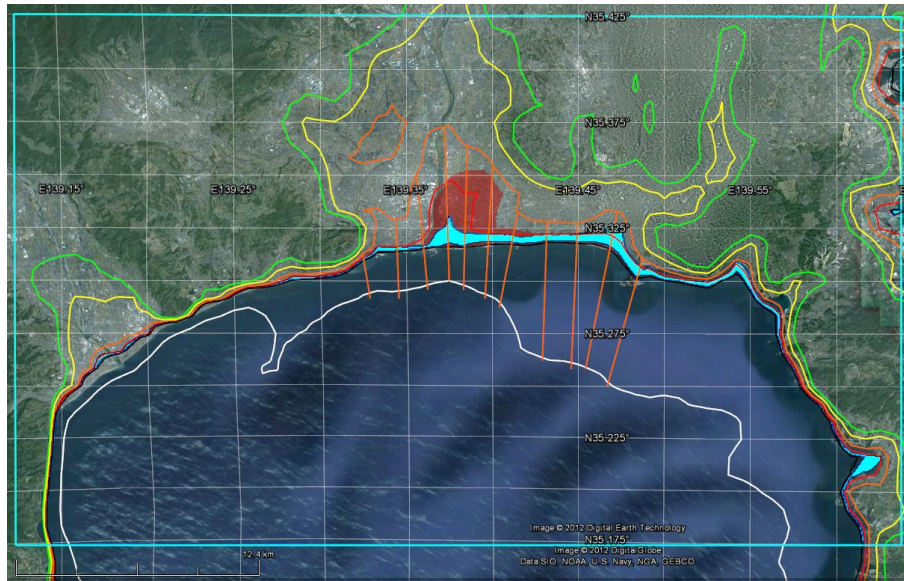


Fig. 2.2.15. Inundation zones from “Kanto, 1923” tsunami calculated for the coastal area 1 by 2D modeling (blue shading) and 1D modeling (red shading) using DEM/DBM GEBCO-30sec. Color lines show relief isolines: white line – isobath 100m, black – position of the shoreline for undisturbed sea water (0 m), red – isoline 5 m, orange – 10 m, yellow – 20 m, green – 30 m. Straight orange lines show vertical cross-sections used for 1D run-up modeling. Incoming wave is introduced to the coastal area during the 2D run-up modeling through the southern boundary.

Coastal area 2

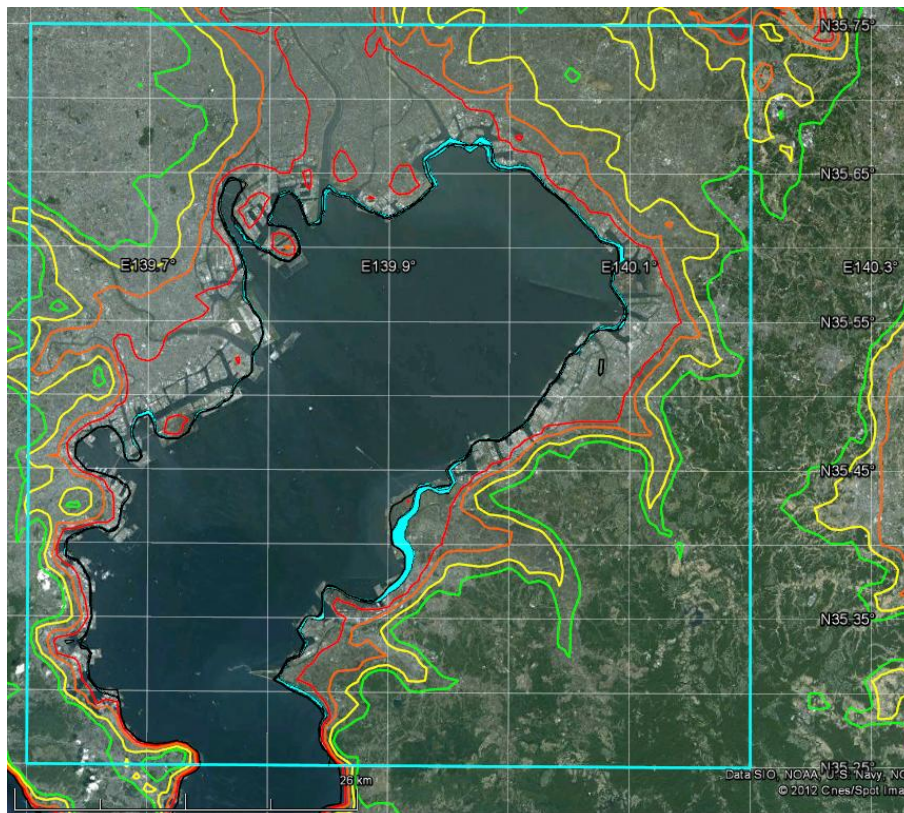


Fig. 2.2.16. Inundation zone (blue shading) from “Kanto, 1923” tsunami calculated for the coastal area 2 by 2D modeling using DEM/DBM GEBCO-30sec. Color lines show relief isolines: black – position of the shoreline for undisturbed sea water (0 m), red – isoline 5 m, orange – 10 m, yellow – 20 m, green – 30 m. Incoming wave is introduced to the coastal area through the southern boundary.

2.3.1944 Tōnankai tsunami

2.3.1. Seismotectonic features of the area. Basic information on earthquake and tsunami

The **Mw8.1 1944 Tōnankai earthquake** occurred in the middle of the day (at 13:35 local time, 04:35 GMT) of December 7, 1944 near the eastern coast of the Kii Peninsula and seriously affected the territory of Wakayama, Nara and Mie prefectures. It was a great subduction earthquake ruptured segments C and D of the Nankai megathrust (Fig. 2.4.1).

The main seismotectonic feature of the area is the presence of the Nankai Trough, a deep-water trough that extends approximately 900 km offshore Honshu in south-west direction from the Shokoku Island to the Sagami Bay where it junks with the Sagami Trough. The Nankai Trough marks the plate boundary separating the subducting Philippine Plate from overriding Eurasian Plate. It the part, it was a source of many large earthquakes in Japan's history. Historically, it is subdivided into three large segments (Nankai, Tōnankai, Tokai) each of them is further subdivided into several smaller segments (Fig. 2.4.1). The 1944 Nankai earthquake is the most recent large-scale earthquake to occur in the segments C and D of the Nankai Trough.

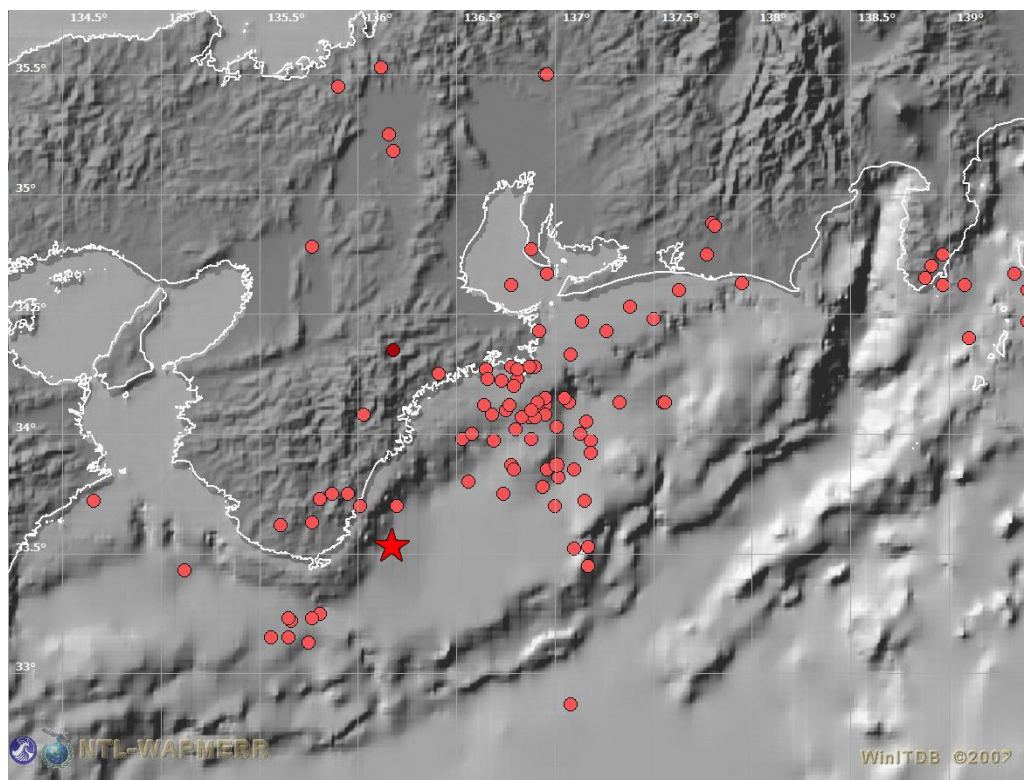


Fig. 2.3.1. Distribution of the first-month aftershocks (solid red dots) for the 1944 Tōnankai earthquake. Aftershock data are from the JMA historical earthquake catalog, visualization is made in the WinITDB graphic shell. Position of the main shock is shown by the red star.

The earthquake occurred during the early instrumental stage of seismological observations when only short-period mechanical instruments were available, so the accuracy of source location and magnitude estimates are low (within half of angular degree and 0.5 unite of the Richter magnitude scale, respectfully). The map of the first-month aftershocks is shown in Fig. 2.3.1. The cloud of aftershocks is clearly grouped near the easternmost edge of the Kii Peninsula where maximal seismic intensity was observed. This quake was felt in large area stretching over 1200 km from the central Kyushu to the northern Honshu (Fig. 2.3.2).

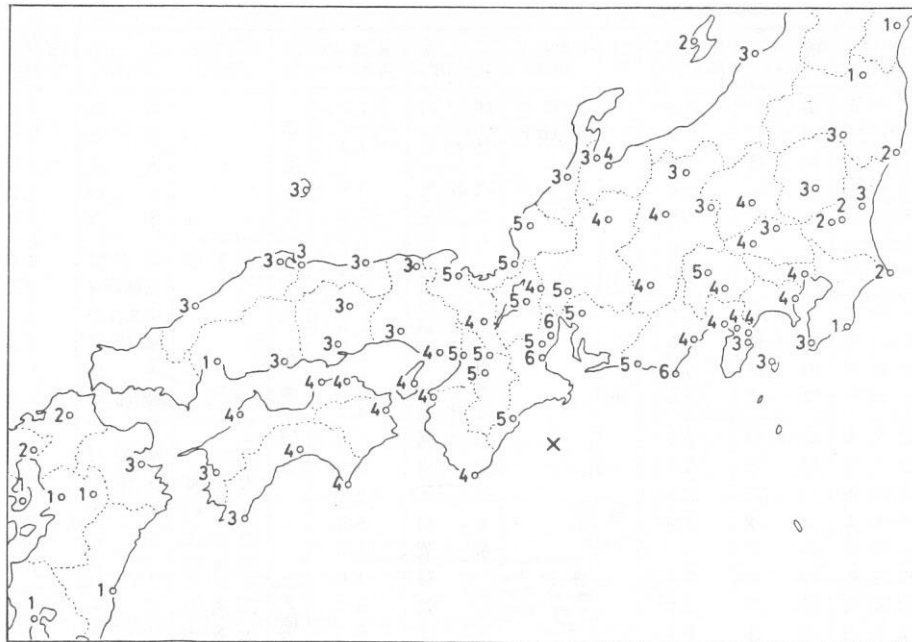


Fig. 2.3.2. Distribution of the reported seismic intensities (on the 7-grade JMA scale) and approximate area of source location for the 1944 Tōnankai earthquake (Watanabe, 1985).

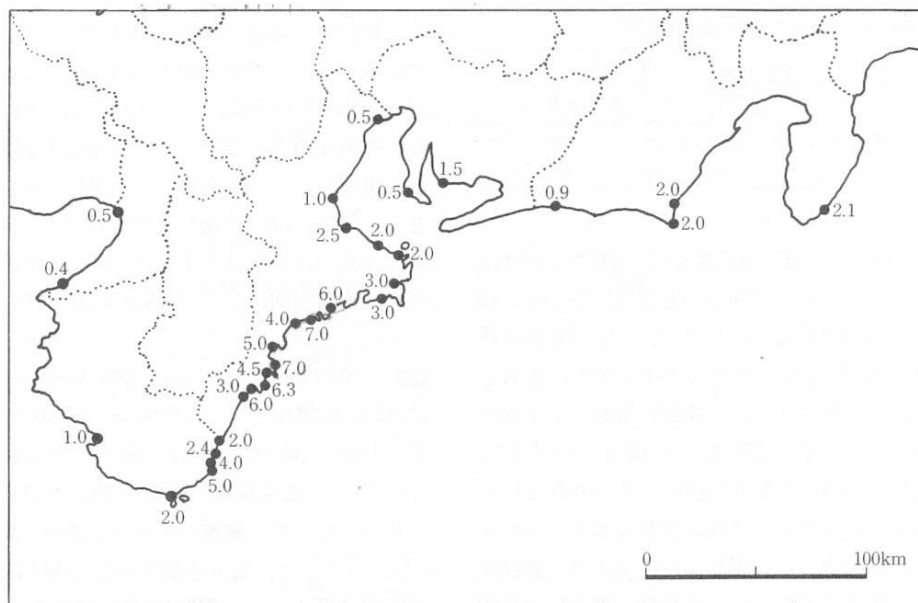


Fig. 2.3.3. Distribution of the measured wave heights for the 1944 Tōnankai tsunami (Watanabe, 1985).

The NGDC/NOAA Tsunami database contains 152 run-ups for this event, with 142 of them reported from Japan. In Hawaii (Honolulu) waves reached only 10 cm in amplitude. The largest far-field amplitudes were recorded by mareograph in Attu, Aleutians (28 cm). The largest near-field run-ups (10m) were reported from two locations – Owase and Attashika in Mie Prefecture (both these reports are absent in the run-up data provided by Watanabe (1985), since they were discovered in more recent time).

There was severe damage from the earthquake on the eastern side of the Kii Peninsula particularly at Shingu and Temma. A total of 26,146 houses were destroyed by the shaking, and a further 3,059 houses were destroyed by the tsunami. Nearly 47,000 houses were seriously damaged by the combined effects of the earthquake and tsunami. Together the earthquake and tsunami caused 1,223 casualties and 2,135 were seriously injured (Soloviev, Go, 1974).

2.3.2. Adopted source model and calculation of initial bottom displacement

Based on consideration of the above data, the following source was adopted as a model for the 1944 Tōnankai earthquake: Coordinates of the center of the lower edge of the fault: $Lat = 33.9^{\circ}N$, $Lon = 136.6^{\circ}E$, magnitude: $M_w = 8.1$, depth of the upper edge of the fault: $h_0 = 10\text{ km}$, fault size: $L = 150\text{ km}$, $W = 50\text{ km}$, displacement: $D_0 = 5.0\text{ m}$, dip-angle: $\delta = 20^{\circ}$, slip-angle: $\lambda = 90^{\circ}$, strike-angle: $\theta = 45^{\circ}$.

Calculated bottom displacement for this model source is shown in Fig. 2.3.4.

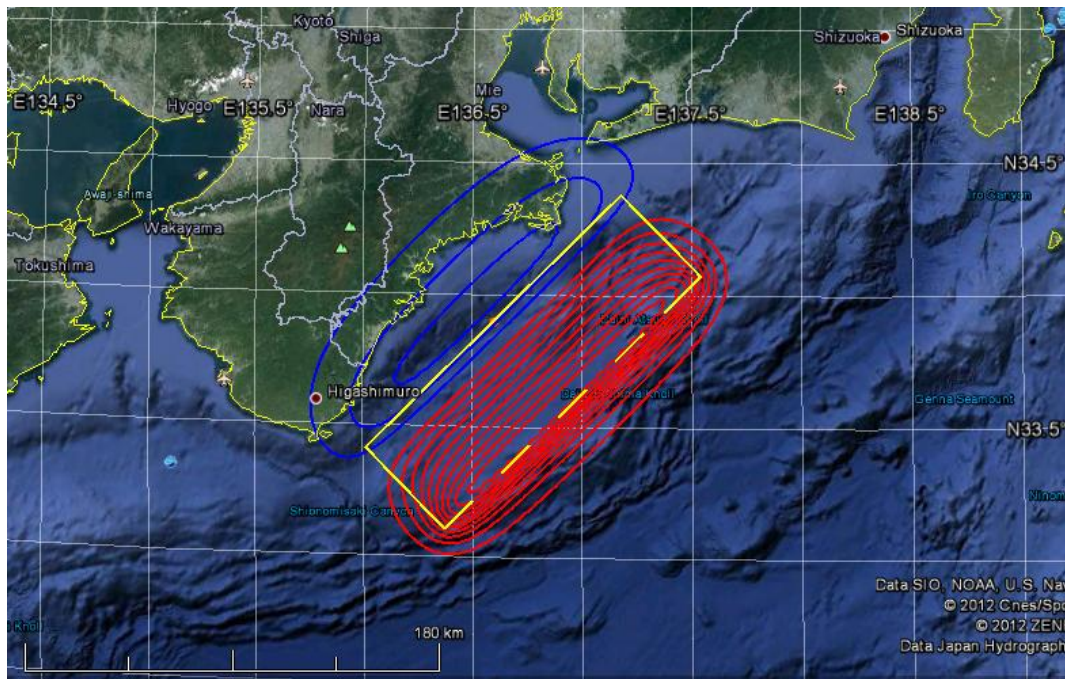


Fig. 2.3.4. Calculated static displacement for the adopted 1944 Tōnankai earthquake source model overlaid on the Google Earth map. Red color shows uplifted areas, blue color – subsided areas.

2.3.3. Calculation domain and virtual coastal points

Modeling of tsunami generation and propagation was carried out in the rectangular computational grid with dimension 2569×1681 and spatial step 15

angular seconds in both directions covering the area within 30°00'N – 37°00'N, 131°18'E – 142°00'E. The minimum water depth h_{\min} in the area was adopted to be equal 10 m. Tsunami heights were calculated at 5592 virtual mareograph points distributed along the coastline (Fig. 2.3.5).

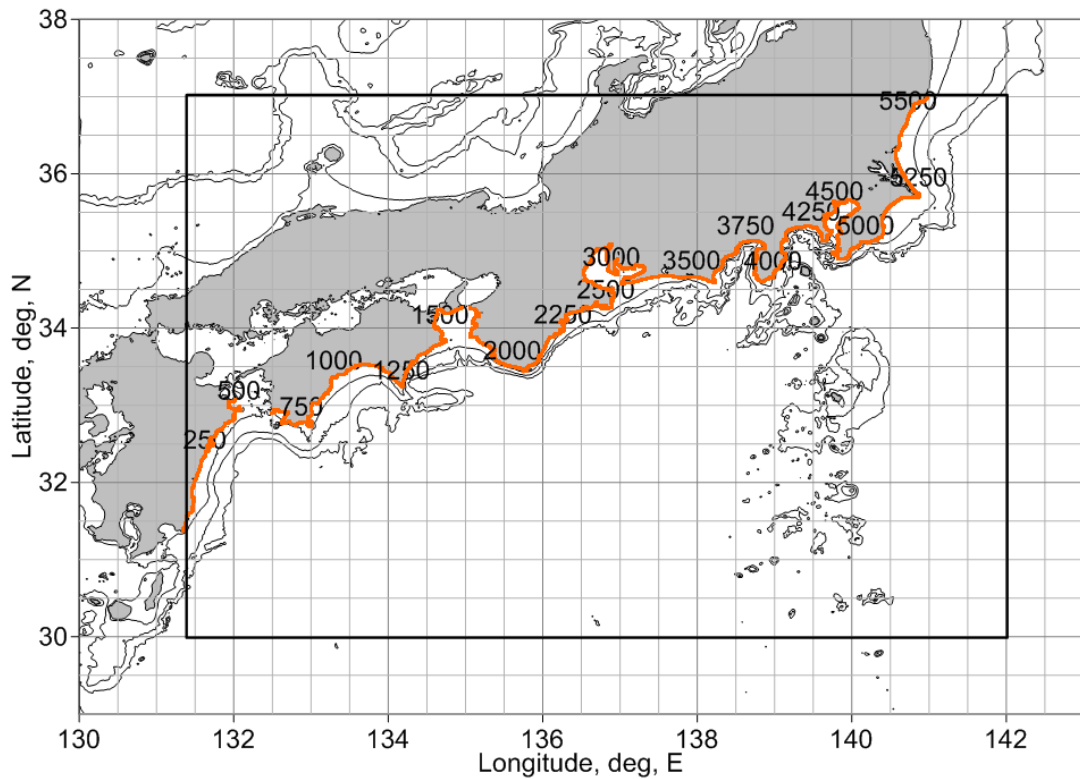


Fig. 2.3.5. The computational domain (plotted as solid black rectangle) with 100m, 500m and 1000m depth isobaths adopted for the 1944 Tōnankai tsunami modeling. Spatial distribution of 5592 coastal virtual gauges is shown as orange numbered dots.

2.3.4. Analysis of computed wave height distribution

Numerical modeling of tsunami propagation was made for 4 hours of physical time using MGC package (Shokin et al., 2008) for tsunami modeling that is based on the non-linear shallow water system written in spherical coordinates. Results of computation are shown in Fig. 2.3.6 – Fig. 2.3.8.

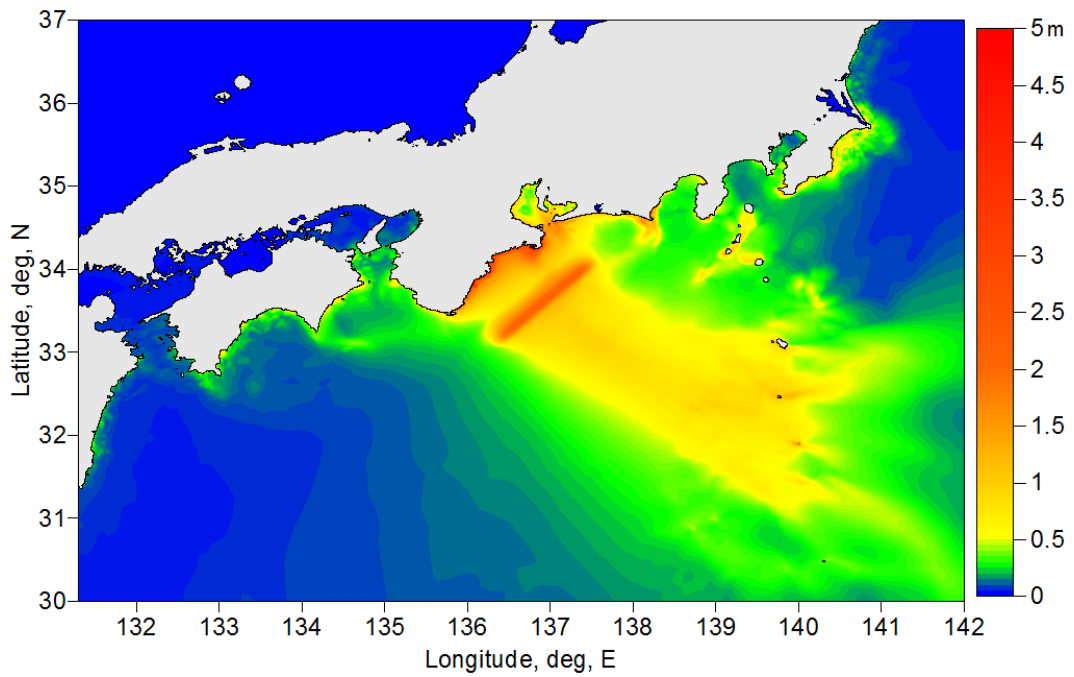


Fig. 2.3.6. Energy flux for the modeled 1944 Tōnankai tsunami.

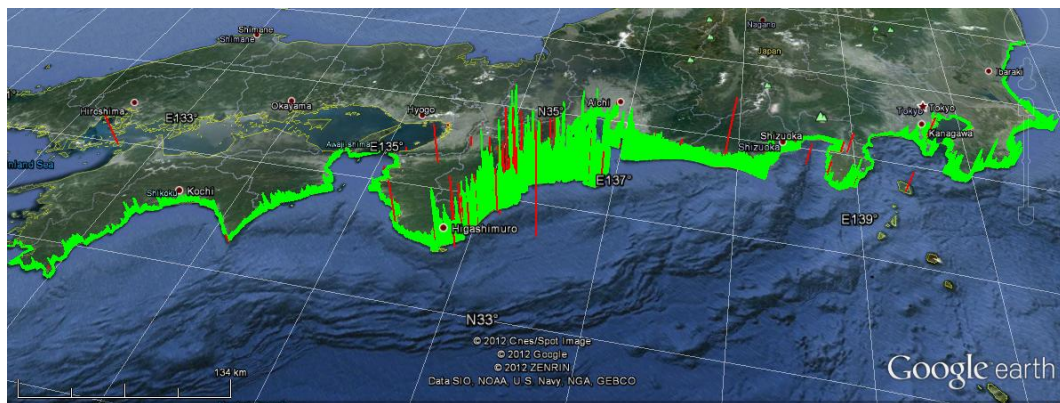


Fig. 2.3.7. Distribution of observed (red) and computed maximum (green) tsunami wave heights calculated at the vertical wall put at the depth of 10 m for 5592 virtual coastal points.

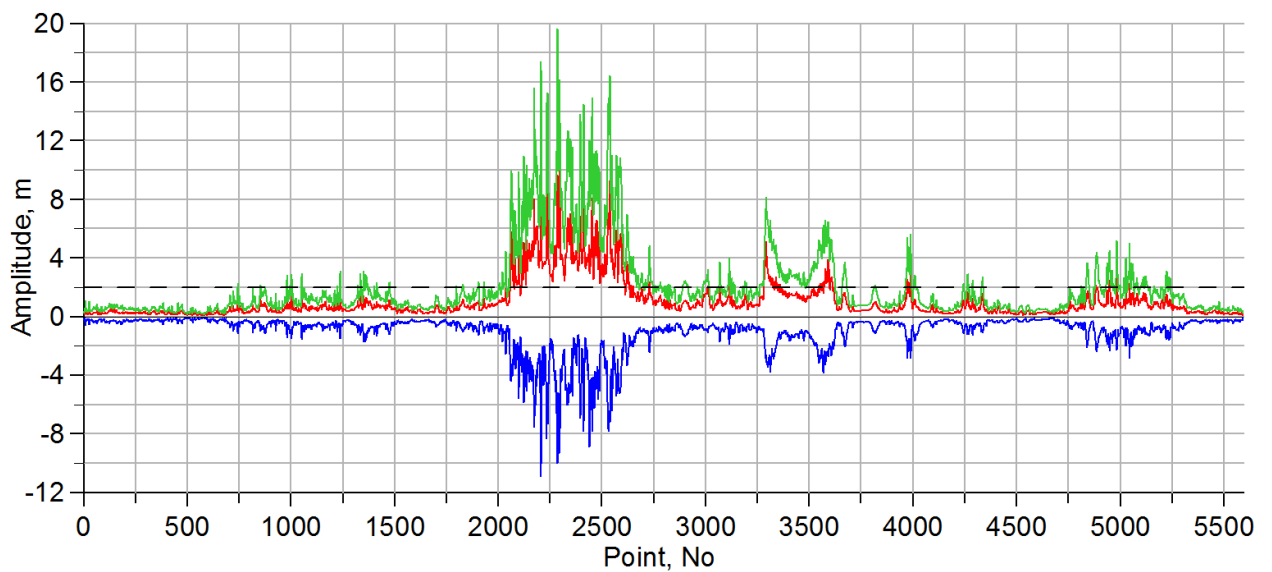


Fig. 2.3.8. Distribution of computed maximum positive (red line) and maximum negative (blue line) amplitudes along with maximum wave heights (green line) over 5592 coastal virtual gauges. Spatial location of these gauges is shown in Fig. 2.3.5.

2.3.5. 1D calculation of tsunami run-up and estimation of inundation limits

For test calculation of run-up heights for the 1944 Tōnankai tsunami, a part of coastal plain near town Shingu, one of the largest cities in the Wakayama Prefecture with population about 33,000 people and part of the coast of Minamimuro district (Pie Prefecture) was selected where 11 profiles for 1D calculation of tsunami run-up were built (Fig. 2.3.9). Position of the coastal profiles selected for 1D run-up modeling relatively to the adopted tsunami source is shown in Fig. 2.3.10.

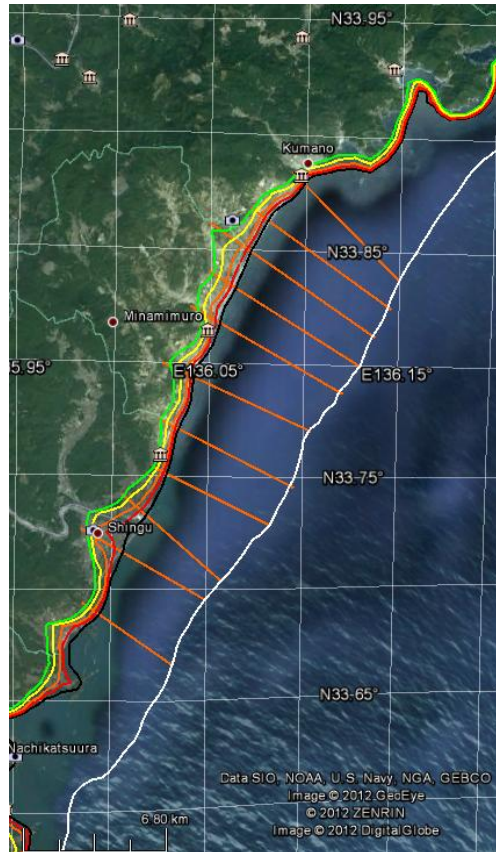


Fig. 2.3.9. Position of 11 profiles, selected for one-dimensional calculations of run-up heights for the 1944 Tōnankai tsunami. Solid black line represents the coastline. Isolines of land relief overlaid on the Google Earth map are for levels of 5 m (red), 10 m (orange), 20 m (yellow), 30 m (green). The white line shows the 100m depth contour.

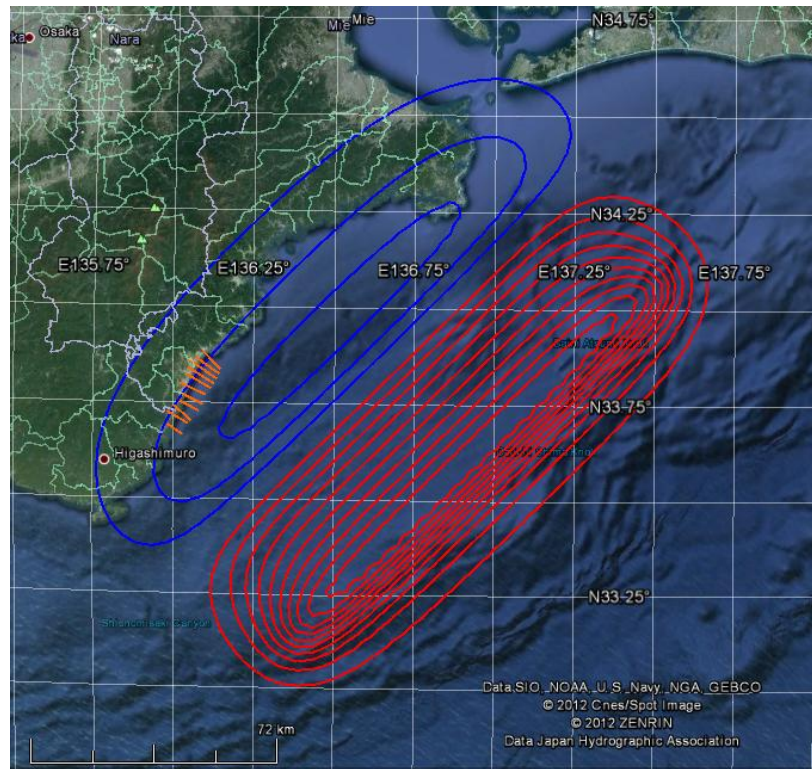


Fig. 2.3.10. Location of coastal profiles (orange lines) selected for 1D run-up modeling relatively source area of the 1944 Tōnankai tsunami. Calculated co-seismic displacements for the adopted earthquake source model are shown as isolines of vertical displacement (red color shows uplifted areas, blue color - subsided areas).

Table 2.3.1. Land and bottom relief along the profiles selected for 1D modeling of run-up of the 1944 Tōnankai tsunami.

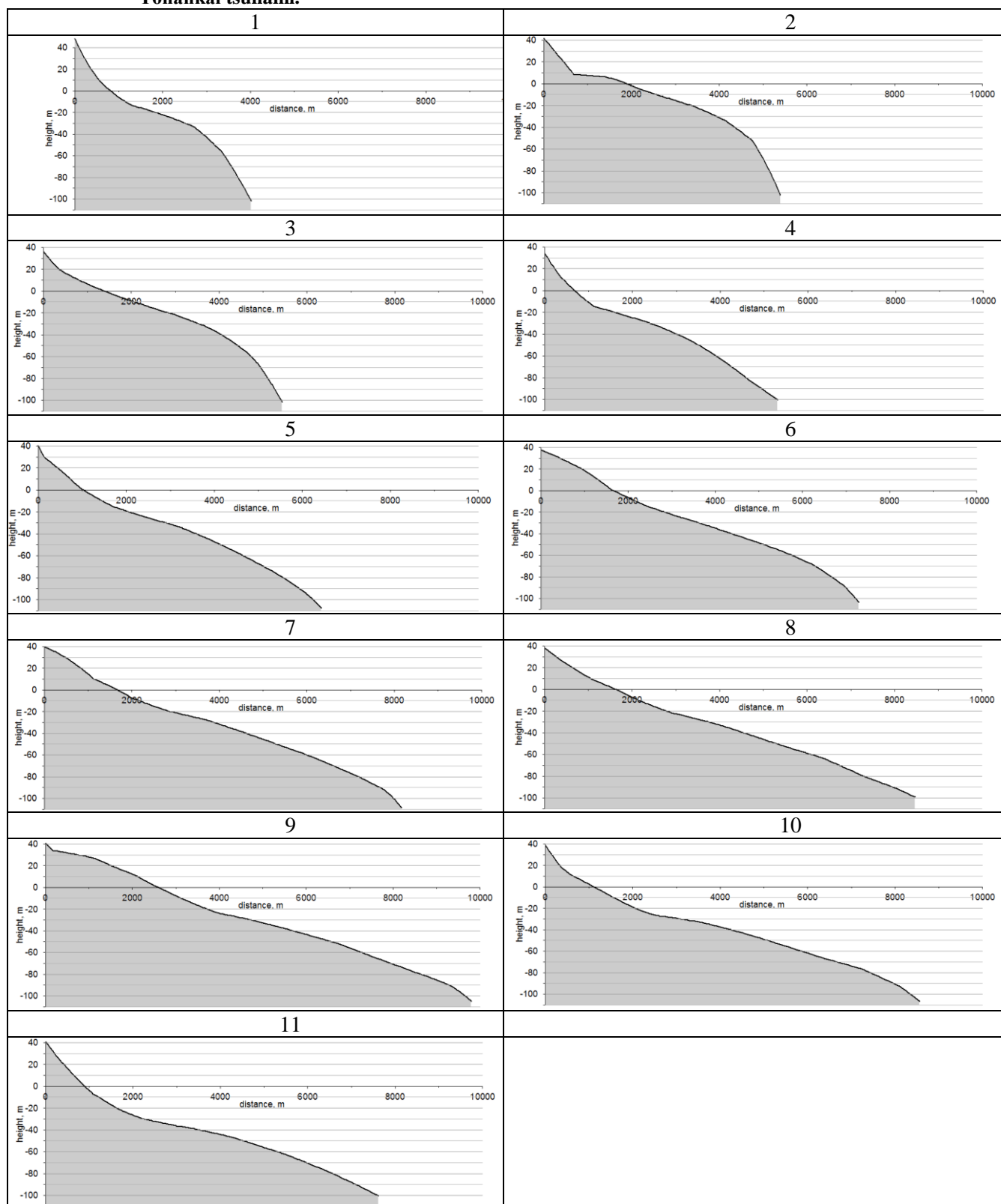


Table 2.3.2. Characteristics of 1944 Tōnankai tsunami runup, calculated in the 1D simulation along the selected cross-sections.

Index number of cross-section	Calculate d runup height (m)	Calculate d runup distance (m)	Initial longitude of shoreline point (grad)	Initial latitude of shoreline point (grad)	Calculate d longitude of runup point (grad)	Calculate d latitude of runup point (grad)
1	4.07	157.7	135.9943	33.6887	135.9930	33.6895
2	4.55	448.0	136.0059	33.7162	136.0019	33.7180
3	4.72	345.0	136.0179	33.7327	136.0152	33.7346
4	4.54	147.7	136.0284	33.7511	136.0271	33.7517
5	4.84	190.9	136.0344	33.7709	136.0327	33.7716
6	5.01	201.9	136.0422	33.7937	136.0403	33.7943
7	5.40	296.1	136.0552	33.8178	136.0525	33.8190
8	5.58	325.0	136.0632	33.8332	136.0603	33.8346
9	5.57	277.5	136.0709	33.8495	136.0685	33.8508
10	5.49	254.5	136.0797	33.8631	136.0775	33.8643
11	5.14	128.7	136.0987	33.8794	136.0977	33.8802

Table 2.3.3. A comparison of characteristics of heights for the 1944 Tōnankai tsunami, calculated in the 2D numerical simulation as “wet line” on the vertical wall, as run-up height obtained in 1D simulation along the selected profiles and calculated by analytical formulas proposed in (Synolakis, 1987) and (Pelinovsky, Mazova, 1992). Red color marks values obtained outside of applicability of analytical formulas.

Index number of cross-section	Maximum positive amplitude on the wall, calculated in the 2D numerical simulation (“wet line”) (m)	Runup heights, calculated in the 1D simulation (m)	Runup height, calculated by analytical formula of Synolakis, 1987 (m)	Runup height, calculated by analytical formula of Pelinovsky, Mazova, 1992 (m)	Observed data (m)
1	3.3094	4.070329	9.899671	3.624181	2.4
2	4.468	4.552243	10.27803	5.942	2
3	4.0884	4.71912	11.15947	5.951107	4.9
4	3.9817	4.54255	11.94665	3.974121	
5	4.2971	4.838745	12.29807	5.809761	
6	5.2028	5.008143	12.94496	6.382586	4
7	5.2601	5.400149	13.32493	6.852413	4
8	4.6596	5.5805	14.77925	6.859579	
9	4.8527	5.574184	14.94974	7.067661	
10	5.8373	5.493716	15.11001	7.715694	
11	5.3472	5.13795	15.39097	6.306484	2; 7
Average	4.664	4.992512	12.916523	6.044144	2.83

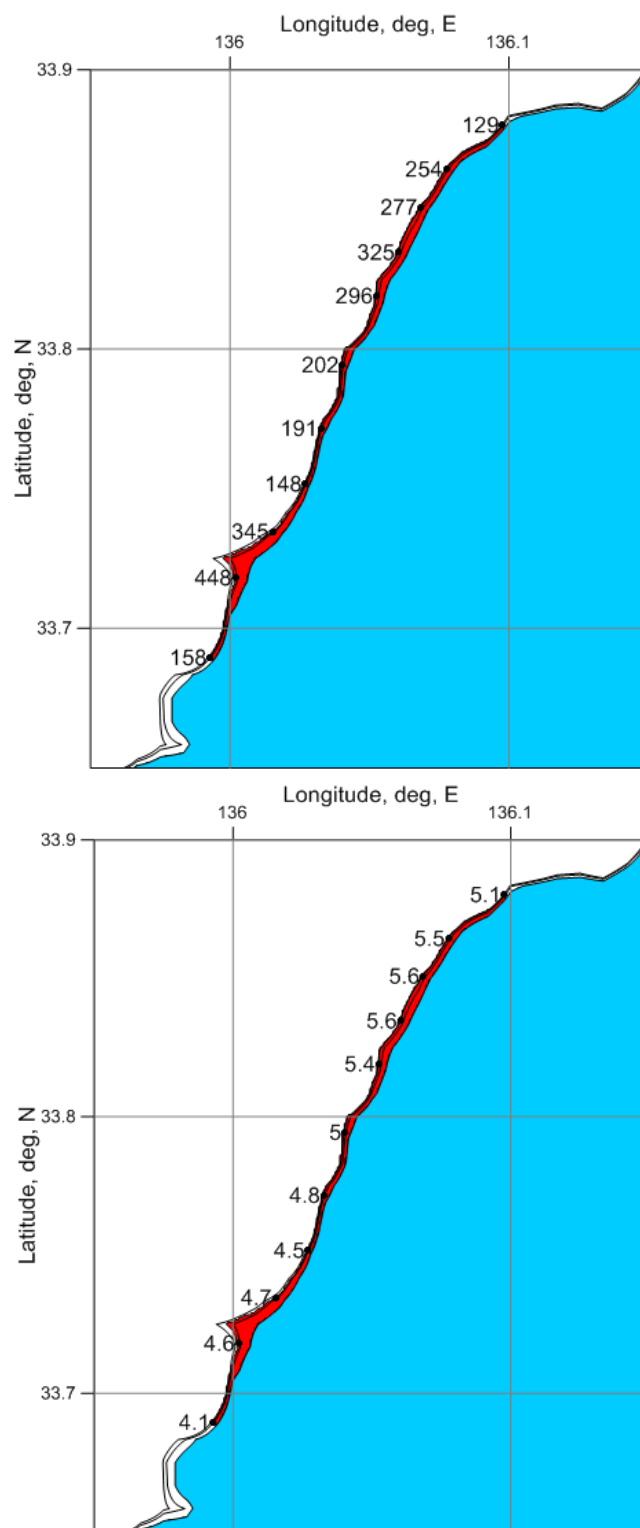


Fig. 2.3.11. The area of coastal flooding and the characteristics of the run-up for the 1944 Tonankai tsunami, calculated in the 1D simulation; digits near black dots show (in m) distance (upper figure) and height (lower figure). 4 m and 6 m isolines of land relief are also shown.

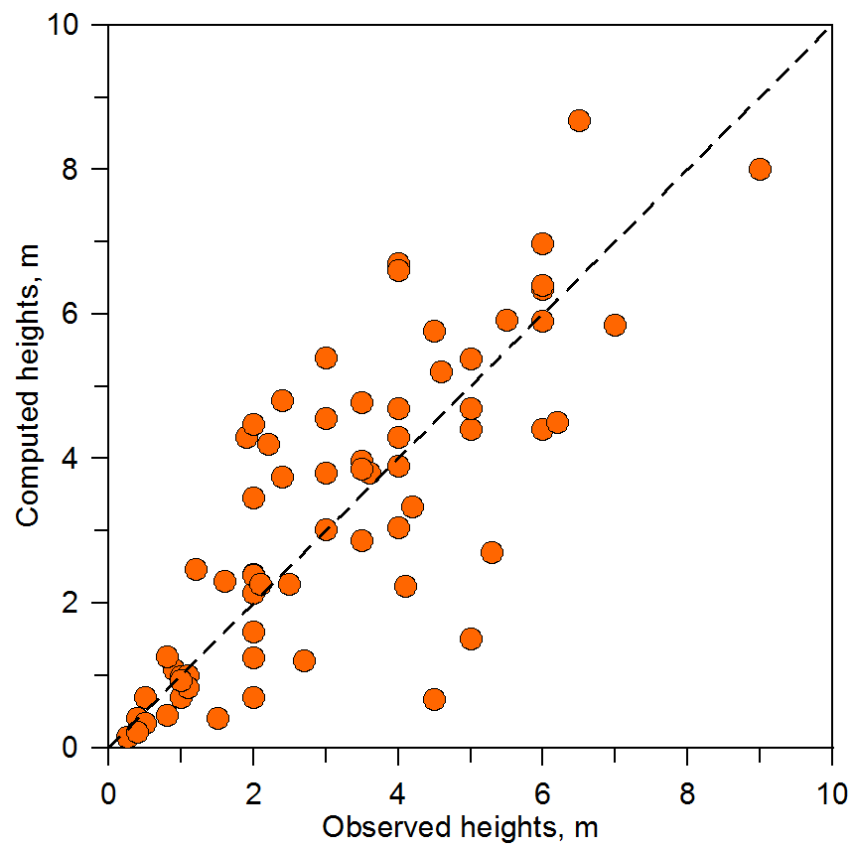


Fig. 2.3.12. Comparison of computed maximum positive amplitudes (red circles) versus measured run-up heights for the 1944 Tōnankai tsunami.

2.3.6. 2D calculation of tsunami run-up and estimation of inundation limits

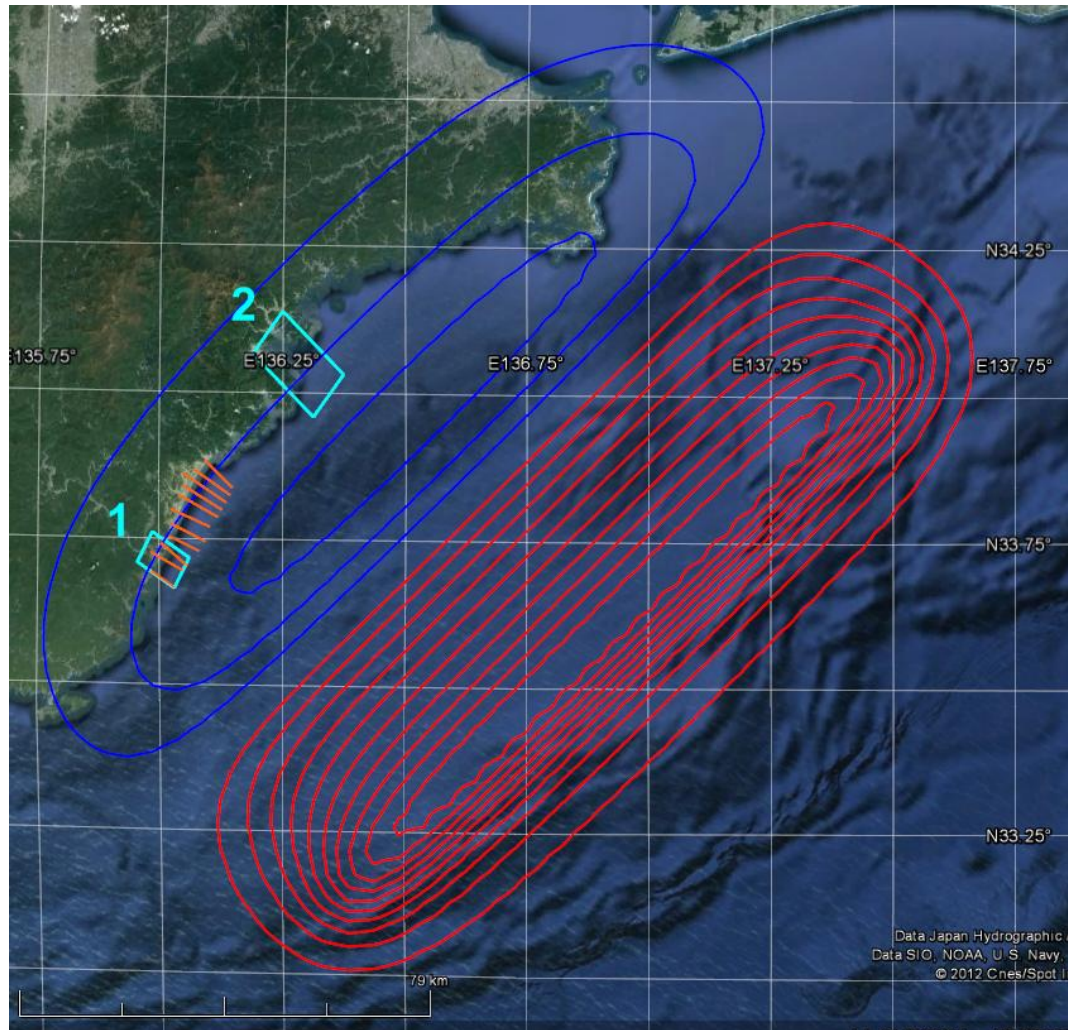


Fig. 2.3.13. Location of two coastal areas (shown as light blue rectangles) selected for 2D modeling of run-up of the “Tōnankai, 1944” tsunami. Position of the model source is shown as isolines of initial vertical bottom displacement (red – uplift, blue – subsidence). Straight orange lines show vertical cross-sections used for 1D run-up modeling.

Coastal area 1

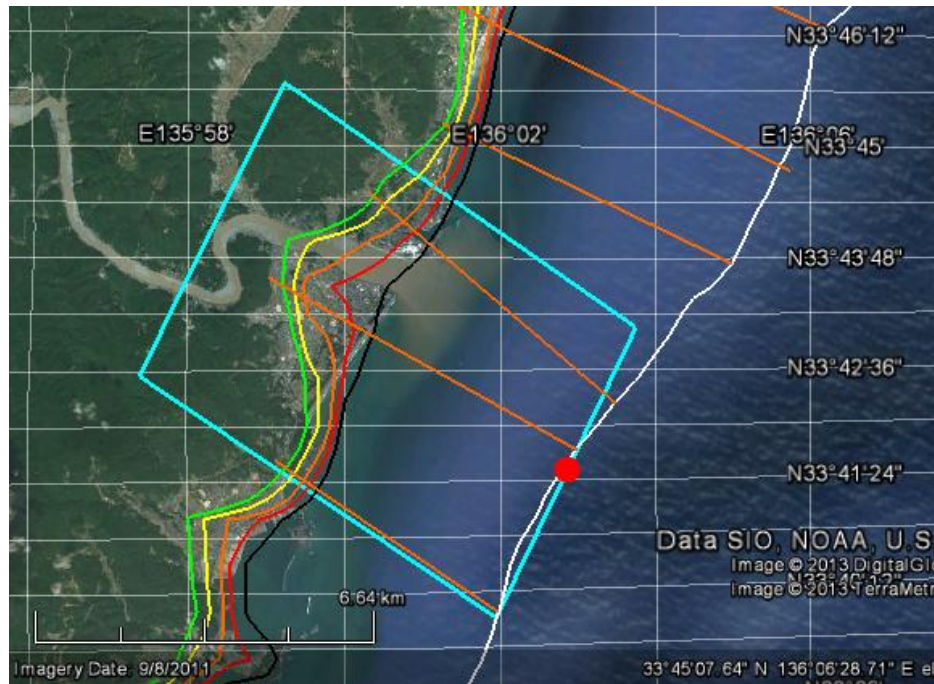


Fig. 2.3.14. Location of coastal area 1 (shown as light blue rectangle) selected for 2D modeling of run-up of “Tōnankai, 1944” tsunami. Color lines show relief isolines of the DEM/DBM GEBCO-30sec: white line – isobath 100m, black – position of the shoreline for undisturbed sea water (0 m), red – isoline 5 m, orange – 10 m, yellow – 20 m, green – 30 m. Straight orange lines show vertical cross-sections used for 1D run-up modeling. Red circle marks the position of the virtual tide gauge for recording the mareogram used as input boundary condition for 2D run-up modeling

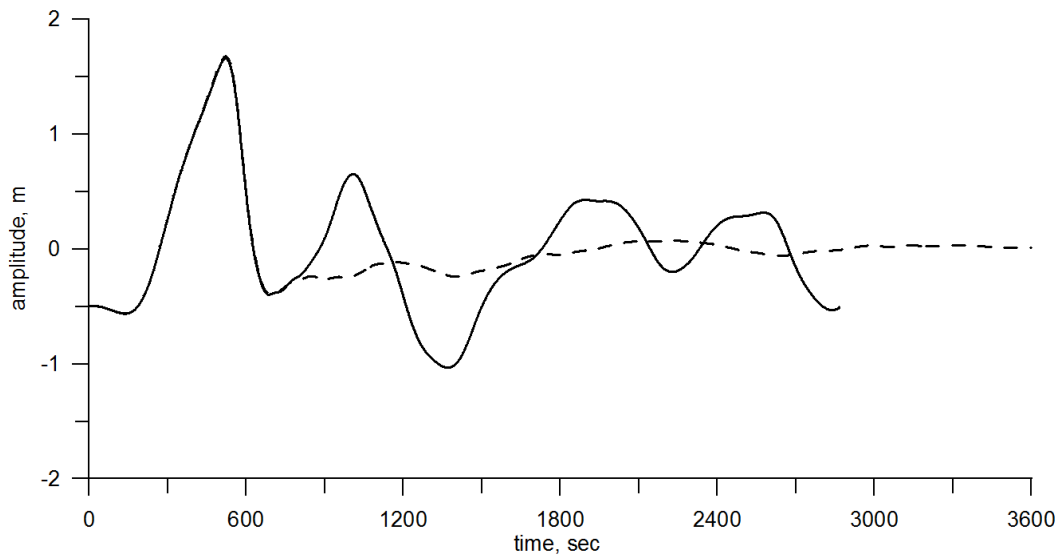


Fig. 2.3.15. Mareogram, calculated at the point shown as red circle in Fig. 2.3.14 that was used as input boundary condition for 2D run-up modeling of “Tōnankai, 1944” tsunami within the coastal area 1. Solid line shows the wave form calculated for the initial DEM/DBM (based on the original GEBCO-30sec), dotted line – the wave form obtained for corrected DEM/DBM where land and depths above $z = -h_{\min} = -10$ m were replaced by this value to suppress the reflected wave.

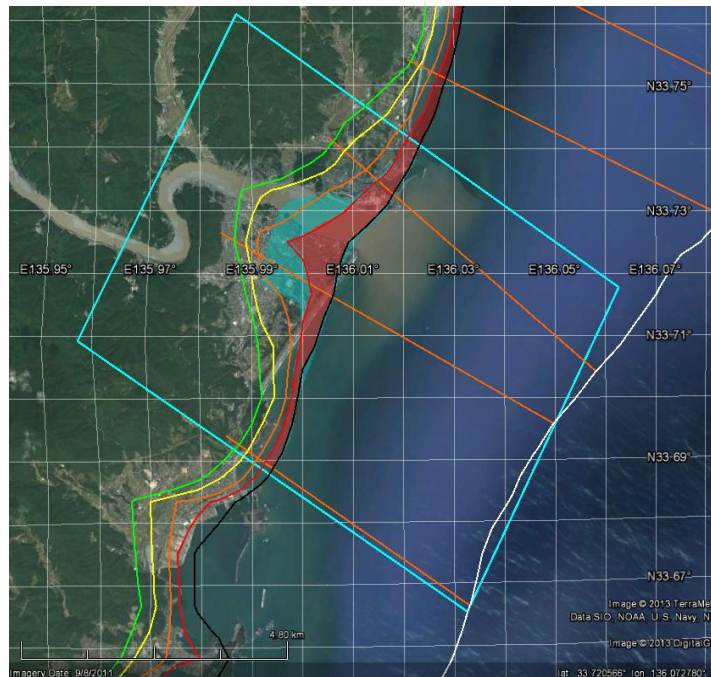


Fig. 2.3.16. Inundation zones from “Tōnankai, 1944” tsunami calculated for the coastal area 1 by 2D modeling (blue shading) and 1D modeling (red shading) using DEM/DBM GEBCO-30sec. Color lines show relief isolines: white – isobaths 100 m, black – position of the shoreline for undisturbed sea water (0 m), red – isoline 5 m, orange – 10 m, yellow – 20 m, green – 30 m. Straight orange lines show vertical cross-sections used for 1D run-up modeling.

Coastal area 2

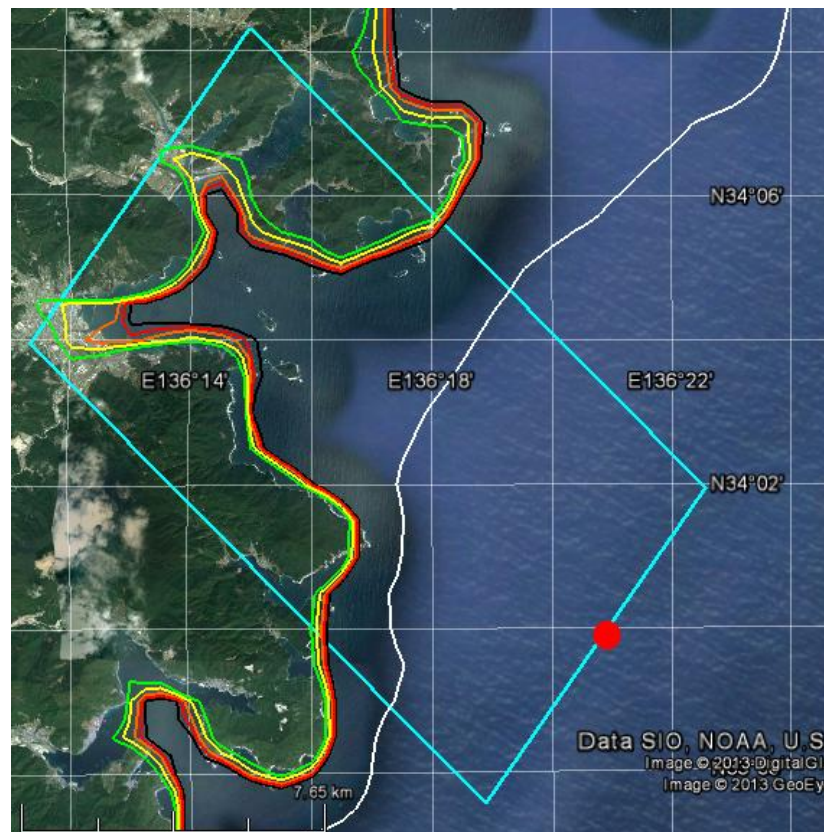


Fig. 2.3.17. Location of coastal area 2 (shown as light blue rectangle) selected for 2D modeling of run-up of “Tōnankai, 1944” tsunami. Color lines show relief isolines of the DEM/DBM GEBCO-30sec: white line – isobath 100 m, black – position of the shoreline for undisturbed sea water (0 m), red – isoline 5 m, orange – 10 m, yellow – 20 m, green – 30 m. Red circle marks the position of the virtual tide gauge for recording the mareogram used as input boundary condition for 2D run-up modeling

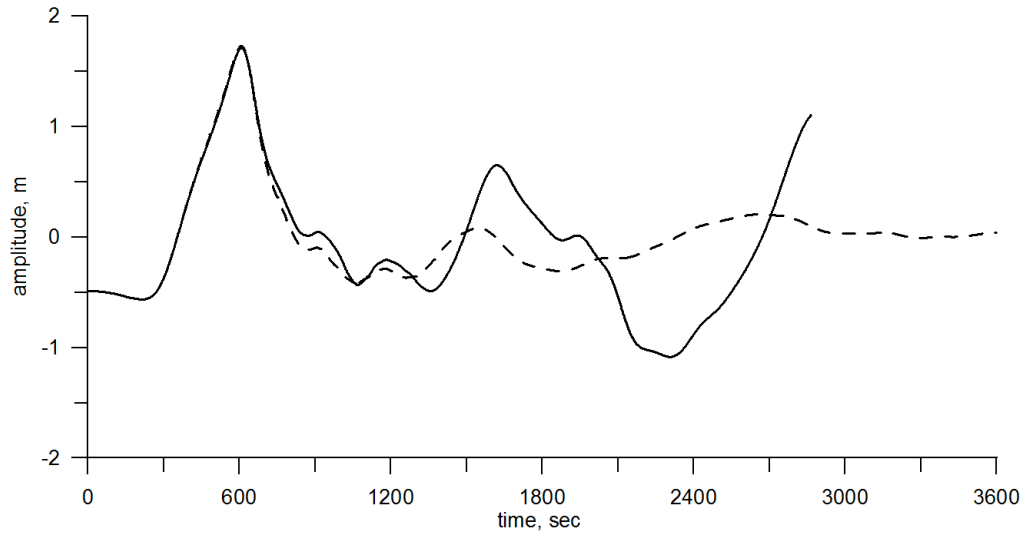


Fig. 2.3.18. Mareogram, calculated at the point shown as red circle in Fig. 2.3.17 that was used as input boundary condition for 2D run-up modeling of “Tōnankai, 1944” tsunami within the coastal area 2. Solid line shows the wave form calculated for the initial DEM/DBM (based on the original GEBCO-30sec), dotted line – the wave form obtained for corrected DEM/DBM where land and depths above $z = -h_{\min} = -10$ m were replaced by this value to suppress the reflected wave.

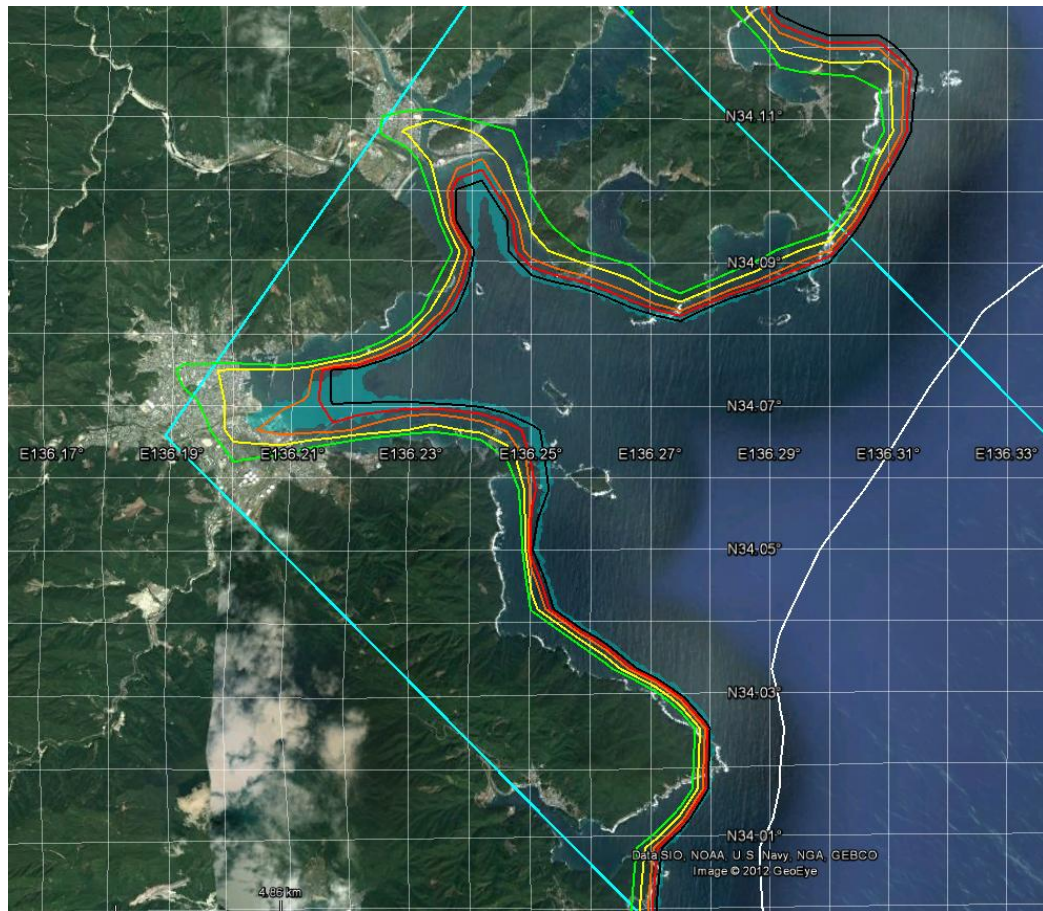


Fig. 2.3.19. Inundation zone (blue shading) from “Tōnankai, 1944” tsunami calculated for the coastal area 2 by 2D modeling using DEM/DBM GEBCO-30sec. Color lines show relief isolines: white line – isobath 100 m, black – position of the shoreline for undisturbed sea water (0 m), red – isoline 5 m, orange – 10 m, yellow – 20 m, green – 30 m.

2.4.1946 Nankai tsunami

2.4.1. Seismotectonic features of the area. Basic information on earthquake and tsunami

The **Mw8.1 1946 Nankai earthquake** was a great subduction earthquake ruptured the south-western part of the Nankai megathrust formed along the main convergent boundary where the Philippine plate is being subducted under the Eurasia plate (Fig. 2.4.1). This area hosted the major (M8+) subduction earthquakes that repeatedly occur through all the Japanese history. The 1946 earthquake occurred just two years after the M_w 8.1 **1944 Tonankai earthquake** which ruptured the adjacent, central part of the same trust fault.

The main seismotectonic feature of the area is the presence of the Nankai Trough, a deep-water trough that extends approximately 900 km offshore Honshu in south-west direction from the Sagami Bay where it junks with the Sagami Trough. The Nankai Trough marks the plate boundary separating the subducting Philippine Plate from overriding Eurasian Plate and it is the source of many large earthquakes in Japan's history. Historically, it is subdivided into three large segments (Nankai, Tonankai, Tokai) each of them is further subdivided into several smaller segments (Fig. 2.4.1). The 1946 Nankai earthquake is the most recent large-scale earthquake to occur in the sections A and B east of the Shikoku Island.



Fig. 2.4.1. Rupture areas on the Nankai Trough megathrust and position of its major segments.

The earthquake occurred during the early instrumental stage of seismological observations, so the accuracy of source location and magnitude estimates are low (within half angular degree and 0.5 unite of magnitude scale, respectfully). The NGDC/NOAA Tsunami database contains 298 run-ups for this event, with 292 of them reported from Japan. In Hawaii (Hilo) waves reached only 10 cm in amplitude. The largest far-field amplitudes were observed in Crescent City, California (23 cm).

The following series of aftershocks turned out to be shorter and less intensive than one could expect for the major subduction earthquake of this magnitude (Fig. 2.4.2). The aftershock area was smaller than the areas of intensive shaking (Fig. 2.4.3), large co-seismic displacement (Fig. 2.4.4) and coastal extent of tsunami flooding (Fig. 2.4.5). The reason for it is not quite clear so far (Soloviev, Go, 1974). Also, it should be noted the absence of large tsunami run-ups – the largest reported run-up is only 6.6 m (Soloviev, Go, 1974; Watanabe, 1985).

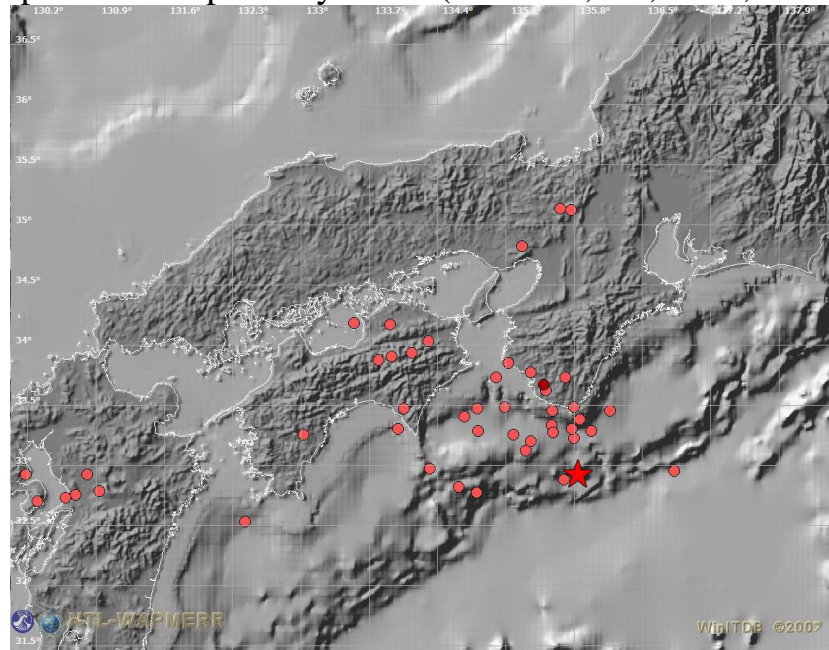


Fig. 2.4.2. Distribution of the first-week aftershocks (solid red dots) for the 1946 Nankai earthquake.
Aftershock data are from the JMA historical earthquake catalog, visualization is made in the WinITDB graphic shell. Position of the main shock is shown by the red star.

The earthquake caused extensive damage, destroying several tens of thousands homes (digits available in literature greatly vary, from 2500 to 36,000). Tsunami waves destroyed another 2,100 homes. Human fatalities include at least 1362 dead, 2600 injured and 100 missing people.

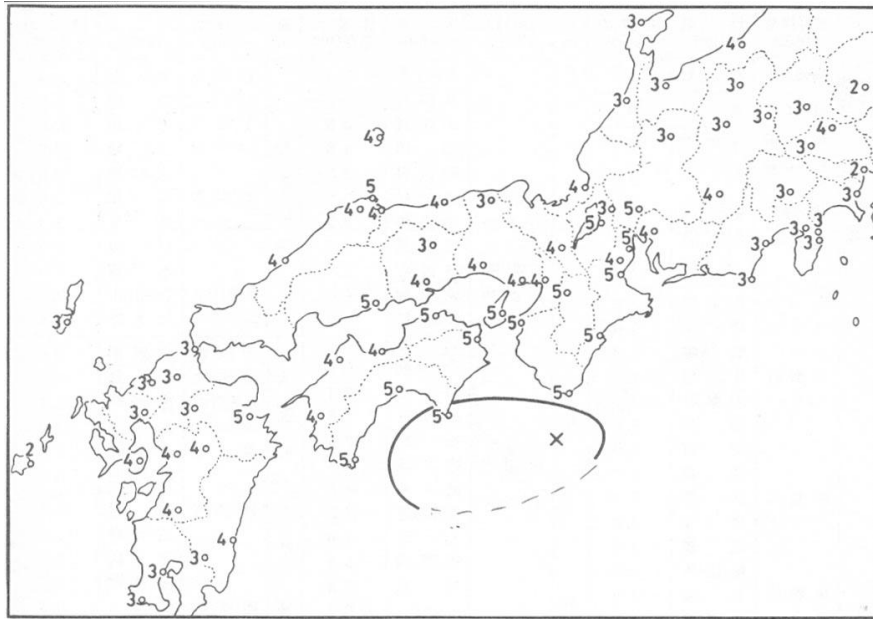


Fig. 2.4.3. Distribution of the reported seismic intensities (on the 7-grade JMA scale) and approximate area of source location for the 1946 Nankai earthquake (Watanabe, 1985).

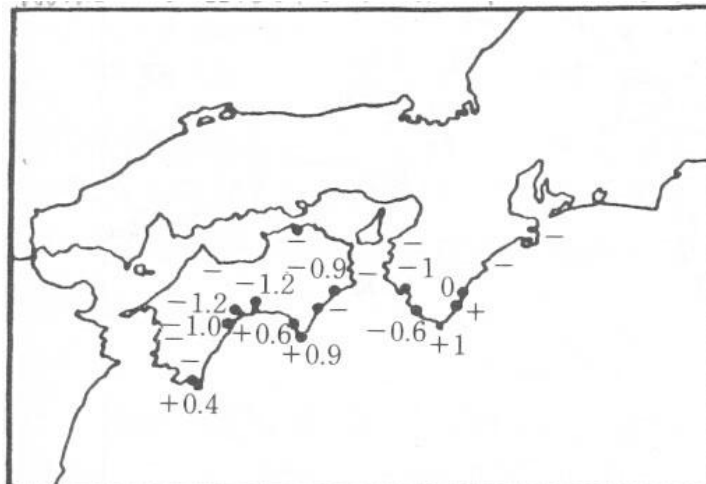


Fig. 2.4.4. Distribution of the measured co-seismic displacement for the 1946 Nankai earthquake (Watanabe, 1985).

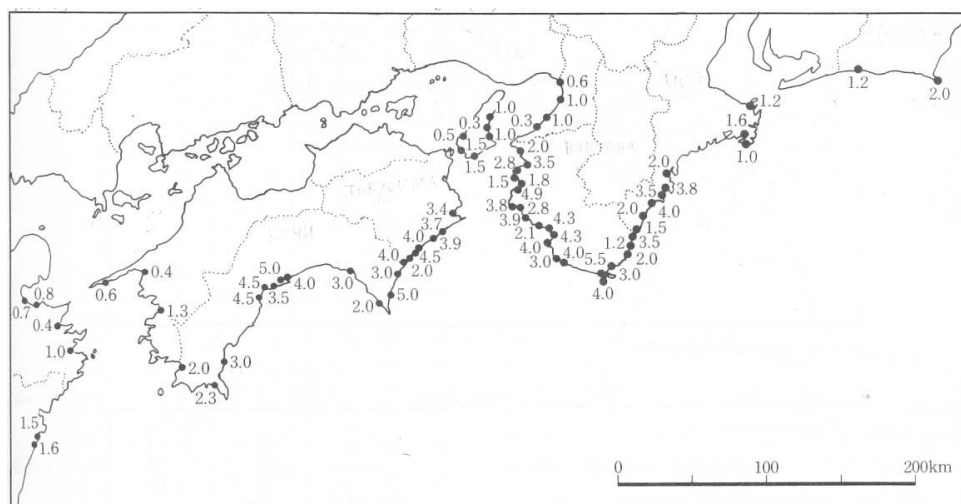


Fig. 2.4.5. Distribution of the measured wave heights for the 1946 Nankai tsunami (Watanabe, 1985).

There is some sort of paradox associated with this earthquake. From one side, the earthquake resulted in large deformation of surface relief, covering more than 300 km of coastal area (all the Shikoku Island and Kii Peninsula). This area of large deformation roughly coincides with the area where large ($>3\text{m}$) tsunami waves were observed. Land surface elevation reached 1.0 m and subsidence -1.2 m that indicates to the large amount of slip released on the fault plane. From other side, area of first-day aftershocks is essentially smaller ($200 \times 100\text{km}$) than area of large co-seismic displacement and tsunami manifestation (as indicated in Soloviev, Go, 1974). Despite the large coastal extent of tsunami impact (300 km), the maximum run-up height is only 6.5 m (Watanabe, 1985), so that distribution of tsunami heights looks very homogeneous along the north-eastern part of the Shikoku Island and south-western part of the Kii peninsula (variation within 3-5 m along more than 300 km of the coastline and absence of any area with prominent maximum heights). All these features are not typical for tsunamigenic earthquakes occurring along the nearby subduction zones.

2.4.2. Adopted source model and calculation of initial bottom displacement

Based on consideration of all the above data, the following source was adopted as a model for the 1946 Nankai earthquake: $Lat = 33.1^\circ\text{N}$, $Lon = 134.5^\circ\text{E}$ (coordinates of the center of the lower edge of the fault), $h_0 = 10\text{ km}$ (depth of the upper edge of the fault), fault size: $L = 150\text{ km}$, $W = 50\text{ km}$, displacement: $D_0 = 5\text{ m}$, dip-angle: $\delta = 20^\circ$, slip-angle: $\lambda = 90^\circ$, strike-angle: $\theta = 50^\circ$. Calculated seismic moment of this model source is $M_0 = 1.8 \cdot 10^{21}\text{ N} \cdot \text{m}$, that corresponds $M_w = 8.1$.

Calculated static displacement for this model source is shown in Fig. 2.4.6.

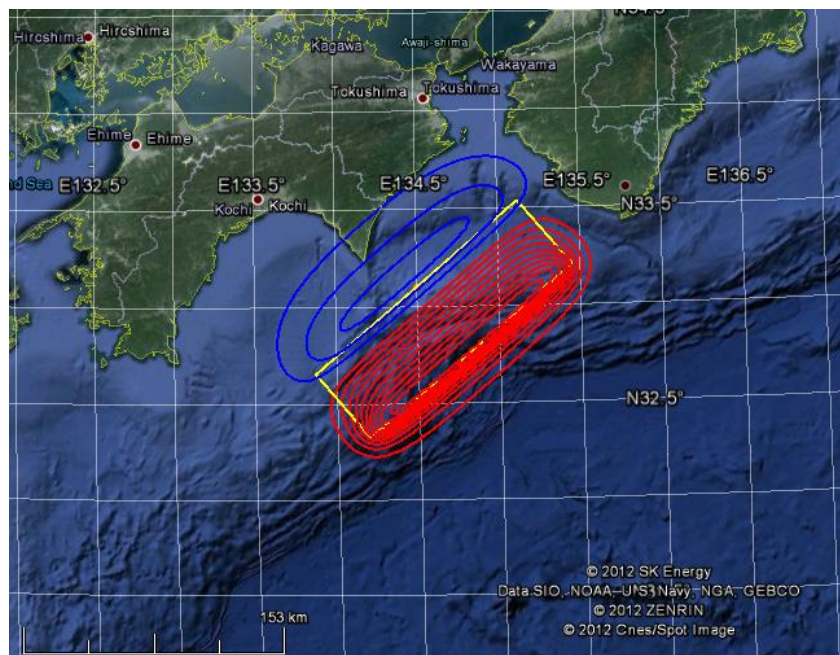


Fig. 2.4.6. Calculated bottom displacements for the adopted model of the 1946 Nankai earthquake overlaid on the Google Earth map. Red color shows uplifted areas, blue color – subsided areas.

2.4.3. Calculation domain and virtual coastal points

Modeling of tsunami generation and propagation was carried out in the rectangular computational grid with dimension 1849x1681 and spatial step 15 angular seconds in both directions covering the area within 29°00'N – 36°00'N, 131°18'E – 139°0'E. The minimum water depth h_{\min} in the area was adopted to be equal 10 m. Tsunami heights were calculated at 3997 virtual mareograph points distributed along the coastline (Fig. 2.4.7).

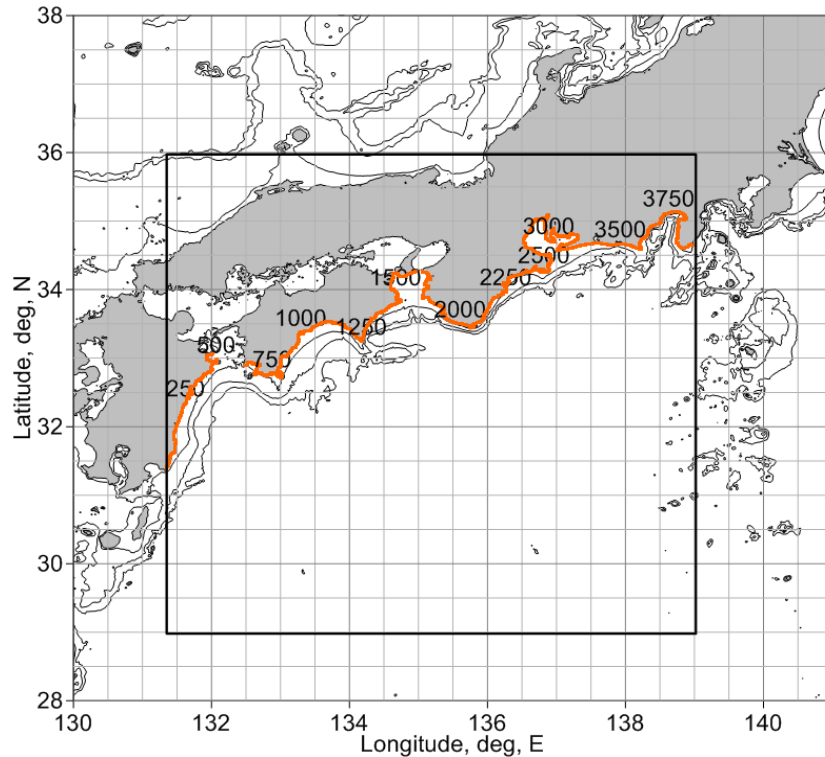


Fig. 2.4.7. The computational domain (plotted as solid black rectangle) with 100m, 500m and 1000m depth isobaths adopted for the 1946 Nankai tsunami modeling. Spatial distribution of 3997 coastal virtual gauges is shown as orange numbered dots.

2.4.4. Analysis of computed wave height distribution

Numerical modeling of tsunami propagation was made for 4 hours of physical time using MGC package (Shokin et al., 2008) for tsunami modeling that is based on the non-linear shallow water system written in spherical coordinates. Results of computation are shown in Fig. 2.4.8 – Fig. 2.4.10.

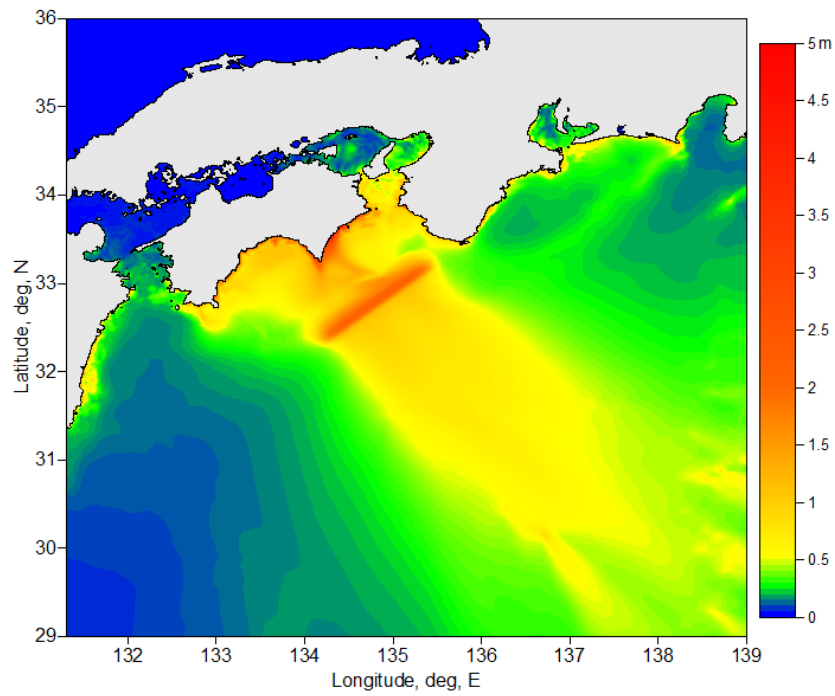


Fig. 2.4.8. Energy flux for the modeled 1946 Nankai tsunami.

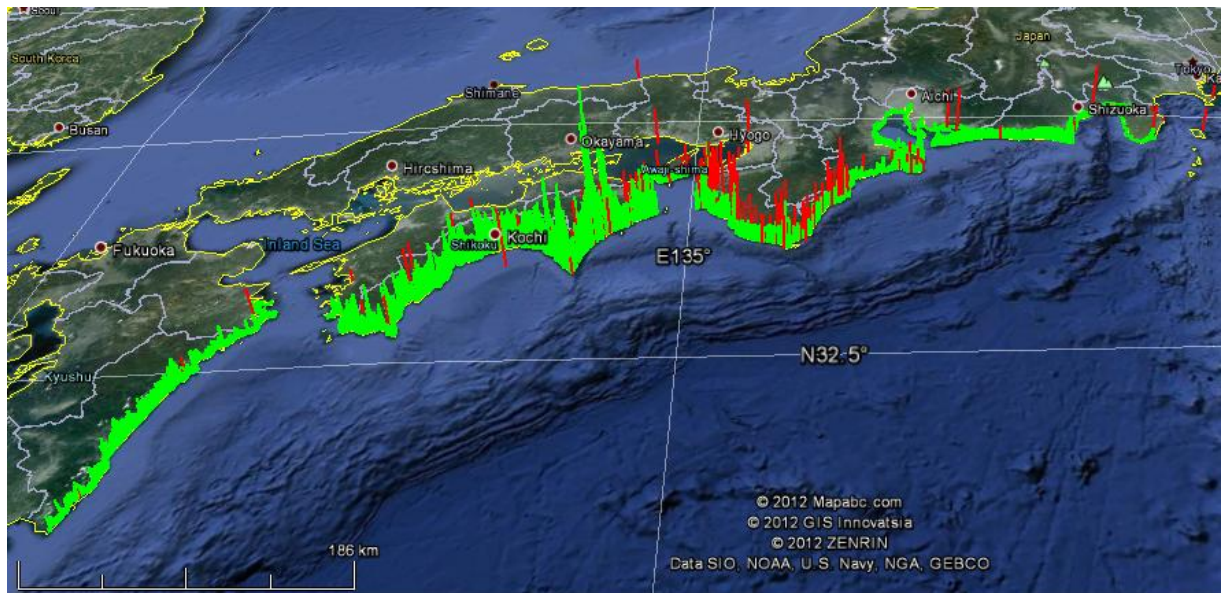


Fig. 2.4.9. Distribution of observed (red) and computed maximum (green) tsunami wave heights calculated at the vertical wall put at the depth of 10 m for 3997 virtual coastal points.

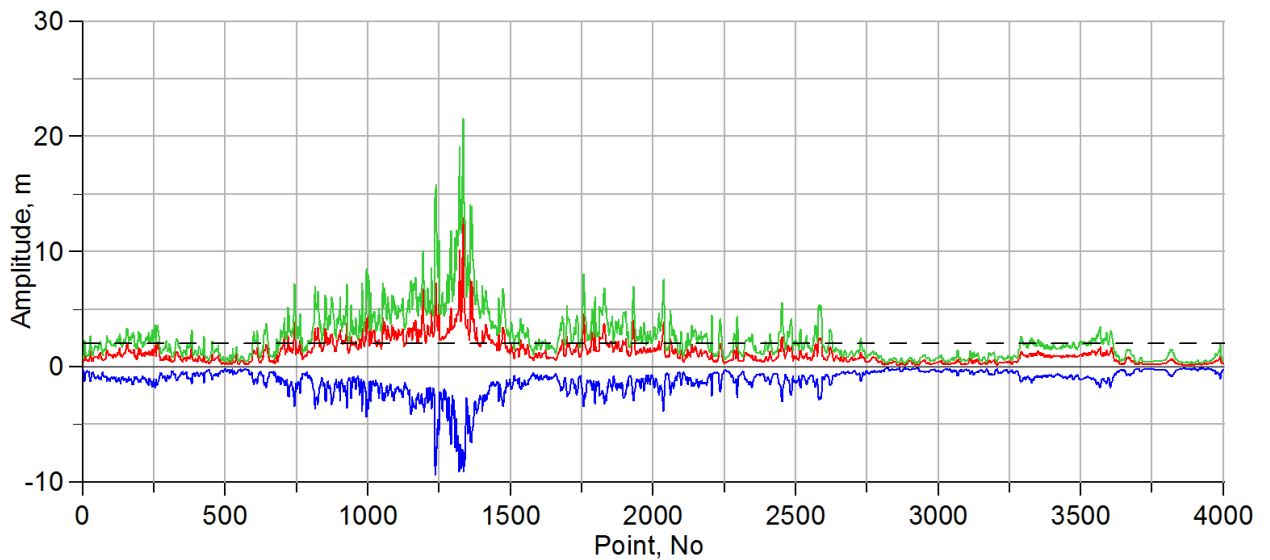


Fig. 2.4.10. Distribution of computed maximum positive (red line) and maximum negative (blue line) amplitudes along with maximum wave heights (green line) over 3997 coastal virtual gauges. Spatial location of these virtual gauges is shown in Fig. 2.4.7.

2.4.5. 1D calculation of tsunami run-up and estimation of inundation limits

For test calculation of run-up heights for the 1946 Nankai tsunami, a part of coastal plain near town Konan (Kochi Prefecture) was selected. Konan lies along the Kiso River, in the northern part of the Owari plain. As of 2004, its population was estimated to be about 55,000.

Since the degree of roughness of land topography essentially increases for elevations above 10 m, the selected vertical cross-sections were stopped at the elevation 10 m. Starting points for all profiles are at the depth 100m (Fig. 2.4.11).

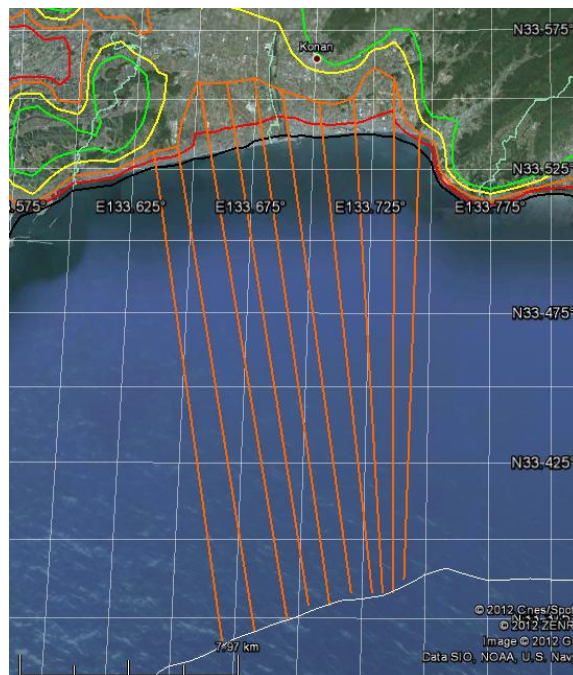


Fig. 2.4.11. Position of 10 profiles, selected for one-dimensional calculations of run-up heights for the 1946 Nankai tsunami. Solid black line represents the coastline. Isolines of land relief overlaid on the Google Earth map are for levels of 5 m (red), 10 m (orange), 20 m (yellow), 30 m (green). The white line shows the 100m depth contour.

Position of the coastal profiles selected for 1D run-up modeling relatively to the adopted tsunami source is shown in Fig. 2.4.12.

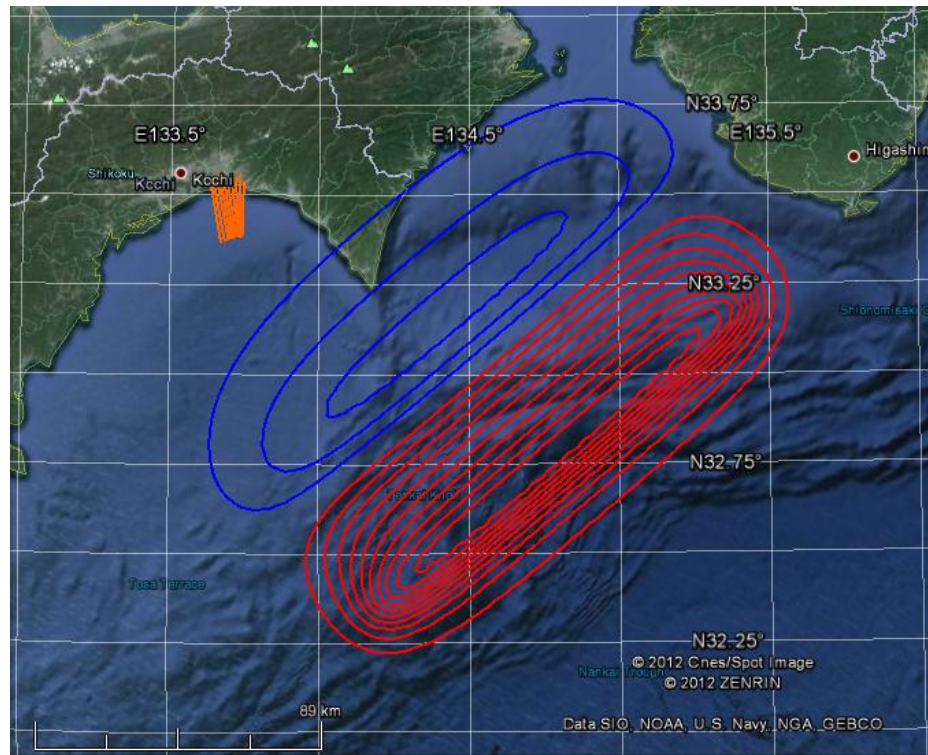


Fig. 2.4.12. Location of coastal profiles (orange lines) selected for 1D run-up modeling relatively source area of the 1946 Nankai tsunami. Calculated co-seismic displacements for the adopted earthquake source model are shown as isolines of vertical displacement (red color shows uplifted areas, blue color – subsided areas).

Table 2.4.1. Land and bottom relief along the profiles selected for 1D modeling of run-up of the 1946 Nankai tsunami.

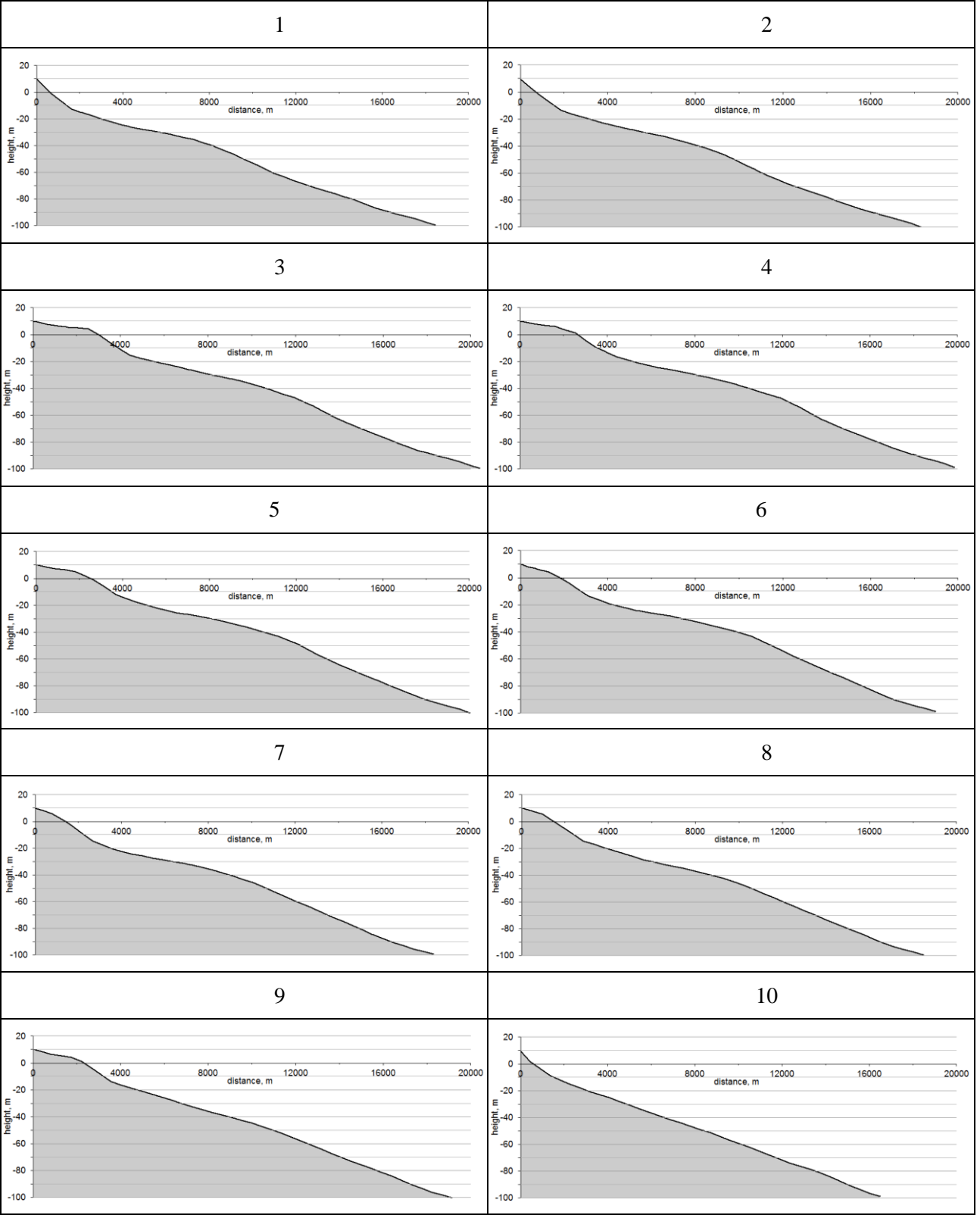


Table 2.4.2. Characteristics of inundation area of the 1946 Nankai tsunami, calculated in the 1D simulation along the selected cross-sections.

Index number of cross-section	Calculated runup height (m)	Calculated runup distance (m)	Initial longitude of shoreline point (grad)	Initial latitude of shoreline point (grad)	Calculated longitude of runup point (grad)	Calculated latitude of runup point (grad)
1	4.17	258.6	133.6344	33.5256	133.6339	33.5279
2	4.42	341.5	133.6445	33.5267	133.6438	33.5297
3	4.56	671.4	133.6574	33.5295	133.6559	33.5355
4	5.12	867.8	133.6681	33.5324	133.6663	33.5401
5	5.1	678.5	133.6788	33.5356	133.6775	33.5416
6	5.03	753.0	133.6895	33.5368	133.6882	33.5436
7	4.71	474.6	133.704	33.5364	133.7033	33.5406
8	4.67	434.7	133.7179	33.5373	133.7175	33.5412
9	4.85	803.0	133.7339	33.5364	133.7338	33.5437
10	4.46	308.9	133.7447	33.5319	133.7448	33.5347

Table 2.4.3. A comparison of the characteristics of the 1946 Nankai tsunami, calculated in the 2D simulation as “wet line” on the vertical wall (maximum positive wave amplitude), as run-up height obtained in 1D simulation along the selected profiles and as run-up height calculated by analytical formulas proposed in (Synolakis, 1987) and (Pelinovsky, Mazova, 1992). Red color marks values obtained outside of applicability of analytical formulas.

Index number of cross-section	Maximum runup on the wall, calculated in the 2D numerical simulation (“wet line”) (m)	Runup heights, calculated in the 1D simulation (m)	Runup height, calculated by analytical formula of Synolakis, 1987 (m)	Runup height, calculated by analytical formula of Pelinovsky, Mazova, 1992 (m)	Observed data (m)
1	3.15311	4.171532	13.27375	5.011921	
2	2.6977	4.420559	13.34585	4.654853	
3	2.91606	4.55572	13.05657	5.292202	
4	2.66919	5.117687	12.90018	4.874767	
5	3.19885	5.097672	13.13815	5.85324	
6	2.9761	5.030892	12.8539	5.56591	
7	2.75261	4.712583	12.76572	4.736687	
8	2.90386	4.67124	12.78961	6.810793	
9	3.20726	4.852344	12.70592	5.297911	
10	2.42708	4.459971	12.61316	5.705611	2.9
Average	2.89018	4.70902	12.94428	5.38039	2.9

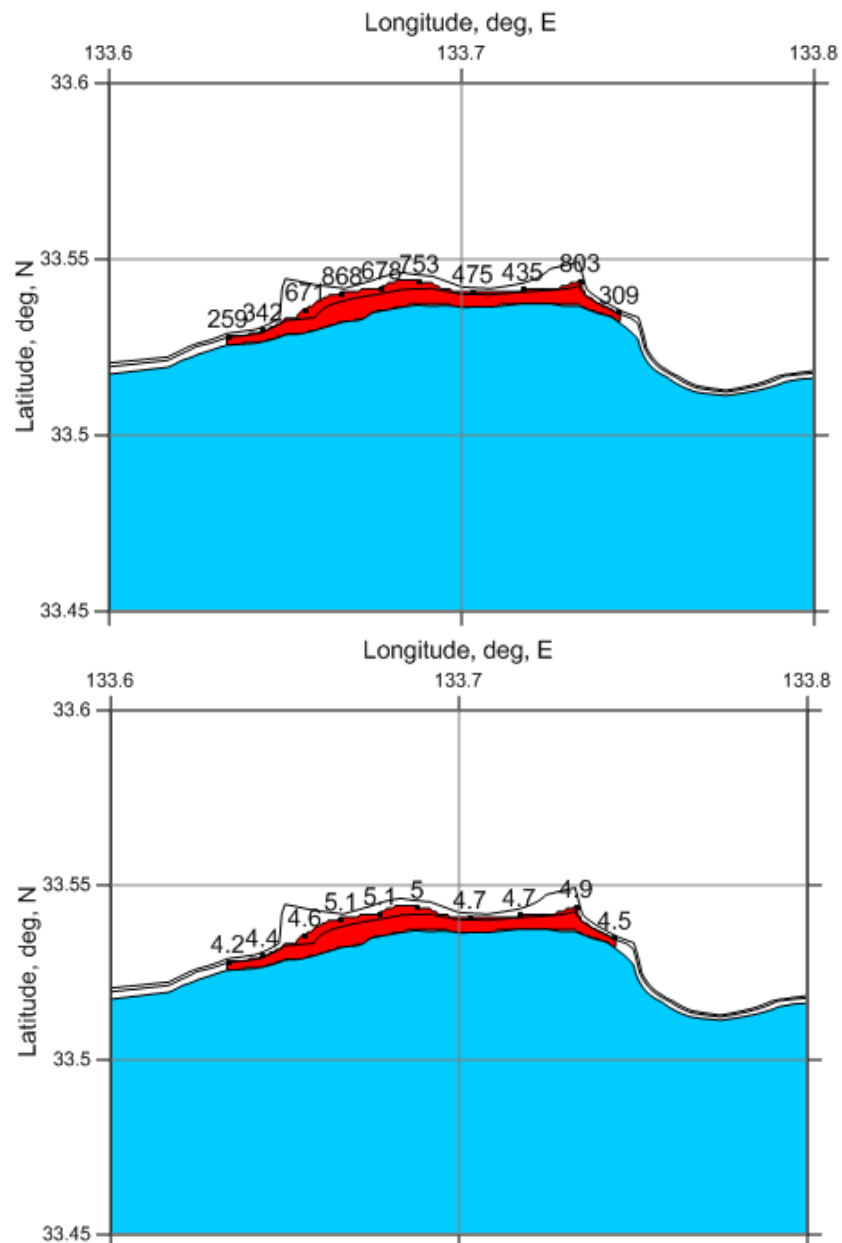


Fig. 2.4.13. The area of coastal flooding and the characteristics of the run-up for the 1946 Nankai tsunami, calculated in the 1D simulation; digits near black dots show (in m) distance (upper figure) and height (lower figure). 4 m and 6 m isolines of land relief are also shown.

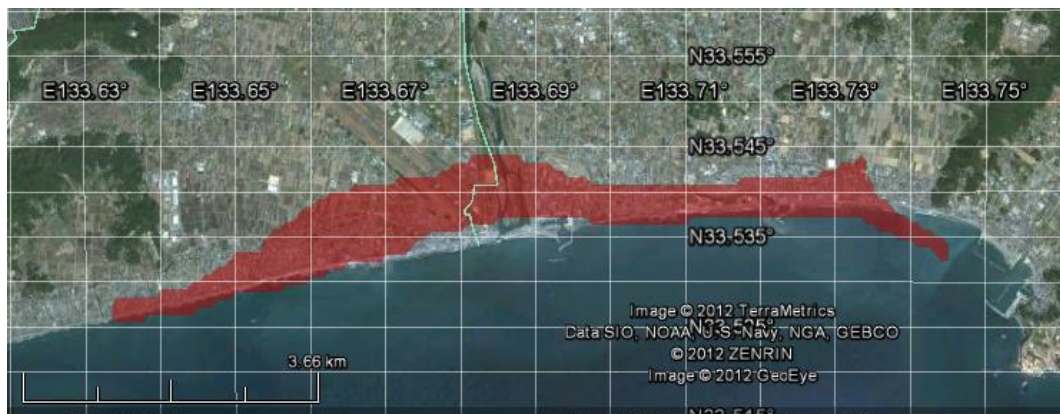


Fig. 2.4.14. Area of inundation calculated in 1D run-up modeling overlaid on the Google Earth map.

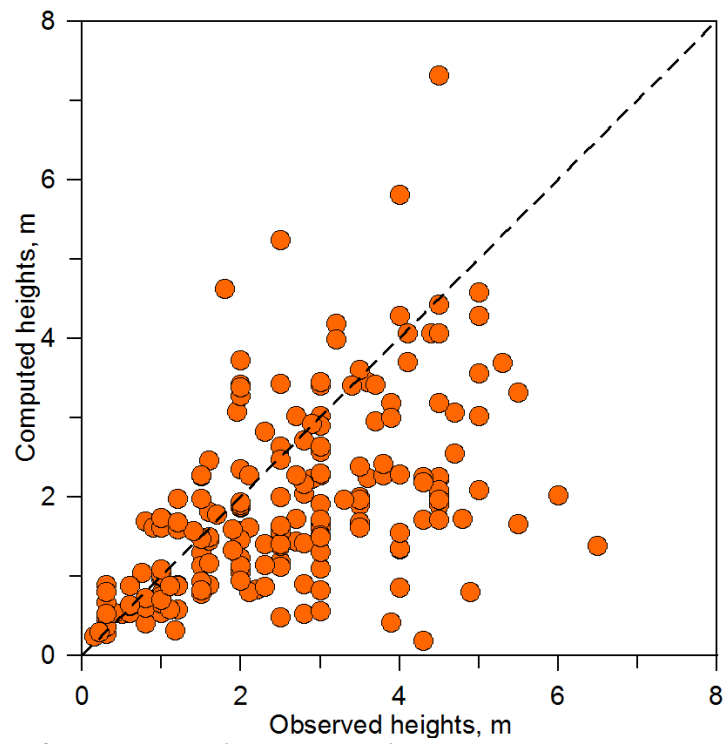


Fig. 2.4.15. Comparison of computed maximum wave heights versus measured run-up heights for the 1946 Nankai tsunami.

2.4.6. 2D calculation of tsunami run-up and estimation of inundation limits

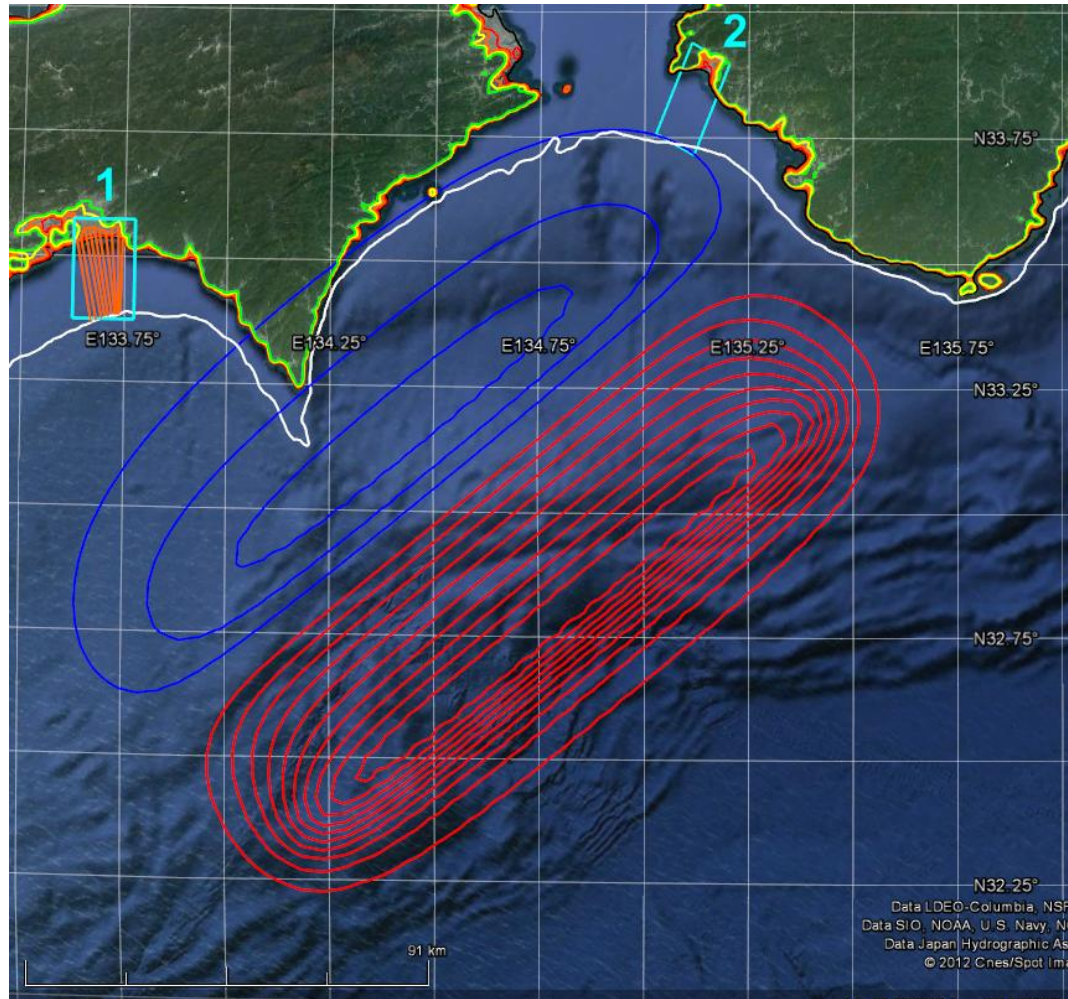


Fig. 2.4.16. Location of two coastal areas (shown as light blue rectangles) selected for 2D modeling of run-up of the “Nankai, 1946” tsunami. Position of the model source is shown as isolines of initial vertical bottom displacement (red – uplift, blue – subsidence). Relief isolines of the DEM/DBM GEBCO-30sec are shown: white line – isobath 100m, black – position of the shoreline for undisturbed sea water (0 m), red – isoline 5 m, orange – 10 m, yellow – 20 m, green – 30 m. Straight orange lines show vertical cross-sections used for 1D run-up modeling.

Coastal area 1



Fig. 2.4.17. Coastal area 1 (shown as light blue rectangle) selected for 2D modeling of run-up of the “Nankai, 1946” tsunami. Color lines show relief isolines of the DEM/DBM GEBCO-30sec: white line – isobath 100m, black – position of the shoreline for undisturbed sea water (0 m), red – isoline 5 m, orange – 10 m, yellow – 20 m, green – 30 m. Straight orange lines show vertical cross-sections used for 1D run-up modeling.



Fig. 2.4.18. Enlarged portion of the coastal area 1 (as shown in Fig. 2.4.16) showing inundation zones from “Nankai, 1946” tsunami calculated by 2D modeling (blue shading) and 1D modeling (red shading) using DEM/DBM GEBCO-30sec. Color lines show relief isolines: black – position of the shoreline for undisturbed sea water (0 m), red – isoline 5 m, orange – 10 m, yellow – 20 m, green – 30 m. Straight orange lines show vertical cross-sections used for 1D run-up modeling. Incoming wave is introduced to the coastal area during the 2D run-up modeling through the southern and eastern boundaries.

Coastal area 2

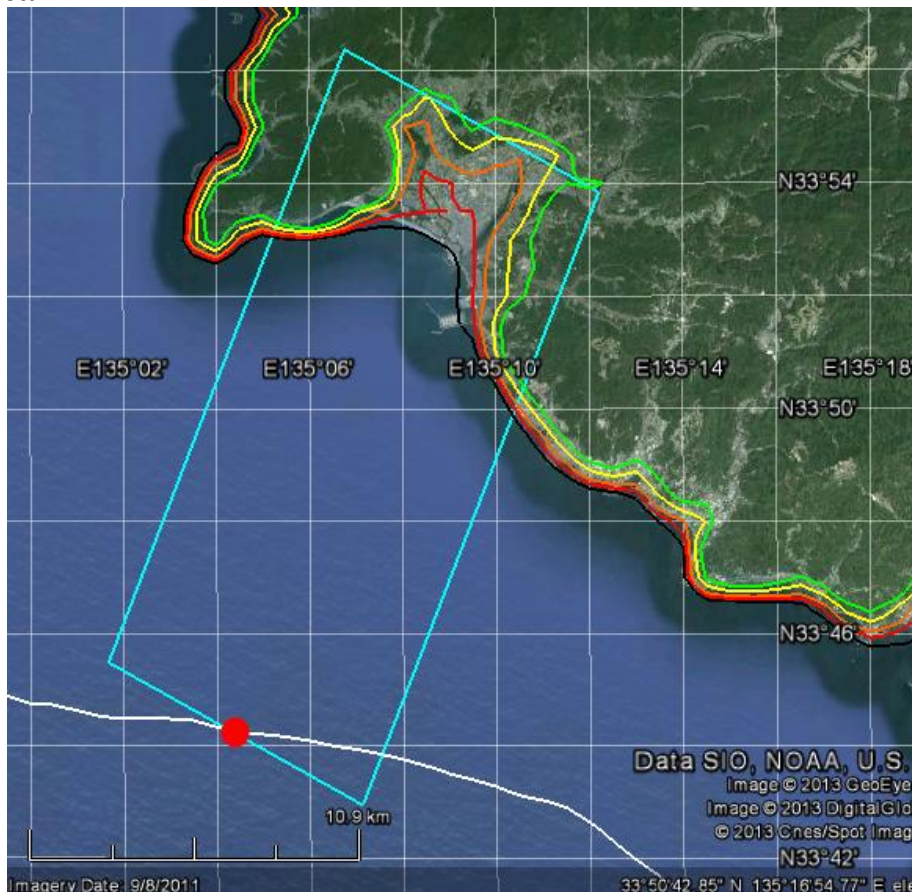


Fig. 2.4.19. Location of coastal area 2 (shown as light blue rectangle) selected for 2D modeling of run-up of the “Nankai, 1946” tsunami. Color lines show relief isolines of the DEM/DBM GEBCO-30sec: white line – isobath 100m, black – position of the shoreline for undisturbed sea water (0 m), red – isoline 5 m, orange – 10 m, yellow – 20 m, green – 30 m. Red circle marks the position of the virtual tide gauge for recording the mareogram used as input boundary condition for 2D run-up modeling

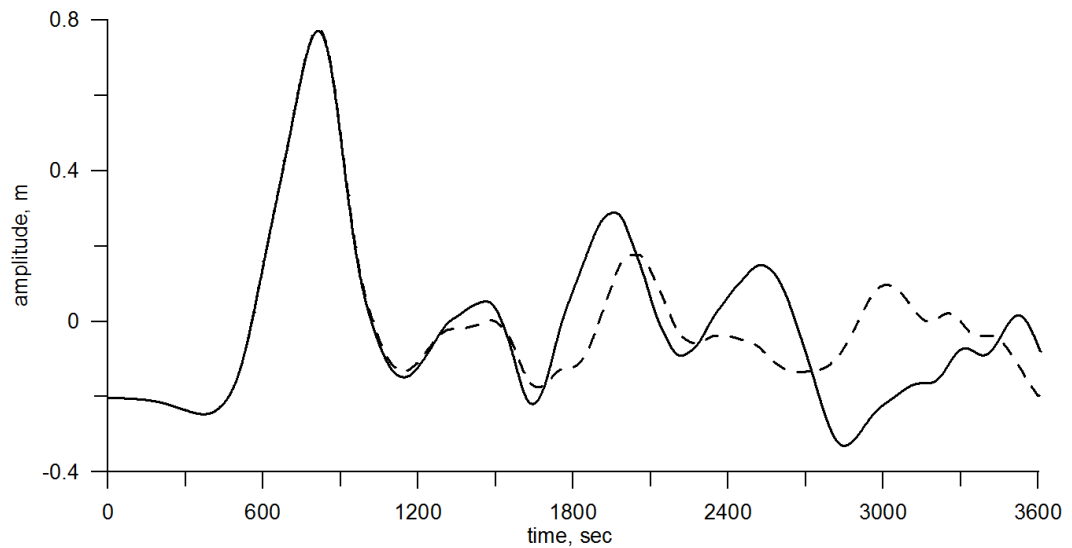


Fig. 2.4.20. Mareogram, calculated at the point shown as red circle in Fig. 2.4.19 that was used as input boundary condition for 2D run-up modeling of “Nankai, 1946” tsunami within the coastal area 2. Solid line shows the wave form calculated for the initial DEM/DBM (based on the original GEBCO-30sec), dotted line – the wave form obtained for corrected DEM/DBM where land and depths above $z = -h_{\min} = -10$ m were replaced by this value to suppress the reflected wave.



Fig. 2.4.21. Enlarged portion of the coastal area 2 (as shown in Fig. 2.4.16) showing inundation zone (blue shading) from “Nankai, 1946” tsunami calculated by 2D modeling using DEM/DBM GEBCO-30sec. Color lines show relief isolines: black – position of the shoreline for undisturbed sea water (0 m), red – isoline 5 m, orange – 10 m, yellow – 20 m, green – 30 m.

2.5.2011 Tohoku tsunami

2.5.1. Basic information on earthquake and tsunami

An earthquake of magnitude 9.0 occurred off the Pacific coast of Tohoku, Japan, on Friday, March 11, 2011 at **14:46:23** Japan Standard Time (5:46:23 GMT). It was the largest magnitude earthquake recorded in Japan and, according to US GS, fourth largest instrumentally recorded since 1900. The rupture area in the earthquake source was estimated to be approximately 450x200km and located off the coast of Miyagi Prefecture. Severe shaking reaching 7 on 7-grade JMA scale was observed in Kurihara city, located at 175 km from the instrumental epicenter (Hoshiba et al, 2011). Seismic intensity 7 was observed for only the second time since JMA introduced instrument-based observations for intensity measurements in 1996. Strong shaking (6-upper and 6-lower on JMA scale) was experienced over the area of approximately 400x100km, from Iwate Prefecture on the north to Chiba Prefecture on the south. In Tokyo metropolitan area observed intensity reached 5-upper grade. In all affected areas, duration of strong ground motions was quite long and in some places exceeded 6 minutes.

The earthquake and tsunami caused extensive and severe structural damage in north-eastern Japan, including heavy damage to roads and railways, failure of electric and communication networks as well as fires in many areas, and a dam collapse. As for 12 September 2012, a Japanese National Policy Agency reported **15,870** deaths, **6,114** injured, and **2,814** people missing across twenty prefectures as well as **129,225** buildings totally collapsed, with a further **254,204** buildings 'half collapsed', and another **691,766** buildings partially damaged. It is estimated that up to **96%** of all casualties were result of drowning in tsunami waves (SEEDS Asia, 2011). Associated economic loss may approach US300 billion, making it the most costly natural disaster of all time (EERI Special Earthquake Report, 2011).

The tsunami caused a severe (rated to level 7 on the IAEA international nuclear event scale) nuclear accident in the Fukushima Daiichi Nuclear Power Plant resulted in meltdowns at three reactors, and the associated evacuation zones affecting nearly **300,000** residents. All three of six reactor units at Fukushima Daiichi, operating in the time of earthquake, were damaged due to a complete station black-out that eventually resulted in core melting. Damaged nuclear reactors in Fukushima Daiichi suffered explosions due to hydrogen gas that had built up within their outer containment buildings after cooling system failure. About 90,000 residents within a 20 km radius of the Fukushima Daiichi Nuclear Power Plant and a 10 km radius of the Fukushima Daini Nuclear Power Plant were evacuated.

Tsunami field survey was conducted by joint research group consisted of almost 300 tsunami, coastal, seismology, geology and geophysics researchers from 63 universities and institutes throughout Japan (The Joint Tohoku Earthquake Tsunami Research Survey Group, 2011). As result of this survey, to date **5770** run-up heights and inundation measurements became available for international

research community (NGDC/NOAA Tsunami Database, 2012), making this the largest collection of tsunami height measurements for a single tsunami event. At the moment, tsunami heights for the 2011 Tohoku tsunami constitute **34%** of the total run-up data available for all historical events occurred in the World Ocean since 2000 BC. Before the Tohoku tsunami, the largest set of wave height data was for the 2004 Indian Ocean tsunami (1058 run-up and inundation measurements).

The highest run-up value **55.88m** was found on steep coastal slope at some point located at 39,3175N, 141,9725E north of Kamaishi City, Iwate Prefecture. The second highest run-up **40.57m** was measured just 25 km farther to the north, near Yamada city, Iwate Prefecture on the same type of coast at the point located at 39,5337N, 142,0464E. The maximum inundation depth **38.56m** was measured at 38,4581N, 141,5175E, on a small island located off the coast of Miyagi Prefecture. The maximum inundation height on the Sendai plain was **19.5m**, and the mean inundation height near the shoreline here was estimated to be about 10m (Mori et al., 2011).

Run-up heights and inundation depths greater than **30m** were measured in 62 coastal points stretching along 200km of the Tohoku coastline between 38.2N and 40.2N. Run-up heights and inundation depths greater than **20m** were measured in 394 coastal points stretching along 290km of the coastline between 37.7N and 40.2N. Run-up heights greater than **10m** were measured in nearly 1848 points stretching along 430km of the coastline between 36.9N and 40.8N.

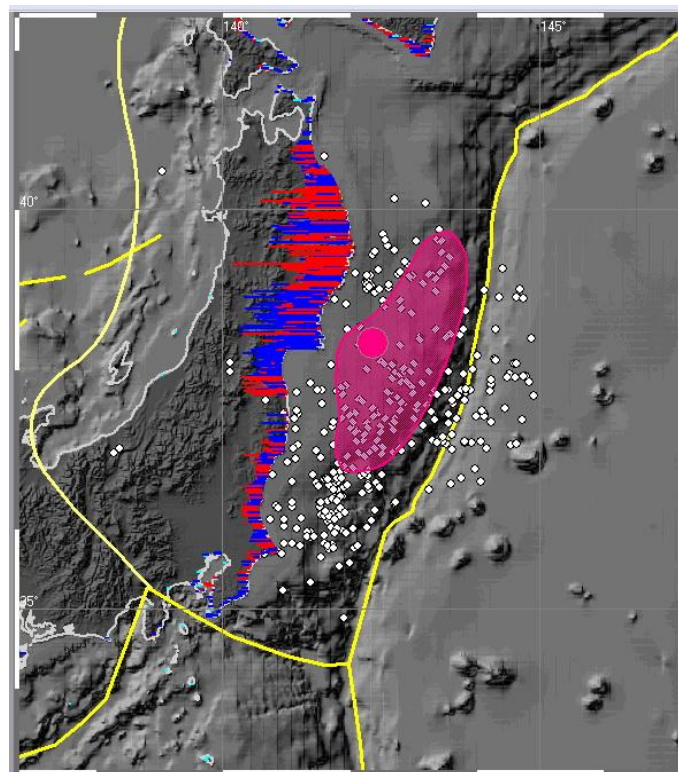


Fig. 2.5.1. Distribution of the measured run-up heights (red lines) and inundation depths (blue lines) along with estimated position of tsunami source (solid red area) and first-day aftershocks (solid white dots) for the 2011 Tohoku earthquake. Yellow lines show the main plate boundaries in the region. Aftershock data are from the JMA historical earthquake catalog, visualization is made in the PDM/TSU graphic shell. Position of the main shock is shown by the large red circle.

2.5.2. Adopted source model and calculation of initial bottom displacement

Based on consideration of the above data, the following source was adopted as a model for the 2011 Tohoku earthquake: coordinates of the center of the lower edge of the fault: $Lat = 38.9^\circ N$, $Lon = 141.7^\circ E$, magnitude: $M_w = 9.0$, depth of the upper edge of the fault: $h_0 = 20 \text{ km}$, fault size: $L = 300 \text{ km}$, $W = 150 \text{ km}$, displacement: $D_0 = 25 \text{ m}$, dip-angle: $\delta = 10^\circ$, slip-angle: $\lambda = 88^\circ$, strike-angle: $\theta = 20^\circ$.

Calculated bottom displacement for this model source is shown in Fig. 2.4.16.

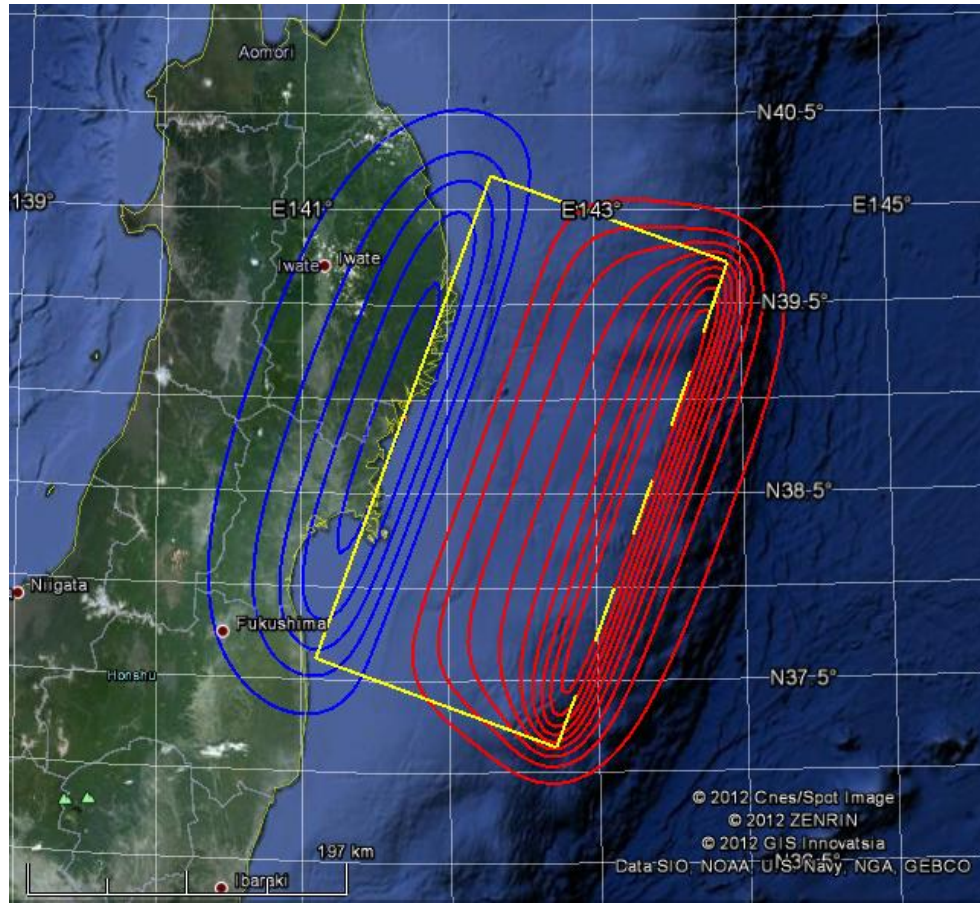


Fig. 2.5.2. Calculated bottom displacements for the adopted model of the 2011 Tohoku earthquake overlaid on the Google Earth map. Red color shows uplifted areas, blue color -subsided areas.

2.5.3. Calculation domain and virtual coastal points

Modeling of tsunami generation and propagation was carried out in the rectangular computational grid with dimension 3193×2761 and spatial step 15 angular seconds in both directions covering the area within $33^\circ 00' N - 44^\circ 30' N$, $135^\circ 42' E - 149^\circ 00' E$. The minimum water depth h_{\min} in the area was adopted to be equal 30 m. Tsunami heights were calculated at 5530 virtual mareograph points distributed along the part of Japan eastern coastline (Fig. 2.5.3).

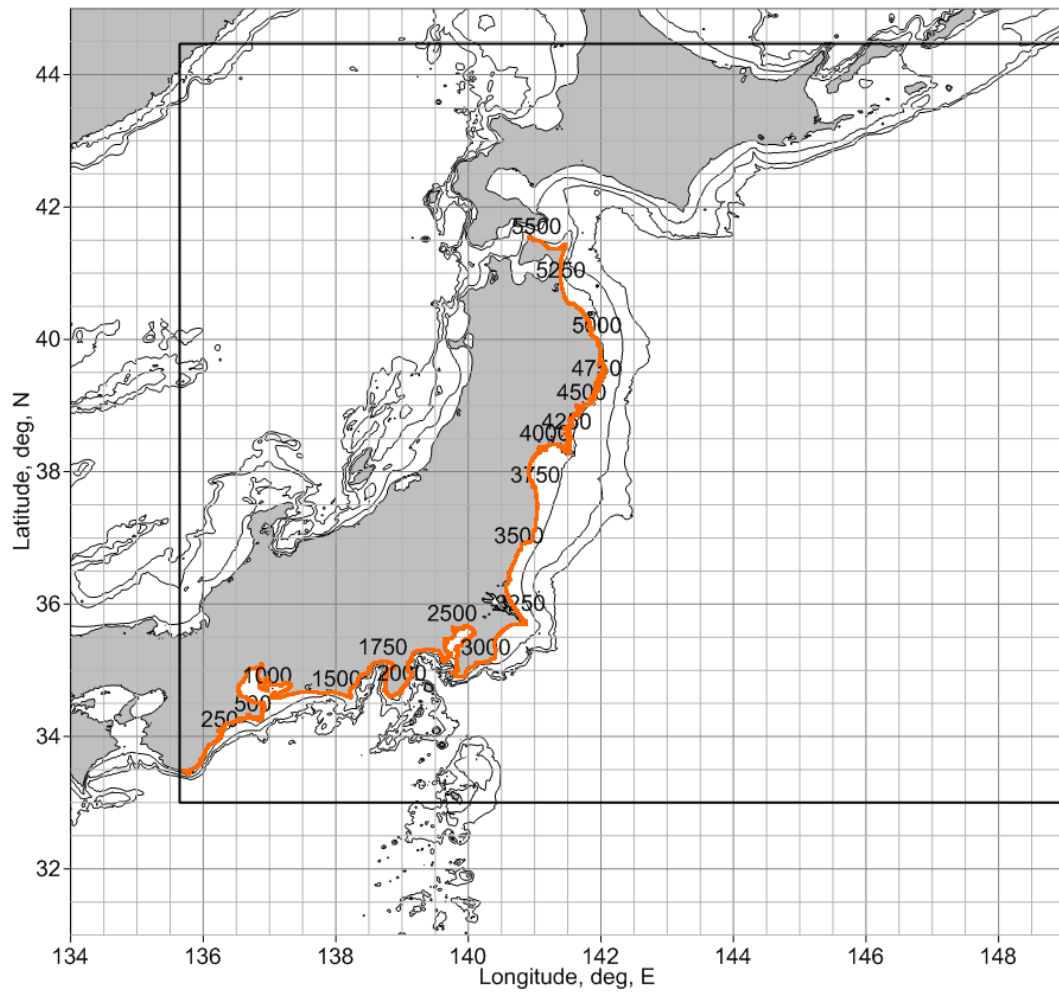


Fig. 2.5.3. The computational domain (plotted as solid black rectangle) with 100m, 500m and 1000m depth isobaths adopted for the 2011 Tohoku tsunami modeling. Spatial distribution of 5530 coastal virtual gauges is shown as orange numbered dots.

2.5.4. Analysis of computed wave height distribution

Numerical modeling of tsunami propagation was made for 4 hours of physical time using MGC package (Shokin et al., 2008) for tsunami modeling that is based on the non-linear shallow water system written in spherical coordinates. Results of computation are shown in Fig. 2.5.4 – Fig. 2.5.6.

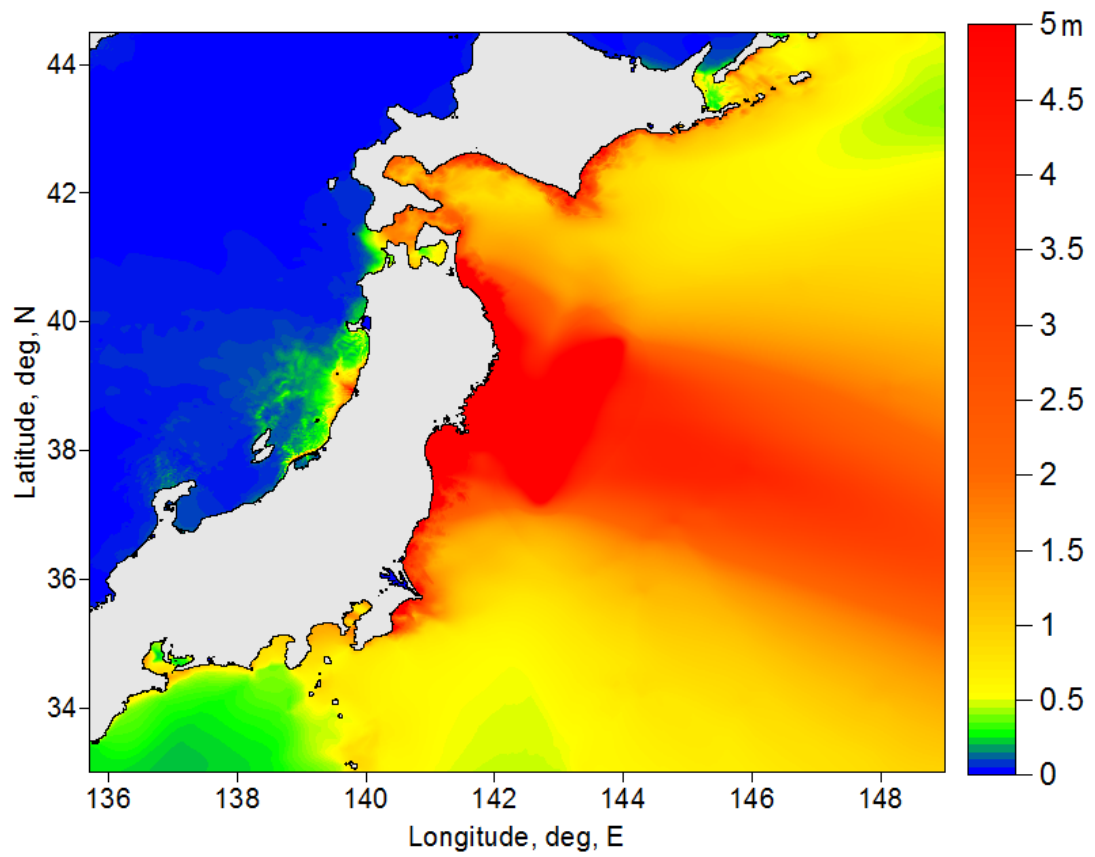


Fig. 2.5.4. Energy flux for the modeled 2011 Tohoku tsunami.

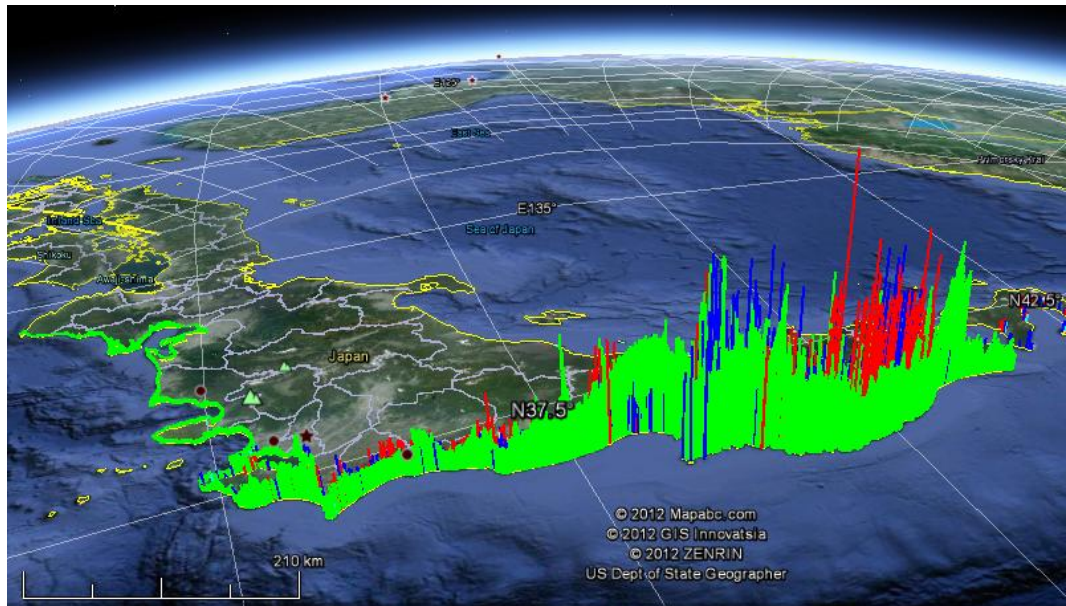


Fig. 2.5.5. Distribution of observed run-ups heights (red) and inundation depths (blue) of the 2011 Tohoku tsunami and computed maximum tsunami wave heights (green) calculated at the vertical wall put at the depth of 30 m for 5530 virtual coastal points.

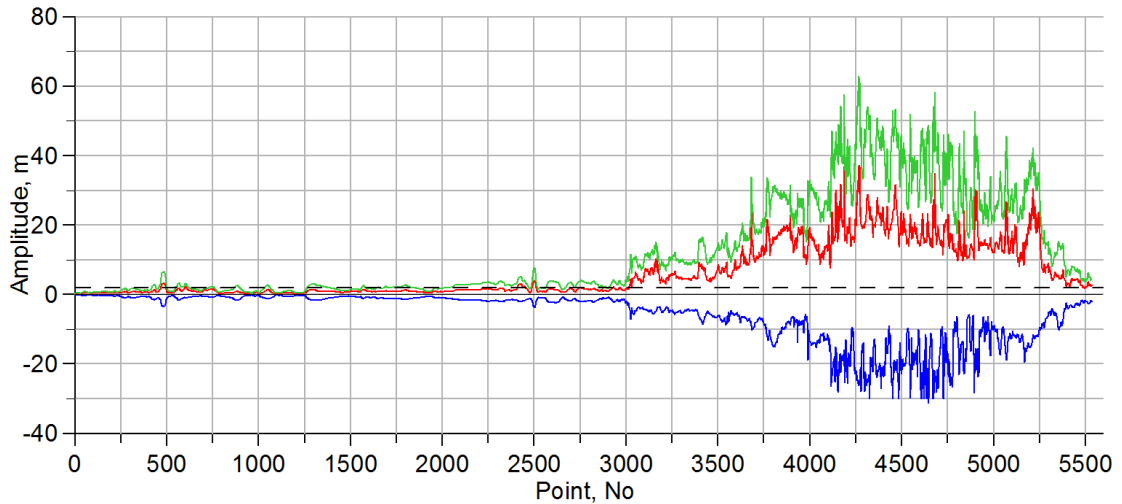


Fig. 2.5.6. Distribution of computed maximum positive (red line) and maximum negative (blue line) amplitudes along with maximum wave heights (green line) over 5530 coastal virtual gauges. Spatial location of these gauges is shown in Fig. 2.5.3.

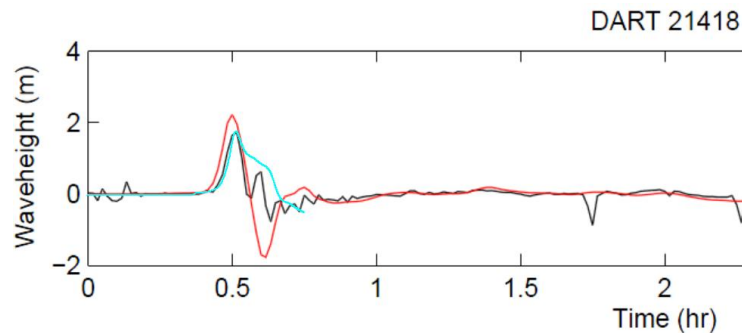


Fig. 2.5.7. Comparison of free surface mareograms, calculated in the framework of the project (blue line), calculated by Grilli et.al. (2012) (red line) and registered by the DART 21418 (black line). DART 21418 is a deep water bottom tsunami recorder located at 38.711 N 148.694 E.

2.5.5. 1D calculation of tsunami run-up and estimation of inundation limits

For test calculation of run-up heights for the 2011 Tohoku tsunami, a parts of coastal plain south of Iwaki town located near the very southern edge of the Ibaraki Prefecture was selected where 14 profiles for 1D calculation of tsunami run-up were built (Fig. 2.5.8). Position of these profiles relatively to the adopted tsunami source is shown in Fig. 2.5.9. Starting points of all profiles was at the depth 100m. These 14 profiles were divided into two groups – southern group (profiles 1-1 to 1-7) and northern group (profiles 2-1 to 2-7).

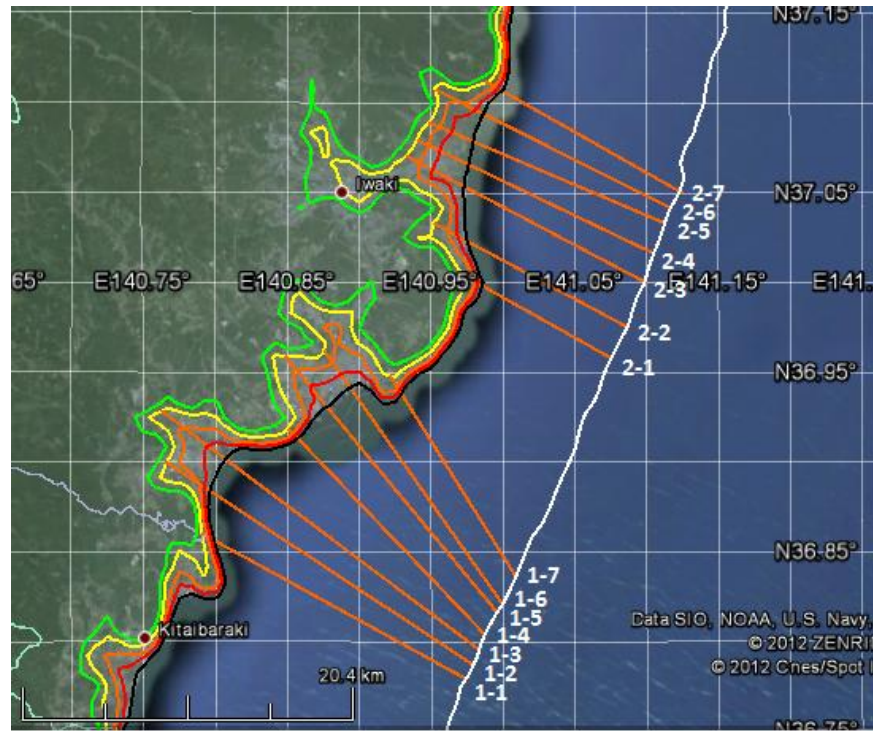


Fig. 2.5.8. Position of 14 numbered (white color text) profiles, selected for one-dimensional calculations of run-up heights for the 2011 Tohoku tsunami. Solid black line represents the coastline. Isolines of land relief overlaid on the Google Earth map are for levels of 5 m (red), 10 m (orange), 20 m (yellow), 30 m (green). The white line shows the 100m depth contour.

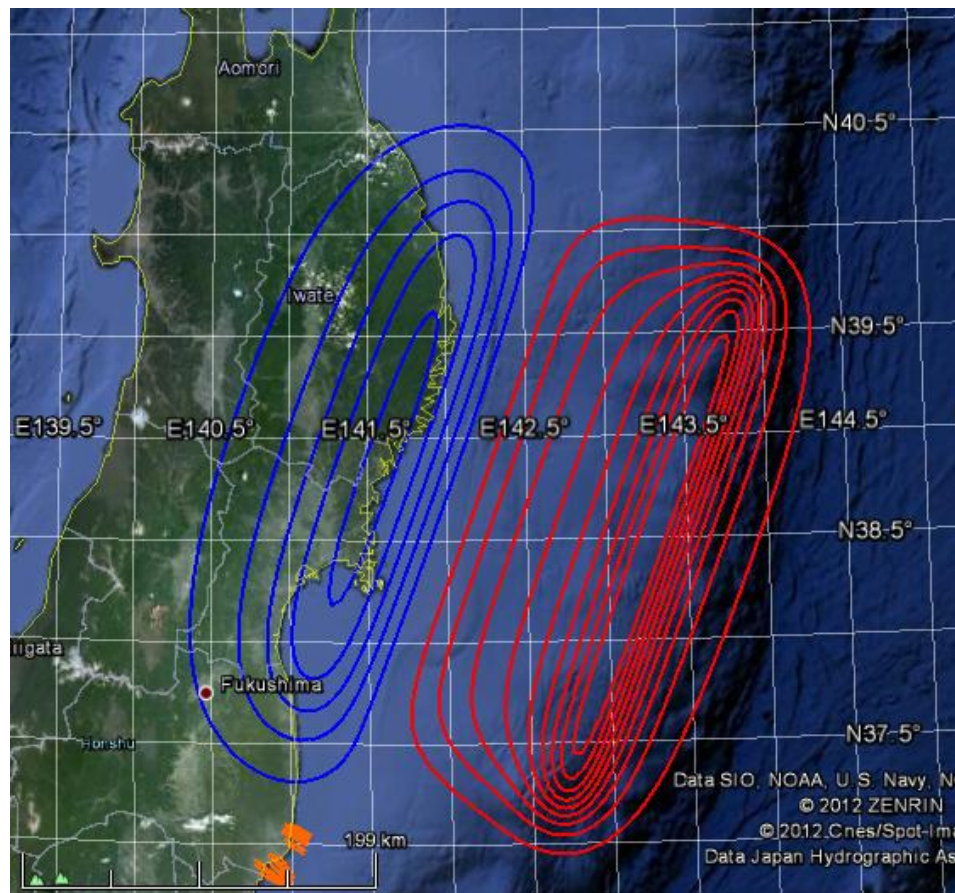


Fig. 2.5.9. Location of coastal profiles (orange lines) selected for 1D run-up modeling relatively source area of the 2011 Tohoku tsunami. Calculated co-seismic displacements for the adopted earthquake source model are shown as isolines of vertical displacement (red color shows uplifted areas, blue color – subsided areas).

Table 2.5.1. Land and bottom relief along the profiles selected for 1D modeling of run-up of the 2011 Tohoku tsunami.

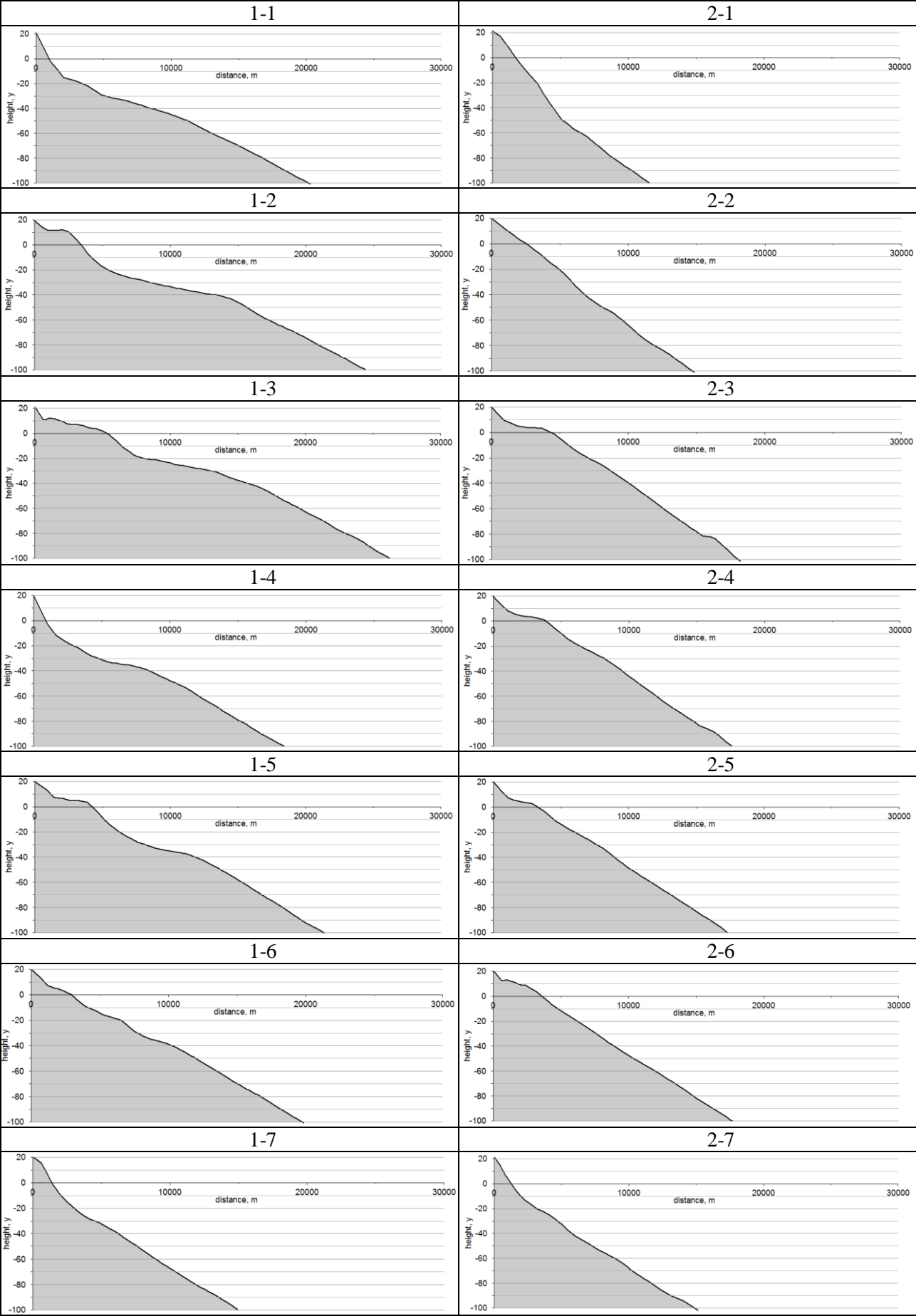


Table 2.5.2. Characteristics of 2011 Tohoku tsunami runup, calculated in the 1D simulation along the selected cross-sections.

Index number of cross-section	Calculated runup height (m)	Calculated runup distance (m)	Initial longitude of shoreline point (grad)	Initial latitude of shoreline point (grad)	Calculated longitude of runup point (grad)	Calculated latitude of runup point (grad)
1-1	8.54	401.8	140.7988	36.8565	140.7952	36.8581
1-2	9.24	813.9	140.7960	36.8839	140.7889	36.8877
1-3	12.29	4221.0	140.8065	36.9018	140.7708	36.9232
1-4	8.35	377.4	140.8572	36.9133	140.8544	36.9156
1-5	12.26	3273.4	140.8774	36.9309	140.8547	36.9528
1-6	12.64	2200.8	140.8937	36.9416	140.8798	36.9573
1-7	8.06	411.2	140.9295	36.9381	140.9271	36.9411
2-1	7.98	490.5	140.9856	36.9984	140.9812	37.0004
2-2	10.91	1488.9	140.9752	37.0232	140.9616	37.0290
2-3	14.07	3837.0	140.9728	37.0537	140.9375	37.0686
2-4	14.70	3439.0	140.9760	37.0659	140.9439	37.0782
2-5	14.60	2870.1	140.9792	37.0787	140.9519	37.0880
2-6	11.49	2157.4	140.9863	37.0940	140.9662	37.1021
2-7	9.39	562.6	140.9994	37.1069	140.9943	37.1092

Table 2.5.3. A comparison of the characteristics of the 2011 Tohoku tsunami, calculated in the 2D simulation as “wet line” on the vertical wall (maximum positive wave amplitude), as run-up height obtained in 1D simulation along the selected profiles and as run-up height calculated by analytical formulas proposed in (Synolakis, 1987) and (Pelinovsky, Mazova, 1992). Red color marks values obtained outside of applicability of analytical formulas.

Index number of cross-section	Maximum positive amplitude on the wall, calculated in the 2D numerical simulation (“wet line”) (m)	Runup heights, calculated in the 1D simulation (m)	Runup height, calculated by analytical formula of Synolakis, 1987 (m)	Runup height, calculated by analytical formula of Pelinovsky, Mazova, 1992 (m)	Observed data (m)
1-1	5.93703	8.536861	34.45078	4.777752	5.62; 8.17
1-2	7.6729	9.240146	37.08319	6.570623	1.8; 2.08
1-3	7.72631	12.28845	36.53053	8.02784	3.35; 7.91; 8.87; 9.21
1-4	5.59981	8.349215	33.01702	8.409104	15.24; 9.38; 7.2
1-5	6.04095	12.25797	34.58192	8.119349	3.52
1-6	5.96426	12.64331	34.15441	8.302718	2.96; 3.74; 7.32; 11.21
1-7	5.35289	8.057803	30.96296	7.920948	4.33; 6.83
2-1	4.79471	7.981722	28.15826	4.277762	6.1; 7.12; 9.74
2-2	6.14463	10.90656	31.18936	7.061848	2.65; 6.79; 9.4
2-3	7.32794	14.0727	34.42032	8.925278	2.32; 7.18
2-4	7.23259	14.69752	36.01336	8.528625	
2-5	7.24038	14.60281	34.00642	8.669588	
2-6	7.23041	11.48893	37.03243	8.553761	2.85; 10.07
2-7	6.42782	9.38998	37.22483	5.518716	
Average	6.47805	11.036713	34.20184	7.404565	6.43

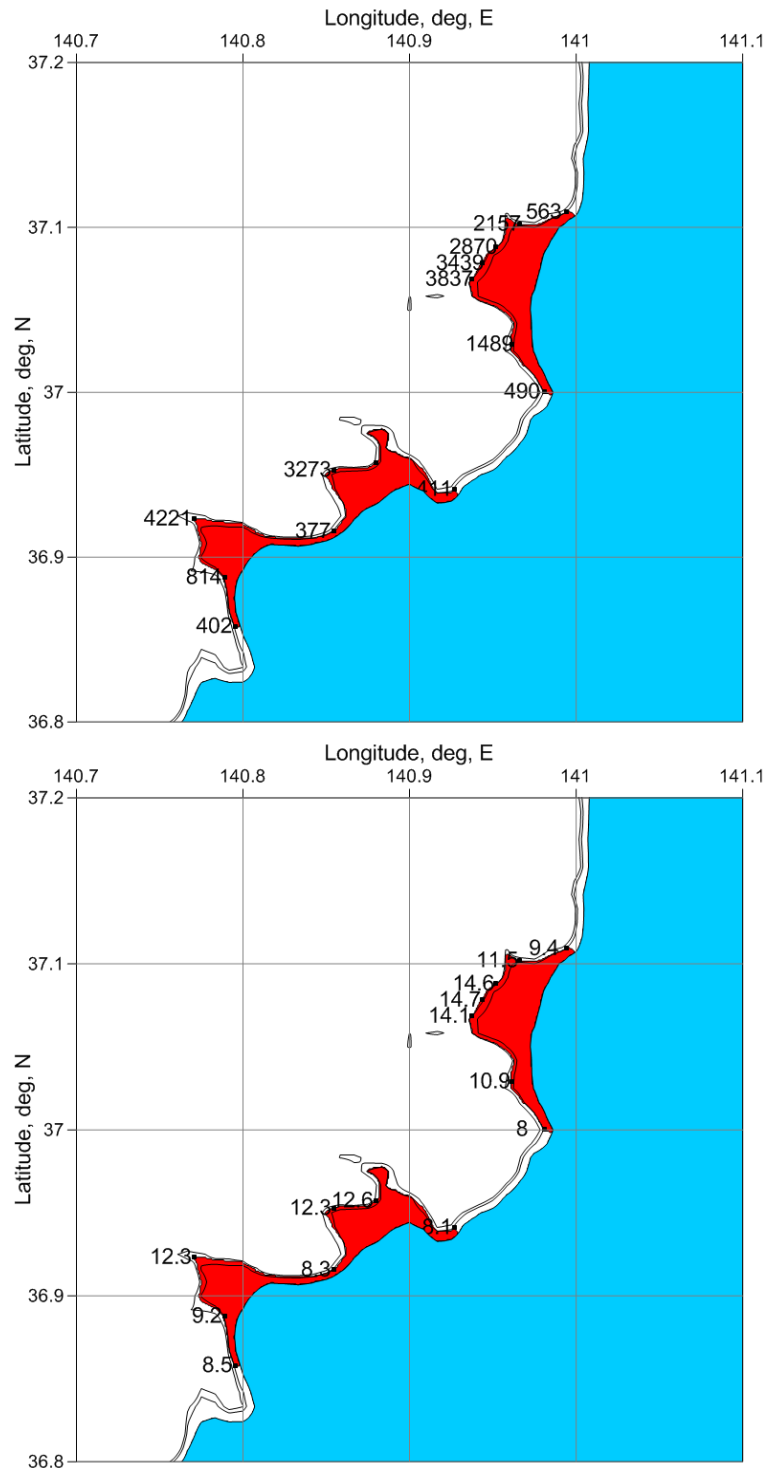


Fig. 2.5.10. The area of coastal flooding and run-up heights for the 2011 Tohoku tsunami, calculated in the 1D simulation; digits near black dots show (in m) inundation distance (upper figure) and run-up height (lower figure). 10 and 14 meter isolines of the relief are also shown.

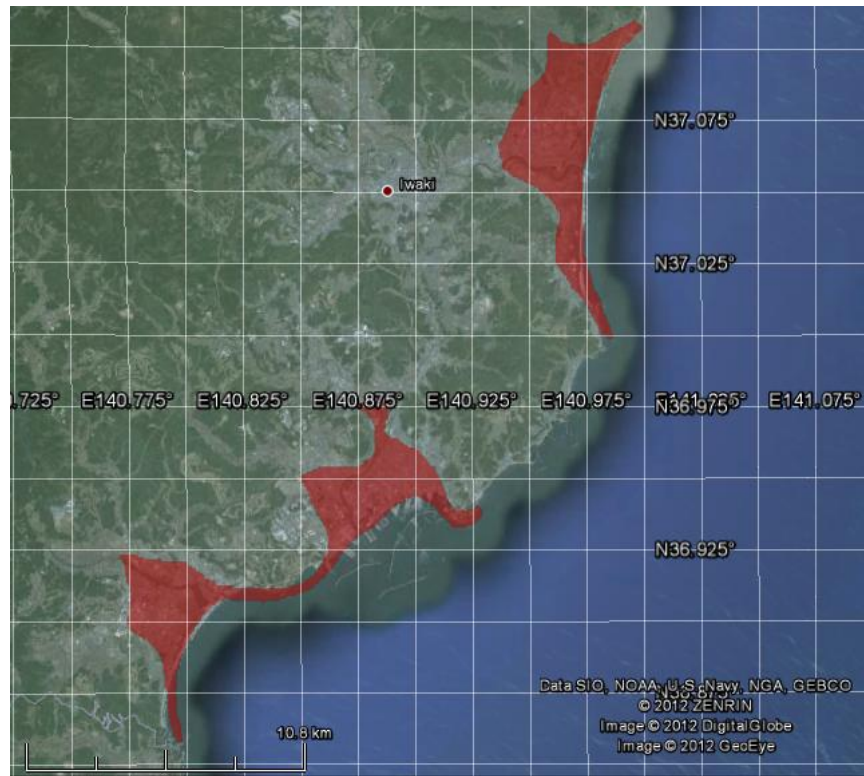


Fig. 2.5.11. Area of inundation near Iwaki calculated in 1D run-up modeling overlaid on the Google Earth map.

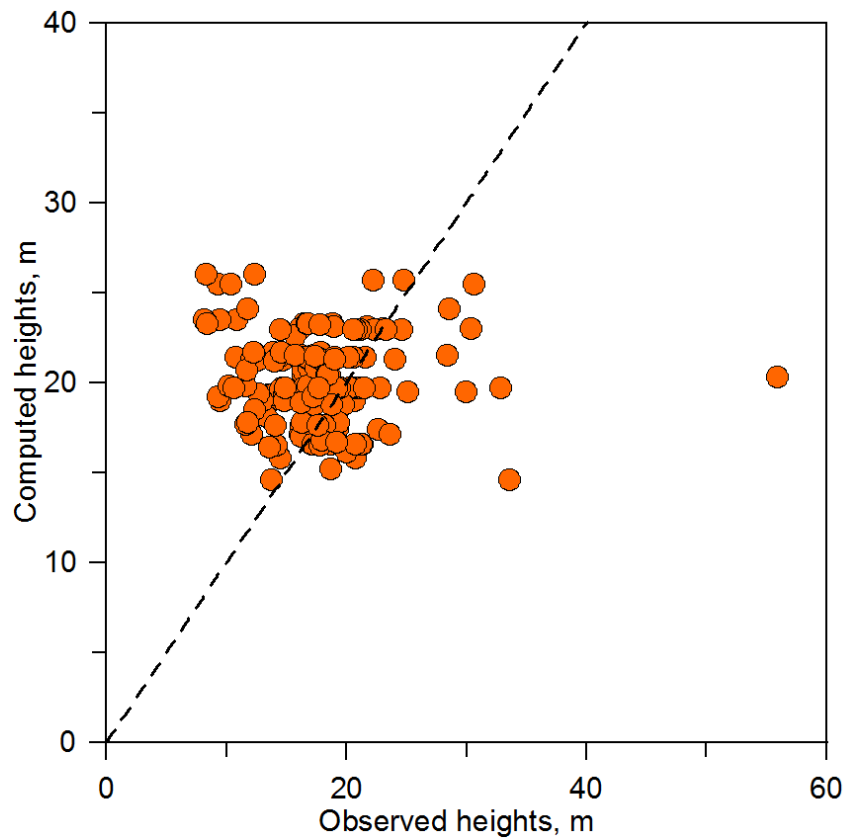


Fig. 2.5.12. Comparison of computed maximum wave heights versus measured run-up heights for the 2011 Tohoku tsunami. Observed data were selected from the part of the Miyagi Prefecture coast located between 39.0N and 39.4N.

2.5.6. 2D calculation of tsunami run-up and estimation of inundation limits

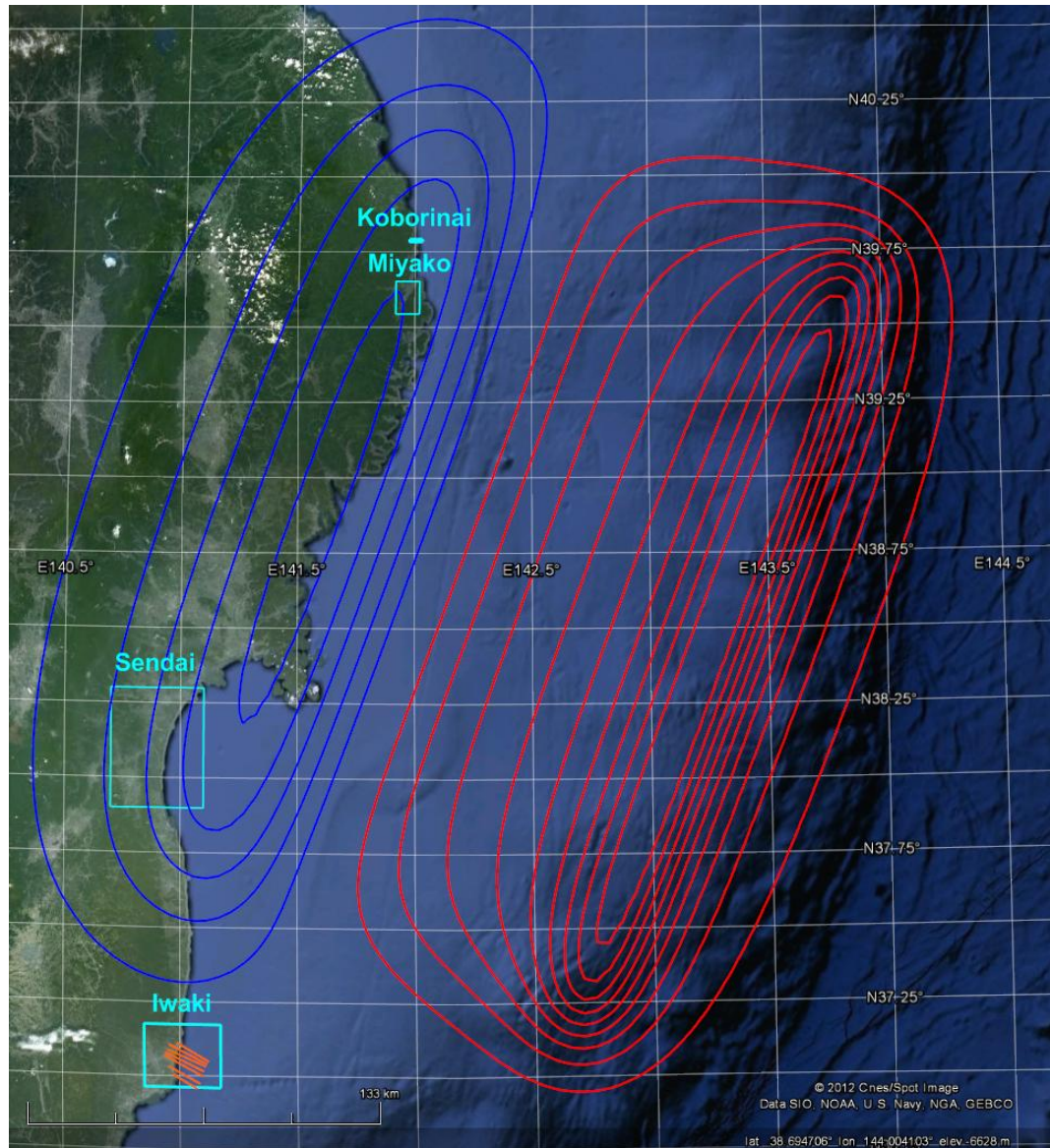


Fig. 2.5.13. Location of four coastal areas (from north to south – “Koborinai”, “Miyako”, “Sendai” and “Iwaki”, shown as light blue rectangles) selected for 2D modeling of run-up of the 2011 Tohoku tsunami. Position of the model source is shown as isolines of initial vertical bottom displacement (red – uplift, blue – subsidence). Orange lines show vertical cross-sections used for 1D modeling of run-up in the “Iwaki” area.

Coastal area “Koborinai”

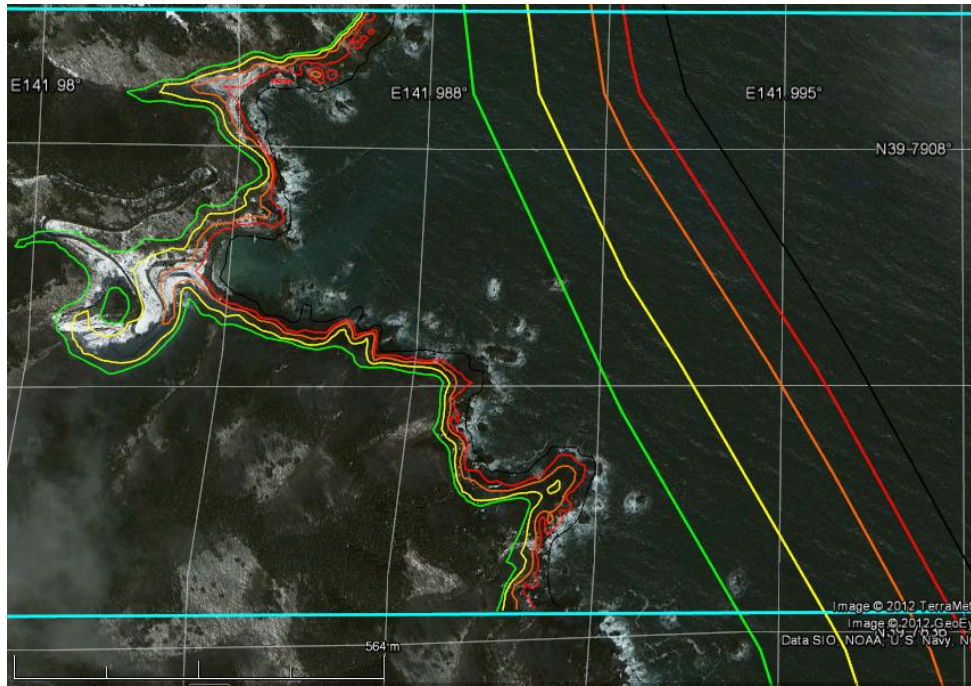


Fig. 2.5.14. Isolines of coastal relief (0m – black, 5 m – red, 10 m – orange, 20 m – yellow, 30 m – green) calculated on the basis of the “Koborinai” digital array having resolution 10 m along longitudinal direction and 12 m along latitudinal direction and overlaid on the Google map of the area. It is seen that isolines are reasonably fit to the actual topography of the site. For comparison, the same set of isolines calculated on the basis of GEBCO array with spatial resolution 30 arc seconds (approximately 900 m) is shown. This array, used for calculation of tsunami propagation from the source to the coastal area cannot reasonably reproduce the actual configuration of the coastline.

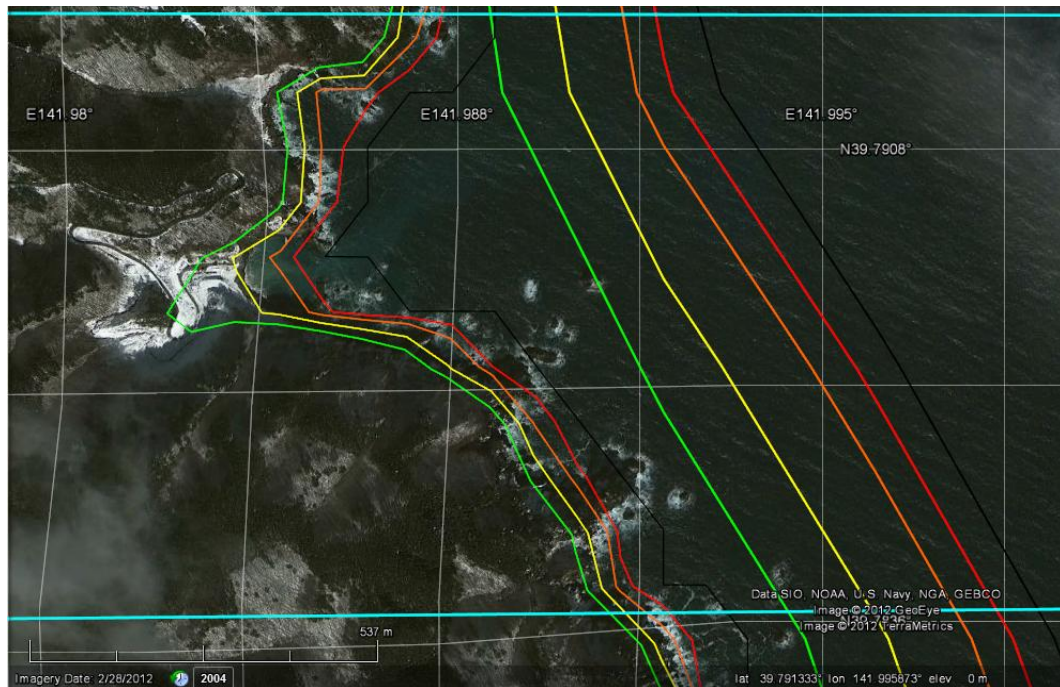


Fig. 2.5.15. Isolines of coastal relief (0m – black, 5 m – red, 10 m – orange, 20 m – yellow, 30 m – green) calculated on the basis of SRTM with 90-m resolution (source of the data: <http://srtm.csi.cgiar.org/>) overlaid on the Google map of the area. The 90-m DEM can represent basic morphological features of the coastal area, but fails in reproducing of actual configuration of small bays and harbors. For comparison, the same set of relief isolines, calculated on the basis of GEBCO30 array with spatial resolution is 30 arc seconds (approximately 900 m) is also shown.

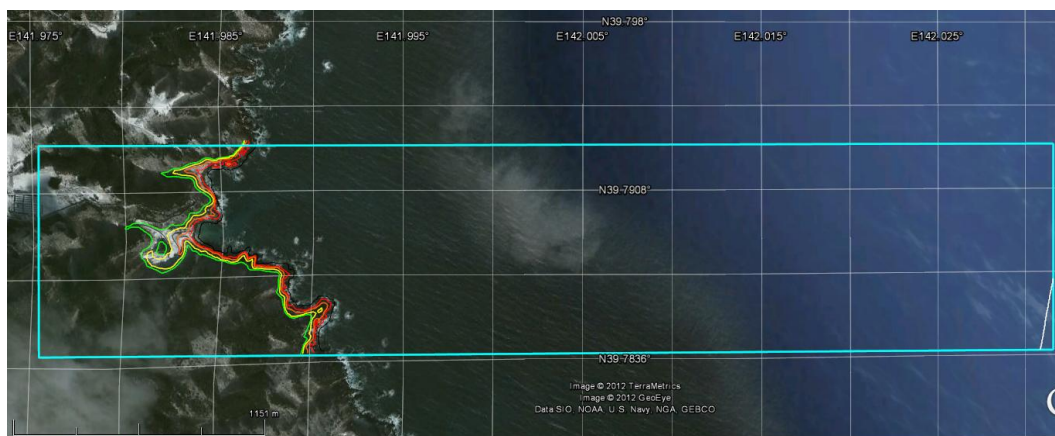


Fig. 2.5.16. Location of the “Koborinai” array (shown as blue rectangle) overlaid on the Google map. This array is used for 2D run-up modeling shown in Fig. 2.5.19 – Fig. 2.5.21. Isolines of coastal relief (0m – black, 5 m – red, 10 m – orange, 20 m – yellow, 30 m – green) calculated on the basis of this array are also shown.

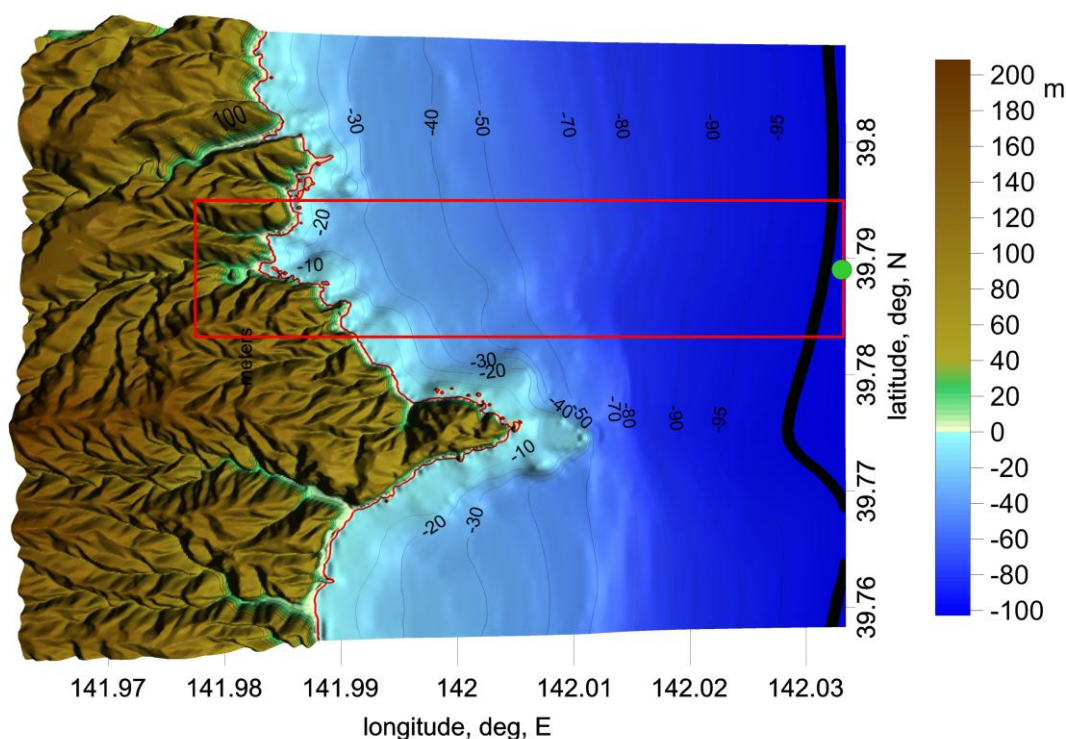


Fig. 2.5.17. Location of the “Koborinai” coastal area (shown as red rectangle) overlaid on the digital elevation and bathymetry model. Solid green circle marks the position of the virtual mareograph used for recording of the wave form used as input boundary condition for 2D run-up modeling within the “Koborinai” coastal area. Red isoline marks the coast line.

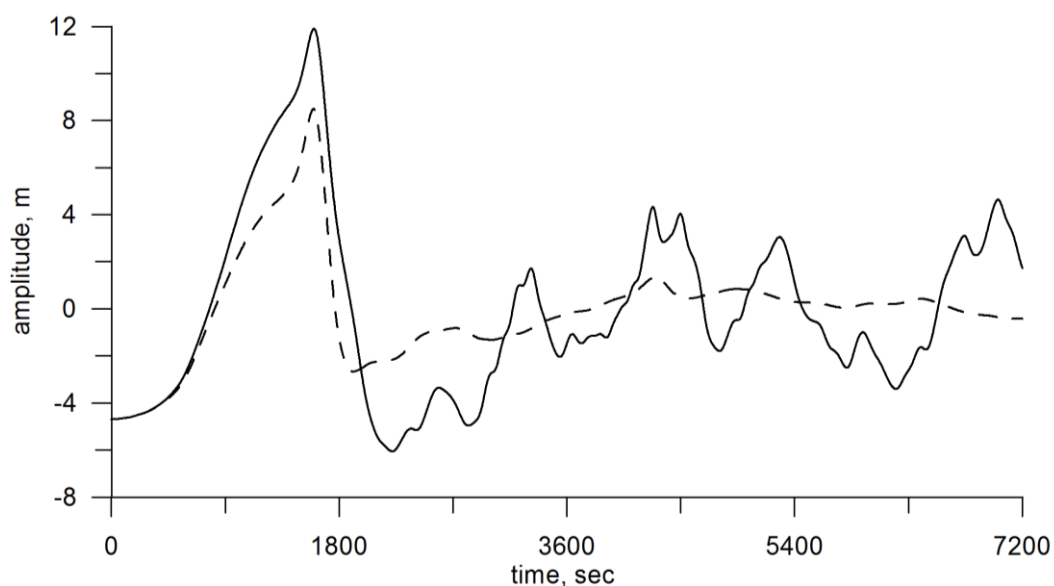


Fig. 2.5.18. Mareogram, calculated at the point shown as green circle in Fig. 2.5.17, that was used as input boundary condition for 2D run-up modeling of “Tohoku, 2011” tsunami within the “Koborinai” coastal area. Solid line shows the wave form calculated for the initial DEM/DBM (based on the original GEBCO-30sec), dotted line – the wave form obtained for corrected DEM/DBM where land and depths above $z = -h_{\min} = -30$ m were replaced by this value to suppress the reflected wave.

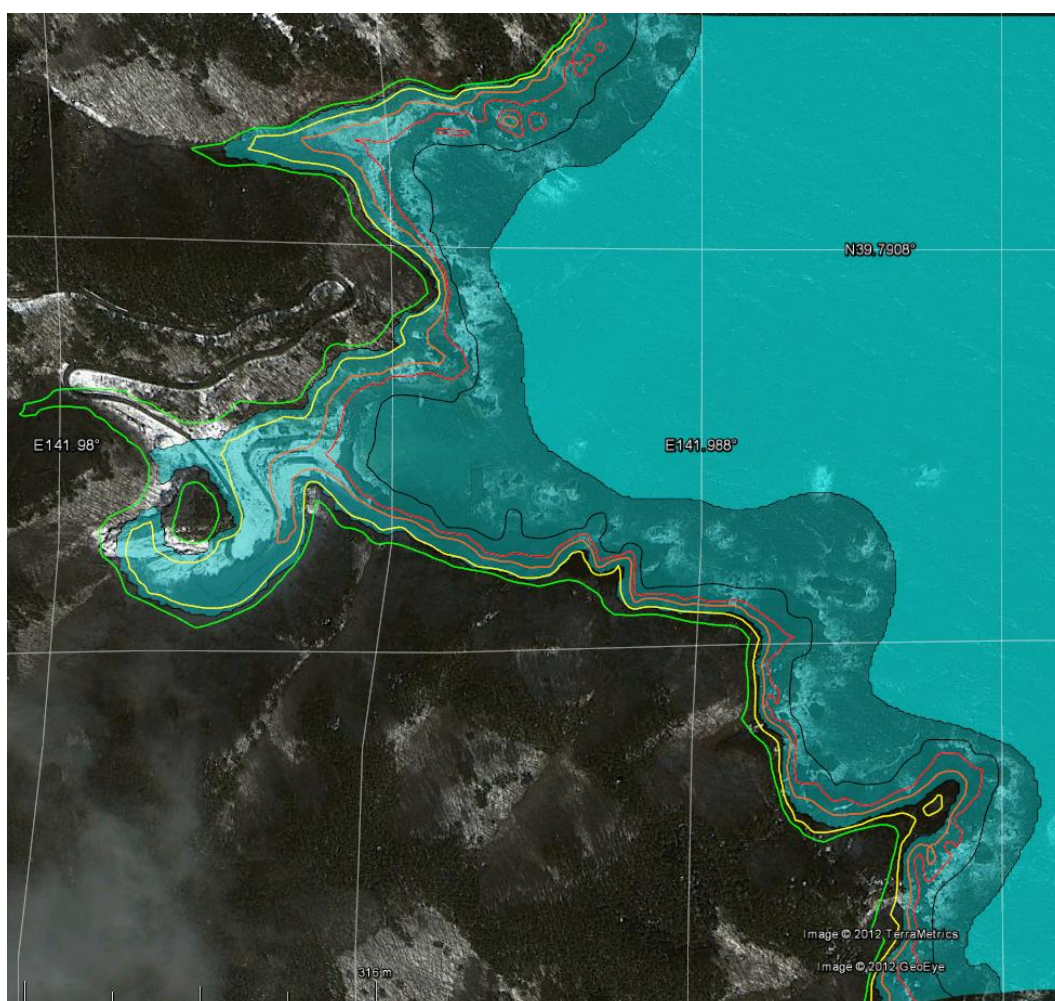


Fig. 2.5.19. Inundation limit of the 2011 Tohoku tsunami run-up calculated for the Koborinai Bay shown as solid blue area. Isolines of land relief are shown as black line (for 0 m level), red line (for 5 m level), orange line (for 10 m level), yellow line (for 20 m level) and green line (for 30 m level).

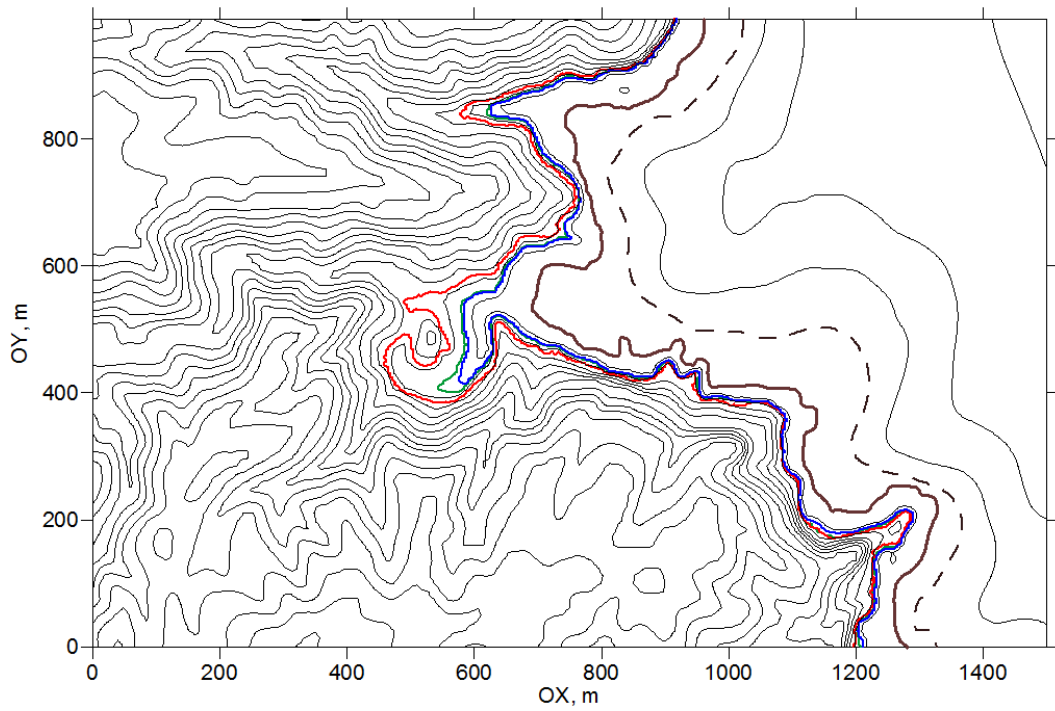


Fig. 2.5.20. Inundation limits of the 2011 Tohoku tsunami run-up within the Koborinai Bay calculated for three different values of Chezy coefficient: red – $n=0$ (basic), green – $n=0.001$, blue – $n=0.005$. Land relief is shown by black isolines drawn for each 10 m of elevation, brown line shows position of the coastline for undisturbed water (at $z=0$ m), dotted line shows the initial position of the coastline corresponding to the isobath -4.7 m. Calculation of run-up was made on the regular rectangular grid with steps $\Delta x = 3$ m, $\Delta y = 2$ m.

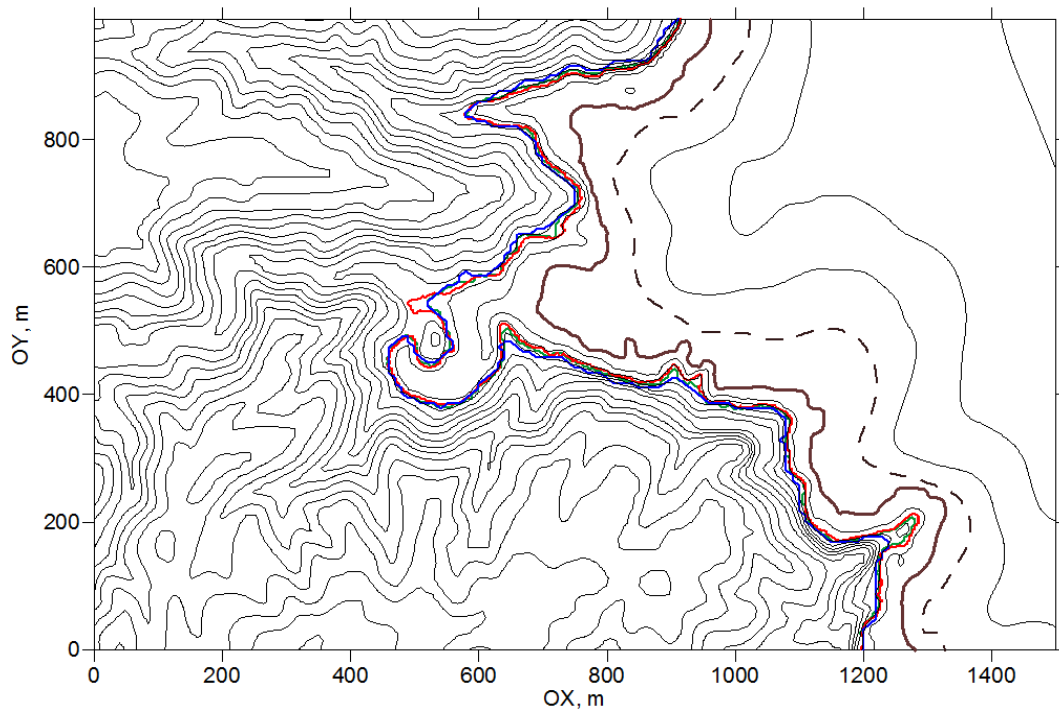


Fig. 2.5.21. Inundation limits of the 2011 Tohoku tsunami run-up within the Koborinai Bay calculated for different grid resolutions: red line – for $\Delta x = 3.0$ m, $\Delta y = 2.0$ m; green – $\Delta x = 5$ m, $\Delta y = 4$ m; blue – $\Delta x = 10$ m, $\Delta y = 8$ m. Land relief is shown by black isolines drawn for each 10 m of elevation, brown line shows position of the coastline for undisturbed water (at $z=0$ m), dotted line shows the initial position of the coastline corresponding to the isobaths -4.7 m. Calculation of run-up was made for Chezy coefficient $n=0$.

Coastal area “Miyako”

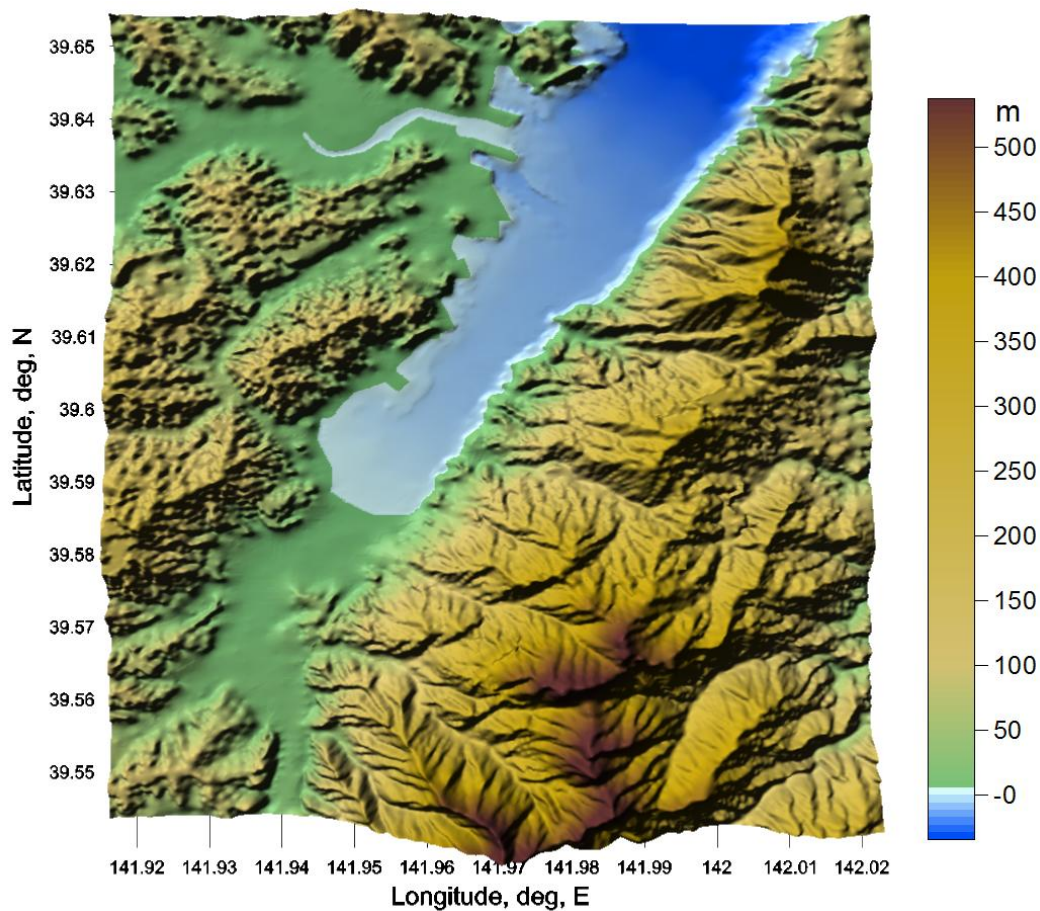


Fig. 2.5.22. Digital relief model of Miyako Bay and the adjacent coastal area, obtained by digitizing Japanese Bathymetric Chart № 6370-1, scale 1:50,000 (map source: JHA).

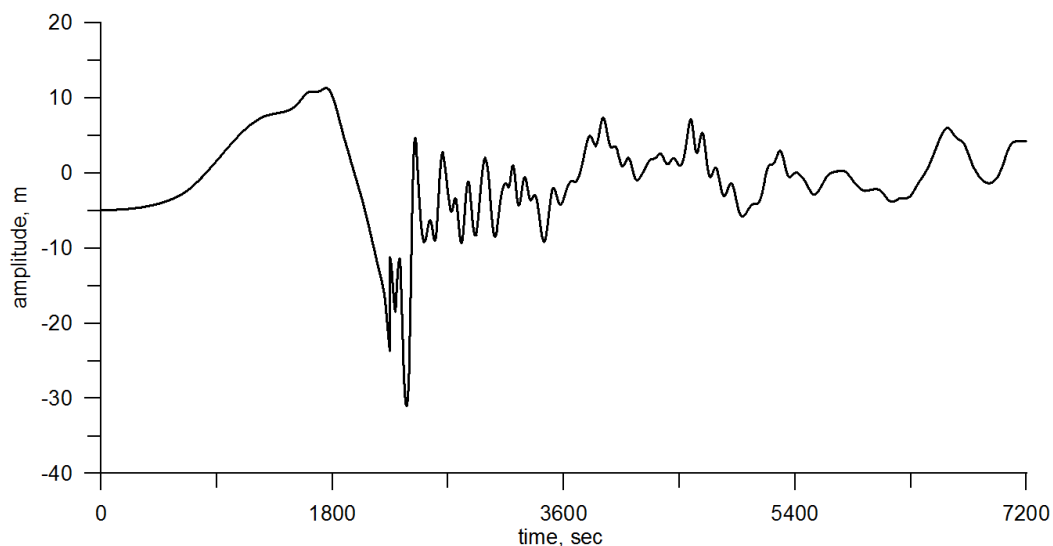


Fig. 2.5.23. Mareogram, calculated at the point of installation of virtual gauge (see Fig. 2.5.24) during modeling the propagation of the "Tohoku, 2011" tsunami, that was used as a boundary condition for the 2D modeling of run-up on the coast of Miyako Bay.

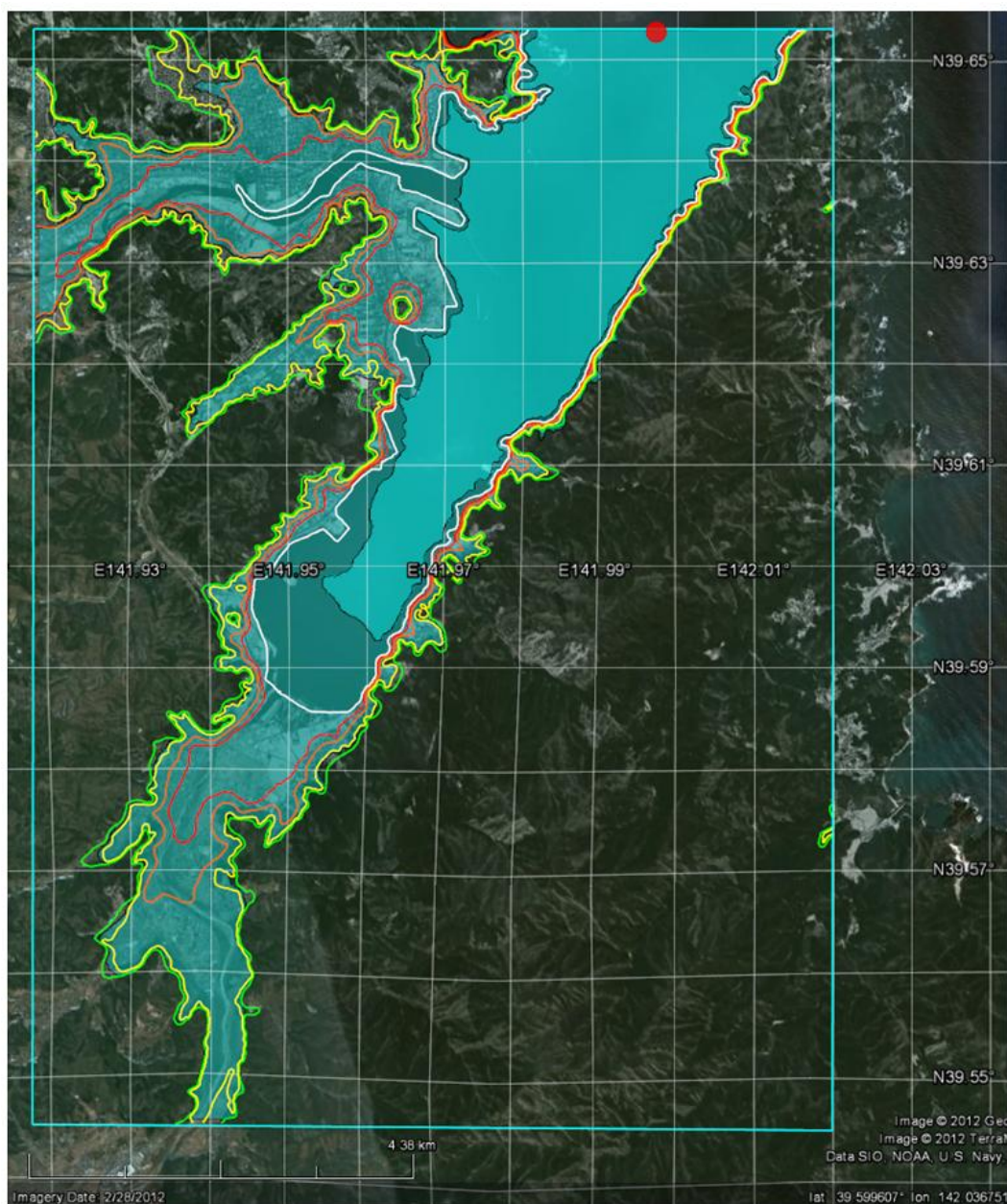


Fig. 2.5.24. Inundation zone (blue shading) from "Tohoku, 2011" tsunami, designed for coastal area «Miyako» (boundary is shown as blue rectangle) based on 2D modeling using data obtained by digitizing Japanese Bathymetric Chart № 6370-1 (JHA). Color lines show isolines of coastal relief: white line – position of the shoreline for undisturbed sea water (0 m), red – isoline 5 m, orange – 10 m, yellow – 20 m, green – 30 m; light blue solid area shows the initial level of the free surface at the level –4.9 m, resulted from co-seismic displacement caused by model earthquake source. Red circle marks the position of the virtual gauge, whose record (see Fig. 2.5.23) was used as the input boundary condition.

Coastal area “Sendai”

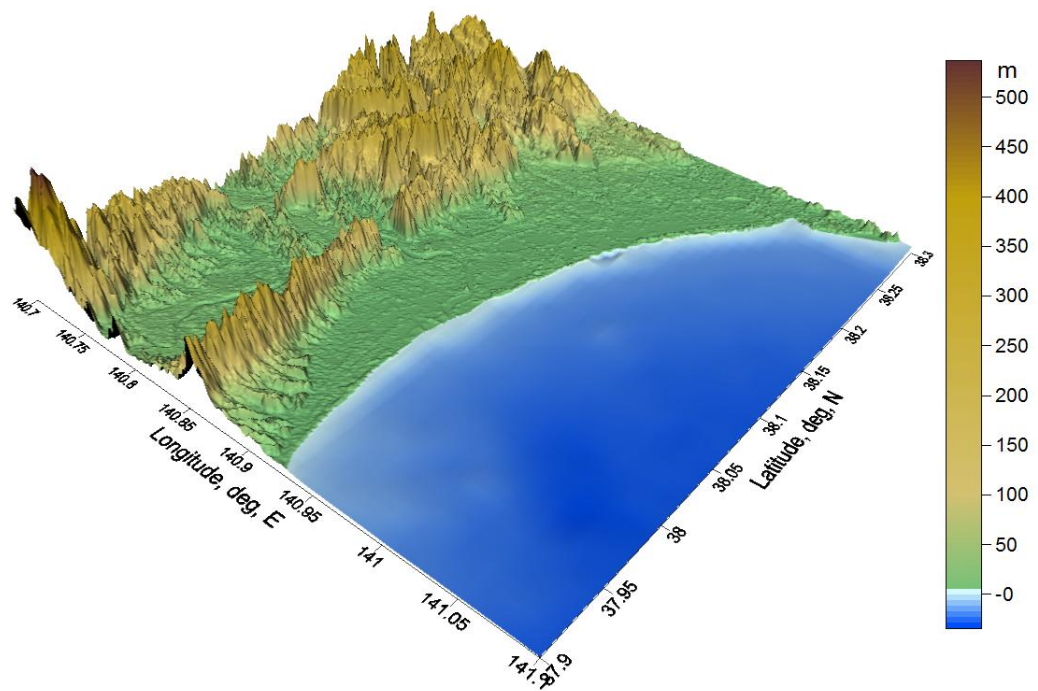


Fig. 2.5.25. Digital relief model of the coastal area “Sendai” from DEM SRTM-3sec (version 2.1) and DBM GEBCO-30sec.

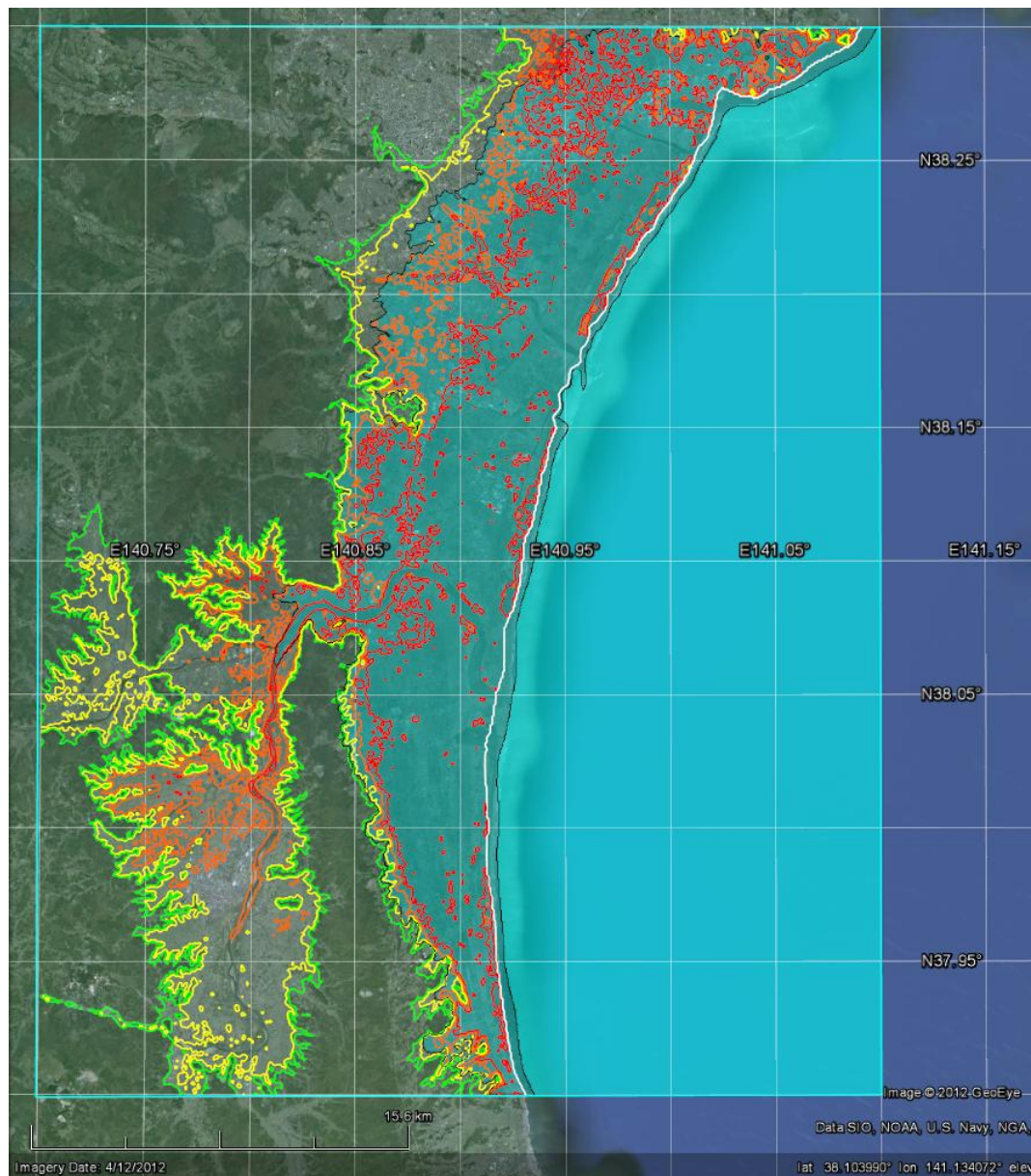


Fig. 2.5.26. Inundation zone (blue shading) from "Tohoku, 2011" tsunami, designed for coastal area "Sendai" (boundary is shown as blue rectangle) based on 2D modeling using digital relief from Fig. 2.5.25. Color lines show isolines of coastal relief: white line – position of the shoreline for undisturbed sea water (0 m), red – isoline 5 m, orange – 10 m, yellow – 20 m, green – 30 m; light blue solid area shows the initial level of the free, resulted from co-seismic displacement caused by model earthquake source. Incoming wave is introduced to the coastal area through the southern and eastern boundaries.

Coastal area “Iwaki”

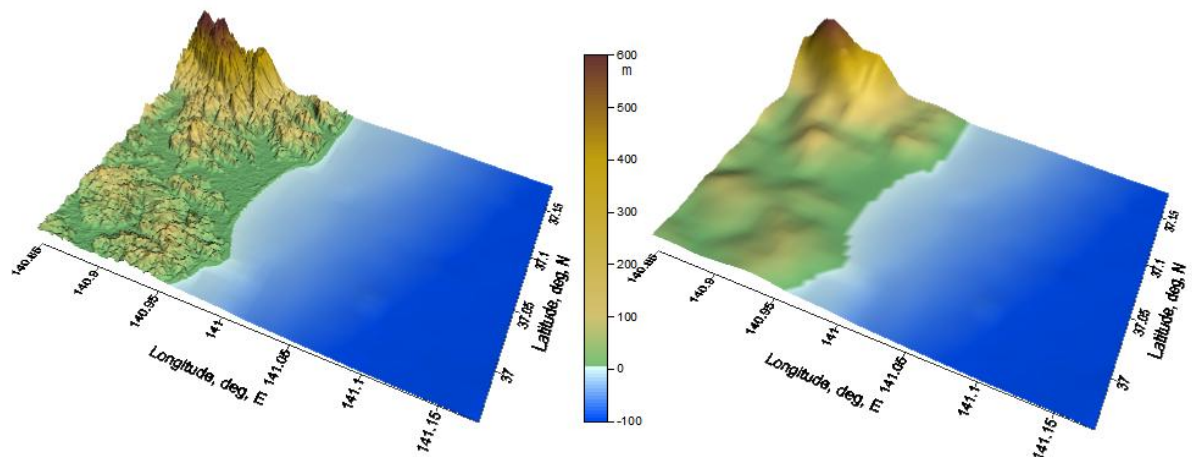


Fig. 2.5.27. Digital reliefs for coastal area “Iwaki” obtained from different DEM: left – SRTM-3sec (version 2.1), right – GEBCO-30sec.

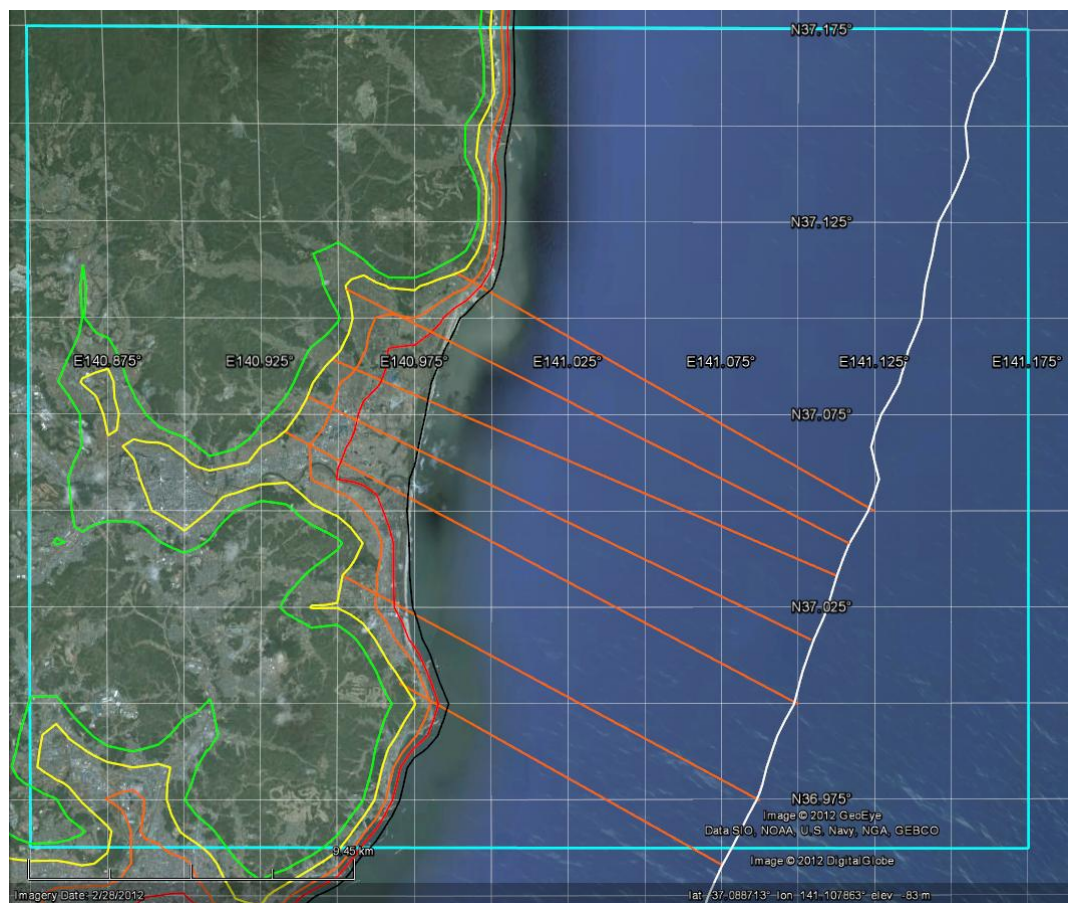


Fig. 2.5.28. Coastal area “Iwaki” (boundary is shown as blue rectangle) for 2D modeling of run-up by “Tohoku, 2011” tsunami. Color lines show isolines of relief from GEBCO-30sec: white line – isobath 100m, black – position of the shoreline for undisturbed sea water (0 m), red – isoline 5 m, orange – 10 m, yellow – 20 m, green – 30 m. Straight orange lines show vertical cross-sections used for 1D modeling of run-up on the first stage.

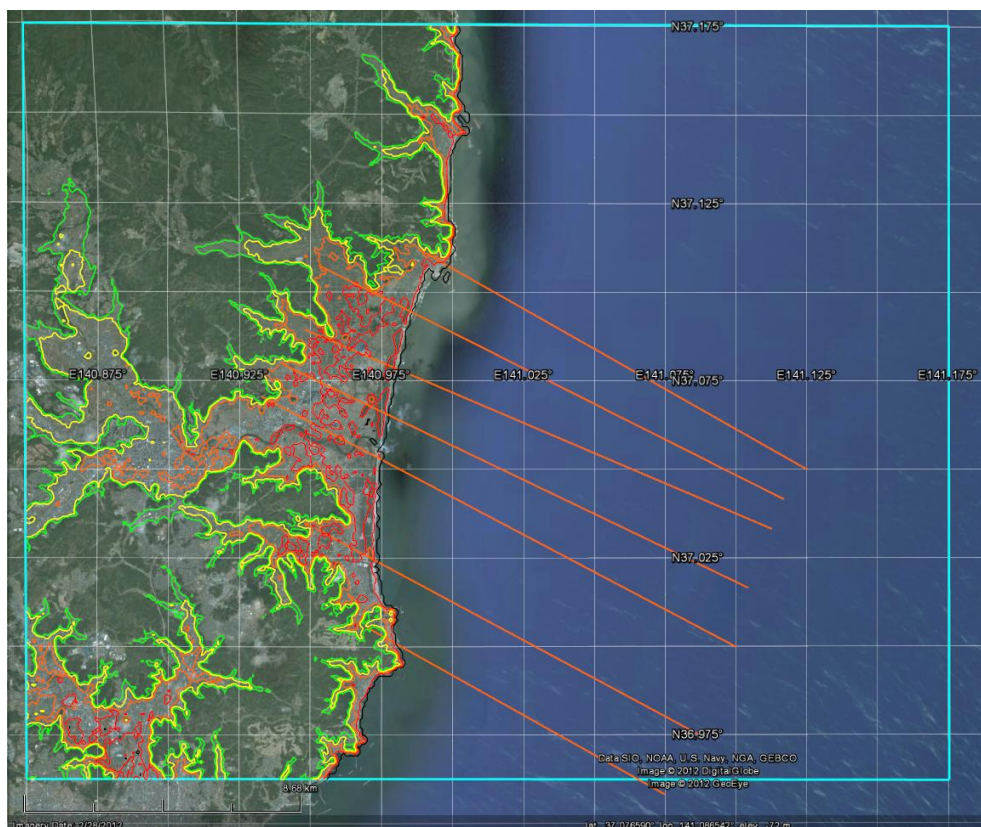


Fig. 2.5.29. Coastal area “Iwaki” (boundary is shown as blue rectangle) for 2D modeling of run-up by “Tohoku, 2011” tsunami. Color lines show isolines of coastal relief from DEM SRTM-3sec (version 2.1): black – position of the shoreline for undisturbed sea water (0 m), red – isoline 5 m, orange – 10 m, yellow – 20 m, green – 30 m. Orange straight lines show vertical cross-sections used for 1D modeling of run-up on the first stage.

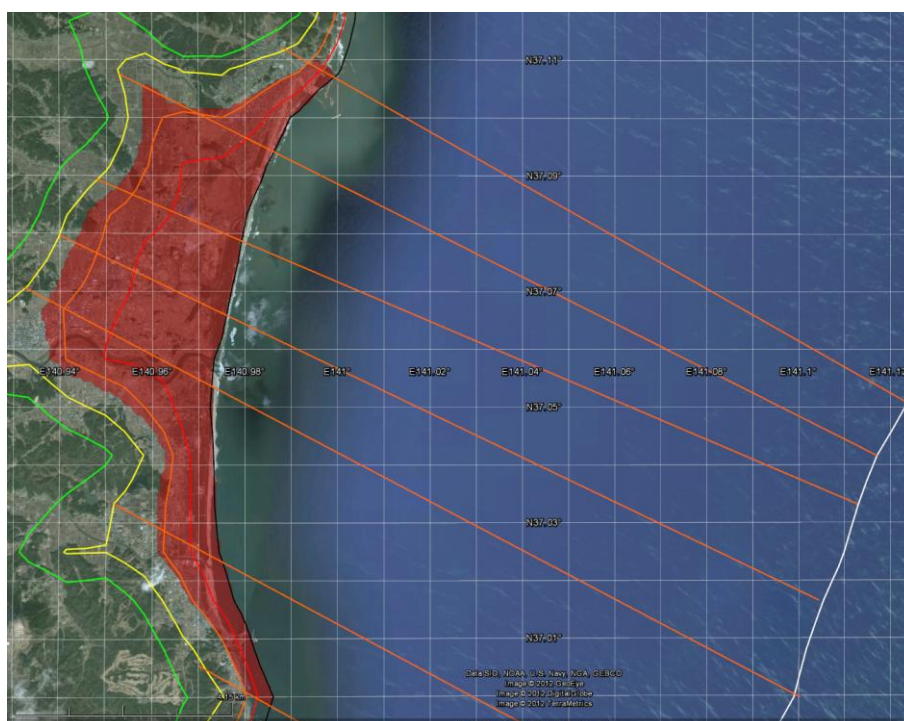


Fig. 2.5.30. Inundation zone (red shading) from “Tohoku, 2011” tsunami calculated for the coastal area “Iwaki” by 1D modeling using DEM/DBM GEBCO-30sec on the first stage. Color lines show relief isolines: white line – isobath 100m, black – position of the shoreline for undisturbed sea water (0 m), red – isoline 5 m, orange – 10 m, yellow – 20 m, green – 30 m. Straight orange lines show vertical cross-sections used for 1D run-up modeling.

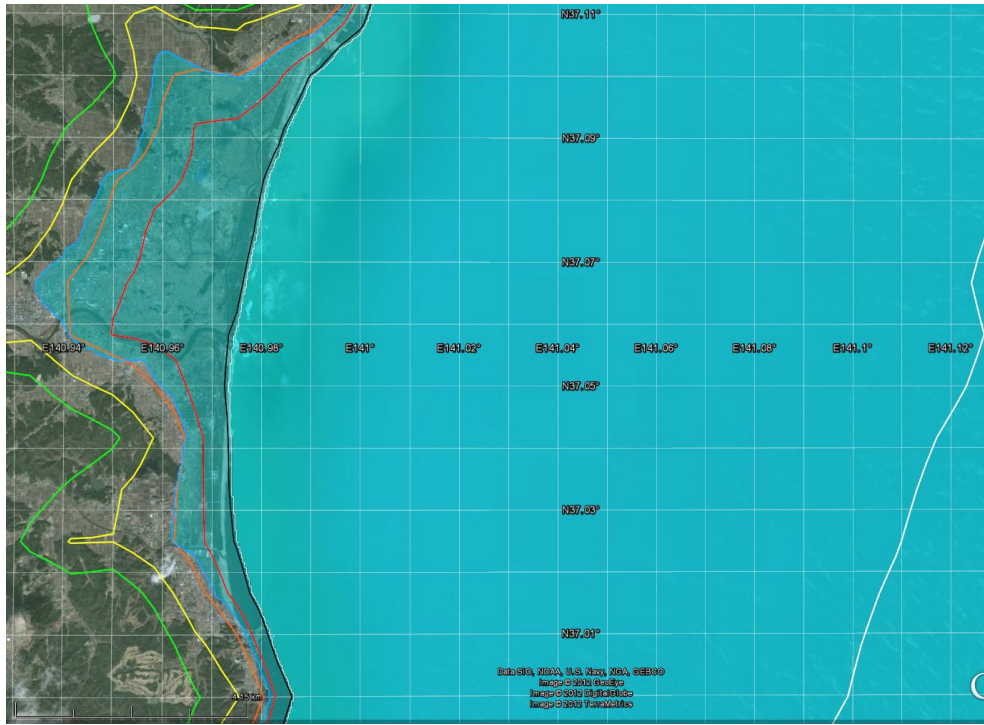


Fig. 2.5.31. Inundation zone (blue shading) from “Tohoku, 2011” tsunami calculated for the coastal area “Iwaki” by 2D modeling using DEM/DBM GEBCO-30sec. Color lines show relief isolines: white line – isobath 100m, black – position of the shoreline for undisturbed sea water (0 m), red – isoline 5 m, orange – 10 m, yellow – 20 m, green – 30 m. Incoming wave is introduced to the coastal area through the southern and eastern boundaries.



Fig. 2.5.32. Inundation zones from “Tohoku, 2011” tsunami calculated for the coastal area “Iwaki” by 2D modeling (blue shading) and 1D modeling (red shading) using DEM/DBM GEBCO-30sec. Color lines show relief isolines: white line – isobath 100m, black – position of the shoreline for undisturbed sea water (0 m), red – isoline 5 m, orange – 10 m, yellow – 20 m, green – 30 m. Straight orange lines show vertical cross-sections used for 1D run-up modeling.

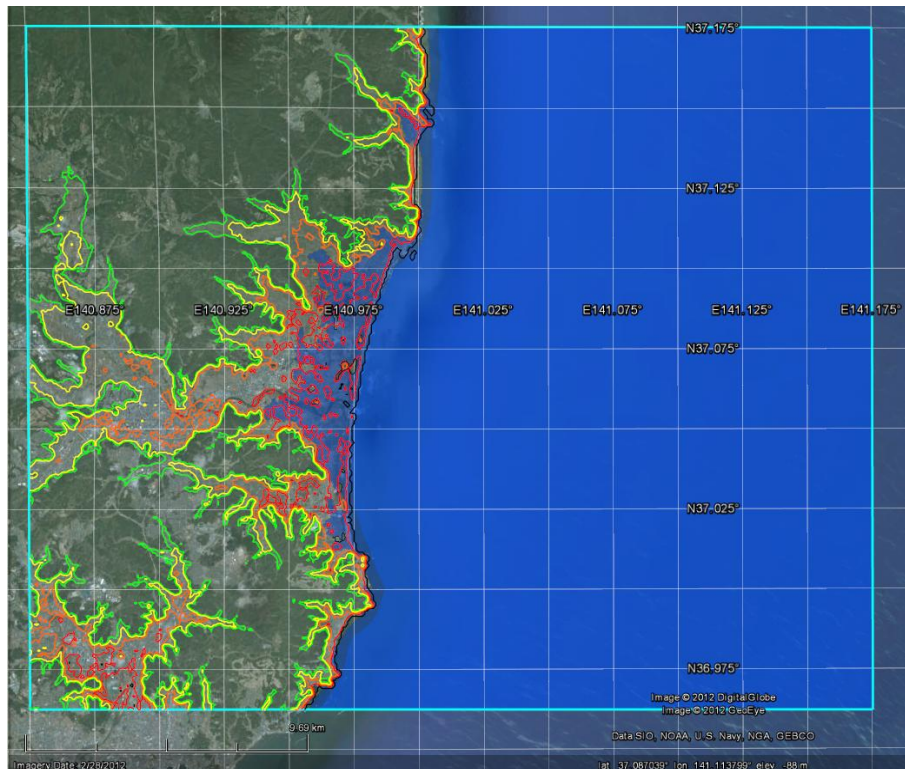


Fig. 2.5.33. Inundation zone (dark blue shading) from “Tohoku, 2011” tsunami calculated for the coastal area “Iwaki” by 2D modeling using DEM SRTM-3sec (version 2.1) and DBM GEBCO-30sec. Color lines show relief isolines: white line – isobath 100m, black – position of the shoreline for undisturbed sea water (0 m), red – isoline 5 m, orange – 10 m, yellow – 20 m, green – 30 m. Incoming wave is introduced to the coastal area through the southern and eastern boundaries.

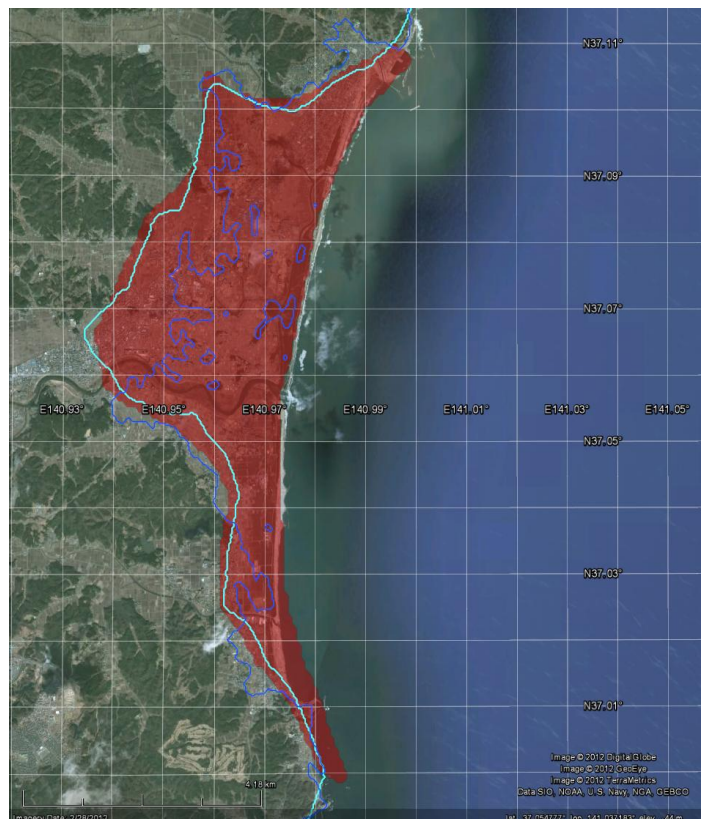


Fig. 2.5.34. Inundation zones from “Tohoku, 2011” tsunami for the coastal area “Iwaki”: calculated by 2D modeling using DEM/DBM GEBCO-30sec – blue line; 2D modeling using DEM SRTM-3sec (version 2.1) and DBM GEBCO-30sec – dark blue line; 1D modeling using DEM/DBM GEBCO-30sec – red shading.

3. Analysis of sensitivity of computed wave heights on the source and friction parameters (for the 2011 Tohoku tsunami)

3.1. Analysis of sensitivity of computed wave heights on the source parameters (for the 2011 Tohoku tsunami)

In order to evaluate the sensitivity of the computed wave heights at the coast on the source parameters, an extensive series of computations was made for the case of the 2011 Tohoku tsunami and for several hypothetical sources on the model bottom relief typical for subduction zones. The full analysis of results will be given in the final report, here we mainly concentrate on the case of the 2011 Tohoku tsunami. In these computations, we use reasonable variations of several basic source parameters around their adopted values and analyze the resulted variations of the computed wave heights along the Sanriku coast. These parameters include dip-angle δ and slip-angle λ of the fault plane, depth of the source h_0 , and its position (coordinates of epicenter, orientation) relatively the coastline. All calculations were made on 15-sec computational grid for 4 hours of physical time.

Fig. 3.1.1 shows distribution of 1521 coastal points along the Sanriku coast as well as position of the adopted model source of the 2011 Tohoku tsunami. Histograms of the maximum (positive and negative) wave heights along these points calculated at different source parameters are shown in Table 3.1.1 – Table 3.1.6.

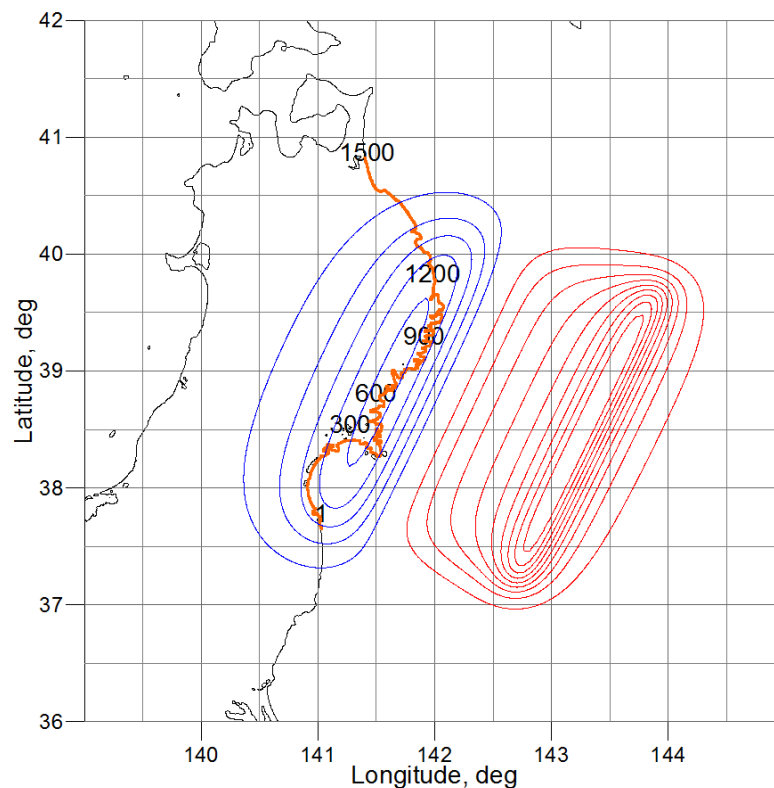


Fig. 3.1.1. Distribution of 1521 coastal points (shown as orange numbered dots) selected for sensitivity analysis and calculated bottom displacements for the adopted model of the 2011 Tohoku tsunami. Red color shows uplifted areas, blue color -subsided areas.

The structure of the Tables with wave height distribution is the follows. First column contains some general statistics related to the whole distribution: SA_{\max}^+ – the rounded (to the nearest integer) sum of maximum positive wave amplitudes over all the coastal points considered, A_{av}^+ – the average of maximum positive wave amplitudes over all the coastal points considered (both are shown in red font), SA_{\max}^- – the rounded (to the nearest integer) sum of maximum negative wave amplitudes over all the coastal points considered, A_{av}^- – the average of maximum negative wave amplitudes over all the coastal points considered (both are shown in blue font), SH_{\max} – the rounded (to the nearest integer) sum of maximum wave range at each point over all the coastal points considered, H_{av} – the average of maximum wave range over all the coastal points considered (both are shown in black font).

The second column contains several integral characteristics of the source area:

ΔV – change in the volume of the basin, calculated by the formula

$$\Delta V = \int_{\Omega_0} U_z(x, y) dx dy,$$

where $U_z(x, y)$ – calculated vertical displacement of the bottom in the source area, Ω_0 – source area;

V_0 – the total volume of bottom displacement in the source area

$$V_0 = \int_{\Omega_0} |U_z(x, y)| dx dy;$$

E_{tsu} – initial (static) tsunami energy, calculated by the formula (Kajiura, 1970)

$$E_{tsu} = \frac{1}{2} \rho g \int_{\Omega_0} U_z^2(x, y) dx dy;$$

and the resulted tsunami intensity I at the coast on the Soloviev-Imamura scale (Soloviev, 1972), calculated by the formula

$$I = \frac{1}{2} + \log_2(A_{av}^+).$$

The third column of the Tables shows the distribution (histograms) of maximum positive (red) and maximum negative (blue) wave amplitudes over the all coastal points along the Sanriku coast.

First, we consider the influence of the dip-angle δ on the resulted wave heights. For modern earthquakes, an accuracy of dip-angle determination, based on the broad-band digital seismograms and CMT (Centroid Moment Tensor) inversion is within $\pm 5^\circ$, however, for old historical earthquakes it can be within $\pm 10^\circ$ or even $\pm 20^\circ$, since this parameter is retrieved mainly from seismotectonic consideration.

Fig. 3.1.2. On the left – vertical cross-section of the initial water displacement in the source area along the line AA' calculated for 3 different dip-angles. On the right – position of the fault planes on the map (it is practically the same for all 3 dip-angle considered). Dotted line shows projection of the upper edge of the

fault. Fig. 3.1.2 shows the vertical cross-section of the initial water displacement in the source area calculated along the line AA' for 3 different values of the dip-angle δ , equal to 0° , 10° (adopted value) and 20° . Table 3.1.1 shows variations of the maximum positive and negative wave amplitude over the coast calculated for 3 different values of the dip-angle δ . Although individual values of height vary within rather considerable range (up to 75-80%, like at the part of coast near the points 920-925), variation in the average height along the coast (shown in the first right column of the Table 3.1.1) are small (within 5%) and the general form of all three height distribution looks pretty similar.

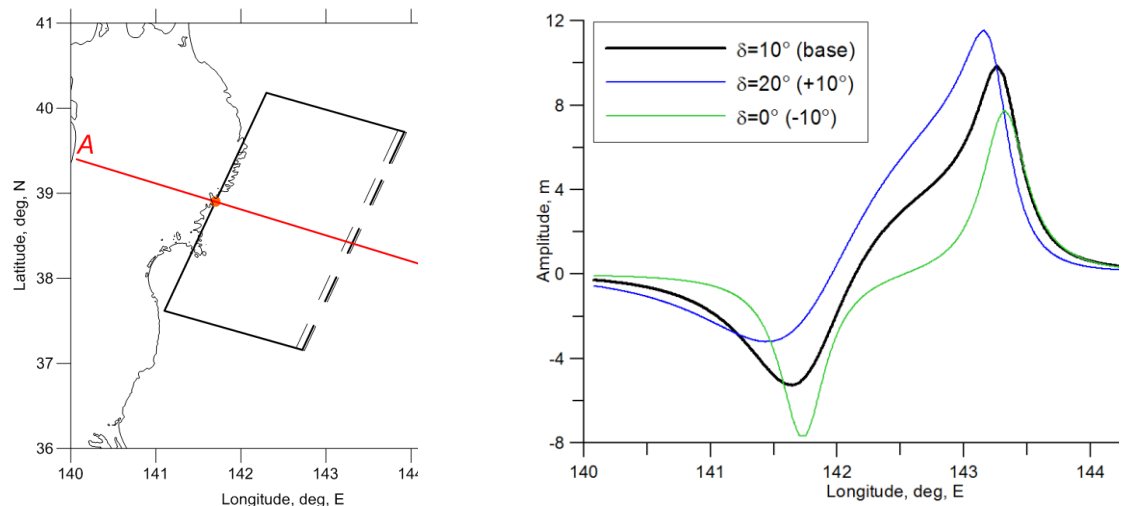
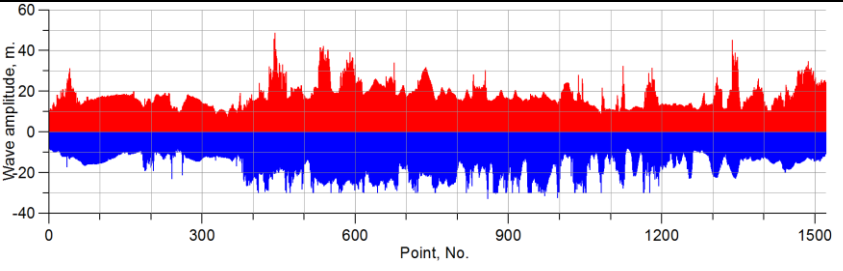
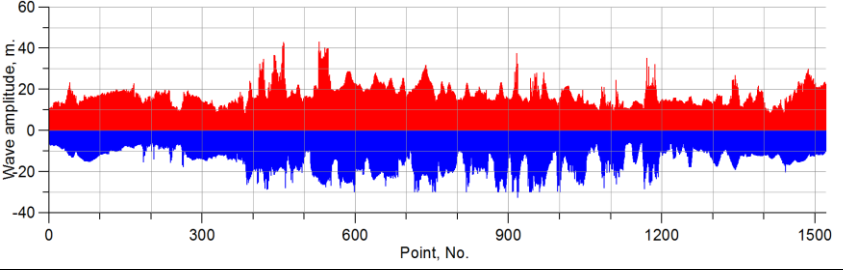
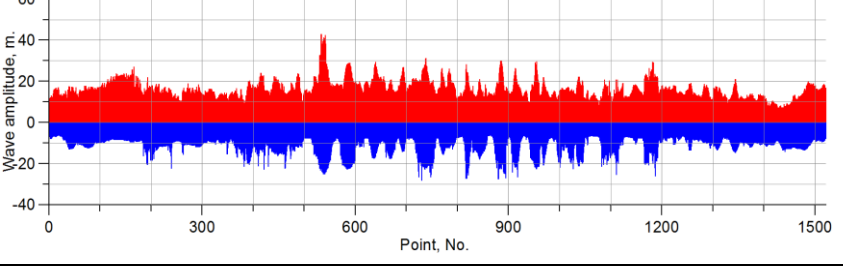


Fig. 3.1.2. On the left – vertical cross-section of the initial water displacement in the source area along the line AA' calculated for 3 different dip-angles. On the right – position of the fault planes on the map (it is practically the same for all 3 dip-angle considered). Dotted line shows projection of the upper edge of the fault.

Table 3.1.1. Distribution of maximum positive (red color) and maximum negative (blue color) wave amplitudes along the selected part of the Sanriku coast for the 2011 Tohoku model source calculated for three different values of dip-angle (they are shown in the first column).

δ	$\Delta V, V_0, E_{tsu}, I$	Histograms
20° (+10°) 27864 m, 18.32 m, 27167 m, 17.86 m, 55032 m, 36.18 m	$\Delta V = 139.70 \text{ km}^3$ $V_0 = 427.14 \text{ km}^3$, $E_{tsu} = 1.016\text{E}+016 \text{ J}$, $I=4.69$	
10° (base) 26761 m, 17.59 m, 23766 m, 15.62 m, 50527 m, 33.22 m	$\Delta V = 66.87 \text{ km}^3$ $V_0 = 374.62 \text{ km}^3$ $E_{tsu} = 7.482\text{E}+015 \text{ J}$ $I=4.64$	
0° (-10°) 25199 m, 16.56 m, 18570 m, 12.20 m, 43770 m, 28.77 m	$\Delta V = 0.90 \text{ km}^3$ $V_0 = 247.41 \text{ km}^3$ $E_{tsu} = 4.881\text{E}+015 \text{ J}$ $I=4.55$	

The same type of analysis for variation of the slip-angle λ is shown in Table 3.1.2. Initial surface displacement in the source area for different slip-angles is shown in Fig. 3.1.3. Slip-angle is less steady parameter of source mechanism determination. Its accuracy for modern earthquakes can be within the range of $\pm 10^\circ - 15^\circ$, but for older events it can vary within the range of $\pm 30^\circ$, since this parameter is controlled by the seismotectonic features of the area to lesser extent than dip-angle. Here we also see that despite large variations (up to 50%) of individual heights, the general wave pattern over the coast looks pretty similar and average amplitudes are within 5-10% even for variation of λ angle up to $\pm 30^\circ$.

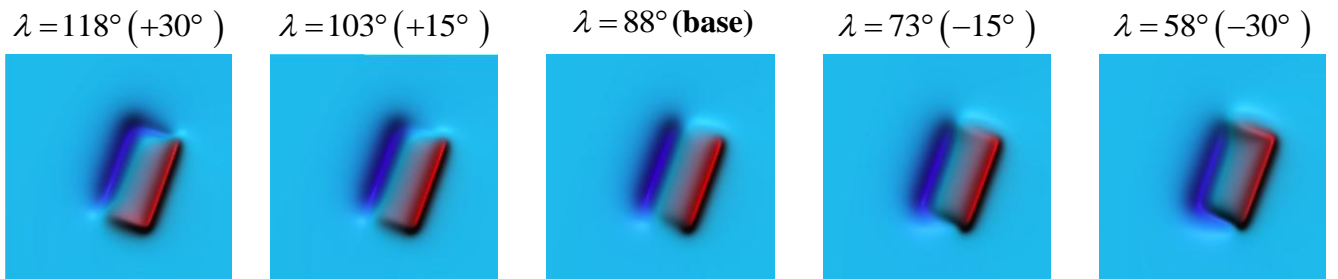


Fig. 3.1.3. 3D view of the initial surface displacement for different values of the slip-angle λ . Blue color corresponds subsidence, red color – uplift.

Table 3.1.2. Distribution of maximum positive (red color) and maximum negative (blue color) wave amplitudes along the selected part of the Sanriku coast for the 2011 Tohoku model source calculated for three different values of slip-angle λ (they are shown in the first column).

λ	$\Delta V, V_0, E_{tsu}, I$	Histograms
118° (+30°)	$\Delta V = 59.05 \text{ km}^3$ $V_0 = 362.37 \text{ km}^3$ $E_{tsu} = 6.480\text{E}+015 \text{ J}$ $I = 4.51$	
24636 m 16.19 m 21941 m 14.42 m 46578 m 30.62 m		
103° (+15°)	$\Delta V = 65.18 \text{ km}^3$ $V_0 = 372.96 \text{ km}^3$ $E_{tsu} = 7.257\text{E}+015 \text{ J}$ $I = 4.60$	
26174 m 17.20 m 23203 m 15.25 m 49377 m 32.46 m		
88° (base)	$\Delta V = 66.87 \text{ km}^3$ $V_0 = 374.62 \text{ km}^3$ $E_{tsu} = 7.482\text{E}+015 \text{ J}$ $I = 4.64$	
26761 m 17.59 m 23766 m 15.62 m 50527 m 33.22 m		
73° (-15°)	$\Delta V = 64.00 \text{ km}^3$ $V_0 = 369.14 \text{ km}^3$ $E_{tsu} = 7.096\text{E}+015 \text{ J}$ $I = 4.60$	
26081 m 17.14 m 23315 m 15.32 m 49397 m 32.47 m		
58° (-30°)	$\Delta V = 56.77 \text{ km}^3$ $V_0 = 353.76 \text{ km}^3$ $E_{tsu} = 6.202\text{E}+015 \text{ J}$ $I = 4.55$	
25187 m 16.55 m 23096 m 15.18 m 48283 m 31.74 m		

Another important group of parameters is the source location and its orientation relatively to the coastline. Accuracy of epicenter determination for the modern events is within $\pm 5 - 10 \text{ km}$, depth determination for shallow earthquakes is less reliable and hypocenter quite often is fixed to the depth of 33 km (bottom of the Earth crust). However, most of tsunamigenic earthquakes in subduction zones occur along the main lithospheric boundary (contact between subducting oceanic

and overriding continental crust) so their depth range are restrained within relatively narrow range (normally, from 20 to 50 km).

Table 3.1.3 shows variations of the maximum positive and negative wave amplitude calculated for 5 different positions of the fault plane obtained by shifting it along the long axis of the fault on +20 km, +10 km, 0 (adopted position), -10 km, -20 km. Location of the fault plane for these cases is shown in Fig. 3.1.4.

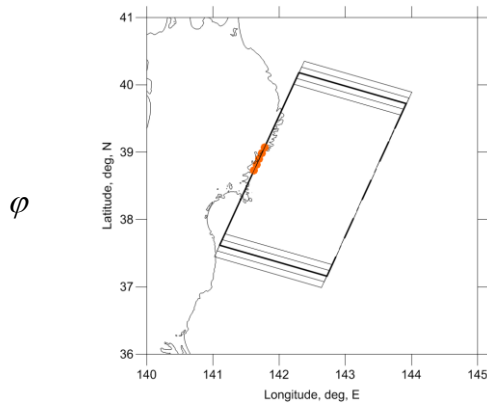


Fig. 3.1.4. Variations in position of the fault plane by shifting along its long axis on +20 km, +10 km, 0 (adopted position), -10 km, -20 km. Orange dots show the position of the center of the lower edge of the fault, used as a reference for its geographical location on the map and indicated in the first column of Table 3.1.3.

Table 3.1.3. Distribution of maximum positive (red color) and maximum negative (blue color) wave amplitudes along the selected part of the Sanriku coast for the 2011 Tohoku model source calculated for 5 different positions of the model source shifted along its long axis on +20 km, +10 km, 0 (adopted position), -10 km, -20 km.

φ	$\Delta V, V_0, E_{tsu}, I$	Histograms
39.07°N 141.78°E (+20km)	$\Delta V = 66.87 \text{ km}^3$ $V_0 = 374.62 \text{ km}^3$ $E_{tsu} = 7.482\text{E}+015 \text{ J}$ $I=4.641$	
26835 m 17.64 m 24073 m 15.82 m 50909 m 33.47 m		
38.983°N 141.74°E (+10km)	$\Delta V = 66.87 \text{ km}^3$ $V_0 = 374.62 \text{ km}^3$ $E_{tsu} = 7.482\text{E}+015 \text{ J}$ $I=4.637$	
26769 m 17.59 m 23894 m 15.70 m 50663 m 33.30 m		
38.9°N 141.7°E (base)	$\Delta V = 66.87 \text{ km}^3$ $V_0 = 374.62 \text{ km}^3$ $E_{tsu} = 7.482\text{E}+015 \text{ J}$ $I=4.637$	
26761 m 17.59 m 23766 m 15.62 m 50527 m 33.22 m		
38.817°N 141.66°E (-10km)	$\Delta V = 66.87 \text{ km}^3$ $V_0 = 374.62 \text{ km}^3$ $E_{tsu} = 7.482\text{E}+015 \text{ J}$ $I=4.613$	
26320 m 17.30 m 23432 m 15.40 m 49752 m 32.71 m		
38.73°N 141.62°E (-20km)	$\Delta V = 66.87 \text{ km}^3$ $V_0 = 374.62 \text{ km}^3$ $E_{tsu} = 7.482\text{E}+015 \text{ J}$ $I=4.606$	
26196 m 17.22 m 23385 m 15.37 m 49581 m 32.59 m		

Table 3.1.4 shows variations of the maximum positive and negative wave amplitude calculated for 3 different positions of the fault plane obtained by shifting it along its short axis on +10 km, 0 (adopted position), -10 km. Location of the fault plane for these cases is shown in Fig. 3.1.5.

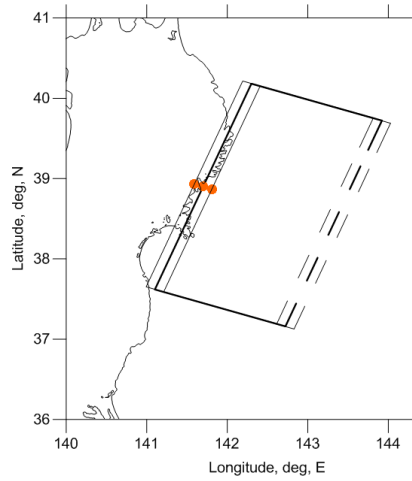


Fig. 3.1.5. Variations in position of the fault plane by shifting along its short axis on +10 km and -10 km relatively its adopted position (shown as solid rectangle). Orange dots show the position of the center of the lower edge of the fault, used as a reference for its geographical location on the map and indicated in the first column of

Table 3.1.4.

Table 3.1.4. Distribution of maximum positive (red color) and maximum negative (blue color) wave amplitudes along the selected part of the Sanriku coast for the 2011 Tohoku model source calculated for 3 different positions of the model source shifted along its short axis +10 km, 0 (adopted position), -10 km (they are shown in the first column).

ψ	$\Delta V, V_0, E_{tsu}, I$	Histograms
38.867°N 141.808°E (+10km)	$\Delta V = 66.87 \text{ km}^3$ $V_0 = 374.62 \text{ km}^3$ $E_{tsu} = 7.482\text{E}+015$ J $I=4.656$	
27123 m 17.83 m 23171 m 15.23 m 50294 m 33.06 m		
38.9°N 141.7°E (base)	$\Delta V = 66.87 \text{ km}^3$ $V_0 = 374.62 \text{ km}^3$ $E_{tsu} = 7.482\text{E}+015$ J $I=4.637$	
26761 m 17.59 m 23766 m 15.62 m 50527 m 33.22 m		
38.933°N 141.592°E (-10km)	$\Delta V = 66.87 \text{ km}^3$ $V_0 = 374.62 \text{ km}^3$ $E_{tsu} = 7.482\text{E}+015$ J $I=4.585$	
25815 m 16.97 m 23721 m 15.59 m 49536 m 32.56 m		

From the data in

Table 3.1.3 and

Table 3.1.4 we can conclude that small (within the accuracy of their determination) variation in source location hardly influence the general characteristics of heights distribution along the coast. Variations in average wave amplitudes, tsunami intensity and integral characteristics of the source area ($\Delta V, V_0, E_{tsu}$) are small (within 1%). However, individual heights at some particular coastal locations can be much more sensitive and for some coastal locations their variations can be up to 50%.

Table 3.1.5 shows variations of the maximum positive and negative wave amplitude calculated for 3 different orientations of the fault plane obtained by changing of its strike-angle θ on $\pm 10^\circ$ relatively to its adopted value. Location of the fault plane for these cases is shown in Fig. 3.1.6.

Orientation of the fault is an important parameter since it defines the directivity of initial energy radiation from the source area. For this particular case of the 2011 Tohoku mega-tsunami small variation in orientation can be less important due to the close proximity of the source area to the coast. Indeed, the data in

Table 3.1.5 show that average heights and, therefore, tsunami intensity I , are within 2 – 3% of their values and the general form of distribution is actually repeated in all three cases considered. As one could expect, the integral characteristics of the source area are pretty stable for all three orientations and their values are similar within 1%.

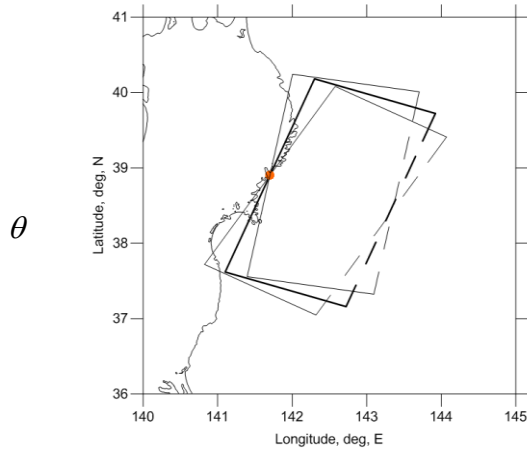
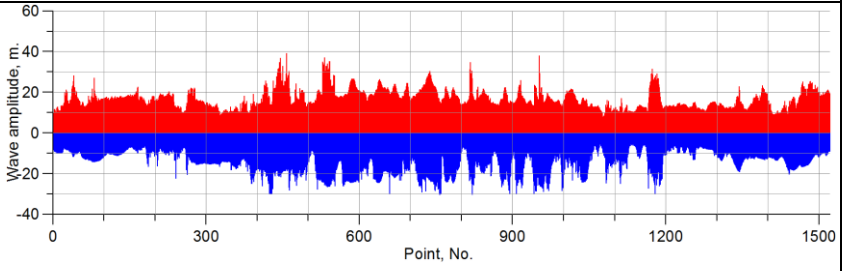
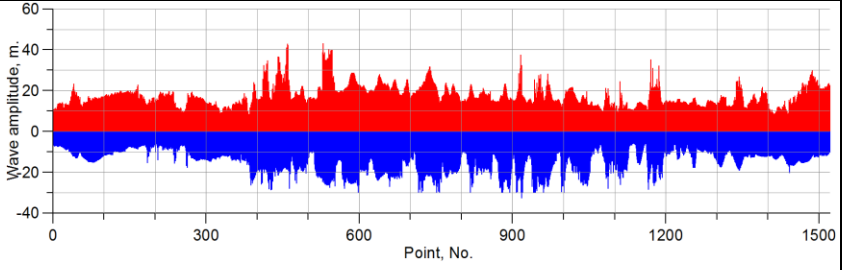
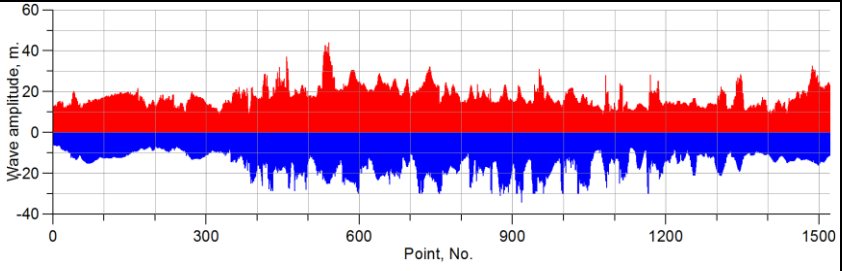


Fig. 3.1.6. Variations in position of the fault plane by changing strike-angle θ on $+10^\circ$ and on -10° relatively its adopted orientation (shown by solid rectangle). Orange dot shows the position of the center of the lower edge of the fault, used as a reference for its geographical location on the map.

Table 3.1.5. Distribution of maximum positive (red color) and maximum negative (blue color) wave amplitudes along the selected part of the Sanriku coast for the 2011 Tohoku model source calculated for three different values of the strike-angle θ (source orientation).

θ	$\Delta V, V_0, E_{tsu}, I$	Histograms
30° (+10°) 25728 m 16.91 m 23310 m 15.32 m 49039 m 32.24 m	$\Delta V = 66.87 \text{ km}^3$ $V_0 = 374.62 \text{ km}^3$ $E_{tsu} = 7.482\text{E}+015$ J $I=4.580$	
20° (base) 26761 m 17.59 m 23766 m 15.62 m 50527 m 33.22 m	$\Delta V = 66.87 \text{ km}^3$ $V_0 = 374.62 \text{ km}^3$ $E_{tsu} = 7.482\text{E}+015$ J $I=4.637$	
10° (-10°) 26899 m 17.68 m 23636 m 15.53 m 50535 m 33.22 m	$\Delta V = 66.87 \text{ km}^3$ $V_0 = 374.62 \text{ km}^3$ $E_{tsu} = 7.482\text{E}+015$ J $I=4.644$	

Finally, the Table 3.1.6 shows variations of the maximum positive and negative wave amplitudes calculated for 3 different values of the source depths h_0 . The source depth is one of the most important parameters, controlling tsunamigenic potential of submarine earthquakes. The vertical cross-sections of the initial water displacement in the source area calculated along the line AA' for 3 different values of the source depth is shown in Fig. 3.1.7. As we can see from the data of Table 3.1.6, the average maximum and minimum values of wave amplitudes and tsunami intensity are rather stable, their variations are less than 2%. The general form of the height distribution is still the same with heights maximums are located near the same parts of coast, but variations in wave amplitudes at some coastal points can be sometime up to 50%.

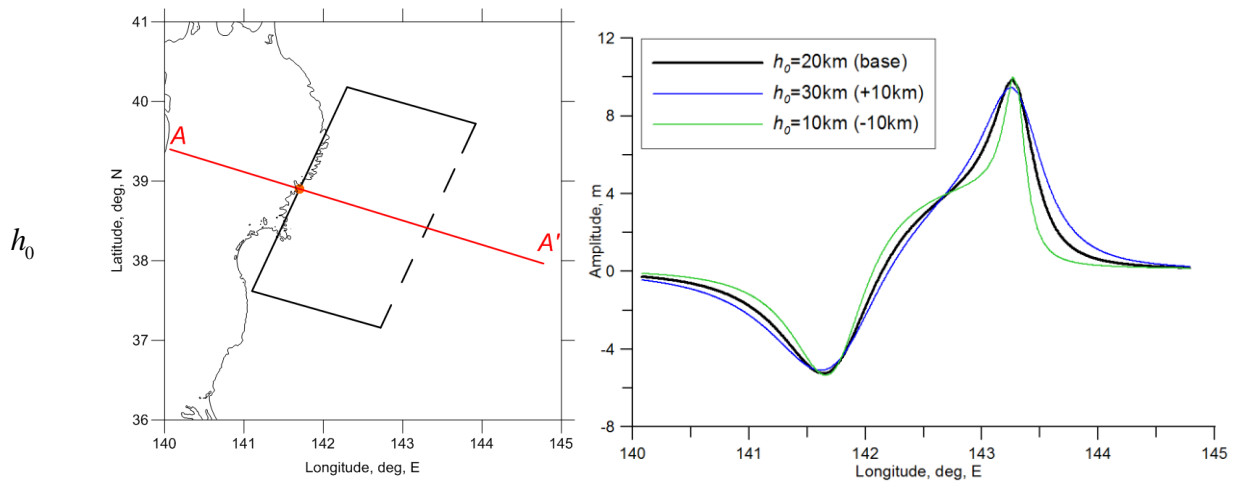


Fig. 3.1.7. Vertical cross-sections of the initial water displacement in the source area calculated along the line AA' for 3 different depths of the model source changing on +10 km, 0, -10 km relatively its adopted value.

Table 3.1.6. Distribution of maximum positive (red color) and maximum negative (blue color) wave amplitudes along the selected part of the Sanriku coast for the 2011 Tohoku model source calculated for three different source depths h_0 (shown in the first column).

h_0	$\Delta V, V_0, E_{tsu}, I$	Histograms
30km (+10km) 26611 m 17.49 m 23450 m 15.41 m 50061 m 32.91 m	$\Delta V = 71.39 \text{ km}^3$ $V_0 = 422.65 \text{ km}^3$ $E_{tsu} = 8.312\text{E}+015$ J $I=4.628$	
20km (base) 26761 m 17.59 m 23766 m 15.62 m 50527 m 33.22 m	$\Delta V = 66.87 \text{ km}^3$ $V_0 = 374.62 \text{ km}^3$ $E_{tsu} = 7.482\text{E}+015$ J $I=4.637$	
10km (-10km) 24541 m 16.13 m 22946 m 15.08 m 47487 m 31.22 m	$\Delta V = 61.82 \text{ km}^3$ $V_0 = 319.38 \text{ km}^3$ $E_{tsu} = 6.059\text{E}+015$ J $I=4.512$	

To check the variability of individual wave heights with variations of the source parameters, 8 coastal points (among the all 1521 points considered in this study) were selected for more detailed analysis. The geographical position of the selected points is shown in Fig. 3.1.8. Their selection was made on the basis of covering the variety of different coastal features (straight coast, indented coast, entrance and heads of the bays, etc.).

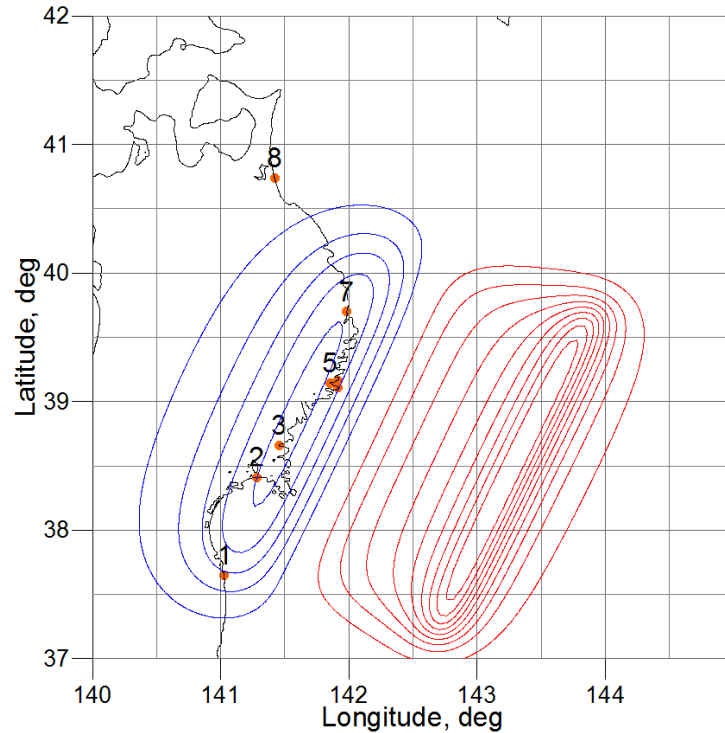


Fig. 3.1.8. Position of 8 coastal points selected for individual analysis of wave amplitude changes relatively variations in source parameters.

Wave amplitudes for them for 3 different δ (Fig. 3.1.2) values is shown in Table 3.1.7. In general, variations in wave amplitudes at the particular points are within 10 – 20%, however, in some specific cases, like for point 6, located near the entrance to the bay, it can be up to 50% (for maximum negative amplitude).

As you can see from the data listed in Table 3.1.7 – Table 3.1.12, variations of individual wave amplitude and heights with variation of source parameters are quite complicated and depend not only on source parameters themselves but several additional factors (for example, positional relationship of coastal point relatively the source area).

In general, variations of individual heights have larger range than their average values listed in Table 3.1.7 – Table 3.1.12. However, this range can be quite different for different points even for the same parameters. Thus, for instance, in Table 3.1.8 variations of maximum positive wave amplitude at point 1 over the 5 slip-angle values is about 38% while for point 3 it is only 19%.

The general rule of thumb is that an individual wave amplitude at the particular location depends on the fraction of the initial wave energy coming to this part of the coast from the source area. If variation of a parameter changes this

fraction considerably, resulted wave amplitude will be essentially changed. If not, the resulted change will be within the range of changing the source parameter.

Table 3.1.7. Maximum positive (red color), maximum negative (blue color) wave amplitudes and maximum wave range (black color) at the selected coastal points calculated for 3 different values of the dip-angle δ . Actual position of each selected point at the coastline is shown in the first column of the Table.

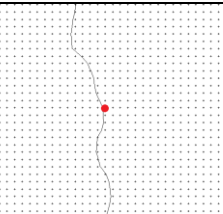
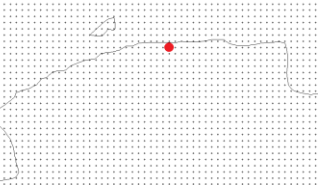
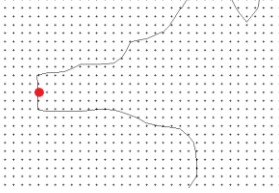
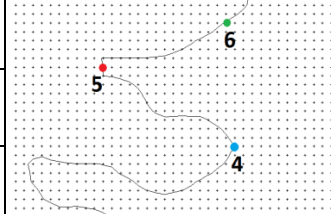
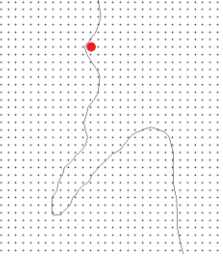
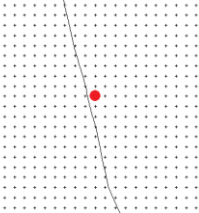
δ		20° (+10°)			10° (base)			0° (-10°)		
1		10.58			10.87			11.59		
		-8.31			-6.63			-6.58		
		18.89			17.50			18.18		
2		14.22			13.94			13.86		
		-13.03			-13.89			-10.82		
		27.25			27.83			24.67		
3		31.53			28.73			28.67		
		-23.80			-25.37			-22.41		
		55.33			54.09			51.08		
4		15.48	20.51	16.54	14.84	23.28	15.76	13.82	30.08	15.39
5		-15.78	-20.89	-20.93	-13.18	-23.14	-13.50	-6.75	-22.56	-7.76
6		31.26	41.40	37.47	28.02	46.42	29.26	20.57	52.64	23.15
7		13.89			15.20			17.92		
		-17.79			-11.27			-9.30		
		31.67			26.46			27.22		
8		25.82			22.48			17.80		
		-14.03			-11.60			-8.32		
		39.85			34.08			26.12		

Table 3.1.8. Maximum positive (red color), maximum negative (blue color) wave amplitudes and maximum wave range (black color) at the selected coastal points calculated for 5 different values of the slip-angle λ . Position of the selected points is shown in Fig. 3.1.8.

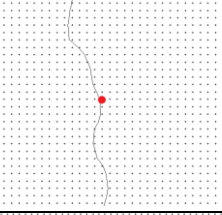
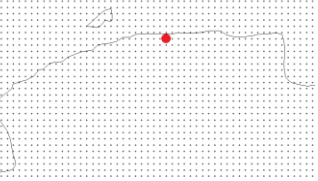
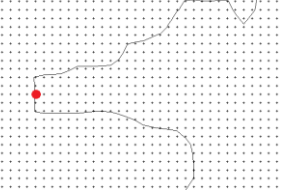
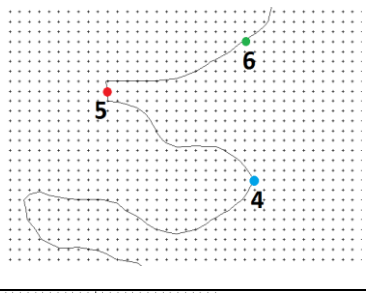
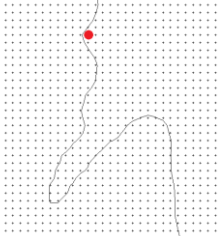
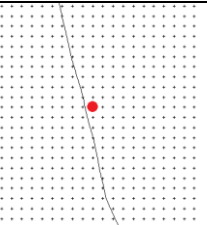
λ		118° (+30°)	103° (+15°)	88° (base)	73° (-15°)	58° (-30°)
1		9.49	8.93	10.87	13.48	15.25
		-9.80	-7.63	-6.63	-6.68	-6.35
		19.29	16.56	17.50	20.16	21.60
2		14.96	14.93	13.94	12.06	13.98
		-13.40	-14.84	-13.89	-12.33	-11.74
		28.37	29.76	27.83	24.39	25.72
3		25.63	28.11	28.73	27.43	24.29
		-24.58	-24.94	-25.37	-24.52	-24.15
		50.21	53.05	54.09	51.95	48.45
4		11.31	13.52	14.84	15.19	14.54
		-9.20	-11.29	-13.18	-13.78	-13.42
		20.51	24.82	28.02	28.96	27.96
5		20.45	20.57	23.28	24.47	24.04
		-24.70	-24.79	-23.14	-23.95	-25.13
		45.15	45.36	46.42	48.41	49.17
6		11.51	14.10	15.76	16.38	15.95
		-8.48	-11.36	-13.50	-14.43	-14.21
		20.00	25.47	29.26	30.82	30.15
7		16.13	16.16	15.20	13.31	10.61
		-7.91	-8.25	-11.27	-13.57	-15.49
		24.04	24.41	26.46	26.88	26.10
8		15.44	19.82	22.48	23.31	23.60
		-11.16	-11.46	-11.60	-13.02	-14.08
		26.60	31.28	34.08	36.33	37.68

Table 3.1.9. Maximum positive (red color), maximum negative (blue color) wave amplitudes and maximum wave range (black color) at the selected coastal points calculated for 5 different positions of the model source shifted along its long axis on +20 km, +10 km, 0 (adopted position), -10 km, -20 km.

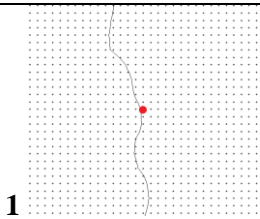
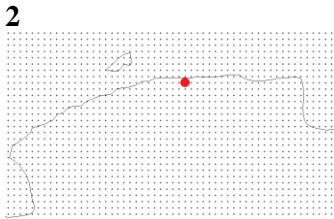
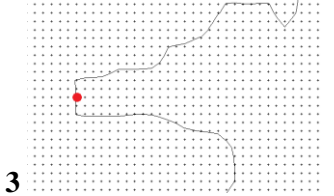
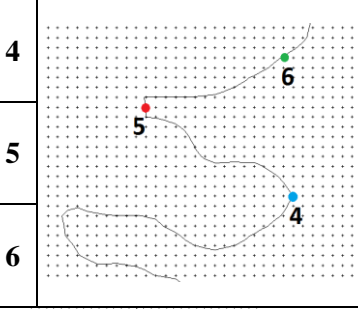
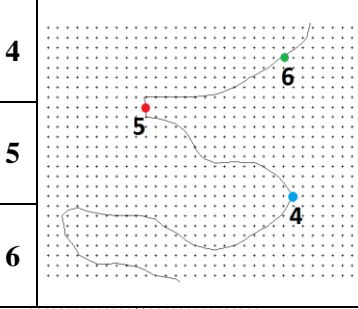
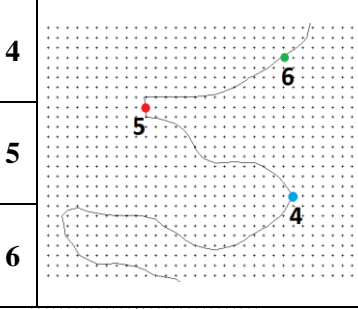
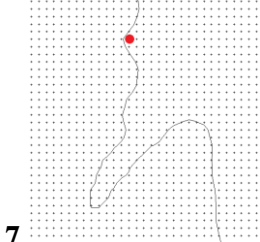
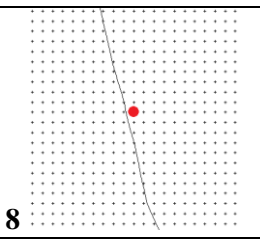
φ		39.07°N 141.78°E (+20km)	38.983°N 141.74°E (+10km)	38.9°N 141.7°E (base)	38.817°N 141.66°E (-10km)	38.73°N 141.62°E (-20km)
1		10.19	10.55	10.87	11.13	11.31
		-5.92	-6.28	-6.63	-7.40	-8.12
		16.10	16.83	17.50	18.53	19.42
2		13.09	13.47	13.94	14.38	14.69
		-11.52	-12.08	-13.89	-15.04	-16.15
		24.62	25.55	27.83	29.41	30.84
3		28.28	28.47	28.73	28.89	28.75
		-24.44	-25.43	-25.37	-25.36	-25.15
		52.72	53.89	54.09	54.25	53.90
4		15.14	14.99	14.84	14.57	14.10
		-14.50	-13.87	-13.18	-12.13	-11.35
		29.64	28.87	28.02	26.71	25.45
5		24.11	23.79	23.28	22.51	21.41
		-23.86	-23.84	-23.14	-23.36	-25.83
		47.97	47.64	46.42	45.87	47.24
6		16.20	16.01	15.76	15.37	14.77
		-15.23	-14.27	-13.50	-13.02	-12.56
		31.42	30.28	29.26	28.39	27.33
7		17.08	16.15	15.20	14.10	12.85
		-12.72	-12.16	-11.27	-10.07	-8.52
		29.80	28.32	26.46	24.16	21.38
8		26.70	24.52	22.48	20.39	18.12
		-13.62	-12.77	-11.60	-11.57	-11.02
		40.32	37.29	34.08	31.96	29.14

Table 3.1.10. Maximum positive (red color), maximum negative (blue color) wave amplitudes and maximum wave range (black color) at the selected coastal points calculated for 3 different positions of the model source shifted along its short axis on +10 km, 0 (adopted position), -10 km.

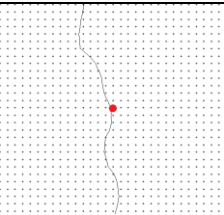
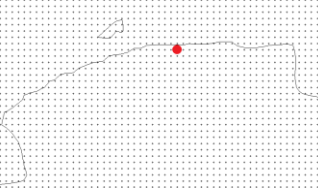
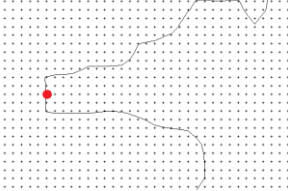
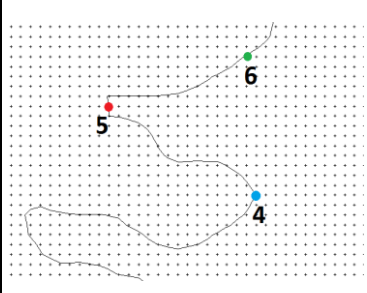
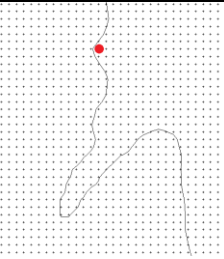
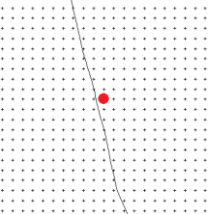
ψ		38.867°N 141.808°E (+10 km)	38.9°N 141.7°E (base)	38.933°N 141.592°E (-10 km)
1		12.01	10.87	9.72
		-7.09	-6.63	-6.12
		19.09	17.50	15.84
2		14.46	13.94	13.18
		-14.13	-13.89	-12.49
		28.60	27.83	25.67
3		30.22	28.73	27.12
		-25.69	-25.37	-24.02
		55.92	54.09	51.14
4		15.18	14.84	14.32
-11.74		-13.18	-13.45	
26.91		28.02	27.76	
5		23.16	23.28	23.09
-21.51		-23.14	-23.81	
44.68		46.42	46.90	
6		15.86	15.76	15.46
-12.36		-13.50	-15.70	
28.22		29.26	31.16	
7		15.17	15.20	14.91
		-12.69	-11.27	-11.18
		27.86	26.46	26.09
8		21.34	22.48	22.67
		-11.95	-11.60	-11.52
		33.29	34.08	34.19

Table 3.1.11. Maximum positive (red color), maximum negative (blue color) wave amplitudes and maximum wave range (black color) at the selected coastal points calculated for 3 different values of the strike-angle θ .

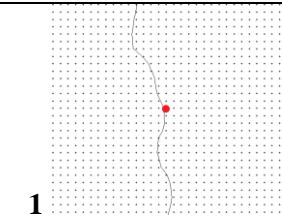
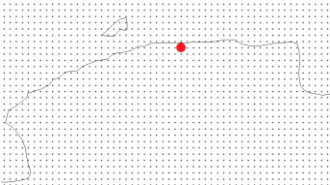
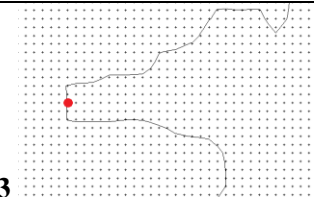
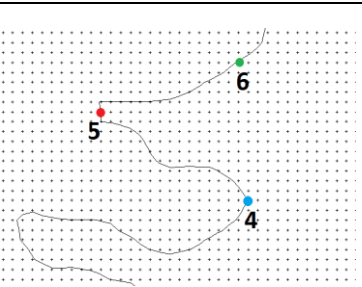
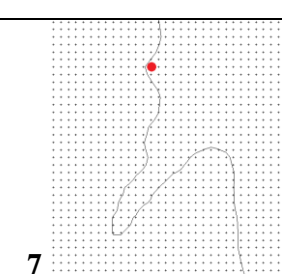
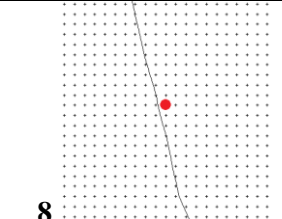
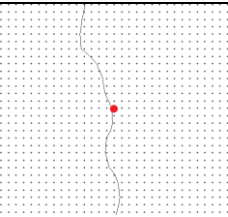
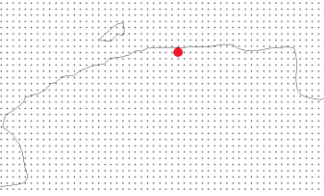
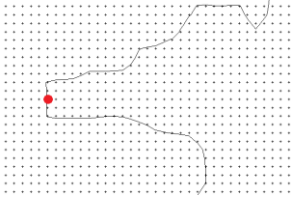
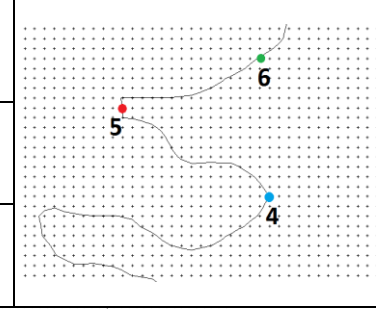
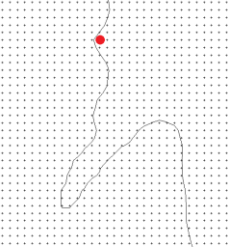
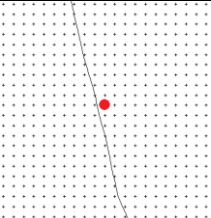
θ		30° (+10°)	20° (base)	10° (-10°)
1		9.81	10.87	12.93
		-8.30	-6.63	-6.00
		18.11	17.50	18.93
2		14.04	13.94	14.09
		-15.05	-13.89	-10.88
		29.09	27.83	24.97
3		26.53	28.73	30.44
		-24.02	-25.37	-24.53
		50.55	54.09	54.97
4		14.23	14.84	14.66
		-10.25	-13.18	-13.94
		24.48	28.02	28.60
5		22.36	23.28	23.34
		-22.71	-23.14	-26.15
		45.07	46.42	49.49
6		15.24	15.76	15.62
		-12.01	-13.50	-16.14
		27.25	29.26	31.76
7		13.43	15.20	15.39
		-10.22	-11.27	-13.85
		23.65	26.46	29.23
8		19.87	22.48	24.39
		-11.68	-11.60	-15.27
		31.55	34.08	39.65

Table 3.1.12. Maximum positive (red color), maximum negative (blue color) wave amplitudes and maximum wave range (black color) at the selected coastal pints calculated for 3 different values of the source depth h_0 .

h_0		30 km (+10 km)	20 km (base)	10 km (-10 km)	
1		10.57	10.87	9.83	
		-6.26	-6.63	-5.76	
		16.83	17.50	15.59	
2		13.79	13.94	12.95	
		-15.21	-13.89	-13.09	
		29.00	27.83	26.04	
3		28.99	28.73	24.97	
		-25.00	-25.37	-24.34	
		53.99	54.09	49.31	
4		13.86	14.84	15.91	
-13.07		-13.18	-12.27		
26.93		28.02	28.18		
5		20.81	23.28	23.07	
-24.04		-23.14	-21.77		
44.85		46.42	44.83		
6		15.08	15.76	16.14	
-12.93		-13.50	-12.34		
28.01		29.26	28.48		
7			14.88	15.20	13.62
			-9.87	-11.27	-13.49
			24.76	26.46	27.12
8		21.90	22.48	21.26	
		-12.67	-11.60	-10.30	
		34.57	34.08	31.56	

3.2. Analysis of sensitivity of computed wave heights on the friction parameter (for the 2011 Tohoku tsunami)

Study of the dependence of the simulation results of tsunami runup on the properties of the land surface (its roughness) was held for Tohoku tsunami, 2011. These calculations were performed for the coastal areas «Miyako» (Fig. 3.2.1), «Sendai» (Fig. 3.2.2) and «Iwaki» (Fig. 3.2.3) for different values of Chezy coefficient: $n = 0.000, 0.001, 0.002, 0.005$. The results show that, as for the model simulations, the calculated inundation zone is highly dependent on the coefficient of friction. This effect is greatly enhanced at shallow coastal areas.

Thus, calculations for the real coastal areas confirm the importance of a fair presentation of the characteristics of tsunami flooded land, determining the dissipative effects of the absorption of wave energy in the waves propagation on land. At the same time, the problem of determining the maximum runup can be solved without such effects.

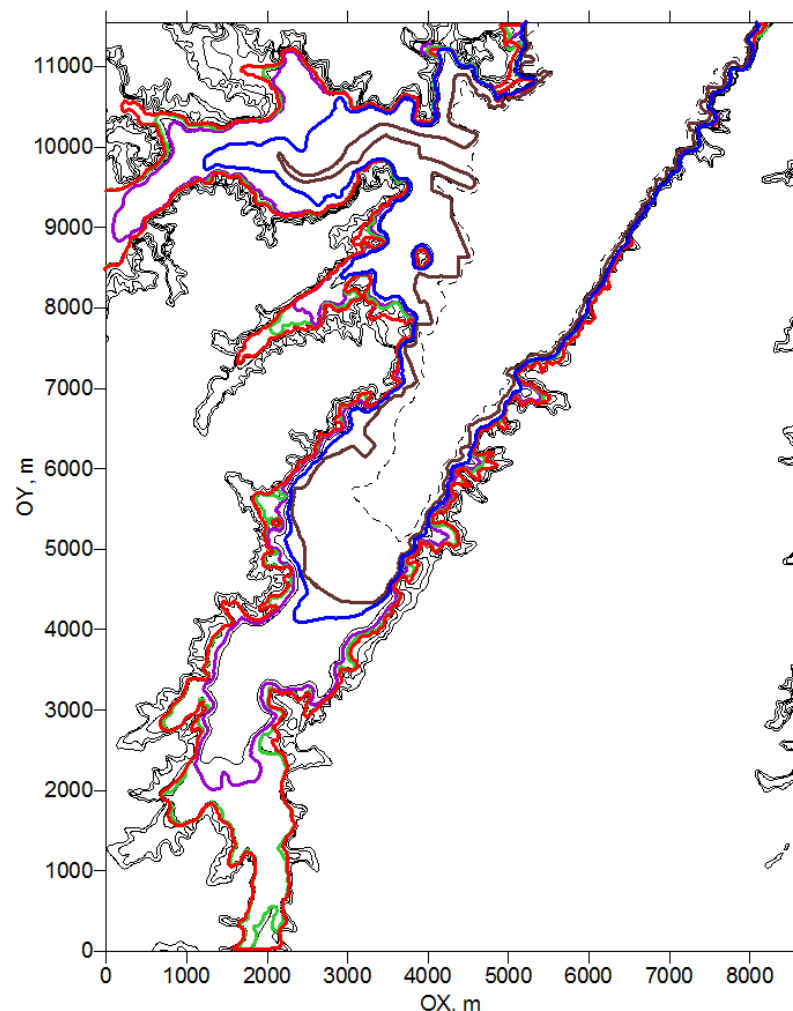


Fig. 3.2.1. Inundation limits of the 2011 Tohoku tsunami run-up within the Miyako Bay calculated for different values of Chezy coefficient: red – $n=0$ (basic), green – $n=0.001$, purple – $n=0.002$, blue – $n=0.005$. Land relief is shown by black isolines drawn for each 10 m of elevation up to 50 m, brown line shows position of the coastline for undisturbed water (at $z=0$ m), dotted line shows the initial position of the coastline corresponding to the isobath -4.9m. Calculation of run-up was made on the regular rectangular grid with steps $\Delta x = \Delta y = 15$ m.

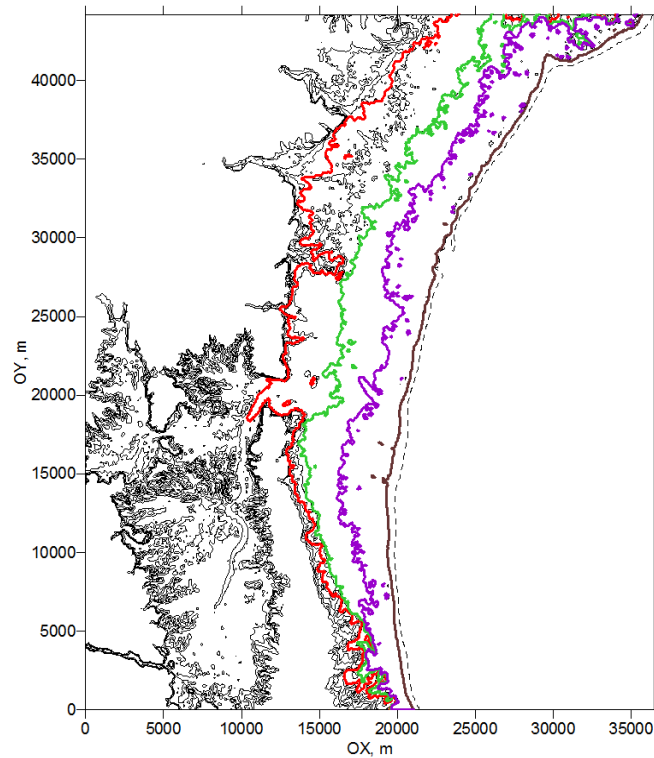


Fig. 3.2.2. Inundation limits of the 2011 Tohoku tsunami run-up within the coastal area «Sendai» calculated for different values of Chezy coefficient: red – $n=0$ (basic), green – $n=0.001$, purple – $n=0.002$. Land relief is shown by black isolines drawn for each 10 m of elevation up to 50 m, brown line shows position of the coastline for undisturbed water (at $z=0$ m), dotted line shows the initial position of the coastline corresponding to the isobath -4.9m. Calculation of run-up was made on the regular rectangular grid with steps $\Delta x = \Delta y = 40$ m.

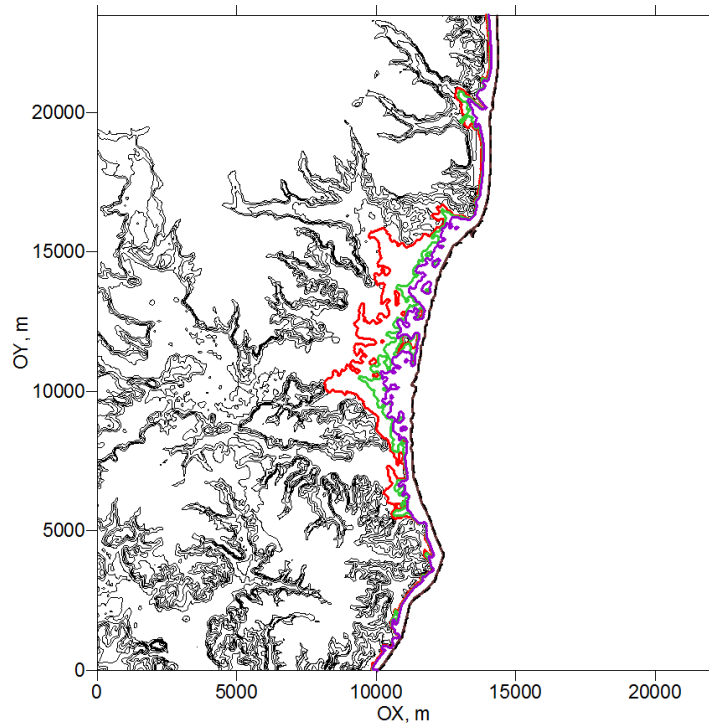


Fig. 3.2.3. Inundation limits of the 2011 Tohoku tsunami run-up within the coastal area «Iwaki» calculated for different values of Chezy coefficient: red – $n=0$ (basic), green – $n=0.001$, purple – $n=0.002$. Land relief is shown by black isolines drawn for each 10 m of elevation up to 50 m, brown line shows position of the coastline for undisturbed water (at $z=0$ m), dotted line shows the initial position of the coastline corresponding to the isobath -4.9m. Calculation of run-up was made on the regular rectangular grid with steps $\Delta x = \Delta y = 30$ m.

4. Conclusions (applicability of numerical algorithms for reproducing of main features of selected historical tsunamis)

4.1. General conclusions

The state-of-the art methodology for calculation of run-up heights and inland flooding has been proposed. This methodology is based on the widely adopted approach to tsunami generation modeling, using analytical formulas for computation of co-seismic bottom displacement in the source area, finite-difference methods of modeling of tsunami propagation in an ocean with a real bathymetry and 1D and 2D methods of calculation of tsunami run-up on the dry land.

This methodology was applied for modeling of five selected historical tsunamis occurred near the east coast of Japan from 1854 to 2011 and modeling results were compare with available observations.

Direct comparison of computed and observed wave heights at the particular coastal locations is hampered for old historical by insufficient accuracy of reported run-up values and uncertainties of their coastal locations. For the recent events (like 2011Tohoku tsunami) the main limiting factor is the absence of the detailed digital bathymetry for the areas under study and, in some cases, uncertainties in the earthquake source mechanism parameters.

Analysis of run-up characteristics shows that adequate modeling of run-up heights and inundation limits at the particular coastal locations can be carried out only for those coastal areas where the accurate digital bathymetry for nearby waters and land relief models can be obtained.

The main result obtained during the Pilot Project implementation is that the joint research team consisted of the tsunami experts and applied mathematicians of the Institute of Computational Technologies SD RAS and the Institute of Computational Mathematics and Mathematical Geophysics SD RAS has enough qualification and expertise and possesses the adequate set of numerical algorithms and computational tools implemented into licensed and registered software packages (MGC, STATIC, PDM/TSU, WinITDB, Golden Software Surfer and Grapher, Google Earth) to be able to make realistic and reasonably credible modeling of historical tsunamigenic events provided that a set of observational data and reliable source parameters for these events are available.

Realistic evaluation of perspectives of application of this computational technology for assessment of hazard and risk of future tsunamis in Japan and assessment of required resources can be made upon receiving from the Customer more detailed specification of tasks planned for the second stage of the project.

4.2. Conclusions for Section 3.1

1. Of six basic source parameters describing the model seismic source, its seismic moment M_0 is the most important parameter controlling the intensity I of the resulted tsunami. In the widely adopted approach to tsunami generation model (using the static co-seismic displacement of the elastic half-space for an inner

dislocation source) calculated by Gusiakov (1978) or Okada (1985) formulas) the tsunami intensity I is directly proportional to the M_0 value, that was first shown Chubarov, Gusiakov (1985).

2. Being calculated on the basis of average tsunami heights along the extended part of the coast, the tsunami intensity I (as measured on Soloviev-Imamura scale) is rather stable parameter that closely correlates with the total tsunami energy that is a part of the total seismic energy radiated by a source and trapped in the ocean in the form of the long gravity water waves (i.e., tsunami).

3. Small variations (within errors of their actual determination) of the source mechanism, representing by the dip-angle, slip-angle and strike-angle of the fault plane, results in minor (within 5%) variations of the tsunami intensity. However, calculated wave heights in a particular coastal location may vary up to 30-50%.

4. Orientation of the fault relatively the coast (strike-angle) is an important parameter since it defines the initial directivity of energy radiation from the source area. Its variation within a reasonable range ($\pm 10^\circ$) almost doesn't change the I value, however, it shifts the area of maximum run-up heights along the coast and, therefore, may considerably change the individual heights in particular coastal locations.

5. The same is true about the geographical position of the source area relatively the coast. Its variation does not change the tsunami intensity at all, but fully determines the position of the area of maximum run-ups along the coast, and, therefore, fully controls the wave heights at the individual locations.

6. Finally, from the model results and actual observations it is known that the source depth h_0 is one of the most important parameters, controlling tsunamigenic potential of submarine earthquakes. However, for most of tsunamigenic earthquakes, the depth of a fault and its vertical extent is pretty well (within ± 10 km) constrained by tectonic features of the area. The general form of the height distribution along the coast only slightly changes with the source depth, but variations in individual wave amplitudes at some coastal points can be sometime up to 50%.

5. References

Alekseev A.S., Gusiakov V.K. (1984) On the estimate of tsunamiefficiency of submarine earthquakes // *Zemletryasenia I preduprezhdenie stikhiinykh bedstvii*, Trudy 27-go Mezhdunarodnogo Geologicheskogo Congressa, Moskva, 4-14 avgusta 1984, T.6, Moscow, Nauka. P. 127-133.

Bautin S.P., Deryabin S.L. (2005) *Mathematical Modelling of Ideal Gas Outflow into Vacuum*. Nauka, Novosibirsk (in Russian).

Bautin S.P., Deryabin S.L., Sommer A.F., Khakimzyanov G.S., Shokina N.Yu. (2011) Use of analytic solutions in the statement of difference boundary conditions on a movable shore line // *Russian Journal of Numerical Analysis and Mathematical Modelling*. Vol. 26, No. 4. P. 353-377.

Belotserkovskii O.M., Davydov Yu.M. (1982) The method of large particles in gas dynamics. Numerical experiments // Nauka. 392 p. (In Russian).

Bryant E. (2001) Tsunamis The underrated hazard. Cambridge University Press, 2001, 320 pp.

Chubarov L.B., Gusiakov V.K. (1985) Tsunamis and earthquake mechanism in the island arc region // Science of Tsunami Hazard, 3, №1, P.3-21.

Comer R.P. (1984) Tsunami generation: a comparison of traditional and normal mode approaches // Geophysical Journal. Royal Astronomical Society. 1984. Vol. 77, No. 4. P. 415 – 440.

Dalrymple R.A., Rogers B.D. (2006) Numerical Modeling of Water Waves with the SPH Method // Coastal Engineering. 53/2-3. P. 141-147. <http://dx.doi.org/10.1016/j.coastaleng.2005.10.004>.

De Leffe M., Le Touze D., Alessandrini B. (2010) SPH modeling of shallow-water coastal flows // Journal of Hydraulic Research. 48 (Extra Issue). P. 118-125.

EERI Special Earthquake Report (2011) The Japan Tohoku Tsunami of March 11, 2011.

Fukao Y., Furumoto M. (1975) Mechanism of large earthquakes along the eastern margin of the Japan Sea // Tectonophysics. Vol. 25. P. 247-266.

Gomez-Gesteira M., Rogers B.D., Dalrymple R.A., Crespo A.J.C. (2010) State-of-the-art of classical SPH for freesurface flows // Journal of Hydraulic Research. 48(Extra Issue). P. 6-27.

Grilli S.T., Harris J.C., Tajallibakhsh T.S., Masterlark T.L., Kyriakopoulos Ch., Kirby J.T., Shi F. (2012) Numerical simulation of the 2011 Tohoku tsunami based on a new transient FEM co-seismic source: Comparison to far- and near-field observations // Pure and Applied Geophysics, DOI 10.1007/s00024-012-0528-y.

Gusiakov V.K. (1974) On the relation of tsunami waves with parameters of earthquake source model. In: Matematicheskiye Problemy Geofiziki, Novosibirsk, VTS SO AN SSSR, Vyp. 5, Part 1. P. 118-140.

Gusiakov V.K. (1976) Calculation of the tsunami energy. In: Nekorrektnyye zadachi matematicheskoy fiziki I problemy interpretatsii geofizicheskikh nablyudeni, Novosibirsk, VTS SO AN SSSR, 46-64 (in Russian).

Gusiakov V.K. (1978) Static displacement of the surface of an elastic halfspace // In: Uslovno-korrektnyye zadachi matematicheskoy fiziki v interpretatsii geofizicheskikh nablyudeni. Novosibirsk, Computing Center, P.23-51 (in Russian)

Gusiakov V.K. (2001) "Red", "green" and "blue" Pacific tsunamigenic earthquakes and their relation with conditions of oceanic sedimentation // Tsunamis at the End of a Critical Decade. G.Hebenstreit (Editor), Kluwer Academic Publishers, Dordrecht-Boston-London. P. 17-32

Gusiakov, V.K., D.G.Khidasheli, A.G.Marchuk, and T.V.Kalashnikova, 2007. Analysis of tsunami travel time maps for damaging historical tsunamis in the world ocean. Report of the NTL/ICMMG SD RAS prepared for IOC/UNESCO, Novosibirsk, Russia, 28 pp. http://tsun.ssc.ru/tsulab/TTT_rep.htm.

Gusiakov V.K. (2009) Tsunami history – recorded // In: A.Robinson, E.Bernard (Eds.). The Sea, Vol.15, Tsunamis, Harvard University Press, Cambridge, USA. P. 23-53.

Gusiakov V.K. (2011) Relationship of tsunami intensity to source earthquake magnitude as retrieved from historical data // Pure and Applied Geophysics, Vol.168, Issue 11, 2033-2041. DOI 10.1007/s00024-011-0286-2.

Harlow F.H. (1955) A Machine Calculation Method for Hydrodynamic Problems // Los Alamos Scientific Laboratory report LAMS-1956.

Hibberd S., Peregrine D.H. (1979) Surf and run-up on a beach: a uniform bore // J. Fluid Mech. Vol. 95. P. 323-345.

Hong-Ming Kao, Tsang-Jung Chang (2012) Numerical modeling of dambreak-induced flood and inundation using smoothed particle hydrodynamics // Journal of Hydrology. 448-449. P. 232-244.

Hoshiba M., Iwakiri K., Hayashimoto N., Shimoyama T., Hirano K., Yamada Y., Ishigaki Y., Kikuta H. (2011) Outline of the 2011 off the Pacific coast of Tohoku Earthquake (Mw 9.0) – Earthquake Early Warning and observed seismic intensity // Earth Planets Space. Vol. 63. P. 547-551.

Iida, K. (1970) The generation of tsunamis and the focal mechanism of earthquakes. In: Tsunamis in the Pacific Ocean, Honolulu, East-West Center Press. P. 3-18.

Iida K. (1984) Catalog of tsunamis in Japan and its neighboring countries. Aichi Institute of Technology, Yachigusa, Yakusa-cho, Toyota-shi, 470-03, Japan, 52 p.

ITDB/WLD (2007) Integrated Tsunami Database for the World Ocean, Version 5.16 of July 31, 2007, CD-ROM, Tsunami Laboratory, ICMMG SD RAS, Novosibirsk, Russia. <http://tsun.sccc.ru/WinITDB.htm>

Kabanikhin S.I. (2009) Inverse and incorrect problems // Siberian Scientific Publishing, Novosibirsk, 309 p.

Kaistrenko, V. (1973) Reverse problem of a tsunami source restoration // Volny Tsunami, Trudy SakhNII, Vyp.29. P. 82-92 (in Russian).

Kajiura K. (1970) Tsunami source, energy and directivity of wave radiation // Bull. Earth. Res. Inst. Vol. 48. P. 835-869.

Kanamori H. (1972) Mechanism of tsunami earthquakes. // Phys. Earth Planet. Inter. Vol. 6. P.346-359.

Kanamori H. (1977) The energy release in great earthquakes // J. Geophys. Res. Vol. 82. P. 2981-2987.

Khakimzyanov G.S., Shokin Yu.I., Barakhnin V.B., Shokina N.Yu. (2001) Numerical Simulation of Fluid Flows with Surface Waves // Sib. Branch, Russ. Acad. Sci., Novosibirsk (in Russian).

Lobkovsky L., Baranov B. (1982) On the tsunami generation problem in the subduction zones // In: Processy vozbuzhdenia i rasprostranenia tsunami, Moscow, Institute of Oceanology. P. 7-17 (in Russian).

Long-wave runup models (1996) Editors: Yeh H., Liu P., Synolakis C. World Scientific, Singapore. 404 p.

Monaghan J.J.(1994) Simulating free surface flows with SPH // J. Comp. Phys. Vol. 110. P. 399-406.

Mori N., Takahashi T., Yasuda T., Yanagisawa H. (2011) Survey of 2011 Tohoku earthquake tsunami inundation and run-up // Geophysical Research Letters. Vol. 38, L00G14, doi:10.1029/2011GL049210.

NGDC/NOAA Tsunami Database (2012)
http://www.ngdc.noaa.gov/hazard/tsu_db.shtml.

Oger G., Doring M., Alessandrini B., Ferrant P. (2006) Two-dimensional SPH simulations of wedge water entries // J. Comput. Phys. 213. P. 803-822.

Okada Y. (1985) Surface deformation due to shear and tensile faults in a half-space // Bull. Seis. Soc. Am. Vol. 75, No.4. P.1135-1154.

Ovsyannikov L.V. (1981) Lectures on the Fundamentals of Gas Dynamics. Nauka, Moscow (in Russian).

Pelinovsky E.N., Mazova R.Kh. (1992) Exact analytical solutions of nonlinear problems of tsunami wave run-up on slopes with different profiles // Natural Hazards. Vol. 6, No. 3. P. 227-249.

Sato R. (1989) Handbook of Earthquake Fault Parameters in Japan, Kashima Press, Tokyo, Japan, 390 p. (in Japanese).

SEEDS Asia (2011) The Great Eastern Japan Earthquake: In depth damage report by affected cities and children, April 28.
<http://www.seedsasia.org/eng/projects-japan.html>.

Shokin Yu.I., Babailov V.V., Beisel S.A., Chubarov L.B., Eletsky S.V., Fedotova Z.I., Gusyakov V.K. (2008) Mathematical Modeling in application to regional tsunami warning systems operations // Computational Science and High Performance Computing III, Springer. Notes on numerical fluid mechanics and multidisciplinary design. Vol. 101. P. 52-68.

Shokin Yu.I., Khakimzyanov G.S. (2006) Predictor-corrector scheme preserving hydraulic jump // J. Comput. Techn. Vol. 11, No. 2. P. 92-99.

Soloviev S.L. (1972) On earthquake and tsunami occurrence in the Pacific Ocean // Volny Tsunami, Trudy SakhKNII, Yuzhno-Sakhalinsk. No. 29. P. 7-47 (in Russian).

Soloviev S.L. (1989) Mediterranean tsunamis and their relation to Pacific tsunamis. Fizika Zemli. No. 11. P. 3-17 (in Russian).

Soloviev S.L., Go Ch.N. (1974) A catalogue of tsunamis on the western shore of the Pacific Ocean. Academy of Sciences of the USSR, Nauka Publishing House, Moscow, 308 p. [Canadian Translation of Fisheries and Aquatic Sciences No. 5077, 1984, translation available from Canada Institute for Scientific and Technical Information, National Research Council, Ottawa, Ontario, Canada K1A 0S2, 447 p.]

Sugawara D., Minoura K., Imamura F., Takahashi T., Shuto N. (2005) A huge sand dome, ca. 700,000 m³ in volume, formed by the 1854 Earthquake Tsunami in Suruga Bay, Central Japan // ISET Journal of Earthquake Technology. Vol. 42, No. 4. P. 147-158.

Synolakis C.E. (1987) The runup of solitary waves // J. Fluid Mech. Vol. 185. P. 523-545.

Synolakis C.E. (1991) Tsunami Runup on Steep Slopes: How Good Linear Theory Really Is // Natural Hazards. Vol. 4. P. 221–234.

Takagi T. (1996) Finite element analysis in bench mark problems 2 and 3 // In: Long Wave Runup Models, Yeh H. et al (ed), World Scientific, Singapore. P. 258-264.

The Joint Tohoku Earthquake Tsunami Research Survey Group (2011) Field survey of the 2011 Tohoku Earthquake Tsunami by the National Tsunami Survey, Japan Soc. of Civil Eng., Tokyo.

Vacondio R., Rogers B., Stansby P., Mignosa P. (2012) SPH Modeling of Shallow Flow with Open Boundaries for Practical Flood Simulation // J. Hydraul. Eng. Vol 138, No. 6. P. 530-541.

Watanabe H. (1985) Catalog of Tsunamis and Their Damage in Japan, Tokyo University, 208 p.